



The  
University  
Of  
Sheffield.

## Shoe-Surface Tribology in Hard Court Tennis

**By:**

John Hale

A thesis submitted in partial fulfilment of the requirements for the degree of  
Doctor of Philosophy

The University of Sheffield  
Faculty of Engineering  
Department of Mechanical Engineering

August 2021

## Summary

A literature review was first conducted, covering rubber friction theory, sports shoe friction studies and biomechanics of tennis movements. A series of tests were then planned to address the gaps in knowledge highlighted by the literature review, the principal finding of which was that we are yet unable to determine, quantitatively or qualitatively, how shoe tread patterns influence friction on dry surfaces.

To address this problem, a tribological investigation was performed, starting with small scale rubber friction experiments, and ending with full-shoe analysis. The small-scale experiments examined the effect of rubber shape on friction using controlled, prismatic cuts of a commercially available rubber. It was observed that the friction between rubber blocks and a hard court surface, increased with the block length in the sliding direction. Whether these effects occur for different types of rubber was then investigated in a study which also used a model to explain the frictional effect of changes in rubber.

Analysis was then extended to tread elements from a real tennis shoe which were tested at loads and velocities close to those expected at the rubber-surface interface during the performance of hard court tennis slides. These identified topographical changes to the tread samples that significantly altered the sliding friction for different directions.

The small-scale friction tests identified shape parameters that influence the friction of rubber, but this was limited to the testing of simple geometries. To investigate whether these same identified parameters (tread length, contact area etc.) influence the friction of full shoes, a pre-existing test device was modified, with which the friction of full shoes, in multiple orientations, was measured. These experiments were coupled with a novel tread analysis technique, allowing the quantification of parameters (contact area, overall leading edge length etc.) previously hypothesised to be important to rubber friction.

No test device is yet able to test the friction of tennis shoes at representative slide speeds of hard court slides. This issue was addressed in the design of a new test device that could be used to better evaluate the sliding performance of full tennis shoes.

The outputs of this thesis detail how the friction of rubber is affected by shape, viscoelastic modulus and wearability. It also presents a new tread quantification method that shows, when testing the friction of shoes which vary only by tread pattern, that shoe friction increases with increased contact area. These outputs, and others from this thesis, improve our understanding of shoe-surface tribology, and can inform footwear manufacturers and designers, to design better performing footwear for hard court tennis.

## Nomenclature

|                 |  |
|-----------------|--|
| 1D              | One-dimensional                                  |
| 2D              | Two-dimensional                                  |
| $a_T$           | Time-temperature shift factor                    |
| $A_0$           | Nominal area of contact                          |
| $A_c$           | Real area of contact                             |
| ANOVA           | Analysis of Variance                             |
| $b$             | Base width                                       |
| $b_1$           | HK open parameter                                |
| $C_1, C_2, C_3$ | Constants  |
| $C^{1D+}$       | A form of one-dimensional power spectral density |
| CA              | Contact area                                     |
| CAD             | Computer aided design                            |
| CoF             | Coefficient of Friction                          |
| CPR             | Court Pace Rating                                |
| $C(q)$          | Power spectrum                                   |
| $d$             | Diameter   |
| DMA             | Dynamic Mechanical Analysis                      |
| E               | Young's modulus                                  |
| $E^*$           | Complex modulus                                  |
| $E', ReE$       | Storage / real modulus                           |
| $E'', ImE$      | Loss / imaginary modulus                         |
| EVA             | Ethylene-vinyl acetate                           |
| f               | Frequency  |
| $\Delta f$      | Frequency range                                  |
| $F$             | Friction force                                   |
| FFT             | Fast Fourier transform                           |
| FFW             | Forefoot width                                   |
| $G^*$           | Complex shear modulus                            |
| $G'$            | Storage / real shear modulus                     |
| $G''$           | Loss / imaginary shear modulus                   |
| $g_s$           | Hedges's g                                       |
| GW              | Greenwood and Williamson                         |
| $h$             | Base length                                      |
| H               | Hurst exponent                                   |
| $\mathcal{H}$   | Hardness   |
| $h_{rms}$       | Root mean square roughness                       |
| $h'_{rms}$      | Root mean square slope                           |
| HK              | Heinrich and Klüppel                             |

|                               |   |
|-------------------------------|---|
| HPS                           | Horizontal pull slip meter                                      |
| $i$                           | Imaginary number  |
| IH                            | Insole height   |
| ITF                           | International tennis federation                                 |
| $I_{xx}$                      | Second moment of area   |
| $k$                           | Beam stiffness  |
| $K$                           | Archard wear coefficient  |
| $L$                           | Measurement length  |
| LABINRS                       | French national research and safety institute laboratory device |
| LE                            | Leading edge  |
| Loss $\delta$ , $\tan \delta$ | Loss tangent  |
| LVDT                          | Linear variable differential transformer                        |
| $M, M_1, M_2$                 | Mean  |
| MDF                           | Medium-density fibreboard                                       |
| MH                            | Midsole height  |
| $N$                           | Normal force  |
| $n, n_1, n_2$                 | Sample size   |
| NBR                           | Nitrile Butadiene Rubber  |
| OH                            | Outsole height  |
| $p$                           | Pneumatic cylinder pressure                                     |
| PDP                           | Produce design process  |
| PL                            | Parallel length   |
| PMMA                          | Poly (methyl methacrylate)                                      |
| $P(q)$                        | Persson contact mechanics function                              |
| PSD                           | Power spectral density  |
| $q$                           | Wavevector  |
| $q_0$                         | Small wavevector cut-off  |
| $q_1$                         | Large wavevector cut-off  |
| $q_L$                         | Roll-off wavevector   |
| $R$                           | Constant  |
| $R_a$                         | Arithmetical mean roughness                                     |
| RGB                           | Red-green-blue  |
| rpm                           | Revolutions per minute  |
| $R_q$                         | Root mean square roughness                                      |
| $R_z$                         | Average height of maximum peak to valley                        |
| RMS                           | Root Mean Square  |
| $S_a$                         | Arithmetical mean surface height                                |
| SBR                           | Styrene butadiene rubber  |
| SD, $SD_1, SD_2$              | Standard deviation  |

|                    |  |
|--------------------|--|
| $Sh_A$             | Shore A hardness                                   |
| $S_q$              | Surface root mean square height                    |
| $S(q)$             | Persson asperity induced correction                |
| $S(\omega)$        | Power Spectral Density as a function of wavelength |
| $t$                | Time   |
| $T$                | Temperature  |
| TH                 | Tread height                                       |
| $T_q(t)$           | Frictional heating function                        |
| $T_r$              | Reference temperature                              |
| TSST               | Tennis shoe surface tester                         |
| UMT                | Universal mechanical tester                        |
| UoS                | University of Sheffield                            |
| $v$                | Speed  |
| $W$                | Normal load  |
| WLF                | Williams-Landry-Ferry                              |
| YT                 | Y-theta  |
| $z_p$              | HK asperity indentation parameter                  |
| $\gamma$           | Surface free energy                                |
| $\delta$           | Phase difference                                   |
| $\varepsilon_0$    | Measured strain                                    |
| $\lambda$          | Wavelength   |
| $\mu$              | Coefficient of friction                            |
| $\mu_{adhesion}$   | Adhesive coefficient of friction                   |
| $\mu_{eff}$        | Effective coefficient of friction                  |
| $\mu_{hysteresis}$ | Hysteretic coefficient of friction                 |
| $\mu_k$            | Dynamic coefficient of friction                    |
| $\mu_{pred}$       | Predicted coefficient of friction                  |
| $\mu_s$            | Static coefficient of friction                     |
| $\sigma_0$         | Nominal contact pressure / applied stress          |
| $\sigma_s$         | Interfacial shearing stress                        |
| $\nu$              | Poisson's ratio                                    |
| $\phi$             | Sliding direction                                  |
| $\psi$             | Wear rate  |
| $\omega$           | Frequency  |

# Contents

|  |    |
|--|----|
| Summary .....  | 1  |
| Nomenclature .....   | 2  |
| Acknowledgements .....   | 7  |
| Publications .....   | 8  |
| Outline of Thesis .....  | 9  |
| Research Highlights .....  | 10 |
| 1 Introduction .....   | 11 |
| 1.1 Aim and Objectives .....   | 13 |
| 2 Literature Review .....  | 15 |
| 2.1 Theory of Rubber Friction on Rough Surfaces .....  | 15 |
| 2.2 Biomechanics of Hard Court Tennis Slides .....   | 36 |
| 2.3 Mechanical Analysis.....   | 39 |
| 3 Surface and Rubber Characterisation .....  | 45 |
| 3.1 Hard Court Characterisation.....   | 45 |
| 3.2 Rubber Characterisation .....  | 47 |
| 3.3 Combining Surface and Rubber Measures.....   | 51 |
| 3.4 Conclusion .....   | 55 |
| 4 The Effect of Rubber Tread Shape on Friction .....   | 56 |
| 4.1 Introduction .....   | 56 |
| 4.2 Methodology .....  | 58 |
| 4.3 Results.....   | 61 |
| 4.4 Discussion .....   | 63 |
| 4.5 Conclusion .....   | 66 |
| 5 Using a Simplified Model for Dry Rubber Friction .....   | 68 |
| 5.1 Introduction .....   | 68 |
| 5.2 Methodology .....  | 69 |
| 5.3 Results.....   | 73 |
| 5.4 Discussion .....   | 76 |
| 5.5 Conclusion .....   | 78 |
| 6 Analysis of the Friction and Wear Mechanisms present during Hard Court Specific<br>Movements ..... | 79 |
| 6.1 Introduction .....   | 79 |
| 6.2 Methodology .....  | 80 |
| 6.3 Results.....   | 85 |

|   |     |
|---|-----|
| 6.4 Discussion .....  | 89  |
| 6.5 Conclusions .....   | 92  |
| 7 The Influence of Tennis Shoe Tread Contact Parameters on Friction ..... | 94  |
| 7.1 Introduction .....  | 94  |
| 7.2 Methodology .....   | 95  |
| 7.3 Results.....  | 104 |
| 7.4 Discussion .....  | 107 |
| 7.5 Conclusion .....  | 110 |
| 8 A Frictional Comparison of Tennis Shoes .....                           | 112 |
| 8.1 Introduction .....  | 112 |
| 8.2 Methodology .....   | 112 |
| 8.3 Results.....  | 115 |
| 8.4 Discussion .....  | 118 |
| 8.5 Conclusion .....  | 120 |
| 9 Novel Tennis Shoe Friction Device – Design and Development.....         | 122 |
| 9.1 Product Design Process.....   | 122 |
| 9.2 Research Requirements.....  | 124 |
| 9.3 Product Specification .....   | 125 |
| 9.4 Conceptual Device Design .....  | 127 |
| 9.5 Concept Evaluation and Selection.....                                 | 129 |
| 9.6 Complete Device Design.....   | 130 |
| 9.7 Device Manufacture .....  | 131 |
| 9.8 Device Output Simulation and Interpretation .....                     | 131 |
| 9.9 Device Limitations and Conclusion.....                                | 134 |
| 10 Discussion .....   | 136 |
| 10.1 Key Outcomes .....   | 136 |
| 10.2 Thesis Limitations .....   | 138 |
| 10.3 Overall Impact and Potential Future Use.....                         | 139 |
| 10.4 Tread Design Recommendations .....                                   | 141 |
| 11 Conclusions .....  | 143 |
| 12 References.....  | 145 |
| Appendix.....   | 153 |

## **Acknowledgements**

Firstly, I thank my supervisor, Professor Matt Carré, who supported me throughout this project. His confidence in me, and support of my work, was essential to the completion of this PhD, and is deeply appreciated.

I would also like to thank all the academic staff at the University of Sheffield who have helped me complete this thesis, including Professor Roger Lewis and Dr Jem Rongong. I want to thank the technical staff at Sheffield, notably Jamie Booth, who helped design and build test equipment. I also thank my sponsors, the EPSRC and ITF, in particular, Dr James Spurr and Jamie Capel-Davies.

I want to thank my colleagues and friends, both in HIG and the tribology CDT. I will miss our Friday C4 lunches and the HIG days out. Thanks is due also, to Sam Hedges for his friendship over the last four years.

I couldn't have completed this thesis without the support, encouragement and love of my family. My sisters, Lucy and Immy, are always my greatest inspiration. In times of struggle, their examples have motivated me to persevere. I thank Dad for his unwavering faith, and Mum, for her crucial help with my education, as well as her overall guidance and care. This thesis, and anything I accomplish, is owed to her.

## **Publications**

### **Directly from the content of this thesis**

Hale, J., Lewis, R., & Carré, M. J. (2020). Rubber friction and the effect of shape. *Tribology International*, 141, 105911. doi:10.1016/j.triboint.2019.105911

Hale, J., Lewis, R., & Carré, M. J. (2020). Shoe–Surface Tribology in Hardcourt Tennis. In *Multidisciplinary Digital Publishing Institute Proceedings*, 49(1), 90. doi:10.3390/proceedings2020049090

Hale, J., Lewis, R., & Carré, M. J. (2021). Effect of simulated tennis steps and slides on tread element friction and wear. *Sports Engineering*, 24(1), 1-9. doi:10.1007/s12283-021-00343-4

### **Additional**

Hale, J., O'Connell, A., Lewis, R., Carré, M. J., & Rongong, J. A. (2020). An Evaluation of Shoe Tread Parameters using FEM. *Tribology International*, 153, 106570. doi:10.1016/j.triboint.2020.106570

### **Presentations**

Content of this thesis has been presented in the form of posters or oral presentations at the following events:

- TriboUK - Sheffield, April 2018
- Footwear Science Meeting – Staffordshire, April 2018
- Leeds-Lyon Tribology Symposium – Lyon, September 2019
- Institute of Physics Winter Tribology Fair – Sheffield, January 2020
- International Sports Engineering Association Seminar Day – Sheffield, February 2020
- International Conference on Biotribology – Online, April 2021

## Outline of Thesis

An introduction to the problem is provided in Chapter 1. Chapter 2 then presents a literature review which address this problem, focussing on rubber tribology, and using this to understand how changes in rubber design affect sliding friction. The aims of the thesis are then presented at the end of Chapter 2.

Chapter 3 gives detail on the measures used in the current friction models to categorise rubber and hard court surfaces. This chapter provides information on how certain measures used throughout the thesis (hard court Power Spectral Density (PSD) and viscoelastic master curves) were obtained.

A set of small-scale rubber friction experiments are presented in Chapter 4. These experiments were conducted between a hard court surface sample and three shapes of rubber to investigate how rubber shape influences friction. Chapter 5 goes into more detail on this subject, with experiments on two different rubbers, observing whether the findings of Chapter 4 are relevant to another rubber type.

Chapter 6 progresses this small-scale analysis to tread elements from a real tennis shoe tread, testing them at loads determined from biomechanical analysis on hard court steps and slides, and sliding speeds close to that observed in real tennis play.

Chapter 7 explores whether the shape parameters found to affect friction in small scale experiments, have the same effect during the sliding of full tennis shoes. To do this, a contact area and tread quantification method is introduced and utilised. In Chapter 8, the methods used in Chapter 7 are used on a range of tennis shoes to evaluate their frictional performance.

Due to mechanical limitations, the full shoe friction tests in Chapters 7 and 8 could not be conducted at slide speeds representative of hard court sliding. The design process and final design of a tennis shoe friction test device, capable of testing the friction of tennis footwear at loads and slide speeds characteristic of hard court sliding, is proposed in Chapter 9.

Chapter 10 gives a review of the findings of this thesis on rubber- and shoe-surface friction, highlighting the trends observed throughout experiments, and how research could be continued in this field. Chapter 11 then concludes the thesis with references. An appendix is provided at the end.

## Research Highlights

- How the shape of rubber influences friction on dry surfaces is better understood. For one rubber, friction increased as shape length (in the sliding direction) increased, while the opposite occurred for a rubber with improved wearability.
- A novel shoe tread quantification method is presented, providing more detail than current tread contact methods e.g. ink print method.
- Frictional analysis of eight commercially available tennis shoes. Comparison of two shoes varying only in tread pattern, shows an increase in contact area to produce an increase in friction.
- Design of a test device to imitate the loads and slide speeds of hard court slides.

# 1 Introduction

Sports shoe-surface friction has been linked to the overall sporting performance and injury-risk of athletes [1–4]. Studies into the frictional performance of sports shoes range from studded football cleats to rubber soled tennis shoes [5,6]. While football cleats use methods of interlocking studs with sub-surface soil to ensure high friction, tennis shoes utilise the high-friction properties of rubber to improve shoe-surface friction, allowing athletes to quickly push off and change direction.

The rubber-surface interaction in tennis is a complex one, whose friction depends on numerous factors, one of which is the corresponding surface. Professional tennis is played on many different surface types including: grass, clay and acrylic hard courts. These surfaces affect the frictional performance of footwear in completely different ways. While surface moisture from grass lubricates the shoe-surface contact on grass courts [7] and sand particles act as third-body rolling elements to reduce friction on clay courts [8], the frictional influencers for hard courts are less clearly defined. Research into shoe-surface friction on hard courts includes biomechanical [9] and mechanical analysis [10].

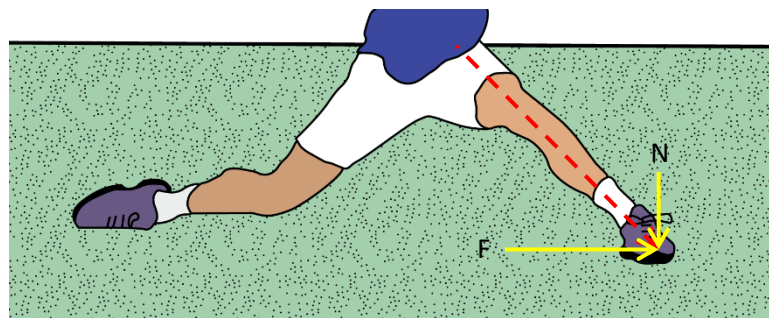


**Figure 1.1** Schematic of a hard court tennis slide.

A hard court slide in tennis is a movement performed to return a shot by sliding across the playing surface. This allows tennis players to quickly reposition themselves post-shot. A recent study found controlled sliding to be an efficient, effective technique [11]. Sliding incidence analysis performed on the men's US and Australian Open finals between 2011 and 2016 showed that, in rallies that consist of 10 shots or more, controlled slides made up around 28% of all shots played [12]. Furthermore, the percentage of slides is increasing; between 2011 and 2015, sliding incidence rose 7% [12].

To perform a hard court slide an athlete is required to, while running, plant their foot on the surface, often with their planted leg at an acute angle to the surface (Figure 1.1). The combination of high running velocity, high load (most of the tennis player's weight) and a shallow leg angle, means the ratio of normal to tangential forces is in favour of the tangential.

Sliding occurs if the Coefficient of Friction ( $\mu$ ) between the contacting shoe outsole and hard court tennis surface is low enough.

If the shoe-surface  $\mu$  is too high, the player must further reduce their leg angle (further increasing the ratio of tangential to normal load) to initiate a slide, or a slide will not occur. Instead, the player must perform a series of stuttered steps to change direction, which due to the repetitive transient loads experienced by the player, could lead to overuse injury at the ankle [11]. Conversely, if the shoe-surface  $\mu$  is too low, although a slide will be easier to perform (leg angle will not need to be as shallow) it may result in the athlete not being able to recover from the slip quick enough. Furthermore, low  $\mu$  at the shoe-surface interface often results in uncontrolled slips which can cause harm to the tennis player and detrimentally affect their performance. A range of optima  $\mu$  values is desired to successfully slide on a hard court tennis court.



**Figure 1.2** The outsoles of three different hard court tennis shoes.

The  $\mu$  present during hard court slides is largely dependent on the characteristics of the two contacting bodies: the tennis shoe outsole and the hard court surface. As the player has no influence on the court characteristics, the greatest way a tennis player can change the  $\mu$ , and hence improve their chances of performing successful slides, is through the selection of their footwear. The huge variance in tennis shoes designed for hard court tennis is easily recognisable (Figure 1.2). The most noticeable difference is in the tread patterns on the shoe's outsole. Tread patterns vary from make to make and model to model. Despite constant iterative changes being made to tread patterns through the design of new shoe models, very little is reported in literature that explains the frictional effects of tread on dry surfaces. In fact,

it can be speculated that this lack of knowledge is exactly the reason for these constant tread pattern modifications, with designers working in a reactive approach to find an optimal tread pattern through trial and error and user feedback. The lack of scientific understanding of the frictional influence of shoe tread on dry surfaces means the consumer is led solely by the bias marketing of shoe manufacturers.

Another way in which tennis shoe outsoles differ, that is less easily noticed by the consumer, is the grade of rubber used in the outsole. Ura (2016) performed modulus measurements on two types of tennis shoes marketed for hard court tennis [12]. The Young's Modulus ( $E$ ) of the shoe outsole rubbers was different, indicating different grades of rubber. This is likely to cause frictional variances, but again little is reported in scientific literature as to how differences in outsole rubber modulus affects shoe-surface friction. All tennis shoes designed for hard court tennis have an outsole made of rubber except for the Wilson Glide. The Wilson Glide is a shoe designed with a plastic component in the rubber outsole to improve hard court sliding [13]. Although, the Wilson Glide can be considered an imaginative approach to encouraging sliding and thus improving performance via quicker repositioning post-shot, it is not yet used by top-flight tennis players in competition, and therefore has little relevance to the modern game. For this reason, only rubber soled shoes will be discussed in the remainder of this thesis.

When tennis players select/purchase their footwear, they have very little, or no scientific rationale to support that choice. It is also of interest to the International Tennis Federation (ITF) to understand how footwear is changing and its influence on the nature of tennis.

To begin to understand how tread patterns and rubber grades affect shoe-surface  $\mu$  during hard court slides, a knowledge of rubber tribology theory is first required.

## **1.1 Aim and Objectives**

### *Aim*

The aim of this thesis was to improve the overall understanding of rubber tribology during sliding on dry surfaces, and then apply this knowledge to the case of tennis shoe friction on hard court surfaces.

This was achieved through a series of experiments ranging from simple rubber block experiments to full shoe analysis. This research also incorporates the design and development of a full-shoe friction test device which imitates key aspects hard court slides. In turn, the friction of real tennis shoes can be evaluated in a way that relates to a real tennis movement.

## Objectives

- **Surface and Rubber Characterisation** – Obtain viscoelastic master curves for rubbers, and PSDs of hard court tennis surfaces. Determine how these measures can be used to predict friction.
- **Rubber Friction Experiments** – Using rubber samples that vary in shape and rubber grade, develop a deeper understanding of the tribological mechanisms present as rubber slides over hard court surfaces, and the effect of tread.
- **Full-Shoe Friction Experiments** – Determine whether the frictional influencers identified in the small-scale rubber friction experiments affect the friction of full shoes with complex tread patterns.
- **Tennis Slide Device Design** – Design a full shoe test device which can imitate hard court slide parameters (slide speed, pressures, etc.) in tennis, and measure friction.

## Flow Diagram

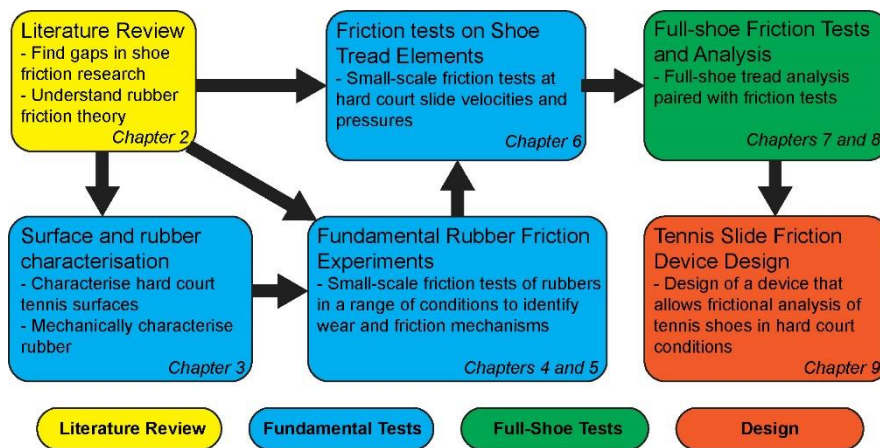


**Figure 1.3** How the work in this thesis is linked.

The diagram in Figure 1.3 compartmentalises the work shown in this thesis, showing how it links together. The chapters where this work appears is noted.

## 2 Literature Review

This chapter explores the literature concerning the friction of rubber on rough surfaces, biomechanical analysis of hard court slides, and mechanical studies performed to understand the relevant frictional characteristics. The chapter ends with some overall critiques of the current literature and the aims and objectives of the thesis.

### 2.1 Theory of Rubber Friction on Rough Surfaces

#### 2.1.1 Background

Research investigating the frictional behaviour of rubber began in the 1940's with the experiments of Roth et al. [14], through to Schallamach [15] and Greenwood and Tabor [16]. Studies investigated both the static coefficient of friction ( $\mu_s$ ) and the dynamic coefficient of friction ( $\mu_k$ ) of rubber as it slides across a surface. Roth et.al [14] found both rubber friction coefficients to be speed and surface roughness dependent, Schallamach [15] theorised that the frictional force of rubber is proportional to the real area of contact ( $A_C$ ), and Greenwood and Tabor [16] described the frictional force of sliding as a contribution of different natures of energy losses, notably from adhesion and hysteresis. Adhesion refers to the forming and shearing of interfacial atomic bonds, and hysteresis relates to the internal bulk friction within the rubber, originating from the internal damping that occurs when rubber is loaded. This remains to be the general understanding that underpins dry-surface viscoelastic friction today.

Though these two frictional mechanisms have been known for the last 60 years, accurate modelling of rubber friction (on dry surfaces) only emerged around 20 years ago [17]. The arrival of these models coincides with the emergence of contact mechanics theories that consider the multiscale entirety of a surface's roughness.

#### 2.1.2 Contact Mechanics

Real surfaces are never truly flat. Magnifying even the smoothest surfaces reveals roughness in the form of asperities. Further magnification of these asperities will reveal another layer of roughness (Figure 2.1). This process of magnifying roughness can continue into the atomic scale. Therefore, to predict the  $A_C$  between two bodies, as many scales of roughness as possible must be considered. The ratio of nominal contact area ( $A_0$ ) to  $A_C$  has strong implications to the friction and wear between two bodies [18]. Contact mechanics can be used to predict this ratio and hence make predictions about the tribological behaviour of an interaction.

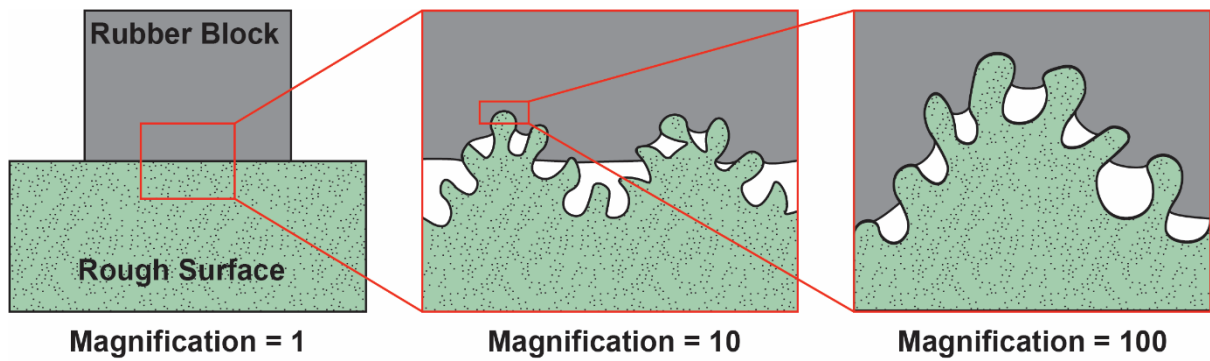


**Figure 2.1** Contact between rubber and a surface with multiscale roughness. As magnification increases, a smaller true area of contact is realised.

In 1882 Hertz produced a contact mechanics model to estimate the  $A_c$  between two contacting bodies. The Hertz contact model assumes a frictionless contact between two smooth, elastic bodies, which as we know, is not accurate to real interactions. Archard adapted Hertz's model to consider rough surfaces [19]. To do this, surface roughness was described as a series of equally spaced asperities of idealised hemi-sphere shape. To consider the multiscale nature of surface roughness, each asperity is made up of smaller hemi-spheres in a fractal-like design. Greenwood and Williamson (GW) again adapted Archard's contact model but also considered the random nature of asperity heights [20]. The GW model utilises a Gaussian distribution to control this. Although the Archard and GW contact models somewhat consider the multiscale nature of surface roughness, they do not consider its entirety, which can cross four decades (macro to nano). The Persson contact model accounts for this through the involvement of a surface roughness Power Spectral Density (PSD) [21]. To understand this measure of surface roughness, the surface roughness trace is interpreted as a one-dimensional (1D) wave made up of numerous waves of different wavelengths ( $\lambda$ ). A simplified single scale example of this is displayed in Figure 2.2.

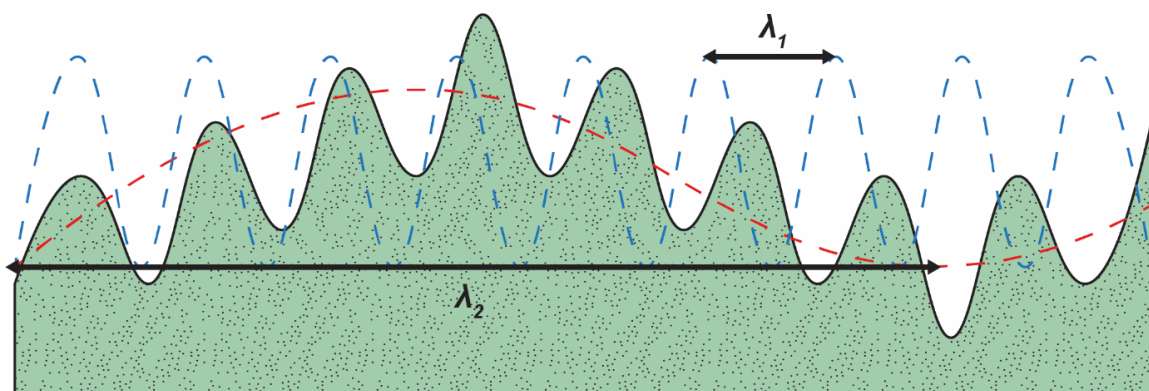


**Figure 2.2** A surface roughness trace as a single wave can be split into its frequencies ( $\lambda_1$  and  $\lambda_2$ ). This is commonly done using a Fourier Transform.

Figure 2.2 only shows roughness on a single scale and with an idealised shape. Real surface roughness traces are more chaotic in nature, and as a result, are made up of multiple wavelengths over multiple decades. A PSD accounts for all these wavelengths (up to the measurement resolution). Figure 2.3 is an asphalt road surface roughness PSD plot obtained using two different measurement techniques [22].

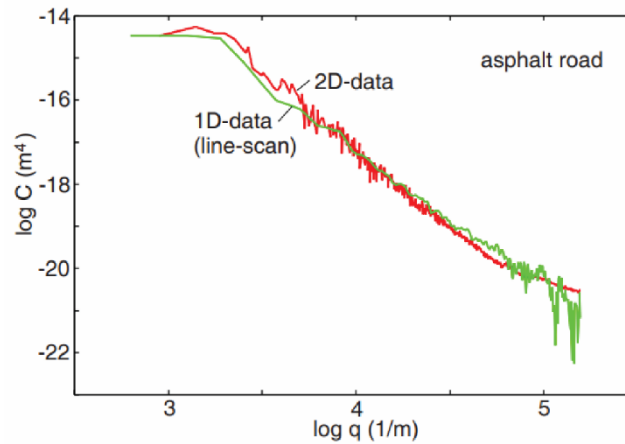


**Figure 2.3** An example PSD of an asphalt road surface measured using 1D and 2D measurement techniques. Image taken from [22].

A surface roughness PSD can be mathematically defined as the squared modulus of the Fourier transform of a surface roughness trace, and provides a measure of all the wavelengths that make up the surface roughness trace, plotting them as wavevectors ( $q = 2\pi/\lambda$ ). Persson states that for self-affine fractal surfaces, the power spectrum ( $C(q)$ ) displays the power-law relationship shown in Equation 2.1 [23].

$$C(q) \approx q^{-2(H+1)}$$

### Equation 2.1

Where  $H$  refers to the Hurst exponent of the measured surface. This power-law relationship means that where the PSD (on a log-log scale) is linear, self-affinity is displayed (such as that shown between  $q_0$  and  $q_1$  in Figure 2.4). A self-affine surface is one that, at different magnifications, looks the same in profile but scaled differently in  $x$  and  $y$  directions.

Figure 2.4 introduces some notable regions of a PSD plot. The roll-off vector ( $q_L$ ), the large wavevector cut-off ( $q_1$ ) and the small wavevector cut-off vector ( $q_0$ ).  $q_0$  relates to the diameter of the largest particles that make up the surface (for road surfaces, the largest stone particles used in the asphalt).  $q_1$  relates to the diameter of the smallest particles on the surface.  $q_L = 2\pi/L$  where  $L$  is the measurement length.

When attempting to characterise surface roughness, PSD provides a greater description than single value measures such as  $R_a$ ,  $R_q$  and  $R_z$  [24]. It has also been stated that each decade in surface roughness holds roughly equal importance in the viscoelastic friction of a sliding rubber [25], providing further rationale to obtain PSD measures.

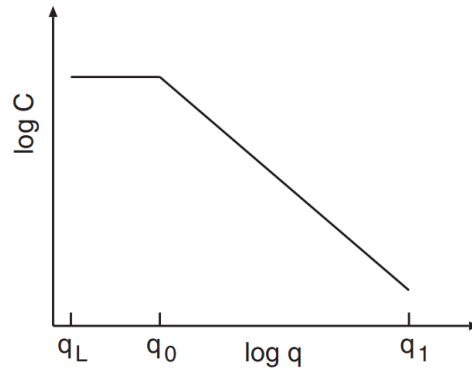


**Figure 2.4** Schematic of a simple PSD plot.  $q_L$ ,  $q_0$  and  $q_1$  correspond to key areas of the plot. Image taken from [89].

Taking the PSD approach to quantifying surface topography, two analytical models have emerged which aim to predict the frictional forces needed to slide rubber across rough surfaces; the Heinrich and Klüppel model (HK) (described in [26]), and the Persson model [21].

### 2.1.3 Current Analytical Rubber Friction Models

Differences between the HK and Persson analytical models are due to disagreement about effective frictional mechanisms. Both agree that the frictional force observed as a rubber substrate slides across a rough surface can be the result of adhesive and hysteretic contributions (neglecting melting or tearing of the rubber). However, the Persson model (for sliding rubber ( $E \approx 10$  MPa) on a rough surface (Root Mean Square (RMS) roughness ( $>1 \mu\text{m}$ )) neglects the adhesive contribution to dynamic friction [27], believing its contribution to be infinitesimal in relation to the hysteretic contribution, especially at high slide speeds ( $\geq 1$  m/s). Conversely, the HK model believes adhesion to have a substantial influence on the overall sliding friction in the same scenario [28].

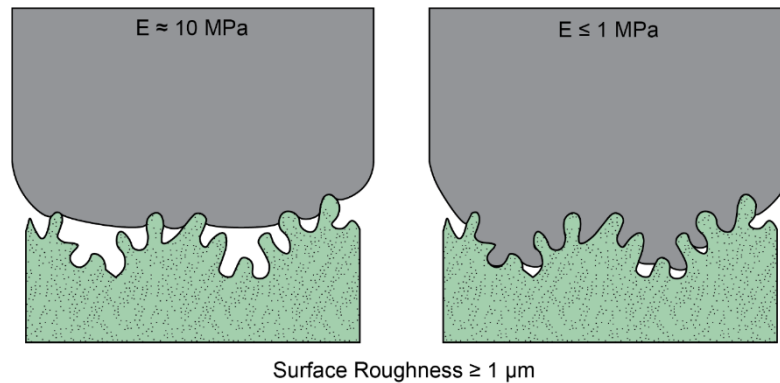


**Figure 2.5** Low modulus rubber can fill roughness and in turn produce a larger real area of contact. There are spaces between contact areas which can lead to crack propagation breaking of adhesive bonds.

Measuring the adhesion between rubber and a surface can prove difficult. A common method used to measure the magnitude of adhesive forces during in an interaction are pull-off experiments [29]. Here, a sphere and flat surface are pressed into contact with known force. The two bodies are then pulled away from one another and the pull-off force is measured. The force used to contact the two bodies is then compared to the pull-off force. For materials such as metals, glass etc, any increase in pull-off force (in relation to contact force) can be attributed to the breaking of adhesive bonds formed during contact. However, using this form of measurement for viscoelastic materials (such as rubbers) is not routine. To illustrate why this is, consider rubber contacting a rough glass surface. As contact is made and contact pressure increases, the rubber is compressed by the surface asperities which elastically deforms the rubber. Consequently, due to rubber's viscoelastic nature, the response of this compressive force changes over time (contact area increases over time as the material relaxes [30]). These response forces produce a push-off force (reducing with time) which works against adhesion, making it easier to retract the bodies from one another when contact time is low. These experiments have been performed by Fuller and Tabor [31] and Briggs and Briscoe [32] who, considering these factors, concluded that as roughness increases, adhesion drastically decreases. Persson and Tosatti [33] further investigated the roughness-adhesion relationship relating to rubber-rough surface interactions. The same pull-off experiments were conducted as to those previously mentioned, but with an understanding of surface roughness on multiple scales, and it was investigated in greater detail the method of detachment between rubber and a surface. For rubber with  $E \approx 10 \text{ MPa}$ , no significant additional force was required to pull-off the rubber ball (when substrate roughness exceeds  $1 \mu\text{m}$ ). Rubbers of very low modulus ( $E < 1 \text{ MPa}$  (similar to the elasticity of adhesives used on sticky tape)) produced high pull-off forces as they were easily squeezed between the multiscale roughness, increasing the true

contact area which increases the adhesive force (see Figure 2.5). Additionally, a crack propagation type detachment occurs from areas where the rubber doesn't contact the surface, such as those that can be seen in the roughness troughs in Figure 2.5. This detachment drastically reduces the adhesive forces when movement is initiated between the contacting bodies.

These experiments, and the further studies of Tiwari et al. [29], show that adhesion is present when rubbers contact rough hard court surfaces. It is believed though that these adhesive forces have no significant influence over sliding friction in hard court tennis, as it is believed the sliding motion causes a crack propagation reduction of adhesion, similar to that shown by Briggs and Briscoe [32], Persson and Tosatti [33] and Tiwari et al. [29]. The belief that hysteresis friction dictates the friction of shoe rubber on hard court surfaces (with adhesion being negligible), is assumed due to the Young's Modulus of the rubber typically being above 1 MPa and the rough texture of hard court tennis surfaces. The dominance of hysteresis over adhesion is also supported by how tyre-road friction experiments have shown a temperature dependence of the  $\mu$  which strongly reflects the temperature dependence of the viscoelastic properties of rubber [23]. That being said, in a recent publication [34], Persson recognised more openly the influence of adhesion to the friction between rubber and road surfaces, though little fundamental rationale is given for this [35].

Since there is no definitive evidence stating that adhesion does or does not influence the sliding friction of rubber, it is still being discussed in scientific literature [25,36]. In turn, when investigating any rubber-rough surface friction, thought must be given to the role of adhesion, regardless of how insignificant it may prove to be. In this spirit, both analytical approaches to predicting the sliding friction of rubber are considered in this thesis. By doing this, insight is provided as to the frictional mechanisms dominating the interaction and hence how changing different parameters (such as surface roughness, rubber type etc.) influences the overall friction produced.

#### 2.1.4 Persson Model

The Persson friction model predicts the dynamic friction ( $\mu_k$ ) of a rubber block sliding over a randomly rough surface. This model, as mentioned previously, predicts hysteresis to be the dominant frictional mechanism and is written as follows (Equation 2.2):

$$\mu(t) = \frac{1}{2} \int_{q_0}^{q_1} q^3 C(q) S(q) P(q) \cdot dq \times \int_0^{2\pi} \cos\phi \operatorname{Im} \frac{E(qv(t)\cos\phi)}{(1-v^2)\sigma_0} \cdot d\phi$$

**Equation 2.2**

Where  $q$  refers to the wavevectors displayed by PSD,  $v$  is sliding speed,  $P(q)$  is a contact mechanics function (utilising the Persson contact theory mentioned in Section 2.1.2),  $S(q)$  is an asperity induced deformation correction, and  $E(qv(t)\cos\phi)$  is a function of the complex modulus of the rubber. How these inputs relate to the sliding friction of rubber can be understood by considering rubber sliding over the idealised roughness in Figure 2.6.

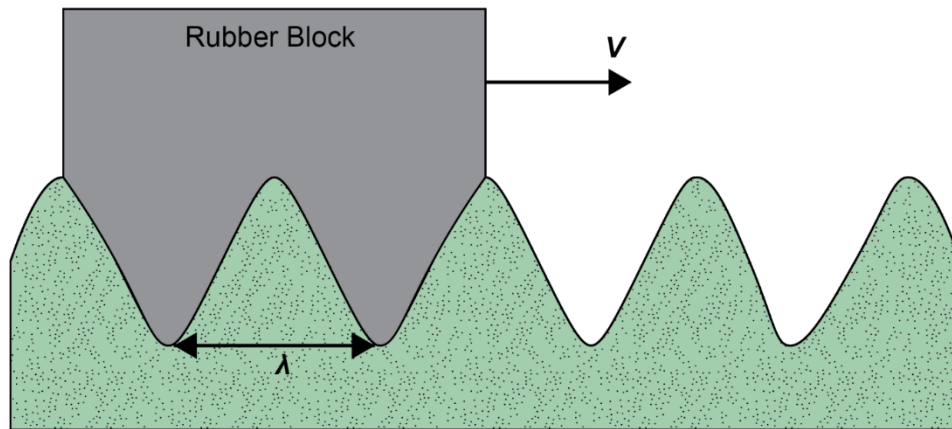


**Figure 2.6** A rubber block moving over a single wavelength surface.

At a constant speed ( $v$ ), these idealised surface asperities exert perturbing frequencies of vibration to the rubber of order  $\omega = v / \lambda$ . The rubber is cyclically deformed at this frequency ( $\omega$ ) resulting in the internal damping of the rubber which dissipates energy. This dissipated energy contributes, and in the case of the Persson model (Equation 2.2), accounts for the entirety of the frictional force, neglecting frictional heat. At  $v > 1$  mm/s it is theorised that frictional heating has a strong influence over dynamic friction (this is explored further in Section 2.1.9).

To understand the viscoelastic response of a rubber at a set frequency, Dynamical Mechanical Analysis (DMA) (Figure 2.7) can be conducted on the rubber, where the frequency that is produced by the sliding is used to determine the rubber's modulus. However, as real surfaces have asperities on multiple scales, the frequencies vibrating the rubber are on multiple scales also. Due to the small size of asperities present, frequencies can be as high as  $10^7$  Hz. Such high frequencies cannot be produced directly by DMA. Instead, the time-temperature relationship of viscoelasticity must be used to determine the modulus across the broad frequency range.

The modulus of rubber is time-temperature dependent. At a set frequency, increasing temperature reduces modulus (increasing free volumes and chain movements within the rubber). At a constant temperature, increasing frequency increases the rubber's modulus (molecular chains do not have time to respond). Using the time-temperature equivalence

principle, master curves can be produced which detail the modulus of rubber outside achievable frequency measurement ranges [37].

The viscoelastic master curves shown in Figure 2.8 are for a tyre tread rubber, detailing how the storage ( $E'$  or  $ReE$ ) and loss ( $E''$  or  $ImE$ ) modulus change with frequency. Complex elasticity ( $E^*$ ) can be calculated from the storage and loss modulus as shown in Equation 2.3:

$$E^* = E' + iE''$$

**Equation 2.3**

An  $E^*$  curve is used by Persson in both the contact mechanics and friction models.

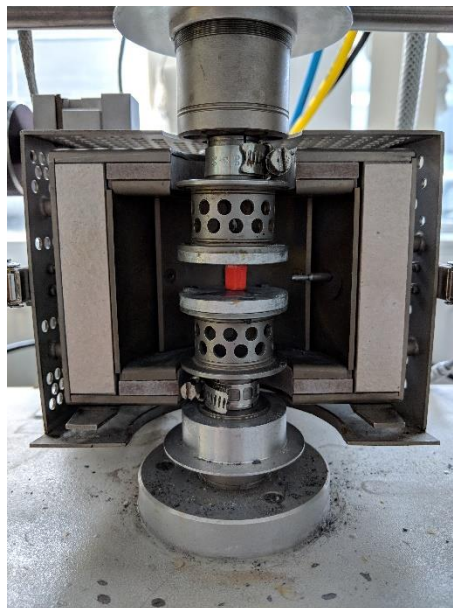


**Figure 2.7** DMA set-up with shoe outsole rubber glued between two plates. The chamber is closed during testing so that temperature can be controlled.

With an  $E^*$  master curve and surface roughness wavelengths (or wavevectors ( $q$ ) from a PSD), a range of  $E^*$  values corresponding to the oscillating frequencies experienced during sliding can be obtained. In turn, the hysteretic response of the rubber is predicted. This understanding of the hysteretic contribution to rubber friction is also the basis of the hysteretic component of the HK model.

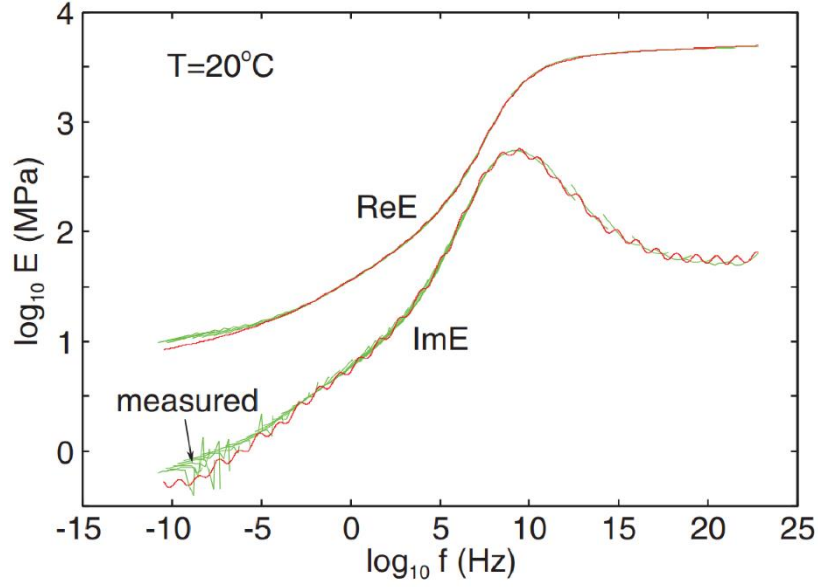


**Figure 2.8** An example of the storage ( $ReE$ ) and loss ( $ImE$ ) modulus of elasticity master curves of a tyre tread rubber. Image taken from [89].

### 2.1.5 Heinrich and Klüppel (HK) Model

As stated in Section 2.1.3 the HK model describes rubber friction as a contribution of adhesive ( $\mu_{adhesion}$ ) and hysteretic ( $\mu_{hysteresis}$ ) energy losses, written as:

$$\mu_k = \mu_{hysteresis} + \mu_{adhesion}$$

**Equation 2.4.1**

$$\mu_{hysteresis} = \frac{1}{2(2\pi)^2} \times \frac{\langle \delta \rangle}{\sigma_0 v} \left( \int_{\omega_{min}}^{\omega_{max}} \omega G''(\omega) S(\omega) \cdot d\omega \right)$$

**Equation 2.4.2**

$$\mu_{adhesion} = \frac{\sigma_s}{\sigma_0} \times \frac{A_C}{A_0}$$

**Equation 2.4.3**

In Equation 2.4.2,  $\langle \delta \rangle = b_1 \times \langle z_p \rangle$ , where  $b_1$  is an open parameter and  $\langle z_p \rangle$  is the mean depth by which the rubber penetrates the rough surface [38].  $S(\omega)$  is the surface's PSD as a function of wavelength (not wavevector as used by Persson),  $G''$  is the shear loss modulus of the rubber and  $G^*$  is the complex shear modulus (Equation 2.5). The remaining parameters are the same as those defined in the Persson model (Equation 2.2).

$$G^* = G' + iG''$$

**Equation 2.5**

In Equation 2.4.3,  $A_c$  is calculated using a multiscale GW based approach, while  $\sigma_s$  is the interfacial shearing stress required to break the atomic (adhesive) junctions. As explored in Section 2.1.3, the influence of adhesion between two bodies on friction is debateable. In turn, the HK model sets  $\sigma_s$  as an open parameter along with  $b$ . The use of these open parameters allows the model to be fitted to already obtained friction results.

The HK model uses the shear modulus ( $G^*$ ) of rubber, instead of the elastic modulus ( $E^*$ ) used by Persson. These two parameters are linked by Equation 2.6.  $G^*$  can be obtained as a master curve in a similar way to that described for a  $E^*$  curve (Section 2.1.4).

$$G^* = \frac{E^*}{2(1 + \nu)}$$

**Equation 2.6**

Where  $\nu$  refers to the Poisson's ratio of the rubber.

Although, to the authors knowledge, no direct comparison has been conducted comparing both models against the same experimental data, both have been shown to accurately describe frictional scenarios. Commonly, the automobile tyre-road surface interaction is modelled. Specifically, the situation in which wheels lock and the tyre rubber slides across the road [27,28]. When considering the tribological influences (rubber type, tread pattern,  $A_0$ , surface type), this interaction is similar to a rubber-surface interaction of a hard court slide.

### **2.1.6 Analytical Models Summary**

Differences are present in the two analytical models described. However, very similar material, surface and environmental measures are used:

- Material –  $E^*$  or  $G^*$  master curves
- Surface – Surface roughness PSD
- Environmental – Slide speed and nominal pressure

Through these analytical models, the parameters that theoretically affect the friction of shoes sliding over rough surfaces are identified. These are useful when interpreting the quality of work done to date in the field of shoe-surface friction, as well as informing future work that investigates the frictional aspects of hard court tennis slides. However, these models fail to provide a means of predicting the friction between rubber and a rough surface, prior to any frictional tests. Instead, they allow the fitting of friction master curves to already obtained friction results [39]. Consequently, throughout this thesis, these analytical models are consulted only for the explanation of friction data and not for predictions. The only friction

model used in this thesis is the simplified Persson model proposed by Ciavarella shown in Equation 2.7.

$$\mu \cong h'_{rms} \frac{ImE(v, q_1)}{|E(v, q_1)|}$$

**Equation 2.7**

Where  $h'_{rms}$  refers to the surface RMS slope,  $q_1$  is the large wavevector cut off from the PSD and  $v$  is the slide speed. Although this model has been shown to give a good estimate of friction values modelled using the full Persson model, it is not proposed that Equation 2.7 accurately predicts the friction of rubber on rough surfaces. This model, for means of simplicity, ignores multiple frictional influences, and instead allows an indication of how the hysteretic response of different rubbers will affect friction at different sliding speeds.

### 2.1.7 Numerical Solutions

Numerical methods exist that predict the sliding friction between rubber and rough surfaces [40,41]. The numerical procedure developed by Carbone & Putignano [40], required the use of the same input parameters used in the Persson Model and was found to produce comparable friction results.

### 2.1.8 Effect of Wear on the Sliding Friction of Rubber

Wear is when volume is lost from one or both bodies, as a product of surface interaction [42]. Numerous wear mechanisms exist, which occur depending on the materials themselves, their surface topographies and the motion, speed and pressure by which they contact [43].



**Figure 2.9** Clear signs of adhesive wear on the sliding rubber surface (left) with the deposited rubber on the hard court surface (right). Image taken from [47].

The wear process of rubber is extremely complex and different from those of other materials [44]. In the situation of hard court tennis slides, it has been proposed by Clarke et al. [45], that the court surface roughness causes the abrasion of the shoe outsole rubber. Abrasion can be

defined as the ploughing or micromachining of a soft surface by a harder countersurface. This often produces parallel grooves in the sliding direction on the softer material's surface [46]. Cole [47] slid Nitrile Butadiene Rubber (NBR) samples across a hard court surface ( $v = 0.05 - 0.2$  m/s) and analysed the resulting wear (Figure 2.9). Cole concluded that adhesive and abrasive wear occurred [47]. Adhesive wear occurs when asperity junctions that form between the two surfaces are sheared in a way that plucks the softer asperity from its surface. This produces discrete areas of material loss across the soft surface. Observations of Figure 2.9 clearly shows signs this type of wear.

A 1992 study on rubber wear labels all types of sliding wear that occur between rubber and a dry rough surface as abrasion [48]. This is because in most test scenarios, the abrasion of rubber does not produce the characteristic parallel grooves typical of metal-metal contact, and the definitions given in most tribology textbooks [43,46]. From this point onwards, abrasion will be used to term all the wear observed in experiments conducted between hard court surfaces and rubber.

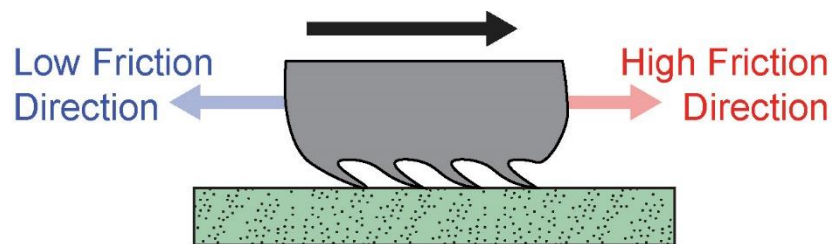


**Figure 2.10** Ridge structures can form on the surface of rubber after abrasion. The black arrow is the sliding direction from which the abrasion was caused. In this same direction, friction is high compared to the reverse direction due to the surface structures.

The wearing of rubber on rough surfaces is widely stated as a contributing factor to the sliding friction [49,50]. This is because removing rubber particles from the bulk means breaking the covalent bonds within the rubber itself (wear has been linked to the tensile strength of rubber [48]). The bond-breaking process consumes energy and therefore increases friction. Contrarily though, if the worn rubber is deposited between the two sliding surfaces, they can act like third-body rolling elements, reducing friction [51]. Furthermore, the topographical changes made to the rubber surface during sliding can have a frictional effect for future sliding. Such topographical changes are the ridge-like structures (see Figure 2.10), that form on the surface of rubber after sufficient abrasion [52]. These ridges have been found to occur after a series of slides on sandpaper, and produce a  $\mu_k$  asymmetry as great as 0.2 during sliding, with the sliding abrasion direction having the higher friction [52]. Topographical changes have been shown to significantly increase the friction between rubber blocks and asphalt road

surfaces. These topographies have not yet been reported in literature concerning footwear. As wear has been shown to occur between rubbers and hard court surfaces [53], it is crucial to measure or observe this when investigating friction. This can be done visually using optical techniques or with mass loss readings.

Indication can be given to the wearability of a rubber by its chemical composition. A key parameter of the rubber's composition that influences its wear is the filler used [54]. Fillers are extra material used in the production of rubber. Two common examples of fillers are carbon black and precipitated silica. By adding fillers to the rubber mix, they influence the modulus, and reinforce the rubber through their adherence and interaction with the polymer chains [55]. This interaction is affected by the size of the filler particles, their level of aggregation and agglomeration, as well as their surface energy [56]. The controlling of these filler properties requires precise manufacturing and can therefore easily vary from batch to batch. Because of this, and the degree of sulphur cross-linking during vulcanisation, it is difficult to determine the exact form of fillers used in a rubber once produced. While viscoelastic master curves can characterise the overall modulus of the rubber, they do not consider the wearing influence of fillers.

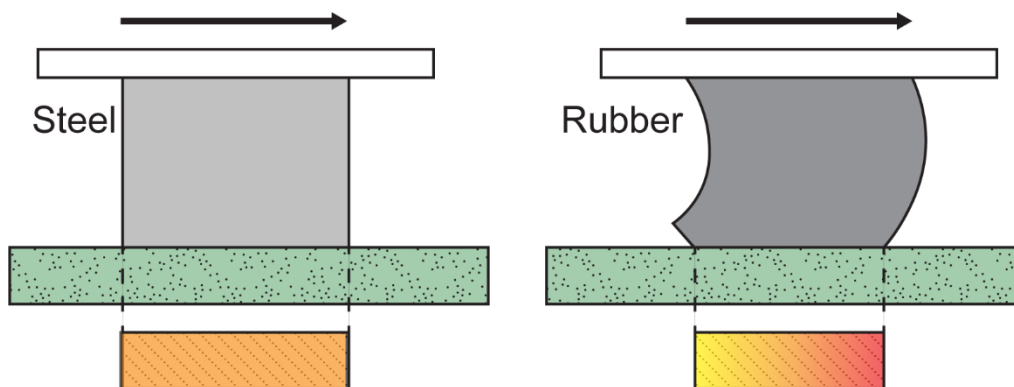


**Figure 2.11** When a low stiffness, viscoelastic material slides, it creates a contact pressure gradient from the leading edge to the rear. This is shown in comparison to a stiff elastic material. Red = high contact pressure, yellow = low pressure.

Like friction, rubber wear is affected by multiple interaction conditions. Studies have shown rubber wear to be affected by temperature [57], material properties [54], surface roughness [51], slide speed [57] and normal load [58]. Normal load influences wear through the change in contact pressure, which for viscoelastic materials is not always uniform across the contact area during sliding. This is due to the structural instability of the material, resulting in the bending and/or contorting of the structure. Figure 2.11 shows how contact pressure distributions vary between high stiffness materials like steel, and low stiffness viscoelastic materials like rubber.

As depicted, the low stiffness of rubber can form a concentration of pressure along the leading edge of the sliding element. If the sliding causes wear, the extent of wear will also vary across the contact area length, concentrating at the leading edge. In a lot of experimental rubber friction research, rubber blocks have their edges chamfered to neglect the effects of leading-edge wear, providing more consistent friction values which can be better modelled.

In conclusion, wear can both increase and decrease the friction of rubber depending on the nature of the sliding scenario. Whether wear occurs, and to what extent, relies on multiple factors from filler particle size to the shape of the rubber's leading edge. Consequently, the accurate prediction and modelling of wear is very difficult, especially when considering the complex case of shoe-surface sliding in tennis, but wear should not be ignored when analysing the friction of tennis shoes as it may be a critical mechanism.

Even if the sliding conditions are not severe enough to cause significant wearing of a rubber tennis shoe outsole, as for all sliding interactions, heat will be generated. As rubber's material properties are temperature dependent, this can also cause frictional differences.

### **2.1.9 Effect of Frictional Heating on the Sliding Friction of Rubber**

The frictional heat that develops at the interface of a sliding rubber and surface is fundamental to the friction that results. In this section, an introduction to frictional heating is provided, identifying the ways in which it affects the friction between rubber and dry rough surfaces.

Flash temperatures are very speed dependent and at speeds over 1 mm/s are great enough to reduce the  $\mu_k$  via strain softening of the rubber [59]. Fortunato et al. found that increasing the  $v$  between a rubber block and a road surface from 0.1 - 2 m/s increased road surface temperatures from 35 °C to 90 °C [59].

To understand how this frictional heat is generated, consider rubber sliding over a single surface asperity (Figure 2.12). When the surface asperity contacts a rubber asperity, a junction is formed from adhesive bonds which occur because of atomic Van der Waals forces. As relative sliding continues between the two bodies, the atomic junction is sheared, releasing energy in the form of heat. It is theorised that because of the insulating properties of rubber, the heat emitted from this shearing process is predominantly retained in the surface asperity (road, tennis court or other). If the sliding speed is great enough to cause this heated asperity to bind to another rubber asperity before the heat is dissipated, then the process of binding and shearing continues to raise the temperature of the surface. In turn, the insulating rubber itself heats up at the hot asperity contacts. As stated in Section 2.1.4, the stiffness of rubber is very temperature dependant. Thus, as depicted in Figure 2.13, the increase in temperature

typically reduces the stiffness and loss tangent of the rubber, subsequently decreasing hysteresis energy losses which can amount to a drop in overall sliding friction.

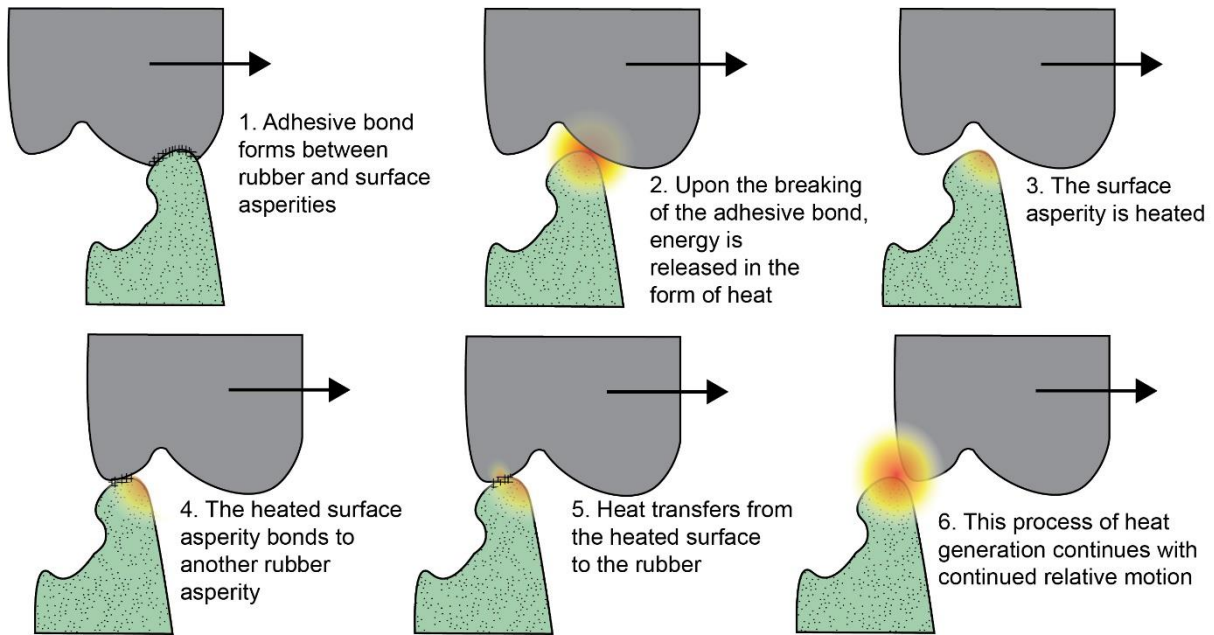


**Figure 2.12** How frictional heat is generated and effects the rubber's temperature (at slide speeds > 1 mm/s).

Due to the nature of how this frictional heat is generated (Figure 2.12), the longer the rubber parallel to the sliding direction, the more asperity junctions will be formed on a select surface asperity. As such, orientation of a rubber block can influence the degree of frictional heat generated, and therefore  $\mu_k$ . By acknowledging that heat is generated in this way, it must be acknowledged that adhesive bonds produce energy losses in the form of heat. As discussed previously, adhesion can be considered negligible between rubber and rough surfaces, which is seemingly contradictory. However, if considered that, by adhesive bonds releasing energy as heat, which in turn has a greater opposing effect by reducing hysteresis, hysteresis can still be considered the dominant frictional mechanism, despite the presence of adhesive bonds.

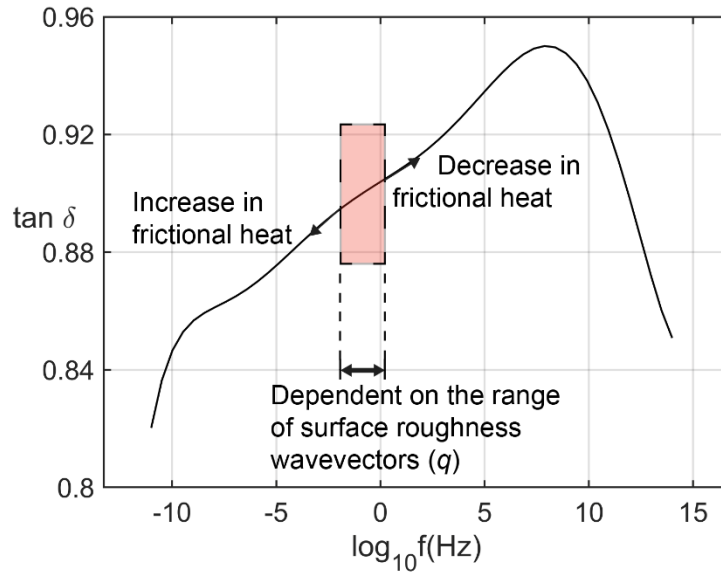


**Figure 2.13** Loss tangent curves reveal that an increase in rubber temperature incurs a decrease in hysteresis in the main region of the curve.

Figure 2.14 shows a rubber block in two orientations relative to the sliding direction. Rubber block 1, laid perpendicular to the slide direction, generates lower overall heat in comparison to block 2, which is laid parallel to the slide direction. It can therefore be inferred that a higher  $\mu_k$  would be observed for block 1 than for block 2 when sliding at speeds above 1 mm/s. This finding was observed experimentally by Fortunato et al. who used heat dissipation theory and thermal cameras to validate their conclusion that the differing frictional temperatures are the cause of the  $\mu_k$  differences between the two orientations of rubber block [59].

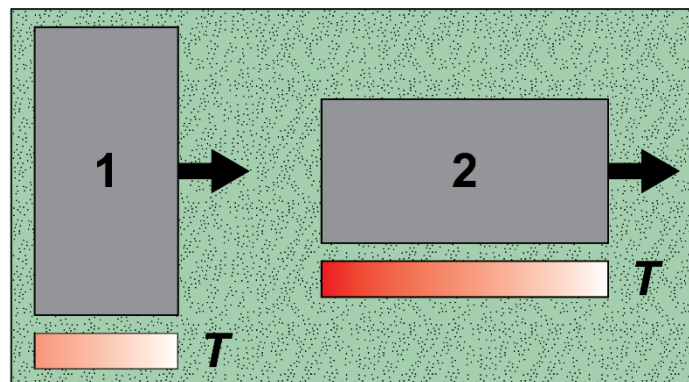


**Figure 2.14** A plan view of two rubber block sliding orientations. At sliding speeds  $> 1$  mm/s block 2 undergoes more frictional heating ( $T$ ) due to its length in the sliding direction.

If frictional heat induced strain softening and/or melting is not occurring, and assuming adhesion can be neglected, increasing the sliding speed would theoretically increase  $\mu_k$  due

to the greater perturbing frequencies experienced by the rubber (represented by the blue curve in Figure 2.15). However, if like the HK model, it is believed that adhesion is influential to  $\mu_k$  of rubber on rough surfaces, this decrease in friction (shown by the red curve) can be explained not by temperature effects, but by the reduction of adhesion that occurs at high speeds. Nevertheless, the argument for frictional heating as the cause of the reduction of  $\mu_k$  at high sliding speeds is more widely supported [27].

Due to the findings of [59], the Persson friction model (explained in Section 2.1.4) was updated as shown in Equation 2.7:

$$\mu(t) = \frac{1}{2} \int_{q_0}^{q_1} q^3 C(q) S(q) P(q) \cdot dq \times \int_0^{2\pi} \cos\phi \operatorname{Im} \frac{E(qv(t)\cos\phi, T_q(t))}{(1-v^2)\sigma_0} \cdot d\phi$$

**Equation 2.7**

Where  $T_q(t)$  is a function to calculate the influence of frictional heating as a function of sliding time ( $t$ ). No version of the HK model directly accounts for frictional heating.

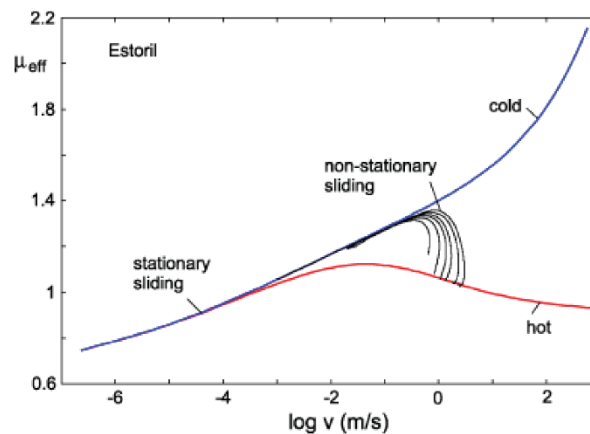


**Figure 2.15** Friction between a rubber block and rough surface changes as speed increases. If frictional heating is not considered, friction will increase with speed. The opposite occurs when frictional heating is considered. Image taken from [27].

Not only do the findings of [59] further emphasise the importance of sliding speed to the sliding friction of rubbers on rough surfaces, but they also provide some implication, via the orientation dependence of frictional heating, as to how tread may affect dry rubber friction also.

### 2.1.10 Effect of Tread on the Sliding Friction of Rubber

In terms of automobile tyres, the primary function of tread is to divert fluid contaminants (water, oil etc.) away from the road-tyre contact regions, thus preventing hydrodynamic lubrication. In turn, tread channels are designed in ways which support this process of dispersing fluids. This is most likely the primary use of tread on footwear also. However, professional hard court tennis matches are strictly played in dry conditions. If rainfall occurs, play is postponed until dry again or the stadium roof is closed. With professional hard court tennis only being played exclusively on dry surfaces, the role of tennis shoe tread (Figure 2.16) is not as clearly defined.



**Figure 2.16** Sole of NikeCourt Air Zoom Vapor Cage 4. Image adapted from Nike.com.

In 1983, a study performed by Nike's research laboratory, slid a variety of basketball shoes over dry basketball court surfaces ( $v \approx 0.4$  m/s) [60]. Tread design and rubber type had a strong effect on shoe-surface friction (Figure 2.17). Although this study used basketball surfaces (typically much smoother than tennis hard courts), it showed not only that rubber type influences  $\mu_k$  (as is predicted by the analytical models), but that tread does also for dry interactions. No rationale was provided to explain these drastic frictional differences.

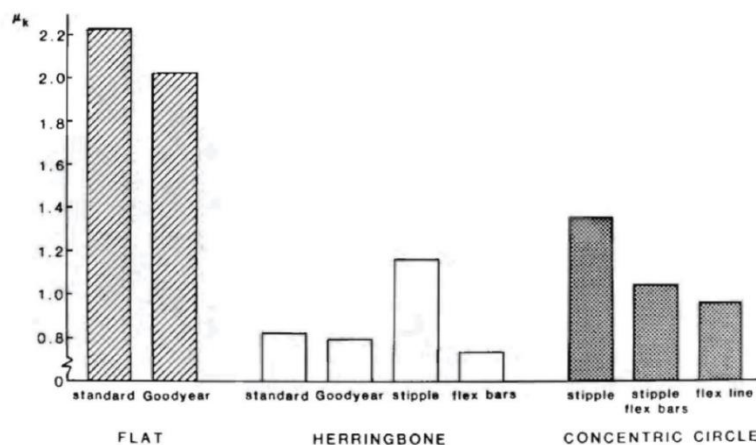


**Figure 2.17** Tread type (Flat, Herringbone and Concentric Circle) and rubber type (Goodyear, standard etc.) influence shoe-surface friction. Image taken from [60].

Studies investigating the effect of tread on small rubber blocks provides insight into how shoe tread effects sliding. Goff et al. [61] cut two rectangular samples from the tread of a tennis shoe and tested their sliding friction on a hard court tennis surface. Additionally, three custom-made rubber samples with simple designs (flat, grooves and holes) were also tested.  $\mu_s$  and  $\mu_k$  were both influenced by tread design, with the holed design having the lowest  $\mu_k$ . Another study by Goff et al. [62] further investigated the holed tread design. Seven rubber samples were manufactured, ranging from where the rubber-to-hole ratio is 0 (flat, no tread) to 0.37 of the sample (Figure 2.18).

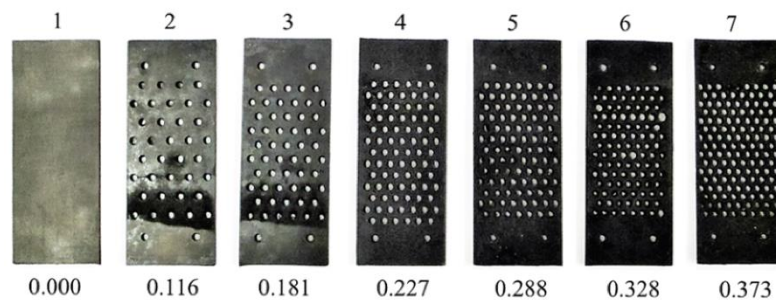


**Figure 2.18** Seven different designs of holed rubber tread used in sliding friction study on hard court tennis surface. Image taken from [62].

Frictional testing of these samples on a dry hard court found that when the rubber-hole ratio  $> 0.23$ , both  $\mu_s$  and  $\mu_k$  decreased. Changing this rubber-hole ratio will, by altering the nominal contact area between the rubber and surface, change the contact pressure, with the higher rubber-hole ratios producing the highest contact pressures. Lang & Klüppel investigated how increasing the nominal pressure on a rubber block influenced its friction and found that an increase in pressure results in a decrease of  $\mu_k$  [28]. This is a commonly observed occurrence in rubber friction experiments and is due to two main mechanisms. The first is that increased nominal pressure causes more heat to be generated during sliding, which reduces the modulus of the rubber, hence reducing the hysteresis. However, the same decrease in  $\mu_k$  with increased pressure is observed at slow slide speeds ( $< 1$  mm/s) where, due to heat dissipation, the temperature of the rubber is not significantly changed [63]. The second cause of rubber's  $\mu_k$  dependency on pressure, is lateral coupling between real areas of rubber-surface contact. As pressure increases, the distance between the discrete areas of real contact is reduced, improving the coupling across the rubber surface and reducing the prominence of stick-slip, reducing  $\mu_k$  [63].

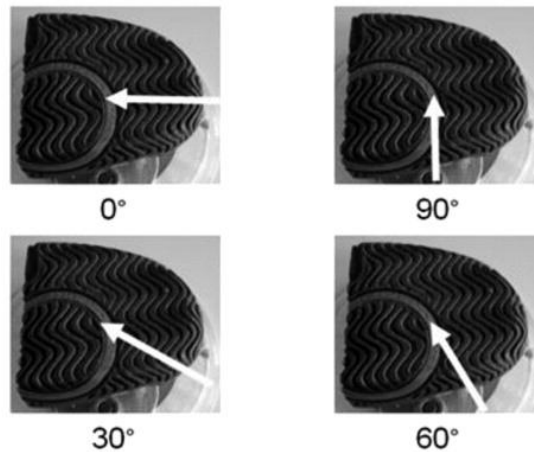


**Figure 2.19** The four orientations of a tennis shoe forefoot, tested on a dry hard court.  
Image taken from [64].

The findings of [60] and [62] described on the previous two pages, could largely be explained by this frictional effect of pressure (though this is only valid if the concentric circle pattern in [60] had a larger contact area than the herringbone). However, one study, whose results cannot be explained by the dependency of friction on pressure, tested the friction of a tennis shoe forefoot on a hard court at different orientations (Figure 2.19) [64]. Hypothetically, the orientation of the tennis shoe should not matter, as the nominal pressure would be the same. Yet results showed that at the 0° set-up, friction was lower than all other orientations, with the 90° orientation producing the highest friction readings.

Scaraggi and Persson wrote that (when considering  $\mu_k$  to be dictated by hysteresis alone) two rubber blocks, one with tread and one without (Figure 2.20), with the same applied normal pressure will produce the same frictional results [65]. This statement contradicts the findings of all the papers cited thus far in this section, hence inferring that additional frictional mechanisms to hysteresis play a role in the  $\mu_k$  of the treaded rubber bodies used in their studies. As explained in Section 2.1.9, this could be frictional heating as all the studies were performed at  $v > 0.1$  m/s, at which it has been found that frictional heating influences  $\mu_k$  [59]. Additionally, in real world scenarios, tread will have influence over the shearing of contaminants on the surface, and the rolling of those contaminants at the shoe-surface interface. Both these mechanisms concerning surface contaminants are likely to have influenced  $\mu_k$  with the addition of wear effects also.

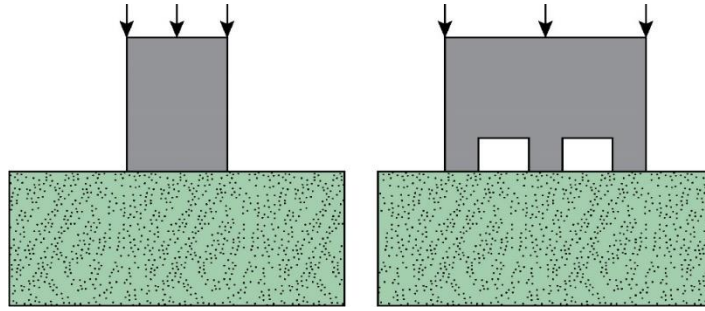


**Figure 2.20** Two rubber blocks described to have the same friction if considering hysteresis alone [65].

An observable feature of sliding rubber tread is the curling of the front edges (Figure 2.21). It is widely acknowledged that this frontal region of tread is influential to the overall  $\mu_k$ , although there is yet to be consensus as to how. Heinrich and Klüppel wrote that, for tyre tread on dry surfaces, this frontal region of the tread is where the majority of energy dissipation takes place [66]. They state that the sliding speed is comparatively low in this region, and as such adhesion is high, increasing friction. Maegawa et al. came to a contrasting conclusion when sliding rubber blocks with differing numbers of grooves across a smooth poly (methyl methacrylate) (PMMA) surface, showing that as the number of grooves increased,  $\mu_k$  decreased [67]. Maegawa et al. deemed this to be due to increased friction induced torque flexing the weak tread structures, causing the nominal contact area to be reduced [67] (Figure 2.21). In turn, the contact pressure increases as the number of grooves increases, which reduces  $\mu_k$ . It must be remembered however, that the study of Maegawa et al. was performed on a smooth surface.

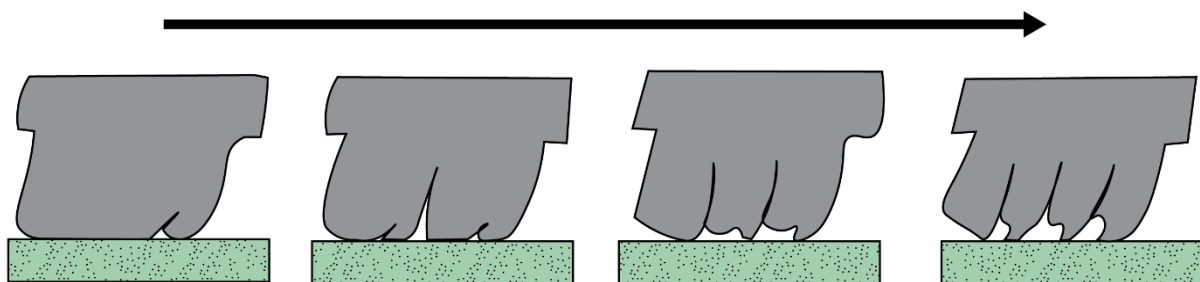


**Figure 2.21** Rubber blocks with ranging number of slits from 0 (left) to 3 (right). The front of each slit curls during sliding. Arrow indicates slide direction. Image adapted from [68].

Based on the literature in this theory section, assumptions can be made as to how different tennis shoe outsoles influence friction e.g., shoes with long tread elements in the direction of sliding will experience higher frictional heat temperatures, and thin tread elements are likely to undergo friction induced torque which will influence the friction through a changing of the shoe's overall contact area. However, it must be remembered that Goff et al. [61,62], Heinrich and Klüppel [66], Hofstatter et al. [68] and Fortunato et al. [59] all only tested small rubber

blocks, with Goff et al. [61,62] being the only studies to use hard court tennis surfaces. Similarities are present between this research and the sliding of a tennis shoe on a hard court tennis surface. Nevertheless, without testing the sliding of full tennis shoes on hard court surfaces under conditions like that experienced in real gameplay, no conclusion can be made as to the wearing and frictional mechanisms that are to ensue, or the precise influence of tread on friction.

## **2.2 Biomechanics of Hard Court Tennis Slides**

As has been explored in the previous sections of this thesis, the sliding friction of rubber on dry rough surfaces depends on numerous parameters such as speed, nominal contact pressure, surface PSD, rubber complex modulus and tread design. To understand the frictional characteristics of hard court tennis slides, the in-situ slide speed and normal load magnitudes must be known. This can be achieved through biomechanical analysis. In tennis, biomechanical analysis provides information regarding injury risk, performance, and player perception of specific tennis movements. This is done by asking participants to perform movements while being monitored. The instrumentation used to monitor the participants dictates the kinetics and kinematics that can be obtained by the study.

Numerous biomechanical studies have been conducted to investigate sliding in tennis [1,4,11,13]. One study analysed the injury risk of sliding on clay, in comparison to a stepping change of direction on hard court [11]. It was found that stepping movements produce higher shoe-surface contact pressures than slides, which imply a greater chance of developing overuse injuries from stepping movements over sliding ones [11]. In another study, the performance of ten non-elite tennis player's change of direction on clay and hard court surfaces was analysed [4]. All participants were instrumented with 11 markers for kinematic data collection via three-dimensional motion capture, and wore pressure insoles in their shoes. This allowed average impact and sliding speeds, as well as sliding distance and average pressure distribution during steps and slides to be monitored. Slide speeds and normal loads, that are (as specified by the analytical rubber friction models) influential to the sliding friction of rubber on rough surfaces, were measured within this study. Unfortunately though, no hard court slides were observed in [4]. Instead of the athletes being asked specifically to perform slides, they were simply asked to play a shot and change direction. On clay courts, this often resulted in the players choosing to slide, but on hard courts all athletes chose to step. Moreover, it would potentially be unethical to ask non-elite tennis players to perform hard court slides due to their high level of difficulty. One biomechanical study specifically analysed hard court sliding [13], but these slides were performed using the Wilson Glide shoe which has a partly plastic outsole to encourage sliding, and is thus uncharacteristic of the shoes worn in

the professional circuits. Furthermore, no loads were measured in this study, only slide distances and times. To the author's knowledge, there is only one study that directly measured forces and speeds during hard court sliding. This study was published within a thesis and details the slides of two non-elite athletes [12]. Ten participants were asked to perform 180° turns as quickly as possible on three different hard court surfaces, varying in Court Pace Rating (CPR). Two of these 10 participants chose to slide, while the remaining eight participants stepped. A force plate beneath the hard court samples measured ground reaction forces and motion capture was used to retrieve slide distances and speeds. Example traces from this study are shown in Figure 2.22.

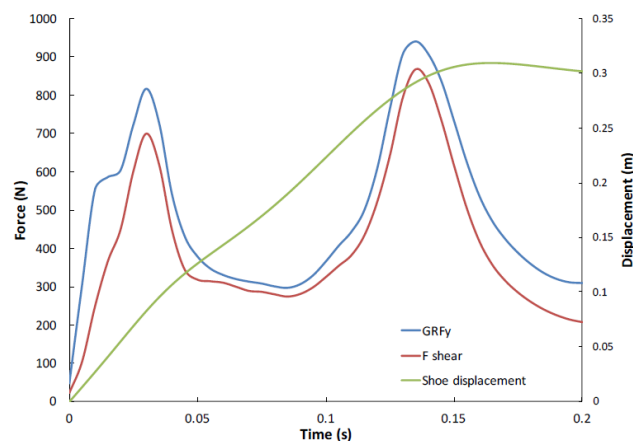


**Figure 2.22** Force-time and distance-time traces obtained during hard court sliding. Image taken from [12].

The force traces initially peak around 700 N and 800 N for shear and normal force, respectively. Following this peak, forces drop to between 300 – 400 N for 0.05 s before a second peak where forces reach between 800 – 900 N. The initial peak constitutes the initial impact load as the athlete contacts the surface. The subsequent drop in force occurs as the slide speed becomes constant at 3 m/s. The second peak then occurs as the athlete initiates breaking mechanisms to stop the slide and push off. Though this study only details the hard court slides of two non-elite athletes, the slide speed (3 m/s) falls within the range of that observed in elite tennis (2.82 – 4.73 m/s) [12]. This was determined through detailed video-analysis of slides that occurred during five hard court tennis matches during the men's ATP tour final event 2015.

A mechanical shoe friction device that is capable of slide speeds between 2 – 5 m/s and normal loads between 300 – 400 N would replicate the tribological conditions at the shoe surface interface of observed hard court slides.

The final parameter to consider when mechanically replicating hard court sliding, is the pressure distribution across the shoe outsole. With modern tennis shoes often consisting of numerous tread patterns on a single shoe, it is important to ensure the pressure distributions experienced in the mechanical test are similar to that during real hard court slides. As previously discussed, we are yet to see a study which directly measures pressure distributions for hard court slides, but the pressure distributions from [4] may be satisfactory. This is because regardless of the movement performed, hard court step or clay slide (both of which were analysed within [4]), the distributions of pressure were remarkably similar, with maximum pressure being measured at the medial forefoot (dark red on Figure 2.23) and minimum pressure measured at the lateral midfoot (clear segment on Figure 2.23). A mechanical test should aim to reproduce these pressure distributions as they are likely to occur during hard court slides.

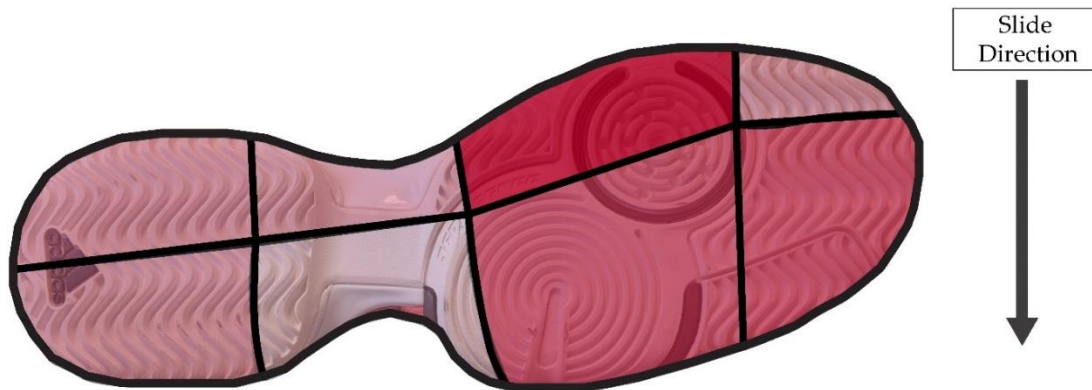


**Figure 2.23** Average pressure readings from Starbuck et al. [4] displayed on a tennis shoe outsole. Darker colour indicates greater pressure.

Hypothetically, a biomechanical study could be conducted to determine loads and speeds directly from hard court slides, and even compare the frictional properties of different shoes during hard court slides. However, not only will professional players need to be recruited to perform such difficult movements repeatedly, but speeds, contact pressures and techniques will inevitably vary both intra- and inter-participant, meaning direct comparisons of the shoes will be difficult to obtain. Additionally, the instrumentation and environment in which the study is conducted will result in a sliding movement not characteristic of that used in real competitive play. In comparison, mechanical devices offer a means of performing repeatable, quantitative frictional analysis of shoe-surface interfaces, replicating estimated competition level forces and speeds without the risk of participation injury.

## 2.3 Mechanical Analysis

Numerous mechanical devices (rigs) have been used to analyse the frictional performance of footwear. Chang et al. critically analysed five full shoe friction measurement devices in terms of their validity, repeatability, reproducibility and usability [69]. Rigs ranged in complexity from a Horizontal Pull Slip meter (HPS) to the French National Research and Safety Institute Laboratory Device (LABINRS), both pictured in Figure 2.24. Chang et al. concluded that although the devices investigated were generally reliable and repeatable, most devices lacked validity and that this could be improved by better replicating human biomechanics [69].

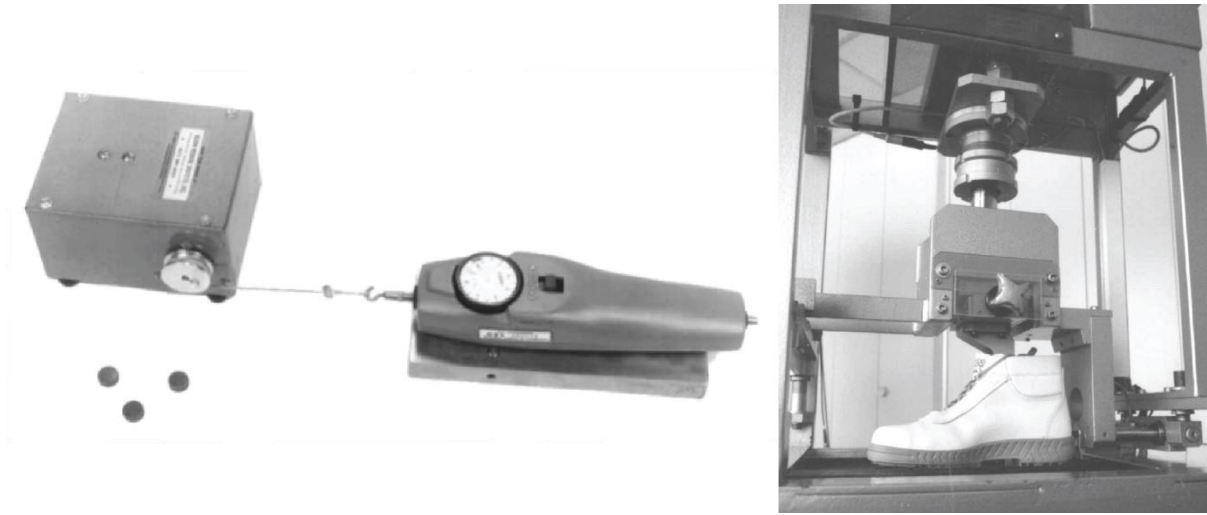


**Figure 2.24** The HPS (left) and LABINRS (right). Images taken from [69].

All the rigs analysed by Chang et al. were manufactured to analyse the shoe-surface friction relating to slipping on wet surfaces. Although the HPS and others could be used to assess sporting footwear, due to discrepancies in loading conditions and surface characteristics when compared with how sporting shoes are used in-situ, they are potentially invalid.

### 2.3.1 Mechanical Tennis Shoe Friction Devices

The UoS Traction Device [70] and Tennis Shoe Surface Tester (TSST) [71] were both designed to analyse the frictional performance of various tennis surfaces. The UoS Traction Device (Figure 2.25) is a laboratory-based rig which slides fore-foot sections of shoes across a surface with a known normal force, measuring the frictional force and hence producing the  $\mu_s$  and  $\mu_k$  as outputs. The aim of this device is to imitate a typical tennis step movement.

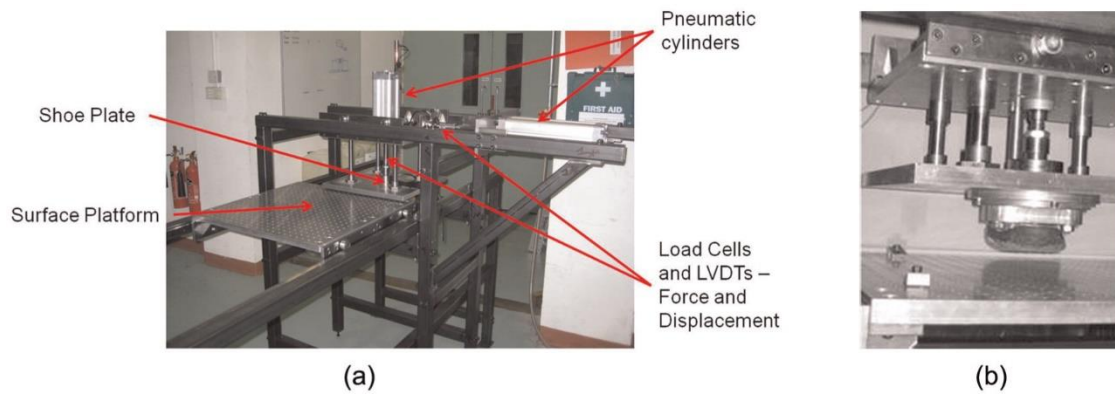


**Figure 2.25** The UoS Traction Device. Image taken from [70].

The UoS Traction Device has been used to investigate the effect hard court surface roughness ( $R_a$ ) and normal load have on the applied frictional force needed to slide a shoe across tennis surfaces [45,72]. It has also been used to investigate the effect of shoe-orientation on friction, where the forefoot segment of a hard court tennis shoe was slid across a hard court in four different orientations [64].

The normal loads that the UoS Traction Device tests at (800 – 1500 N) cover an archetypal range of normal forces to those measured during tennis steps [73]. The UoS Traction Device creates sliding using two pneumatic cylinders, one providing horizontal force and the other providing the vertical normal force. During operation, the shoe is pressed down onto the surface by the vertical cylinder, before the horizontal cylinder is initiated, hence sliding the shoe. In tennis, slides occur through the application of an angled force from start to finish. Moreover, by applying forces using pneumatic cylinders, the UoS Traction Device is mechanically hindered to low speed sliding (typically  $v = 0.05 - 0.2$  m/s). Although, application of an exhaustion valve can increase the extension speed of pneumatic cylinders to  $\leq 0.8$  m/s, this is below the 2 – 5 m/s speeds of hard court tennis slides. This difference in speed is an important one (as mentioned in Section 2.1) as changes in speed can alter the frictional and wearing mechanisms between rubber and rough surfaces.

Regardless of the speed and motion oversight, the UoS Traction Device has been used to provide useful and interesting insight into the shoe-surface friction of hard court tennis movements, particularly the roughness-friction and the shoe orientation-friction relationships.

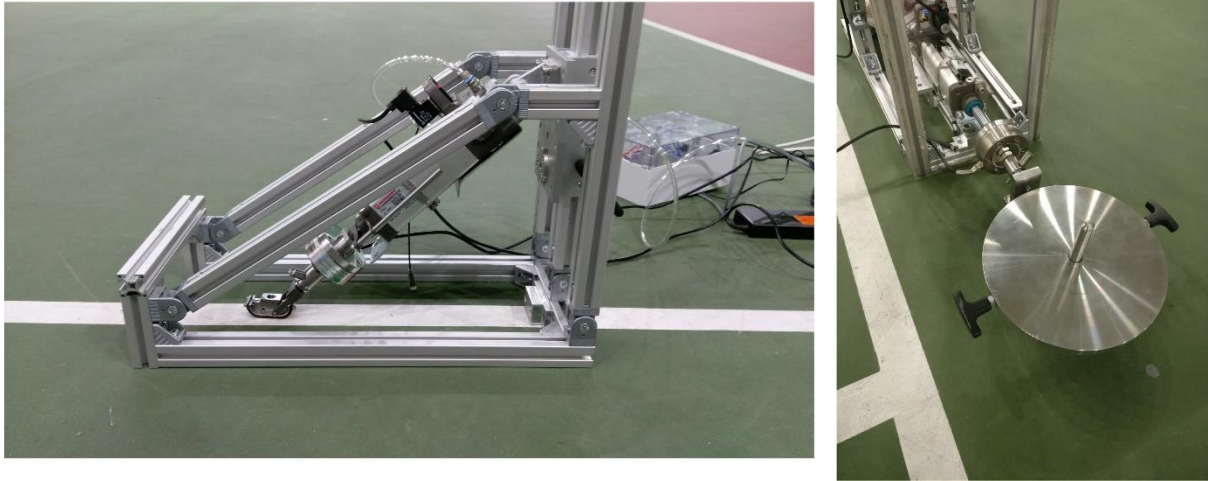


**Figure 2.26** TSST in angled (left) and sled (right) configurations.

The TSST (Figure 2.26) had a more representative force application motion. The TSST used a single pneumatic cylinder to apply an angular force to a small, rectangular rubber sample. This sample touched the court surface at a set angle and slid. The applied normal load was lower than those recorded during biomechanical analysis of tennis slides (162 N). However, as the size of the sliding rubber sample was smaller than a full sports shoe, the contact pressures were comparable. The TSST was designed in this manner to be portable, and to be used on full tennis courts so had to be light and transportable. The TSST is being trialled by the International Tennis Federation (ITF) to characterise tennis surfaces.

Though, comparable contact pressures and impact angles are replicated by the TSST, there are factors the TSST fails to account for, lessening its validity in imitating a tennis player performing a hard court slide. The construction of the TSST means that almost any impact angle can be produced. Nevertheless, when sliding begins, the angle will continually increase about the pivot which connects the pneumatic cylinder to the structure. This is unlike tennis slides where, because the athlete moves with the slide, the angle remains relatively constant throughout. Because of the increasing angle,  $\mu_k$  cannot be easily outputted in this configuration. Even though the TSST can be put into a sled configuration (Figure 2.26), hence allowing output of both  $\mu_s$  and  $\mu_k$ , it sacrifices the replicable contact angles to do this.

Similarly to the UoS Traction Device, the TSST uses a pneumatic cylinder to initiate sliding. Consequently, the TSST suffers the same deficiency in speed when compared to real hard court slides, and as the TSST uses a small rubber sample, the frictional properties of a whole shoe outsole cannot be tested. Instead, only simplified tread designs or cut sections of shoes can be tested (see [61,62]). The TSST was designed as a portable test device capable of

testing the frictional properties of tennis surfaces. The limitations of the TSST to test the frictional performances of tennis shoes are characteristic of its portability.

Neither the UoS Traction Device nor TSST allow for the testing of full-sized tennis shoes at speeds typical of hard court slides. To comprehensively understand the shoe-surface friction of a tennis slide, a full shoe rig is required, capable of sliding speeds of 2 - 5 m/s.

### **2.3.2 Tread Quantification**

One difficulty when interpreting shoe friction results from prior literature, stems from the under characterisation of the tread patterns being studied. For example, friction measurements of futsal [74], basketball [60] and tennis shoes [64] have shown that different tread patterns (and shoe orientations) produce different friction. However, because the tread patterns, and more importantly, the tread that contacts the surface during testing, are not quantified in any way, a detailed understanding of which tread features influence friction is incomplete. Contacting areas of shoe tread can be identified through visual observations of wear on the shoe after testing (performed on rubber blocks in [62]), by the ink print method of placing paper over the test surface before applying ink the shoe tread and pressing the shoe onto the surface [10], or by using a frustrated total internal reflection approach [75]. This final approach uses a camera beneath a clear surface (lined with lights) which the shoe contacts, allowing images to be taken of the areas where the tread contacts. One study used this method to quantify shoe-surface contact area [76]. In Chapter 7, a method is presented which uses frustrated total internal reflection images with the addition of image processing to provide greater detail of shoe-surface contacts to help interpret shoe friction results.

### **2.3.3 Discontinuities between Mechanical Analysis and Rubber Friction Theory**

Before concluding this literature review, consideration is given to the current state of shoe friction analysis in relation to rubber friction theory.

Qualitative observation of the aforementioned analytical friction models (Section 2.1.4 and Section 2.1.5) informs us that when analysing shoe-surface friction, the shoe rubber need only be characterised by its viscoelastic master curve ( $E(\omega)$  or  $G(\omega)$ ). Current research investigating shoe-surface friction commonly ignores this, describing shoe outsole rubbers in terms of hardness (typically Shore A hardness) [77]. Although, according to theory, the rubber's hardness is not the principal factor which influences friction, it will influence the degree of indentation made by hard court asperities into the rubber, and thus hysteresis. Additionally, it may influence the frictional performance of rubber over a rough surface when the interaction causes significant tearing and wear of the rubber. The tearing of the rubber substrate consumes additional energy, which can in turn increase the net energy consumption,

thus increasing friction. As hardness is often used to predict wear, such as with the Archard wear equation (Equation 2.8), it could be hypothesised that Shore A hardness is linked to wear and therefore friction.

$$wear = K \times \frac{W}{\mathcal{H}}$$

### Equation 2.8

In Equation 2.8,  $K$  is the wear coefficient,  $W$  is the normal load and  $\mathcal{H}$  is the hardness of the wearing material. A wear equation used to describe the abrasion of plastics also includes a hardness parameter, though a more specific Grosch and Schallamach rubber wear model omits hardness and instead uses the stress and strain at failure during tensile testing of the rubber [48]. Even if a rubber's Shore A hardness is linked the abrasion of rubber, often the research which uses hardness as a rubber parameter fails to report that the interaction ensues any noticeable wear, and thus provide insufficient reasoning to using the parameter instead of  $E(\omega)$ , which has been linked to the friction of rubber.

Shore A hardness readings can be converted to elasticity values through Equation 2.9 [78]:

$$E = \frac{1 - \nu^2}{2RC_3} \times \frac{C_1 + C_2Sh_A}{100 - Sh_A} \times (2.6 - 0.02Sh_A)$$

### Equation 2.9

$R$ ,  $C_1$ ,  $C_2$  and  $C_3$  all represent constants while  $\nu$  is the Poisson's ratio of the rubber (commonly 0.5) and  $Sh_A$  is the Shore A hardness reading of the rubber. This equation calculates a modulus value from a Shore A hardness reading. However, since the hysteresis response of rubber is resultant of a summation of perturbing frequencies, a single elasticity reading is not enough to predict the sliding friction of rubber on rough surfaces. Instead, a viscoelastic master curve must be used. A reason for this neglect of viscoelastic master curves may be due to the difficulty of cutting a uniform piece of rubber from an outsole that can be used in DMA.

Studies often under characterise the rough surface also. Both Persson and HK models use the surface PSD as the only surface measurement. This is not reciprocated in most of the research investigating shoe-surface friction. Instead, surfaces are described exclusively in terms of arithmetic average roughness ( $R_a$ ) or RMS roughness ( $R_q$ ) [72,79]. Different roughness measures ( $R_a$ ,  $R_q$ ,  $R_z$  etc.) describe roughness in different ways. For example,  $R_a$  is a measure of average surface height whereas  $R_z$  is the average peak-to-valley height [46]. Hence, these measures give completely different measures for the same surfaces. It is therefore essential that the surface topography factors that most influence the described

friction, are known before selecting a roughness measure. Taking the scenario of rubber sliding over rough dry surfaces, it can be argued that  $R_z$  is somewhat relevant. Understanding that hysteretic contributions of  $\mu_k$  are related to the perturbing frequencies generated by the sliding speed and roughness wavelengths ( $\omega = v/\lambda$ ),  $R_z$  can be interpreted as a measure of the surface's largest wavelengths (Figure 2.27 (C and D)). However, if  $R_z$  is being used due to this reasoning it is assuming that the smaller wavelengths of roughness have no effect on the friction. This is known not to be true, for instance in Figure 2.27, (C) would produce a greater hysteretic frictional response than (D).

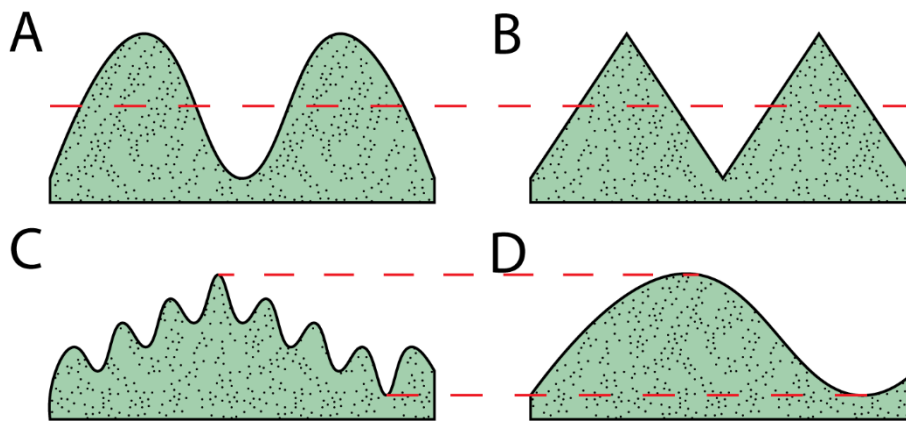


**Figure 2.27** The same surface roughness measurement does not mean similar topographies. Surfaces (A) and (B) give the same  $R_a$  value while (C) and (D) give the same  $R_z$  value.

Future studies looking to understand and predict the friction between dry rough surfaces and rubber soled shoes have little theoretical rationale for using single value hardness and roughness measurements alone, as these measures misrepresent and overlook crucial surface and rubber characteristics integral to the consequent friction. Nevertheless, measures such as Shore A Hardness and  $R_a$  are more universally understood than  $E(\omega)$  mastercurves and PSD's, which are only typically present in specialist tribology literature. Subsequently, the more simplistic measures do provide a valuable qualitative understanding of the type of surfaces and/or rubbers being used in a given study.

Shoe-surface friction research that includes both simplistic (Shore A Hardness and  $R_a$ ) and in-depth measures ( $E(\omega)$  mastercurve and PSD) provides both a qualitative understanding of the rubbers and surfaces used while also allowing a detailed analysis.

### 3 Surface and Rubber Characterisation

The friction between a tennis shoe and a tennis hard court is resultant of an interaction between a rubber and a rough surface. As mentioned in the previous chapter, when predicting the friction between rubber and a rough surface, there are two measures that must be obtained: the PSD of the surface, and the viscoelastic master curve of the rubber. This chapter details the collection of these measures and how they can be used to provide both quantitative and qualitative understanding of tennis shoe friction, as well as the assumptions that are made when using them.

The hard court surface described in this chapter is the same as that used for all the experiments in this thesis. As such the PSD presented is referenced in subsequent chapters. Additionally, the rubber described in this chapter is later used in the friction experiments of Chapter 4 and 5.

#### 3.1 Hard Court Characterisation

As introduced in Section 2.1.2, a 1D surface roughness trace can be considered a combination of numerous sine waves of differing amplitude and frequency. Thus, by applying a Fourier Transform (FFT) to the 1D trace, the wave frequencies of the surface are output. PSDs are presented in many ways, making it difficult to compare between surfaces [80]. In this thesis, an online PSD calculator (contact.engineering, University of Freiburg and University of Pittsburgh) is used. This calculator takes a map of heights and outputs two types of PSD: 2D and 1D. The 1D PSDs are the same form as that used in the Persson model, and are widely presented in other rubber friction research [34,36,81–83]. The 1D PSD is the only type presented in this thesis, and is in the form of a 1D PSD  $C^{1D+}$  (Figure 3.1) as described in [80].

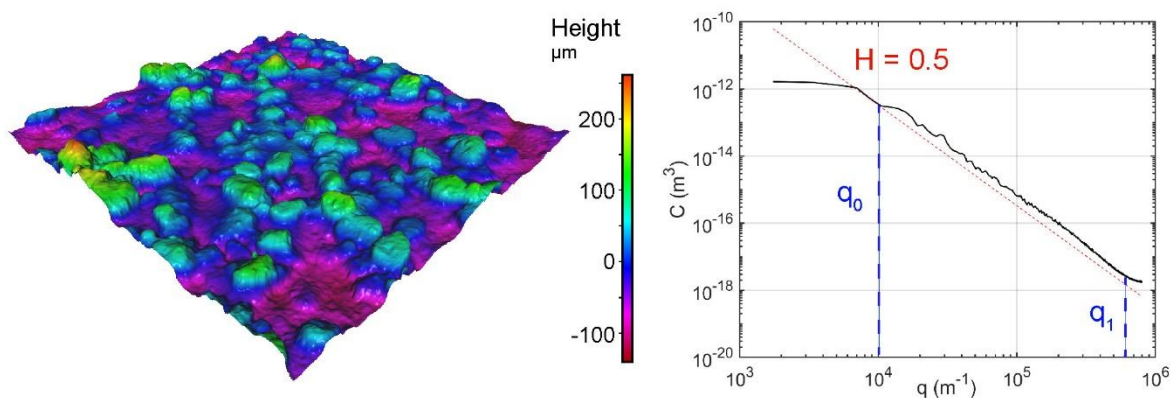


**Figure 3.1** Using a dataset of 850,000 data points (left), a 1D PSD  $C^{1D+}$  was calculated (right). The dashed red line represents a power-law relationship with a Hurst exponent of 0.5.  $q_0$  is the small wavevector of the hard court.  $q_1$  is the large wavevector.

The primary benefit of PSDs, in comparison to other roughness measures, is that they are largely unbiased by scan size and measuring resolution [80,84]. Nevertheless, the same equipment ( Alicona InfiniteFocus SL, Optimax, Leicestershire, UK) and scan size (2.6 × 2.6 mm, 850,000 points) were used throughout this thesis for consistency. An example PSD, made as described, is shown in Figure 3.1. The  $q_0$  wavevector and Hurst exponent are annotated on the PSD plot. The  $q_0$  wavevector describes the wavelength of the largest scale surface roughness ( $q_0 = 0.1$  mm), which in the case of the hard court are provided by the largest paint-covered sand particles. Additionally, from this PSD, RMS roughness ( $h_{rms}$ ) can be reliably determined using Equation 3.1. Note that here,  $h_{rms}$  specifically describes the surface RMS roughness calculated from a 1D PSD  $C^{1D+}$ .

$$h_{rms}^2 = \frac{1}{\pi} \int_0^{\infty} C^{1D+}(q) \cdot dq_x$$

**Equation 3.1**

As Equation 3.1 shows,  $h_{rms}^2$  is the integral of the PSD. The PSD RMS slope ( $h'_{rms}$ ) is calculated as the double integral of the PSD, and is used in some rubber friction models to inform the choice of  $q_1$  [85], which is largely subjective. Both  $h_{rms}$  and  $h'_{rms}$  values mentioned in this thesis were calculated automatically by the contact.engineering software.

Figure 3.1 shows the hard court surface to have a Hurst exponent of 0.5. This is common among natural surfaces [84], but smaller than the Hurst value of 0.8 typical for asphalt road surfaces, on which most analytical rubber friction models are based.

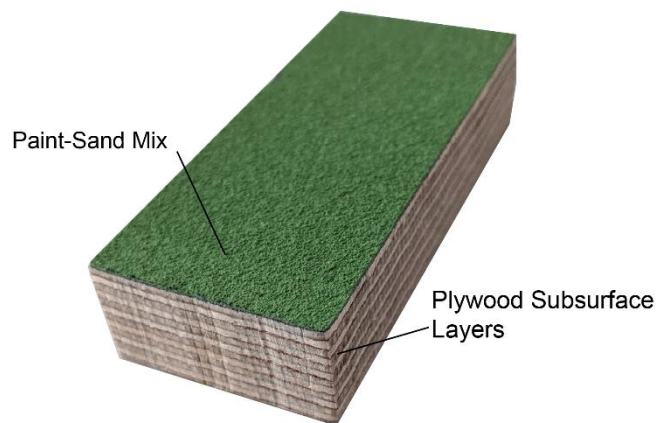


**Figure 3.2** A cut of the hard court tennis surface used in experiments.

As the principle aim of this thesis is to investigate the effects of tennis shoe outsole design on friction, and not the court, only one type of hard court surface (LMG1, Ace Surfaces North America) was used in all experiments herein. This surface represents a standard hard court

surface. As well as the PSD,  $R_a$  and  $R_q$  readings are referenced throughout this thesis to provide a general description of the surface topography.

Characterising the hard court surface by topographical measures alone, assumes the effects of surface compression are negligible. This is valid for the experiments within this thesis as the construction of the surface ensured its rigidity. As shown in Figure 3.2, the hard court had little cushioning and therefore was deemed not to deform enough during slide experiments to induce any additional frictional effects. However, this is not true for all hard court surfaces. Sometimes surfaces have a cushioning layer below the sand-paint layer. If shoe-surface contact pressures are high enough during sliding to deform the tennis surface, it is likely to provide additional frictional effects due to the increased contact area and the additional horizontal force required to overcome or plough the surface bulge that forms at the leading edge of the slide (Figure 3.3).

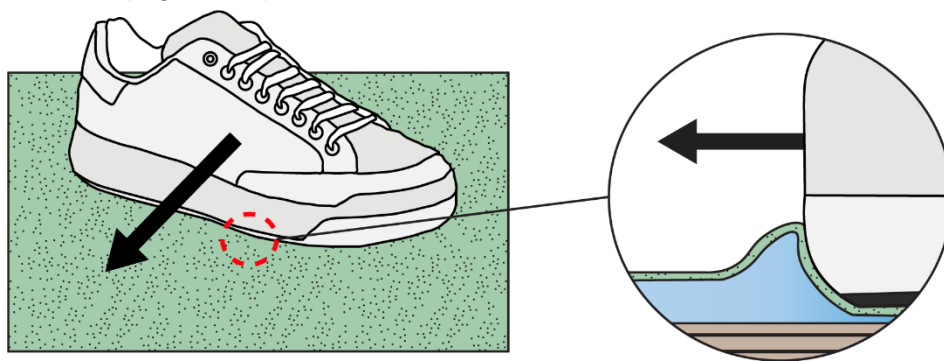


**Figure 3.3** A deformable sub-surface layer (blue) may alter the mechanics of sliding. It would increase friction due to the increased contact area with the lateral sides of the outsole, and the increased force needed to either push or overcome the build-up of surface at the leading edge.

### 3.2 Rubber Characterisation

Rubber is a viscoelastic material made up of polymer chains that, prior to vulcanisation, can freely move around one another in a liquid state. Upon heating with sulphur (vulcanisation), these chains are bonded to one another at discrete locations. These bonded chains are intertwined with one-another, giving the rubber its time-dependent viscoelastic nature through the internal friction that derives from the movement of polymer chains against each other during the deformation of the rubber. Rubber can be divided into two main types: Natural and Synthetic, the difference being that natural rubber contains rubber from its natural source, the *Hevea Brasiliensis* tree, while synthetic rubbers are purely synthetic. In the production of car tyres, and most likely shoe outsoles, natural rubber is scarcely used, and synthetic rubbers are often preferred. Synthetic rubbers can be manufactured in a multitude of ways using a

plethora of materials in multiple combinations and ratios. These details are often protected as company secrets and are almost impossible to determine through reverse engineering of the rubber compound. As such, without working directly with a rubber manufacturer, it is very difficult to determine the complete chemical composition of a rubber. The work presented in this thesis was conducted without the cooperation of a rubber manufacturer, meaning that the link between friction and rubber chemistry cannot be sufficiently investigated. Instead, rubber is characterised by its mechanical properties alone.

Referring to the Persson rubber friction theory (Section 2.1.4), when calculating friction, the rubber is also only characterised mechanically, via viscoelastic master curves. This indicates that the frictional effect of the various manufacturing techniques, materials and fillers are manifested and observable in the master curves. This is true when rubber friction is deemed purely dependent on hysteresis.

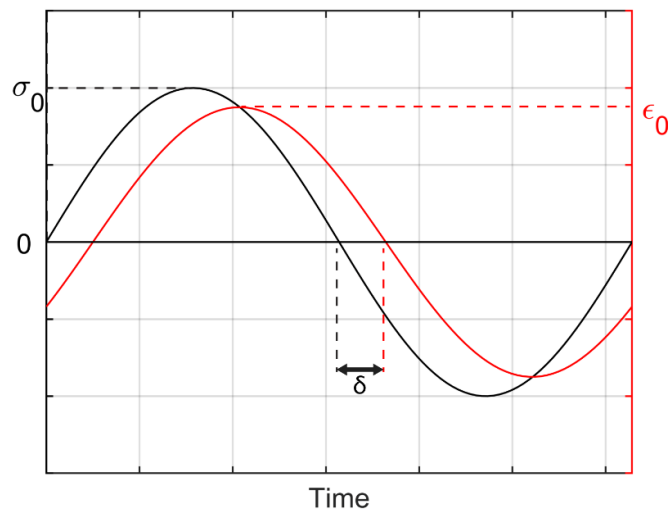


**Figure 3.4** Stress and strain curves from DMA annotated to show the factors used to calculate  $E'$  and  $E''$  at a set frequency and temperature.

To generate a viscoelastic master curve a block of rubber is vibrated sinusoidally at a range of frequencies and temperatures. Measurements of displacement are used to determine the resultant strain of the rubber, from which the modulus can be calculated. Figure 3.4 with Equations 3.2 and 3.3 show how the application of sinusoidal stresses to rubber, with the resultant strain, can be used to generate modulus values ( $E'$ ,  $E''$ ) at a set temperature and frequency:

$$E' = \frac{\sigma_0}{\epsilon_0} \cos \delta$$

**Equation 3.2**

$$E'' = \frac{\sigma_0}{\varepsilon_0} \sin \delta$$

**Equation 3.3**

Where  $\sigma_0$  is the applied stress,  $\varepsilon_0$  is the measured strain and  $\delta$  is the phase difference.

By conducting this calculation at numerous frequencies and temperatures (as can be done using DMA), the time-temperature superposition principal (introduced in Section 2.1.4) can be employed to determine the modulus of the tested rubber outside the measurable range. For all the original master curves presented in this thesis, measurements were taken between 1 – 30 Hz at temperatures between -50 – 100°C. Figure 3.5 shows a set of these modulus readings for a rubber compound.

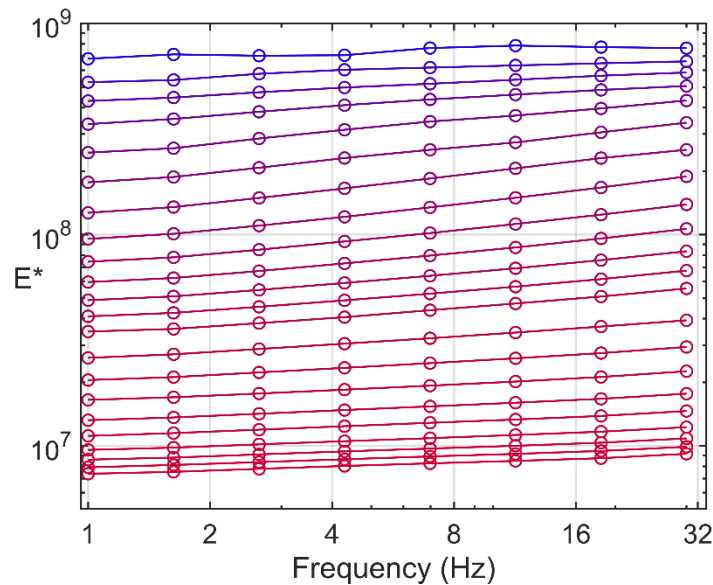


**Figure 3.5** A set of complex modulus readings calculated at numerous frequencies and temperatures. The change in colour indicates the temperature tested at, with the low temperatures being blue and the high being red.

The Williams-Landry-Ferry (WLF) equation is the most widely accepted method for generating master curves from discrete modulus data like that shown in Figure 3.5. Equation 3.4 is the WLF equation used to generate the time-temperature shift factor,  $a_T$ ;

$$\log(a_T) = \frac{-C_1(T - T_r)}{C_2 + (T - T_r)}$$

**Equation 3.4**

Where  $T_r$  is a reference temperature,  $T$  is the temperature being shifted to, and  $C_1$  and  $C_2$  are both constants. In practice, these constants and shift factors are generated automatically by the DMA machines (DMA VA2000, Metravib, France), outputting the modulus master curve polynomials to allow plotting. Figure 3.6 shows the real and imaginary master curves for the rubber whose raw data is in Figure 3.5. As is shown, from testing at a frequency of 1 – 30 Hz,

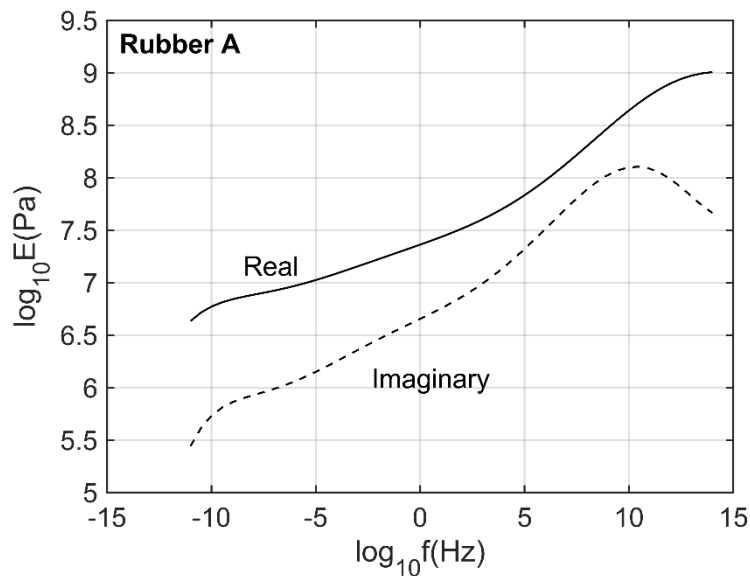


**Figure 3.6** Complete master curve for a synthetic rubber. The raw data set is depicted in the previous figure. The coefficients  $C_1$  and  $C_2$  were calculated as 156 and 1018, respectively.  $T_r$  was 25.9 °C.

across a 150°C temperature range, the modulus of a rubber can be determined over a frequency range of  $10^{-10} - 10^{10}$  Hz.

As useful as these master curves may seem, especially when evaluating the hysteretic friction of sliding rubber, they are not without assumptions. The master curve in Figure 3.6 was generated at low strain (0.001% strain), meaning the magnitude of the forces subjected to the rubber during the DMA process were low, resulting in low strain of the tested rubber. This is generally the accepted practice when formulating master curves, as at low strain, the rubber's stress-strain relationship is linear. At higher strain the stress-strain relationship of rubber becomes non-linear for a variety of reasons including Payne and Mullins effects [25]. Strains greater than 0.001% are experienced by shoe outsole rubber during hard court sliding, especially as tread elements flex and wear. It may therefore seem apparent that viscoelastic master curves should be generated at high strain as opposed to low strain. However, high strain DMA has its complications: the rubber can be easily broken during testing, the master curve is not easily produced by the machine, and manual methods must be utilised.

When comparing high and low strain viscoelastic master curves, the high strain curves show similar trends against change in frequency and temperature as the low strain curves, but at lower modulus magnitude [25]. This is shown in Figure 3.7.

As the DMA machines at the University of Sheffield were capable of only conducting low strain tests, only low strain master curves are shown in this thesis. Although this reduces accuracy when calculating a rubber's hysteresis during sliding, it still gives information on how their material characteristics influence friction.

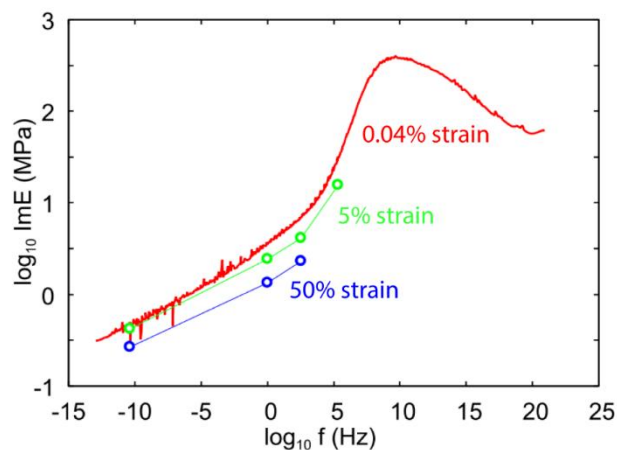


**Figure 3.7** An imaginary master curve obtained at low strain (0.04%) with modulus points measured at two higher strains (5% and 50%). Image taken and adapted from [25].

Viscoelastic master curves only consider hysteresis when being used to model friction. As explored in Section 2.1.8, wear can also contribute to the friction of rubber on dry surfaces, especially on very rough surfaces like sandpaper and hard courts. It must therefore be acknowledged that in the analysis of sliding scenarios which produce noticeable wear, a viscoelastic master curve, and hence the friction models discussed in Sections 2.1.4 and 2.1.5, represent only one component of the observed friction.

### 3.3 Combining Surface and Rubber Measures

The previous two sections in this chapter provide detail on the surface and rubber measures used to interpret rubber friction on dry surfaces. This section takes the PSD of a hard court tennis surface and the viscoelastic master curve of a Styrene-Butadiene Rubber (SBR) to explore how these measures are used in combination, and what information they can deliver on the friction between the rubber and surface.

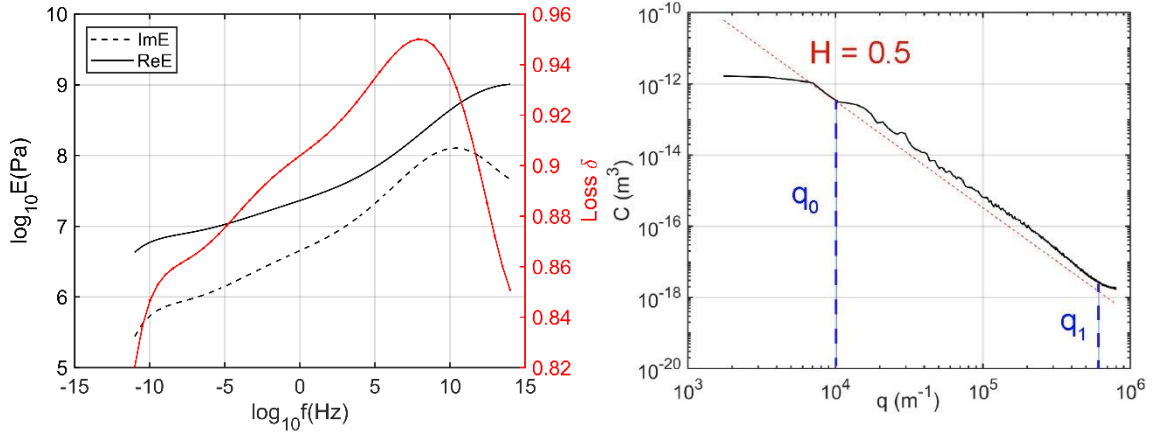


**Figure 3.8** Modulus master curves for a SBR (left). PSD for a hard court surface (right).

As depicted in Figure 3.8, modulus values are presented as a function of frequency. Therefore, once the key wavevectors ( $q_0$  and  $q_1$ ) are identified from the PSD, they are converted into frequencies. Using Equation 3.5, the frequency range,  $\Delta f$ , subjected to a rubber can be calculated from the PSD wavevectors;

$$\Delta f = \frac{v}{2\pi / (q_0 - q_1)}$$

**Equation 3.5**

Hence by knowing the slide velocity,  $v$ , and the PSD for the surface, a working frequency range can be identified, and the corresponding modulus values found. In these examples,  $q_0 = 0.1 \text{ mm}$  and  $q_1 = 1.58 \text{ }\mu\text{m}$ .

As shown in Figure 3.9, an increase in slide velocity means an increase in the frequencies that perturb the rubber. For most of the master curve shown, this increase in velocity corresponds to an increase in imaginary modulus, loss tangent, and therefore hysteresis. So, with a minimal number of steps, from the PSD and master curve, quick assumptions can be made about how changes in slide velocity affect the hysteretic response of the rubber.

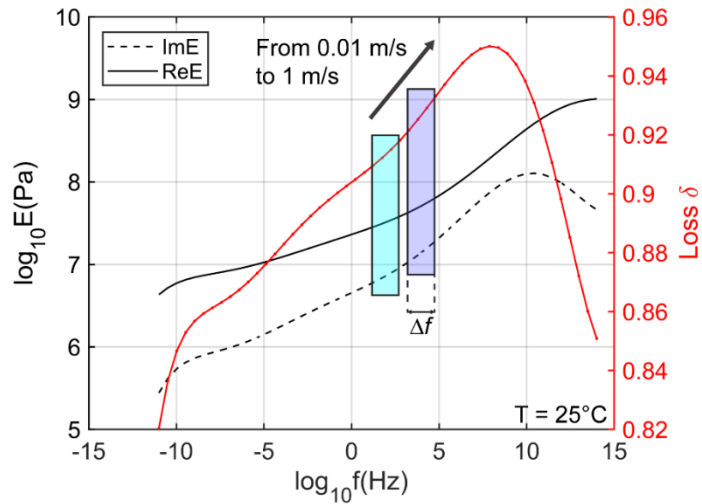


**Figure 3.9** Master curves for SBR with individual lines for imaginary modulus, real modulus and loss tangent (reference temperature of 25°C). Increase in slide velocity results in higher orders of frequency perturbing the rubber.

Similarly, the effect of changes in temperature can be shown. By setting the reference temperature,  $T_r$  in Equation 3.4, and finding the corresponding frequency range. These modulus values can then be found on the master curves generated with a different  $T_r$ . An example of this is shown in Figure 3.10, depicting how a 10°C increase in temperature results in a reduced imaginary modulus, loss tangent, and thus hysteresis.

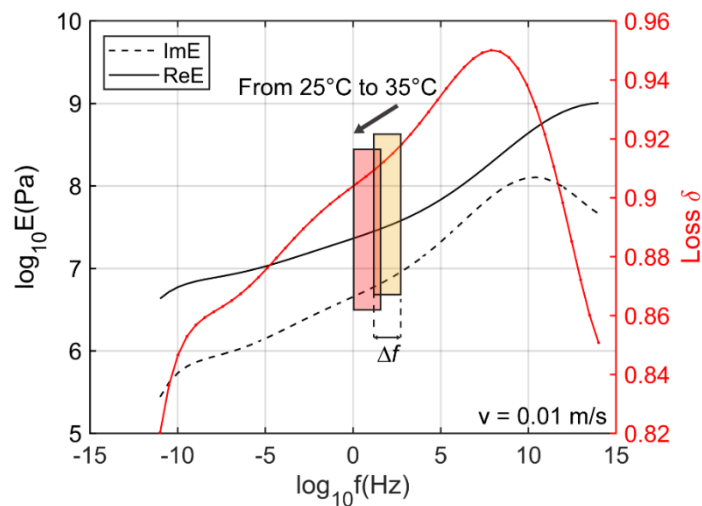


**Figure 3.10** Master curves from the same rubber shown in the previous figure. Here an increase in temperature shows a decrease in modulus values. Sliding velocity is set at 0.01 m/s.

In addition to changes in velocity and temperature, it can be observed how changes in surface roughness, by way of wavevectors, and differences in rubbers, alter the amount of hysteresis. However, as the focus of this thesis is principally on how the shoe influences friction, multiple surfaces will not be considered. Moreover, it is still contested as to how  $q_1$  should be identified from a PSD plot (which will vary dependent on the measurement device used) and how they are used to predict friction [39,80]. These issues need to be further investigated before attempting to compare how surfaces of different PSD influence rubber friction.

The size of the  $\Delta f$  regions shown in Figures 3.9 and 3.10 are simplified in two ways: they assume complete contact between the surface and the rubber, and a two-dimensional interaction. By taking  $q_0$  and  $q_1$  from the PSD and applying them directly to calculate the hysteresis of the sliding rubber, implies all of those roughness wavelengths are filled by the rubber during contact. In most cases this is not a fair assumption as complete contact would require very high local pressures, especially for the small roughness wavelengths in the lower regions of the roughness. Within the Persson friction model, this is accounted for by a series of functions including a correction factor,  $S(q)$ , shown in Equation 3.6.

$$S(q) = \gamma + (1 - \gamma)P^2(q)$$

**Equation 3.6**

Where  $\gamma$  is the surface free energy and  $P(q)$  is a relative contact area function.

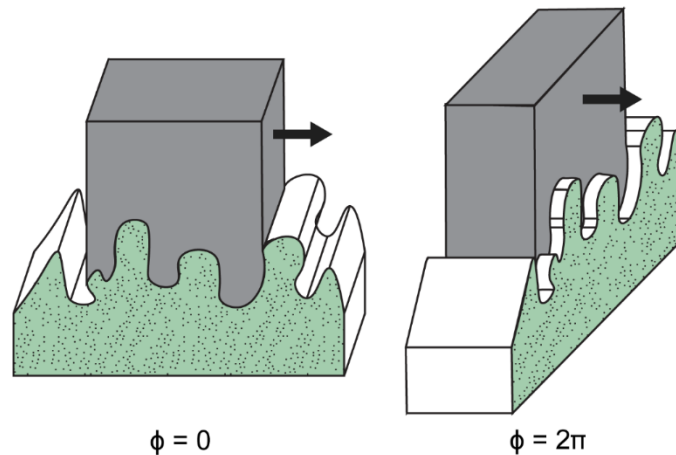


**Figure 3.11** Surface roughness orientation. At  $\phi = 0$ , max frequencies are experienced by the rubber for the chosen topography. At  $\phi = 2\pi$ , no perturbing frequencies are transmitted to the rubber and therefore no hysteresis. Image adapted from [21].

The assumption of a two-dimensional interaction relates to the roughness orientation against the sliding direction,  $\phi$  (Figure 3.11). In the Persson friction model, the calculated values of imaginary modulus are multiplied by  $\cos\phi$ , integrating over values  $2\pi \geq \phi \geq 0$ . For the above

graphs  $\phi = 0$ , meaning the roughness is perfectly perpendicular to the slide direction, generating maximum perturbing frequencies. All angles of  $\phi$  will be experienced by the rubber during sliding, hence the multiplication by the range of  $\phi$  in the model (Equation 2.7).

In the simplified Persson model described in section 2.1.6, the range of wavevectors are not used to predict friction, instead only  $q_1$  is used. It is considered that the  $q_1$  wavevectors have the greatest influence on the observed friction (as they perturb the rubber by the highest order frequencies). This simplified version of Persson's model is considered a useful tool to quickly, and without the need for any fitting, compare the hysteretic response of different rubbers and their response to changing slide velocities. As such, the simplified equation is used in subsequent chapters. If  $h'_{rms} = 1$  and  $q_1 = 10^{5.8}$  this gives Equation 3.7.

$$\mu_{pred} = \frac{ImE\left(\frac{v}{2\pi/10^{5.8}}\right)}{\left|E\left(\frac{v}{2\pi/10^{5.8}}\right)\right|}$$

**Equation 3.7**

Due to the inherent complexity and assumptions involved in the quantitative calculation of friction from PSDs and master curves, this thesis uses these measures only to provide an understanding of the factors affecting observed friction values, not to accurately predict friction values. This level of analysis is something that is generally vacant among shoe-surface friction research, presumably due to the complexities of these measures.

### **3.4 Conclusion**

By assessing tennis shoe-surface friction at this level of detail means that identifying factors influencing friction and changing them accordingly can become a scientific process. For example, consider two shoes with the same tread pattern provide different amounts of friction during sliding. The master curves of the two rubbers and the PSD of the surface can be obtained and it can thus be observed whether this difference in friction is due to differing amounts of hysteresis. If not, then it could be due to a change in wear and a harder wearing rubber could be employed. As such, within this thesis, when comparing the friction of different rubber's, wear tests are also conducted to improve analysis.

The PSD and master curve obtained in this chapter (Figure 3.8) are used throughout the thesis. The same hard court is used in all presented tribology experiments (Chapters 4 – 8) and the master curve describes the rubber used in the following chapter (Chapter 4) and Chapter 5 (Rubber A). An additional rubber master curve is presented in Chapter 5 (Rubber B) which was calculated in the same way as described in this chapter.

## 4 The Effect of Rubber Tread Shape on Friction

The following chapter is adapted from my published full-length research article - Hale, J., Lewis, R., & Carré, M. J. (2020). Rubber friction and the effect of shape. *Tribology International*, 141, 105911.

### 4.1 Introduction

As shown in Section 2.1.10, shoes and tyres of different tread patterns often produce different friction coefficients during sliding in dry conditions. However, due to the geometric complexities of the tested tread patterns, very little scientific rationale is provided to explain why such frictional differences occur. Assumptions can be made as to why some tread patterns, when made of the same rubber, produce different friction coefficients: It is known that increased nominal contact pressure results in a decrease in rubber friction [28,82], and that, as introduced in Section 2.1.9, the length of rubber, parallel to the sliding direction, influences friction via heating effects. Tennis shoe tread patterns often differ in contact area as well as length of their rubber elements. Their tread patterns also differ in terms of tread height (defined in Figure 4.1).

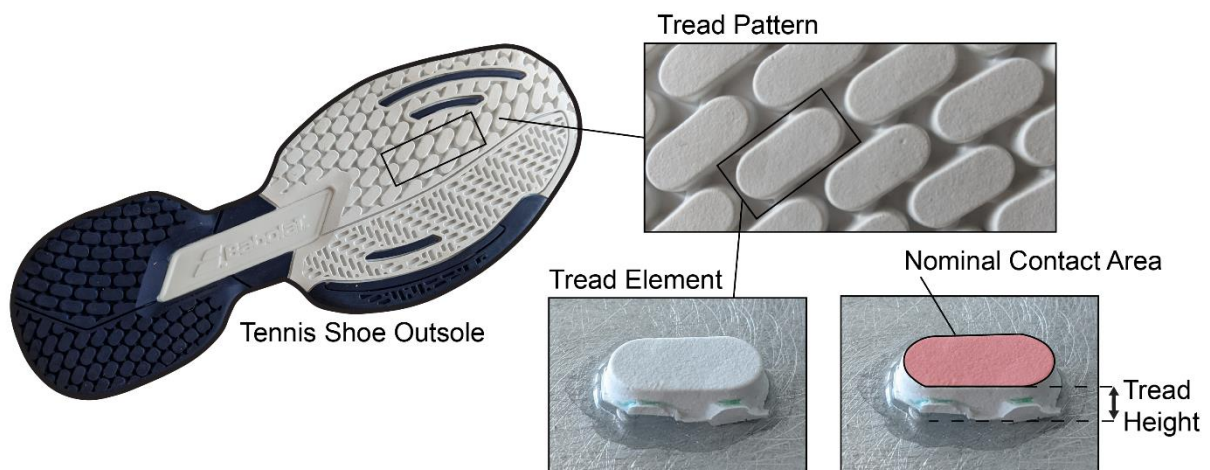


**Figure 4.1** Tread properties such as tread height and nominal contact area.

It has been suggested that rubber's hysteretic contribution to friction can be subcategorised into "surface" and "bulk" hysteresis [86], implying that tread of a greater height will demonstrate higher  $\mu$  due to an increased "bulk" hysteresis through a reduction in the tread's beam stiffness. This is directly opposed by the findings of Maegawa et al. [87] which states that the taller the tread element (reducing beam stiffness), the greater the presence of friction-induced torque which reduces the total real contact area, leading to a decreased friction force (Figure 4.2). This inconsistency in the literature could be due to the different counter surfaces used in both studies. Maegawa et al. used a smooth PMMA surface and Kummer used rough road

surfaces. The friction mechanisms present when sliding rubber over rough and smooth surfaces can greatly differ in both nature and magnitude. This especially affects the presence of adhesion which is thought to reduce as roughness is increased [33]. Many studies indicate that rubber tread shape and stiffness influence the friction of rubber. However, uncertainties are still present as to exactly how.

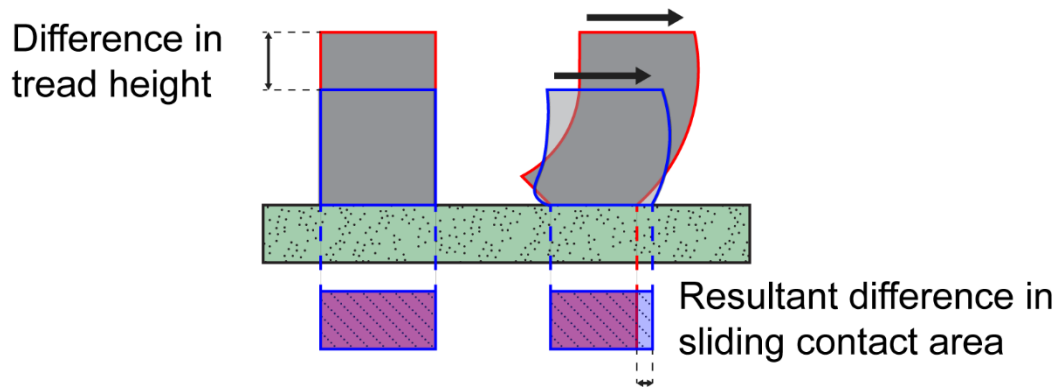


**Figure 4.2** Two blocks of rubber of different heights, produce different sliding contact areas which can influence friction. This is because the increase in height reduces the beam's stiffness, resulting in greater deflections.

A likely influence of beam stiffness on the sliding of a rubber tread is on the stick-slip experienced. Stick-slip is an interesting phenomenon which is particularly prevalent during the sliding of rubbers and describes the attachment-detachment cycle of the rubber to the surface as it slides. It is considered that the bulk sliding of rubber over dry surfaces is the accumulation of stick-slip across multiple length scales [93]. Tread elements of a lower beam stiffness can stick to the surface for longer than tread with a high beam stiffness, meaning they produce more stick-slip, shown by large peaks and troughs in the friction force during sliding.

This chapter describes a series of rubber sliding experiments performed on three different shaped blocks of rubber, clamped at different heights, to identify the influencing factors of rubber tread that may cause frictional differences when rubber slides on rough surfaces, principally hard court tennis surfaces.

It is hypothesised that shape will have a frictional effect, with the longest sliding-direction shape having the lowest friction due to increased frictional heating. At speeds below 1 mm/s, due to frictional heating being negligible, frictional differences between shapes are not expected. Additionally, it is hypothesised that higher friction will be observed for a decrease in beam stiffness due to increased "bulk" hysteresis and that an increase in speed will produce an increase in friction due to a greater hysteresis.

## 4.2 Methodology

### 4.2.1 Surface and Rubber Samples

A single elite tennis hard court surface sample ( $R_a = 72 \mu\text{m}$ ,  $R_q = 91 \mu\text{m}$ ) was used in all sliding experiments (LMG1, Ace Surfaces North America). The sample was constructed of a Medium-Density Fibreboard (MDF) base topped with a sand-acrylic paint mix to give a rough texture. A PSD of this surface is shown and described in Chapter 3, Figure 3.8. All rubber treads were cut from a sheet of commercially available Styrene Butadiene Rubber (SBR) (purchased from Rubberstock.com) and had a Shore A hardness value of 75. To characterise this rubber, a small-strain viscoelastic master curve was generated, detailing the real (storage) and imaginary (loss) modulus of the rubber over 20 decades of frequency. These curves are also shown in Chapter 3.

When analysing wet-surface sliding friction, the rubber's surface roughness has been shown to be influential [88]. On the contrary, the surface roughness of rubber has been shown to have little effect on the friction when in contact with dry rough surfaces [89], unless the rubber has been sufficiently run-in, which can cause sliding friction inversion symmetry [52]. As the rubber tread samples were tested without run-in and on a dry rough surface, rubber surface roughness measures were not taken.

### 4.2.2 Experimental Procedure

A Universal Mechanical Tester (UMT) tribometer (CETR-UMT2, Bruker, Massachusetts, USA) was used to slide the hard court surface beneath three rubber samples of different geometries at 0.5 mm/s and 10 mm/s. Unlike at 10 mm/s, at 0.5 mm/s it is assumed that frictional heat will be negligible [90]. This allowed an assessment of how frictional heat influences  $\mu_k$ .

All samples were loaded with a nominal contact pressure of 0.1 MPa, produced by applying a normal load of 10 N. The UMT control system maintained this normal load throughout sliding. Slides were 30 mm in length. Three slides were performed for each rubber shape in each condition. After each slide, the rubber and surface were lightly brushed with a fine-bristled paint brush to reduce the potential influence of wear contamination at the rubber-surface interface. The experimental set-up is shown in Figure 4.3.

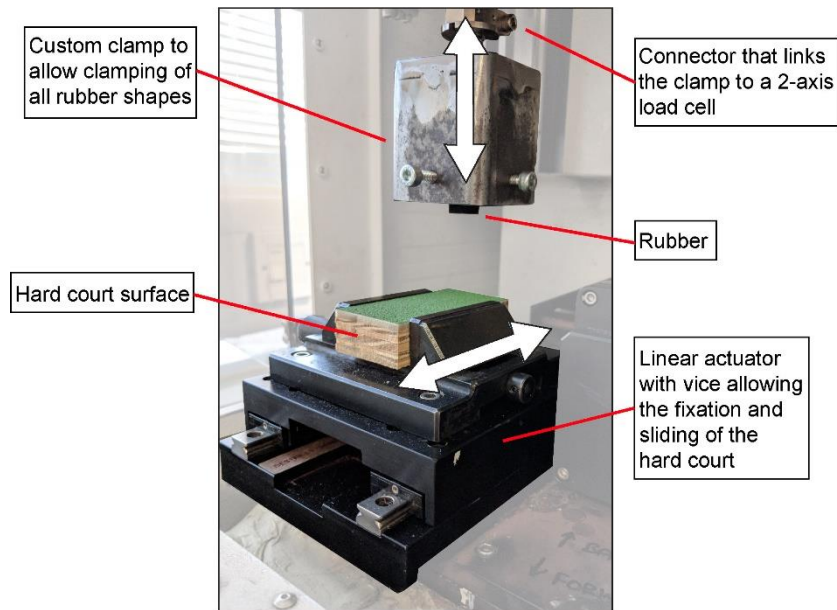


**Figure 4.3** Experimental set-up.

Figure 4.4 shows the three shapes of rubber tread used (S1, S2 and S3). All samples had an equal nominal contacting surface area (100 mm<sup>2</sup>) but differed in second moment of area ( $I_{xx}$ ) in the slide direction ( $x$ ). This ensured the frictional differences due to varied nominal contact area, and therefore nominal contact pressure, were controlled and negated.

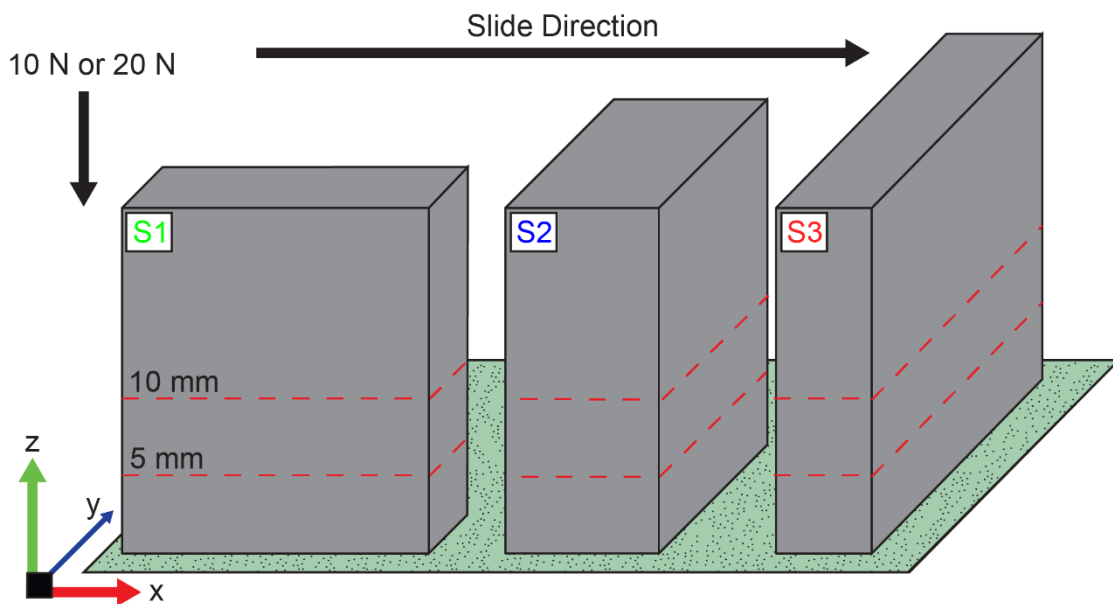


**Figure 4.4** All shapes of rubber tested at clamp heights of 5 and 10 mm. Using Equation 4.1, the  $I_{xx}$  values were calculated as 3333 mm<sup>4</sup>, 833 mm<sup>4</sup> and 208 mm<sup>4</sup> for treads S1, S2 and S3 respectively.

$$I_{xx} = \frac{bh^3}{12}$$

#### Equation 4.1

where 'b' is the base width in  $y$ , and 'h' is the base length in  $x$ . Tread height was modified by clamping the rubber tread elements at two different points along their height (5 mm and 10 mm in the  $z$ -axis from the contacting face). Equation 4.2 was used to determine the beam stiffness ( $k$ ) of the rubber during each test. Beam stiffness here refers to the stiffness of the rubber tread element, not to be confused with the modulus 'E', which represents the material characteristic.

$$k = \frac{3EI_{xx}}{l^3}$$

#### Equation 4.2

In Equation 4.2, the tread clamp height was used for  $l$  and the tensile modulus of 3 MPa was used for  $E$ . Equation 4.2 is typically used in the analysis of long beams undergoing small deflections. Though the case here concerns short beams, undergoing comparatively large deflections,  $k$  is still considered a sufficient way of generally expressing a 3D shape's stiffness.

#### 4.2.3 Wear Analysis

For one series of tests (0.1 MPa, 0.05 mm/s and 5 mm tread height), all three rubber samples had their mass measured (Satorius BasicPlus BP210D, Göttingen, Germany) before and after three slides. Additionally, to investigate the wearing regions on the rubber, three slides were performed at higher pressure (0.2 MPa) and at a 10 mm/s slide speed, clamped at 5mm. Photos were taken before and after these slides.

#### 4.2.4 Definition of $\mu_s$ and $\mu_k$

$\mu_s$  is defined as the  $\mu$  that is overcome to initiate sliding and  $\mu_k$  is the mean  $\mu$  needed to be overcome to maintain motion at a constant speed. Figure 4.5 is a  $\mu$ -time trace labelled with  $\mu_s$ , which is taken as a single value and  $\mu_k$  which is the average of the proceeding readings as sliding is maintained.

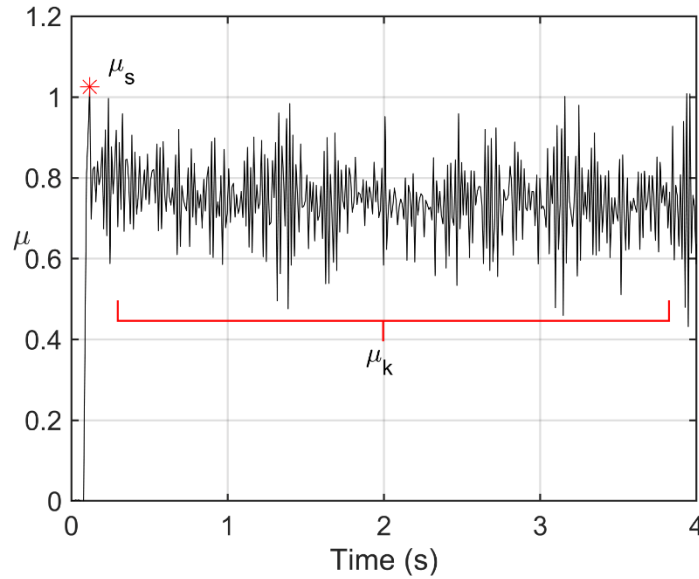


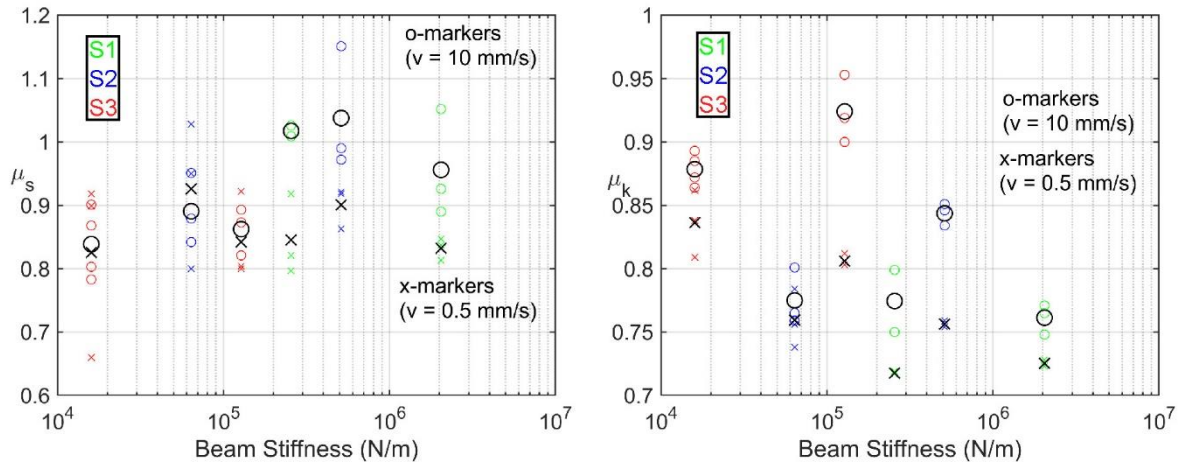
**Figure 4.5** Example  $\mu$ -time trace annotated with static ( $\mu_s$ ) and dynamic ( $\mu_k$ ) friction coefficients.  $\mu_k$  is calculated as the average of all  $\mu$  values that follow the  $\mu_s$  value, excluding the first and last 10.

#### 4.2.5 Data Analysis

A series of t-tests and univariate Analysis of Variance (ANOVA) tests with Bonferroni post hoc tests were conducted to investigate the effect of slide speed and slide-direction length on both  $\mu_s$  and  $\mu_k$ . Bonferroni post hoc tests were performed to investigate the effects of all three individual shape lengths while controlling Type 1 error [91]. Pearson-r tests were conducted to investigate the correlation between  $\mu_s$  and  $\mu_k$  against beam stiffness and slide-direction length. A  $p < 0.05$  significance value was used for all statistical tests. Prior to the running of this analysis, Shapiro-Wilk normality checks were performed. All statistical analysis was conducted using IBM SPSS Statistics 25.

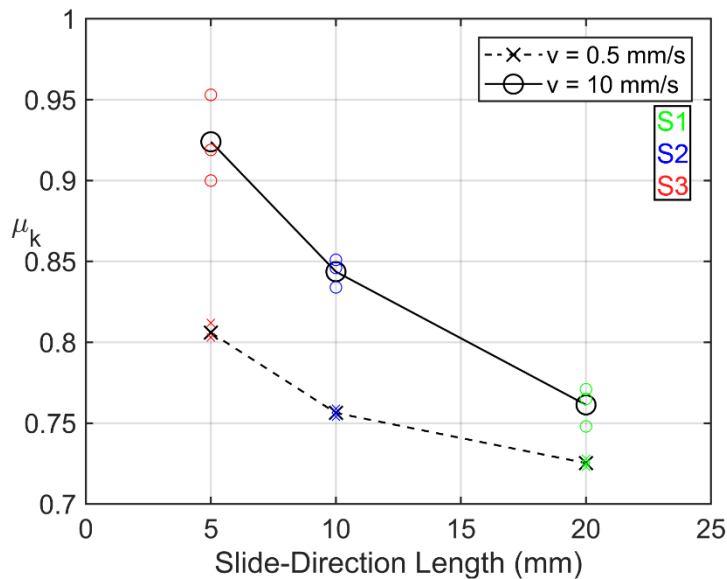
#### 4.3 Results

Figure 4.6 shows that the beam stiffness of the tread elements had no linear relationship with  $\mu_s$  ( $r = 0.10$ ,  $n = 36$ ,  $p = 0.55$ ) but were negatively correlated with  $\mu_k$  ( $r = -0.44$ ,  $n = 36$ ,  $p = 0.007$ ). Although there is a negative correlation between beam stiffness and  $\mu_k$ , it is not definitive enough to conclude that increasing tread stiffness decreases  $\mu_k$ . As shown, though the overall trend is a decrease in  $\mu_k$  with an increase in beam stiffness, this trend is composed of peaks and troughs at both slide speeds. Lower magnitudes of  $\mu_k$  were measured at the slower speed 0.5 mm/s.



**Figure 4.6**  $\mu_s$  (left) and  $\mu_k$  (right) against beam stiffness for all shapes at both 5 mm and 10 mm tread heights at 0.1 MPa. Coloured points represent the raw  $\mu$  data for each shape. Black markers and lines indicate calculated means.

Both  $\mu_s$  and  $\mu_k$  were affected by the increase in slide speed from 0.5 mm/s to 10 mm/s. For  $\mu_s$ , there was a significant increase in friction with the increase in speed: 0.5 mm/s ( $M = 0.86$ ,  $SD = 0.08$ ) vs 10 mm/s ( $M = 0.92$ ,  $SD = 0.09$ ) speeds;  $t(34) = 2.09$ ,  $p = 0.045$ . A greater significance in scores was observed for  $\mu_k$  between 0.5 mm/s ( $M = 0.77$ ,  $SD = 0.05$ ) and 10 mm/s ( $M = 0.83$ ,  $SD = 0.06$ );  $t(34) = 3.52$ ,  $p = 0.001$ .



**Figure 4.7**  $\mu_k$  vs the shape's slide-direction length (clamped at 5 mm). For each shape, increased velocity increased  $\mu_k$ . Black markers and lines indicate calculated means.

Figure 4.7 shows the  $\mu_k$  and slide-direction length relationship for both slide speeds when clamped at a 5 mm height. Significant differences were observed for  $\mu_k$  with a change in slide-direction length ( $F(2,33) = 28.86, p < 0.001$ ). Additionally, Bonferroni post hoc tests found significant differences in  $\mu_k$  for all shapes ( $p < 0.05$  for all group comparisons). Although significance was also recorded for changes in slide-direction length for  $\mu_s$  ( $F(2,33) = 4.08, p = 0.026$ ), there was no significant linear correlation ( $r = 0.22, n = 36, p = 0.20$ ).

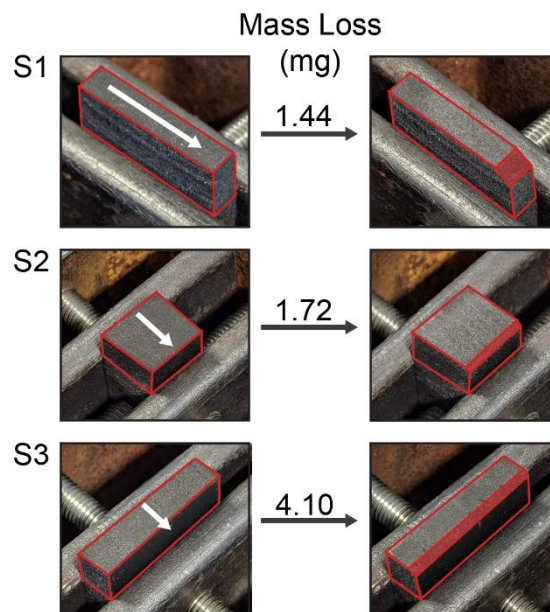


**Figure 4.8** All shapes before (left) and after (right) three slides at 0.2 MPa and 10 mm/s to produce visual differences. Mass loss values were taken from three slides at 10 N and 0.5 mm/s. White arrows are slide direction, and red lines are shape outlines.

When sliding with a pressure of 0.1 MPa and at a speed of 0.5 mm/s, different amounts of wear were measured. Figure 4.8 shows that S1 wore the least, with a mass loss of 1.44 mg, followed by S2 with a mass loss of 1.72 mg. S3 recorded the greatest mass loss of 4.10 mg.

#### 4.4 Discussion

The classical laws of friction state that in dry sliding scenarios the shape of a sliding sample has no influence on the body's friction. Figure 4.7 shows that this was found not to be true for the rubber tested in this chapter. Using rubber tread of varying second moment of area in the sliding direction, and clamping at two different heights, the effect of overall beam stiffness and tread height on friction was investigated. As highlighted in Figure 4.6, no beam stiffness-friction relationship can be implied, and  $\mu_k$  is more affected by the sliding direction-length of the rubber (regardless of its second moment of area) and slide speed. The effect of speed has been well reported and as expected, the increase in speed in combination with the surface roughness over multiple scales, increases the oscillating frequencies transferred to the rubber. In turn, as

observed by moving from left-to-right on the loss tangent curve of the rubber (Figure 3.8), energy loss increases and therefore so does the hysteretic and overall  $\mu_k$ . An increase in slide speed has been found in previous research to result in an increase in  $\mu_k$  up to the speed of around 10 mm/s where  $\mu_k$  peaks [27,92]. Above this speed the contribution of frictional heating becomes dominant, reducing hysteresis even with the increase in oscillating frequencies [27]. Although the effect of adhesion is likely to be secondary in comparison to hysteresis on rough surfaces, it is stated that adhesion decreases with increased slide speed beyond 10  $\mu\text{m/s}$  [26]. A combination of the frictional reductions caused by increased frictional heating and decreased adhesion is likely to explain why  $\mu_k$  often peaks at 10 mm/s before dropping. As the maximal speed tested in this chapter is equal to the 10 mm/s speed threshold, the increase in speed from 0.5 mm/s was expected to increase  $\mu_k$ . Moreover, at 10 mm/s a greater degree of stick-slip was observed which is also likely to contribute to the increased friction.

The stick-slip illustrated in Figure 4.9 represents that undergone by the entire tread element. Figure 4.9 shows three  $\mu$ -time traces from slides at 10 mm/s for all three of the tested shapes. The shape with the shortest sliding edge, and hence the lowest bending stiffness, exhibits a greater severity of stick-slip behaviour than the other shapes. This instability during sliding is a feature of low stiffness beams, such as S3, as the low stiffness allows a longer sticking period, which temporarily increases friction force, before detachment which then decreases the frictional force.

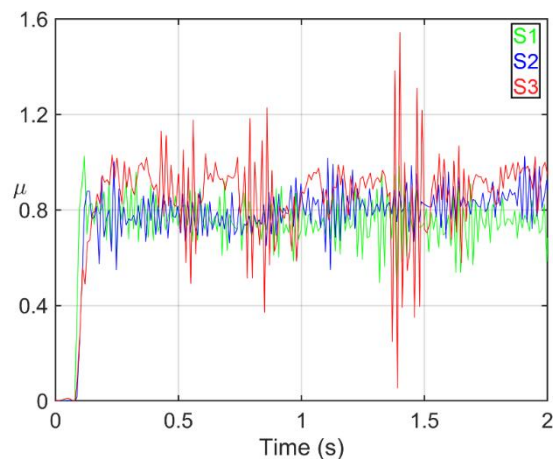


**Figure 4.9** The first two seconds of three  $\mu$ -time traces for the three shapes tested.

These tests were all run at 10 mm/s and at tread heights of 5 mm.

Although the prevalence and severity of macro-level stick-slip is clearly different for the three shapes, it is not seen as the principal reason for the increased  $\mu_k$  values recorded. Observation of Figure 4.9 shows that when a sharp spike occurs in the  $\mu$ -time trace of S3, it is followed by a drastic drop in  $\mu$  of comparable magnitude. Furthermore, the sections of the

S3 trace between these events, with low amplitude oscillations, are still of higher  $\mu$  value than that of S1 and S2. Since this whole trace is averaged in the calculation of  $\mu_k$  (see Figure 4.5), the presence of the stick-slip spikes will have little influence on the reported  $\mu_k$  value.

Shapes producing different dry  $\mu_k$  for rubber has been recorded in another dry rubber sliding study [59]. Fortunato et. al hypothesised that the frictional difference occurred because of varying amounts of frictional heating, with the longer rubber shapes (parallel with the sliding direction) producing the greater amount of frictional heating. It is true that for the current study, that the longer shapes produced the lowest  $\mu_k$  and that this is more pronounced at the greater slide speed at which frictional heating is likely to be influential. However, differences in  $\mu_k$  were also recorded between the three rubber shapes at slow speeds (Figure 4.7) at which frictional heat is unlikely to build up [59,90]. Hence, suggesting an additional frictional mechanism that differentiates between the frictional behaviour of shapes of rubber even at speeds where frictional heat has little or no influence. The mass loss values in Figure 4.8, show a positive correlation between wear mass and  $\mu_k$  for the 0.5 mm/s slide speed (Figure 4.10).

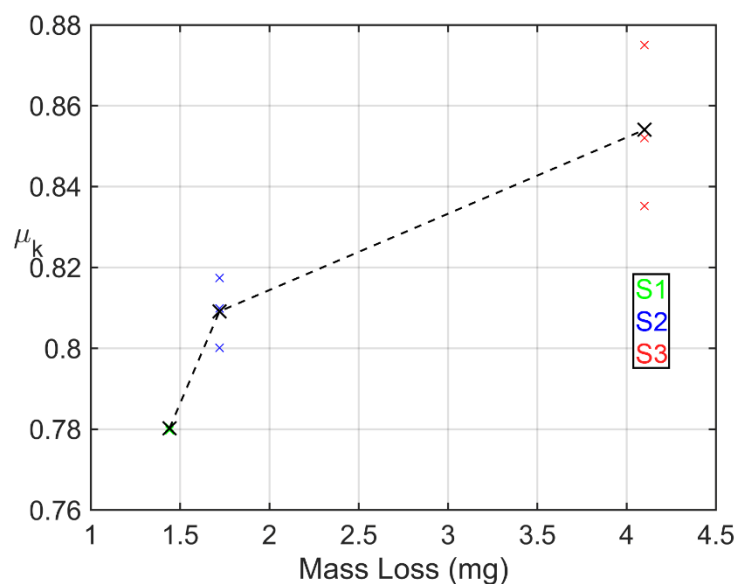


**Figure 4.10**  $\mu_k$  against mass loss for sliding at 0.5 mm/s. After three slides for each shape, mass was taken and plotted at the mean (black crosses).

The tearing of rubber by sharp surface asperities is a process which consumes energy [25,36]. Hence, it is not surprising that the shape with the highest friction has produced the greater wear. Emami & Khaleghian found the same positive correlation between mass loss and friction when sliding SBR blocks on two forms of asphalt surface [36]. What is of interest, is why the shapes wore at different rates. One possible explanation is provided through interpretation of the wear images in Figure 4.8. The photographs show that wear mostly occurred along the

leading edge of the shape. As depicted in Figure 4.11, when rubber slides the leading edge curls inwardly and comes under increased pressure. This has been shown both through Finite Element Models (FEM) and experimental results alike [68,93]. This increased pressure and stress will consequently increase the wear rate at the leading-edge. Due to the wear observed in this chapter, subsequent friction tests in chapters 5 and 6 are coupled with friction tests to further investigate the effect of wear on friction.

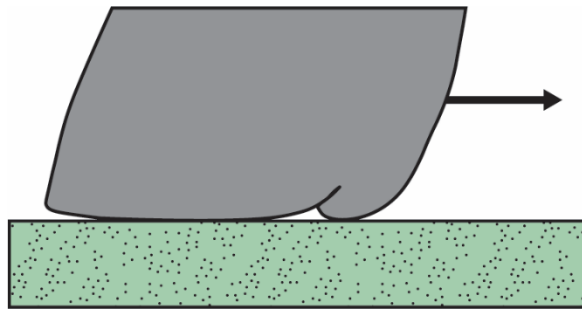


**Figure 4.11** A sliding rubber block showing curling at the leading edge.

This study cannot differentiate the frictional effect of leading edge length (linked to friction by wear) with that of the tread's slide direction length (linked to friction by frictional heating). By controlling the nominal contact areas of the shapes to negate the effect of differing nominal contact pressures, a change in block length inevitably produces a change in block width. In future work, similar experiments could be conducted with shapes that are tested both with and without defined leading edges. These could be chamfered before testing to reduce wear.

In this study, the increased leading-edge length increases  $\mu_k$  as there is a larger region of curling and therefore wearing which consumes energy. This is deemed to be the primary reason why shape had a frictional effect at slow speeds. This friction mechanism will be less prominent for harder-wearing rubbers or at lower nominal contact pressures as wear is less likely to occur.

#### **4.5 Conclusion**

The study described in this chapter shows that shape has a definitive effect on the  $\mu_k$  of rubber sliding over a hard court surface. This implies that different tennis shoe treads will produce frictional differences even if the nominal contact areas are equal. However, this chapter addresses only the simplest case of a sliding rubber on a hard court, not complex tread patterns or under loads and speeds likely during hard court slides. More complex scenarios are tested in subsequent chapters and are then compared with these initial findings.

This study rejected the influence of tread beam stiffness as an influencing factor to  $\mu_s$  and  $\mu_k$ , though it is found to affect the nature of sliding via the incidence and magnitude of macro-level

stick-slips. The findings of this chapter support the theory that, at speeds  $> 1$  mm/s, longer shapes (parallel to the slide direction) have lower  $\mu_k$  due to increased frictional heating. However, as was not foreseen, a lesser but still significant frictional difference was found at a speed  $< 1$  mm/s (0.5 mm/s). Investigating the wear rate and locations, found that the leading edge length also had an effect, with longer front edged shapes (perpendicular to the slide direction) producing the highest  $\mu_k$  through additionally wearing.

The results of this chapter identify tennis shoe tread geometry parameters that will influence both  $\mu_s$  (relevant for the initiation of sliding and step movements) and  $\mu_k$  (relevant for sliding) when a tennis shoe slides over a hard court tennis surface. Moreover, tribological mechanisms that produce frictional variances were identified.

# 5 Using a Simplified Model for Dry Rubber Friction

## 5.1 Introduction

Chapter 4 identified the wearing of rubber tread elements to influence the  $\mu_k$  of rubber sliding over hard court surfaces. Shapes with longer leading edges wore at a greater rate than shapes of equal nominal contact area, but shorter leading edges. Additionally, shapes with longer leading edges also had higher friction. This positive leading edge length-wear-friction relationship was observed even at slow slide speeds, where the effects of frictional heat will be negligible, and therefore not explain the frictional differences. If wear is the reason shapes with longer leading edges produce higher friction, it is expected that rubber grades with greater wear-resistance will have a lesser effect of shape on friction. To test this, and further understand the wearing of different rubber shapes, this chapter details a series of experiments conducted to monitor the wear-friction relationship of two rubbers (Rubber A and Rubber B) over multiple slides. Rubber A is the same as the rubber tested in Chapter 4; Rubber B is a rubber with improved wear-resistance.

By testing two rubbers of differing wear-resistance allows the influence of wear on rubber shape friction to be better investigated. However, rubbers of varying wearability are likely to vary in modulus also, which will influence their friction by varied hysteretic energy losses. To account for these hysteretic contributions to friction, a model that predicts the hysteretic contribution to friction from the rubber's master curves can be implemented. In Section 2.1 various friction models are introduced that model the friction of rubber blocks on rough surfaces. In practice most of these models work by curve-fitting to previously obtained friction data. However, the simplified Persson model (introduced in section 2.1.6) is truly predictive and includes no fitting parameters. As such, this model can be used to predict the friction of rubbers using only surface PSD and rubber master curves.

It is hypothesised that a lower wearing rubber will produce smaller frictional differences for different shapes, as less wear will occur. The simplified Persson model is expected to predict which rubber produces the highest overall friction, as hysteresis will be the most influential factor of a rubber's friction.

## 5.2 Methodology

### 5.2.1 Surface

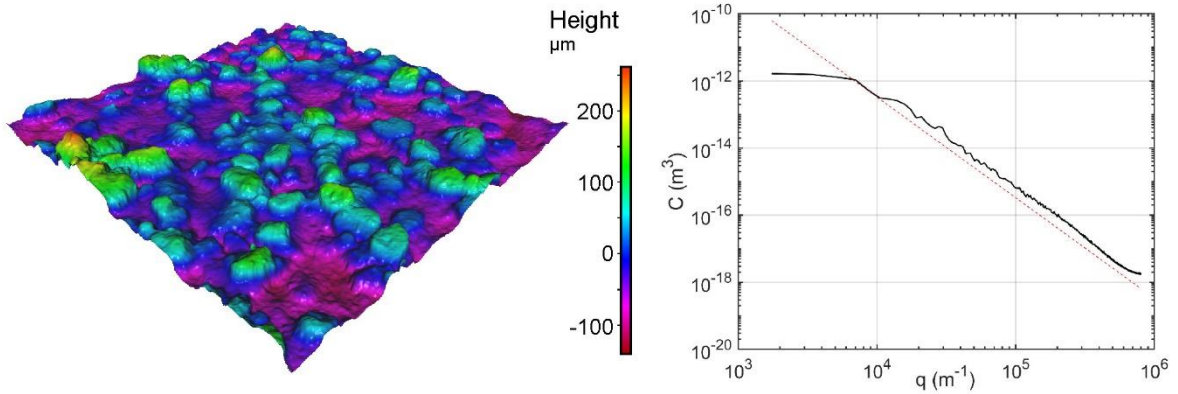


**Figure 5.1** 3D scan of the surface used for all friction tests (left) with PSD (right).

Dashed red line on the PSD indicates a Hurst exponent of 0.5.

A different cut of the same surface used in Chapter 4 was used for the experiments in the current chapter. Figure 5.1 shows a scan of this surface. Surface topography was imaged using optical profilometry (Alicona InfiniteFocus SL, Optimax, Leicestershire, UK). The PSD shown in Figure 5.1 is of the form of a 1D PSD  $C^{1D+}$  as described in [80]. This was generated from a  $2.6 \times 2.6$  mm surface scan. The Hurst exponent of the test surface was 0.5 and the RMS height ( $h_{rms}$ ) was 0.06 mm and calculated from Equation 5.1.

$$h_{rms} = \sqrt{\frac{1}{\pi} \int_0^{\infty} C^{1D+}(q_x) \cdot dq_x}$$

**Equation 5.1**

Where  $q_x$  are the surface wavevectors. The RMS slope ( $h'_{rms}$ ) is calculated as the second order integral of the PSD.  $h'_{rms}$  is later used to partially explain frictional outcomes.

### 5.2.2 Rubber

Experiments were run on two different rubbers: Rubber A and Rubber B. Rubber A was the same as that used in Chapter 4 and Rubber B was provided by a footwear company.

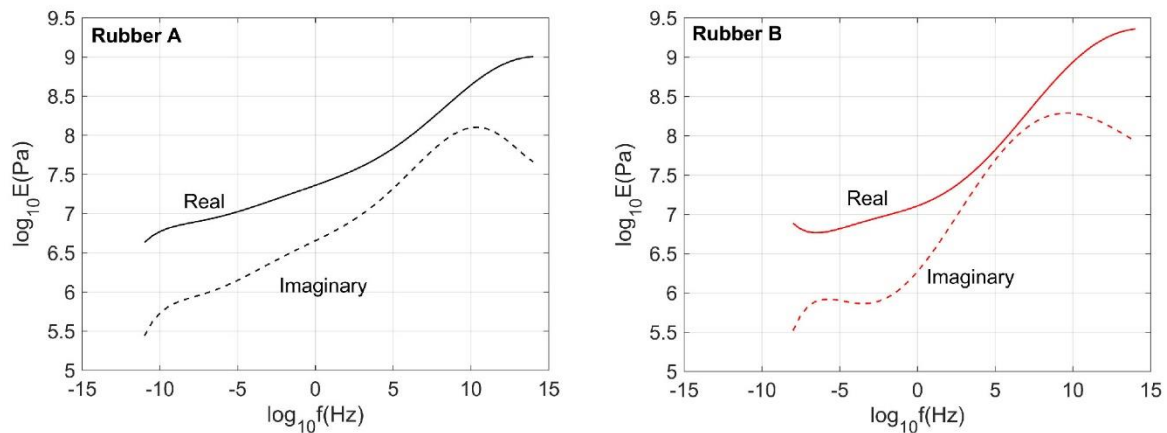


**Figure 5.2** The master curves of both rubbers obtained using DMA.

Mechanical characterisation measures consisted of low-strain viscoelastic master curves ( $10^{-3}\%$  dynamic strain), tensile stress-strain plots and Shore A hardness testing. DMA was conducted at frequencies in the range of 1 - 30 Hz and at several temperatures between  $-50$  -  $100^{\circ}\text{C}$  with a reference temperature of  $26^{\circ}\text{C}$ . The viscoelastic master curves generated for both rubbers are shown in Figure 5.2 with their tensile stress-strain curves in Figure 5.3.

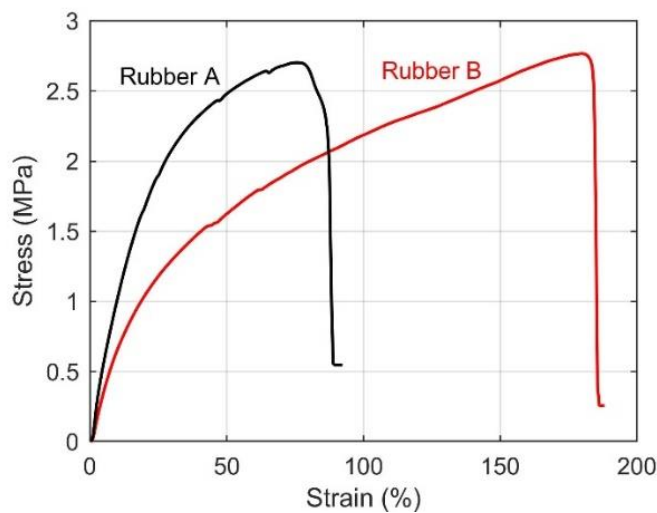


**Figure 5.3** Stress-strain curves of both rubbers obtained using tensile test.

Stress-strain curves were produced using by tensile test (Shimadzu EZ-LX 5kN with clamp grips). The rate of applied extension was 1 mm/s. The Shore A hardness readings were 75 and 69 for Rubber A and B, respectively.

### 5.2.3 Analytical Theory

To quantify the contribution to rubber friction by hysteresis, a simplified form of the Persson rubber friction formula by Ciavarella is used [39]. This simplified form is shown in Equation 5.2.

$$\mu \approx h'_{rms} \frac{ImE(q_1 v)}{|E(q_1 v)|}$$

**Equation 5.2**

where  $ImE$  and  $|E|$  are the imaginary and real modulus values shown in Figure 5.2, and  $v$  is the slide speed. The same surface is used for all the friction experiments, so when using Equation 5.2,  $h'_{rms}$  was set at 1.3. This  $h'_{rms}$  value is recommended when using the full [85] and simplified forms of the Persson friction model by Ciavarella. To determine the  $q_1$  cut-off that corresponds to  $h'_{rms} = 1.3$ , the PSD was modelled as self-affine beyond the resolution of the scan, resulting in  $q_1 = 10^{7.4}$ . As Equation 5.2 only uses the viscoelastic master curves to determine the ratio of imaginary to real modulus (loss tangent), no strain-shift is applied to the low-strain master curves, as these are superfluous to the calculation of the loss tangent. Equation 5.3 shows how model estimates were calculated from Equation 5.2, where  $v$  is either 0.0005 m/s or 0.01 m/s.

$$\mu_{pred} = 1.3 \frac{ImE \left[ \log_{10} \left( \frac{v \times 10^{7.4}}{2\pi} \right) \right]}{\left| E \left[ \log_{10} \left( \frac{v \times 10^{7.4}}{2\pi} \right) \right] \right|}$$

**Equation 5.3**

It was not assumed that Equation 5.3 would accurately predict the friction of the two rubbers (a feat yet to be conclusively achieved anywhere in the literature on rubber friction at the time of writing, without the post-hoc inclusion of arbitrary constants and fitting parameters). Instead, this equation was used to investigate whether the frictional differences found with rubber type and slide speed, can be simply explained from just the rubber's viscoelastic properties. Ciavarella has published a variation of the model shown in Equation 5.2, that includes an additional term, and models the low-frequency region of the viscoelastic modulus as linear [94]. This model was decidedly not used in the current study, as the frequencies used do not fall within the linear region of the master curves.

### 5.2.4 Wear Testing

As previously mentioned, friction can be influenced by wearing of the rubber itself. Therefore, a simple wear test was performed to develop a greater understanding of both Rubber A's and

B's susceptibility to wear, comparing with friction results to see if such a relationship between friction and wear was present here also.

A sample of both rubbers of identical geometry (a nominal contact area of 20 mm × 5 mm, and a height of 5 mm) were used in a wear test on a rotary UMT (CETR-UMT2, Bruker, Massachusetts, USA). A normal load of 15 N was applied to both rubbers, with an angular speed (5.45 rpm) applied to the surface (P40 sandpaper), equivalent to an average linear speed of 20 mm/s across the rubber samples (block centre 35 mm from axis of rotation). The normal load and slide speed used for wear testing were deliberately higher than those used in the friction tests, to ensure measurable wear of both rubbers.

All slides were 2 m in length and mass measurements were taken using an analytical balance (Satorius BasicPlus BP210D, Göttingen, Germany) before and after wearing to calculate total loss. After wear testing, the leading edges of both samples were imaged using a microscope.

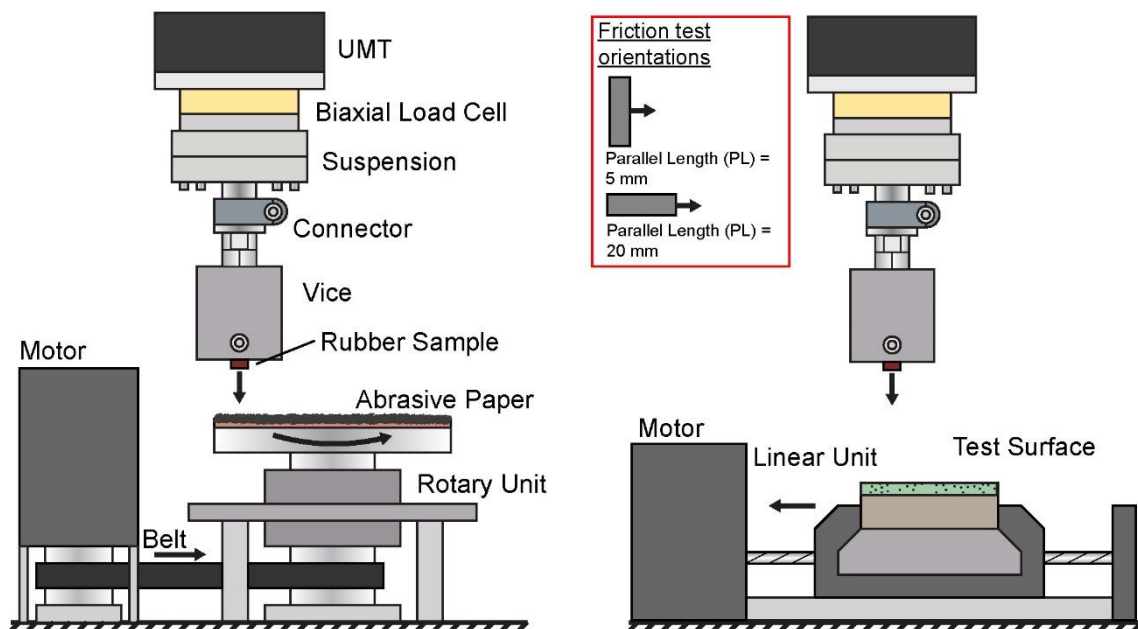


**Figure 5.4** Wear test schematic (left) and the friction test schematic (right). Both used the same UMT and clamping method. The red box next to the friction test schematic shows the two orientations at which the rubber was tested. Parallel Length (PL) refers to the length of the rubber parallel to the sliding direction.

### 5.2.5 Friction Testing

Friction tests were conducted using the same UMT and rubber clamping method used for wear testing (Figure 5.4). The only difference was the rotary module on which the abrasive paper was attached, was swapped for a linear actuator to allow friction tests to be conducted in a linear motion on the hard court surface.

For the friction tests, a normal load of 10 N and linear speeds of 10 mm/s and 0.5 mm/s with a slide distance of 30 mm were selected. Both rubber types were tested with 10 slides in each of the two orientations (shown in Figure 5.4) at 10 mm/s to investigate how the friction changes as test number increases. At the lower speed (0.5 mm/s), only three repeat tests were run for each orientation, and compared with the first three from the 10 mm/s tests. Different rubber samples were used for the alternate orientation and speed tests so that friction results were not influenced by the wear experienced in the preceding tests. After each slide, the surface and rubber were lightly brushed to remove wear debris, and at least two minutes waiting time was allowed between tests for the rubber to return to ambient temperature.

$\mu_k$  was recorded for all tests and was calculated as the mean of the  $\mu$  readings 0.1 s after the initial friction peak (static friction) to the end of the slide (Figure 5.5).

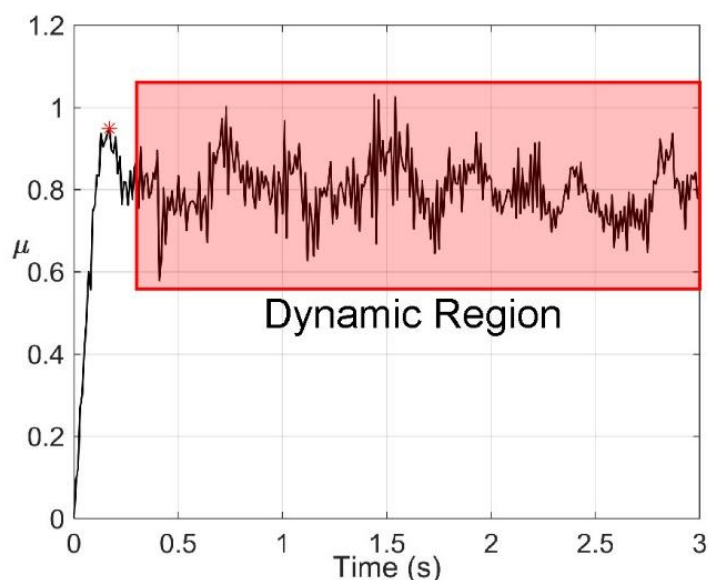


**Figure 5.5** A typical  $\mu$ -time trace from the friction experiments ( $v = 10$  mm/s). The red asterisk marks the static coefficient of friction. The mean of the data in the shaded box is used to calculate  $\mu_k$ .

### 5.3 Results

The friction of both rubbers varied with slide speed and orientation (Figure 5.6). Figure 5.6 also shows the  $\mu_k$  values predicted for both rubbers at the two slide speeds using the simplified model in Equation 5.2. Each point of the experimentally obtained readings refers to the mean of the first three repeat tests, the standard deviation of which is shown by the error bars. Raw data points were not shown to improve graph readability.

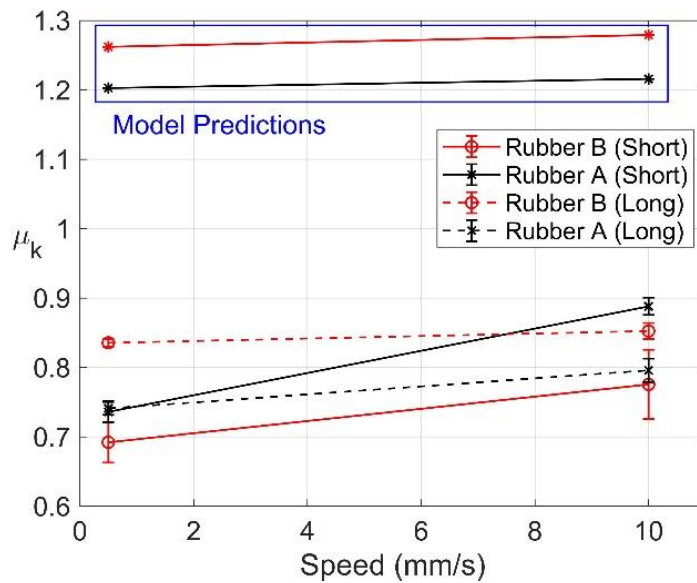


**Figure 5.6** Experimental and modelled  $\mu_k$  readings for both rubbers at both test orientations and slide speeds. Black indicates Rubber A, and the red indicates Rubber B.

As the model does not consider rubber block shape, one set of predictions is shown for each rubber. The model predicted Rubber B at 10 mm/s to produce the highest friction and for Rubber A at 0.5 mm/s to produce the lowest friction. This latter prediction was found to be correct of the experimental data, when averaging across the two orientations, though Rubber A was shown to produce a higher mean  $\mu_k$  (0.84) than Rubber B (0.81) at the slide speed of 10 mm/s. The model correctly predicted that  $\mu_k$  would increase with slide speed for both rubbers, and that in the long orientation, Rubber B would produce a higher  $\mu_k$  than Rubber A. In the short orientation however, Rubber A recorded a higher friction than Rubber B, which the model did not predict. The difference in magnitude between the model and experimental findings is unsurprising as no fitting or frictional constants were added to the model.

Figure 5.7 shows ten repeat friction tests for Rubbers A and B at 10 mm/s at two orientations. In the long orientation (PL = 20 mm), Rubber A  $\mu_k$  was relatively constant, fluctuating around  $\mu_k = 0.8$ . In the short orientation (PL = 5 mm), the Rubber A  $\mu_k$  increased with test number from 0.87 at test one, to 0.94 at test ten. For all tests of Rubber A, the short orientation produced higher friction than the long orientation.

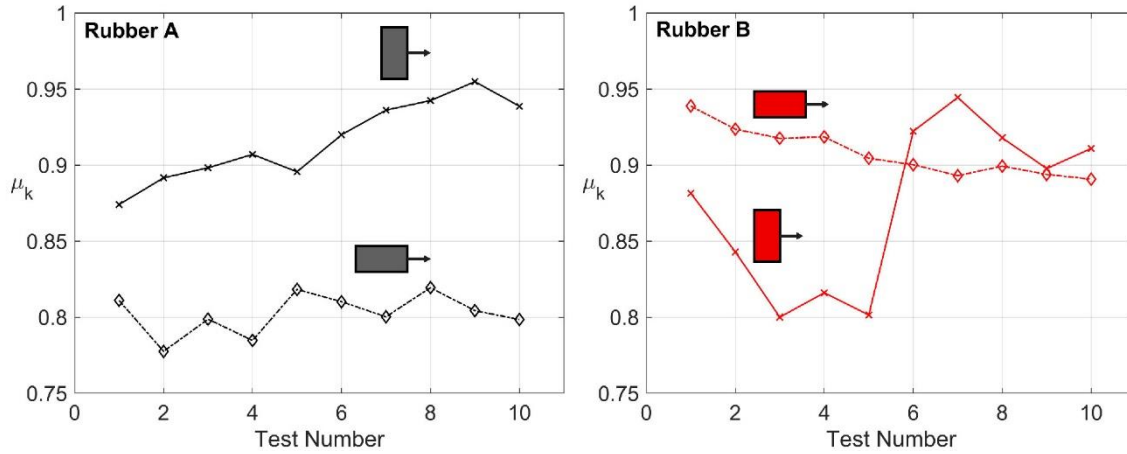


**Figure 5.7** Ten repeat friction tests of Rubber A (left) and Rubber B (right) at 10 mm/s in both orientations.

For Rubber B, the short orientation only produced higher friction than the long orientation in the last five tests. In the first five, the long orientated rubber yielded the higher friction before the drastic rise in friction of the shorter orientation. The friction of the long shape of Rubber B steadily decreased with increased number of tests, from 0.94 at test one to 0.89 at test ten.

During the wear tests, Rubber A underwent a 14% mass loss. Under the same conditions, Rubber B experienced a 1% mass loss. Microscope images of the leading edges of both rubbers after the wear tests are shown in Figure 5.8.

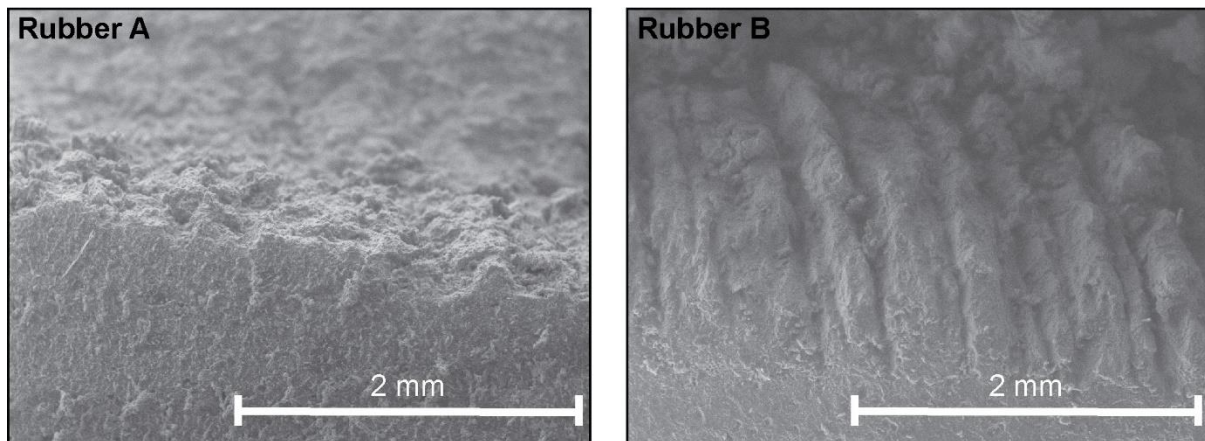


**Figure 5.8** Microscope images of both rubber's leading edges after the wear test.

The wear marks left on the rubbers were visually different. Rubber B showed parallel abrasion grooves typical of the abrasion of stiff materials, while Rubber A seemed to wear evenly along the leading edge, with no clear grooves.

## 5.4 Discussion

In Chapter 4 the shorter orientation of rubber produced higher friction. The rubber used in Chapter 4 is the same as Rubber A used in this chapter, hence why rubber A showed that same relationship. However, for Rubber B the shorter shape only produced higher friction after five initial tests. Within these first five friction tests the shorter orientation of rubber gave friction readings, on some occasions, over 0.1 lower than the longer shape. To better understand why Rubber B does not display the same effect of orientation as Rubber A, the wear properties of both rubbers were compared. Rubber A recorded a 14% mass loss, and Rubber B a 1% mass loss. This was expected from the stress-strain curves of the respective rubbers in Figure 5.3. In which Rubber A was shown to fail at strains  $< 100\%$ , which has been estimated previously to be the degree of strain experienced by rubber asperities during sliding on dry asphalt surfaces [35,95]. This would imply, if the estimation of strain at asperity contact is even relatively close to those experienced, that as Rubber A slides the strain causes a plucking of rubber asperities away from the bulk. This explains the wear pattern shown in Figure 5.8 and why Rubber A experienced much greater mass loss. In contrast, Rubber B is shown to withstand strains  $> 150\%$ . Meaning that wear was unlikely to occur from the plucking of asperities from the bulk as Rubber B had a high enough tensile strength to withstand this mechanism. Instead, as proved by Rubber B's wear image in Figure 5.8, wear only occurs as a result of prominent surface asperities abrading the leading edge, explaining the visual similarity in the abrasion marks of Rubber B to that observed on high stiffness materials. Rubber B's higher tensile strength explained why a much lower mass loss was recorded for Rubber B in comparison to Rubber A. It is also theorised to be the reason the frictional effect of orientation is different for both rubbers.

Considering minimal wear to occur in the first five slides of Rubber B, the shorter shape would produce high contact pressures as its lower stiffness induces more friction induced torque, causing the rubber to lean onto its leading edge. Higher contact pressures in rubber often produce a lower friction due to higher temperatures and reduced lateral coupling between real areas of rubber-surface contact [63]. This justifies the frictional difference in orientation observed for Rubber B in the first five tests. However, as more slides were performed the friction orientation relationship changed for Rubber B, with the shorter orientation producing higher friction than the long. This was because the leading edge of the short orientation, under the high pressure, was finally worn away and chamfered, increasing the contact area causing a drop in contact pressure and an increase in friction. In a lot of rubber friction research edges are manually pre-chamfered, which may explain why this is not observed in many other studies. Though this manual chamfering of rubber test samples allows more consistent friction

readings, by neglecting the complexities of edge wearing, it does not allow an understanding of how rubber tread performs when first used. This could have implications particularly to sports footwear, as how a shoe performs during the athlete's initial movements can determine whether the shoe is purchased/chosen or not.

As expected, for each rubber type and orientation, testing at 0.5 mm/s produced lower friction compared to testing at the greater speed of 10 mm/s. This is because, as the rubber slides over the rough surface quicker speeds increase the perturbing frequencies transferred to the rubber increasing the loss tangent and hence hysteresis. This is the premise for the simplified model in Equation 5.2 and is thus predicted in the model estimations in Figure 5.6. The model predicted the  $\mu_k$  of Rubber A and Rubber B to increase by 0.01 and 0.02, respectively for the increase in slide speed from 0.5 – 10 mm/s. In the experiments this increase was (averaging across the two orientations) 0.1 and 0.05 for Rubber A and B, respectively. Consequently, the predicted difference for both rubbers was smaller than that measured experimentally—especially in the case of Rubber A. This again implies that the large amounts of mass loss experienced by Rubber A acts as an additional friction mechanism. As for Rubber B, which experienced little wear, the general frictional performance can be explained by the simple model used, particularly for the 20 mm PL orientation where the difference in friction for the two speeds was 0.02 and therefore the same as that predicted by the model.

The simplified model proposed by [39], uses only a few easy to obtain parameters to provide an insight into the frictional performance of rubbers on rough surfaces. More detailed models are available for this application [21,66], but require a much larger collection of parameters, numerous functions and often require fitting to large data sets (e.g. recorded friction for a rubber over a range of speeds). Hence, for the case of trying to understand how the friction of a rubber may vary at two different slide speeds, or how one rubber may compare to another on a single surface, the simplified Persson model could be of use. However, as only two cases are tested in this chapter, the chance of the model predicting which rubber has the highest friction is high. Future work should compare results from this simplified model for several grades of rubber to assess its performance more accurately. The simplified model has been shown in one example to correspond well to the results from the original Persson model [39].

Rubber friction models are typically very complex, especially those that can also consider the influence of frictional heating [59], as the nature of this interaction itself is highly complex. This is due to: multiscale surface roughness, non-linear material characteristics, the multitude of ingredients and fillers used to produce rubbers, altering their mechanical performance and wear resistance, surface contamination, and chemical reactions occurring at the sliding interface, to name but a few. By using a simplified model, as done in this chapter, numerous

assumptions were made, explaining the discrepancies between the model predictions and experimental results in Figure 5.6.

This chapter (and thesis) is limited by its use of a single surface type, which is very abrasive compared to most flooring and road surfaces (on which rubber friction models are usually based), as well as the limited range of test loads and speeds. Future work which addresses how well this model works in describing the friction of rubber on multiple surfaces and rubbers at varied loading conditions could determine its overall applicability to providing a simplified description of rubber friction. However, this chapter has shown that on a hard court surface the shape effect of rubber friction varies dependent on the grade of rubber used in a shoe outsole. As such, a high friction tread pattern for one grade of rubber will not necessarily be a high friction pattern for another grade of rubber.

## **5.5 Conclusion**

The friction of two rubber types was measured at two slide speeds. The effect of rubber shape was investigated by testing both rubbers in two orientations. Frictional differences between the rubbers were partially explained using a simplified version of the Persson friction model considering only the hysteresis of the rubbers. Wear analysis of the two rubbers identified contrasting wear mechanisms which were partly explained by the stress-strain curves of the respective rubbers. The friction of different shapes of rubber are suggested to be dependent on the resultant contact areas (which can vary due to differing degrees of friction induced torque), the resultant contact pressures, and the wear resistance of the tested rubber. For the rubber with the greatest wear resistance (Rubber B), the orientation-friction relationship changes as more repeat slides are performed. This is deemed to be because of the abrasion, and hence chamfering, of the rubber's leading edge, a process considered to have occurred immediately for the less wear-resistant rubber.

The experiments in both this and the previous chapter (Chapter 4) were conducted using commercially available rubber cut into simple shapes. Moreover, the slide speeds and nominal contact pressures used were not comparable to those of tennis movements. Using commercially available rubbers meant DMA could be performed (requiring a relatively large sample of rubber which can be difficult to obtain directly from tennis shoes), and the low speeds used in the friction tests allowed the use of the well-controlled UMT to accurately measure the frictional differences. These experiments identify a frictional effect of rubber grade and shape on friction during sliding. The question remains however, whether the frictional effects observed in these experiments will occur on real tennis shoe tread elements at loads and velocities representative of hard court tennis slides.

## 6 Analysis of the Friction and Wear Mechanisms present during Hard Court Specific Movements

*The following chapter is adapted from my published conference proceeding and full-length research article:*

- Hale, J., Lewis, R., & Carré, M. J. (2020). *Shoe–Surface Tribology in Hardcourt Tennis*. In *Multidisciplinary Digital Publishing Institute Proceedings* (Vol. 49, No. 1, p. 90).

- Hale, J., Lewis, R., & Carré, M. J. (2021). *Effect of simulated tennis steps and slides on tread element friction and wear*. *Sports Engineering* (Vol. 24, No. 5).

### 6.1 Introduction

The previous two chapters detail a series of experiments which were conducted to identify some of the influential factors that affect the friction between rubber and a dry hard court surface. To accomplish this, experiments were performed on simple rectangular cuts of rubber with simplified loading conditions. Although these tests were successful in identifying numerous frictional factors, such as wearing at the leading edge and tread length in the direction of sliding, the prominence of these mechanisms for actual tread designs in sliding conditions replicative of real hard court tennis movements is still unknown.

This chapter describes the calculation and application of characteristic normal loads from tennis step and slide movements to real tennis shoe tread elements from a Babolat Propulse tennis shoe. Two orientations of the tread elements were tested to investigate whether the shape induced frictional effects are present for real tennis shoe tread elements. By testing real tread elements in real tennis movement conditions, a better understanding of the dominant frictional parameters, from those previously identified, is possible.

In Chapter 4 no difference in static friction was observed for the different shapes of rubber, though a difference was observed in the dynamic friction, with longer shapes (in the sliding direction) having a lower friction. However, for a hard wearing rubber in Chapter 5, longer shapes in the sliding direction produced higher friction. It is therefore hypothesised that, though rubber type and nominal contact area are the same, tread orientation will have no effect on the static friction observed during hard court steps. Tread orientation is however expected to influence the dynamic friction of hard court steps and slides due to the effects of frictional heating and wearing recorded in similar interactions in previous chapters, and in other studies [36,59]. It is also hypothesised that the sliding tests will result in wear that will alter the topography of the tread elements, causing a frictional asymmetry over repeated slides [52].

## 6.2 Methodology

### 6.2.1 Tread Elements

Four identical rubber tread elements were cut from a Babolat Propulse tennis shoe (size UK 9). Each tread element had a surface area of  $54.64 \text{ mm}^2$  and a Shore A hardness of 76. Due to the size and shape of the tread elements, DMA could not be performed. The topography on the contacting face of a tread element was imaged (Alicona, InfiniteFocus SL, Optimax, Leicestershire, UK), and its arithmetical mean surface height ( $S_a = 3.3 \text{ }\mu\text{m}$ ) and surface root mean square height ( $S_q = 4.1 \text{ }\mu\text{m}$ ) measured. This was done to identify how the rubber topography changes over time. An image of one of the tread elements and a scan of its topography is shown in Figure 6.1.

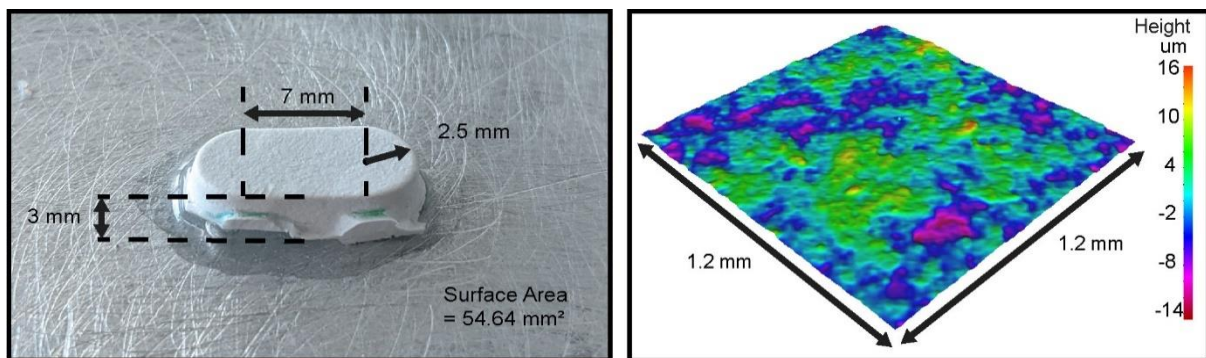


**Figure 6.1** Annotated tread element used in experiments in this chapter (left). Rubber surface topography before friction tests (right).

Each of the four tread elements were glued to individual flat steel plates which were then attached into the UMT in Figure 6.2. The same hard court surface as detailed throughout this thesis was used as the surface for these experiments also.

### 6.2.2 Experimental Set-up

The test set-up is shown in Figure 6.2. Contrary to the previous friction experiments, a rotary unit was used to move the hard court surface, instead of a linear one. This was necessary to produce the slide velocities required to replicate those observed during hard court slides (the maximum achievable velocity of the linear module was  $10 \text{ mm/s}$ ).

Although the use of a rotary unit allowed testing at higher slide speeds, it did mean there was a velocity gradient across the tested tread elements, as well as a small lateral force, generated by the lateral bending of the tread element. For four tests, the biaxial load cell was orientated to measure this lateral load instead of the frictional force. A fluctuating lateral force of  $0.2 \text{ N}$  was present during step tests, which increased to  $0.4 \text{ N}$  for the slide tests. There was no difference between orientations. Although, these lateral forces are negligible, not being able to perform linear tests at high speeds must be noted as a limitation of the test method. An

athlete performs a hard court slide in a single direction, meaning the slide speed is the same across all contacting areas of the shoe's tread, and no rotational bending will be experienced by tread elements.

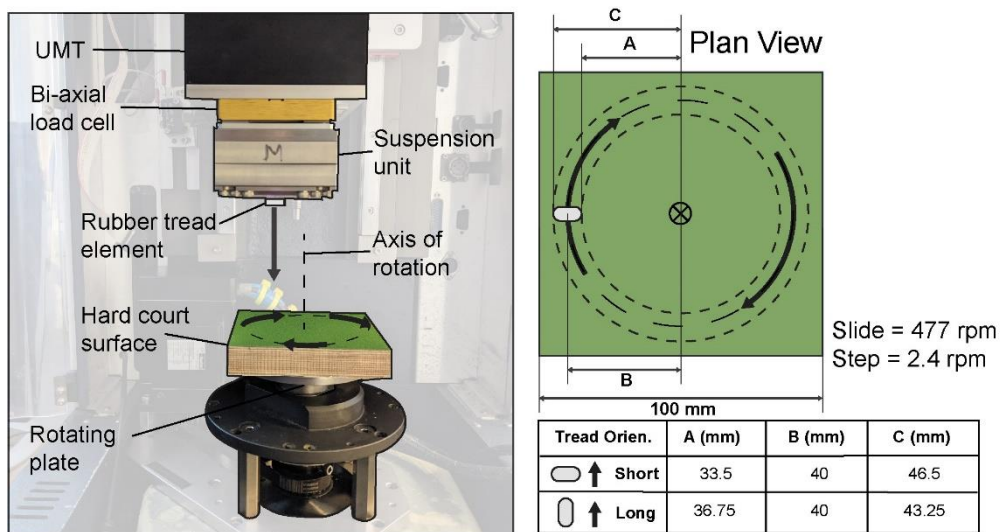


**Figure 6.2** The experimental set-up. Representation of short and long tread orientations is shown with revolutions per minute (rpm) of the surface for step and slide tests.

The bi-axial load cell measured the shear and normal forces, the ratio of which was  $\mu$ . Figure 6.3 shows how  $\mu_s$  and  $\mu_k$  were determined for the step tests, and  $\mu_k$  for the slide tests. As during the sliding tests, the surface was already at full speed as the tread element made contact, which was necessary to test at the high speed, no  $\mu_s$  could be obtained and was hence omitted from the analysis.

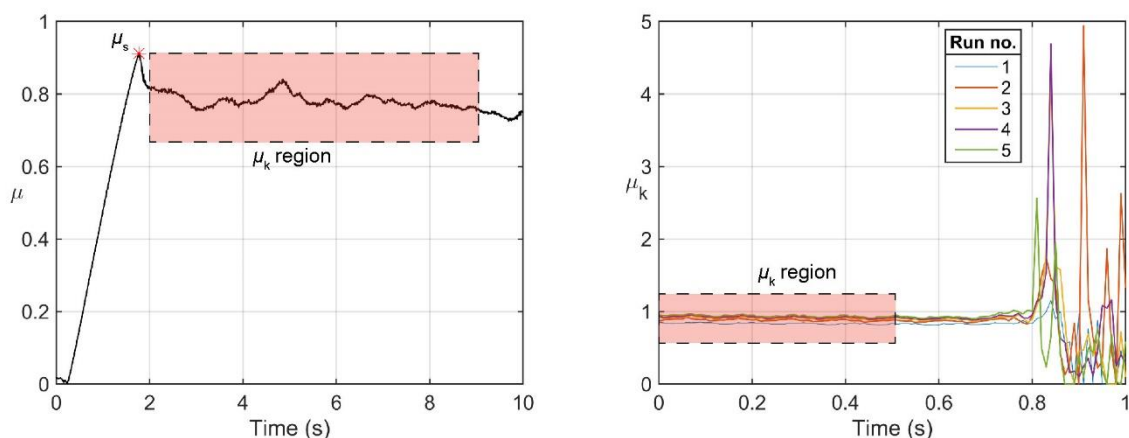


**Figure 6.3** A typical  $\mu$ -time trace from the step experiments (left), the red star indicates the  $\mu_s$  value and the red box refers to the readings from which a  $\mu_k$  value was calculated. The first five  $\mu$ -time traces from the slide experiments on the short orientated tread, with labelled  $\mu_k$  region (right).

Mass losses of the rubber elements were taken after every five tests using an analytical balance (Satorius BasicPlus BP210D, Göttingen, Germany). Topographical analysis of the tread elements was conducted before and after testing using non-contact profilometry (Alicona InfiniteFocus SL, Optimax, Leicestershire, UK).

### 6.2.3 Calculation of Normal Loads for Step and Slide Tests

Two separate tests are detailed in this chapter, a step test and a slide test. The step and slide tests differed in the slide speeds and normal loads used. For the step test, tread elements were loaded with a normal load of 33 N and a surface speed of 2.4 rpm (producing an average linear speed of 10 mm/s across the tread elements). Rubber-surface contact lasted for 10 s (100 mm slide length). For the slide test, a normal load of 25 N was used with a surface speed of 477 rpm (producing an average linear speed of 2 m/s across the tread elements). Rubber-surface contact lasted for 0.8 s (1.6 m slide length).

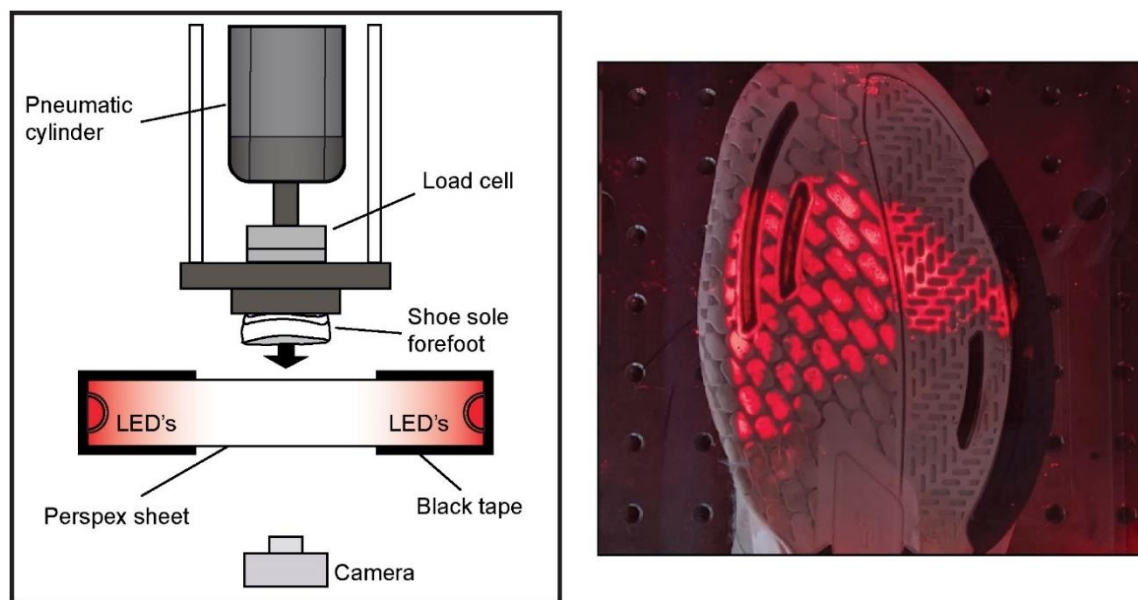


**Figure 6.4** Contact area image set-up (left). Contact area image of Babolat Propulse UK 9 forefoot normally loaded with 1106 N (right).

Biomechanical analysis has shown that peak normal loads of 1237 N and 835 N occur at shoe surface impact during hard court steps and slides, respectively [12,96]. Using these normal loads, contact area tests were conducted to obtain an estimate of the tread-surface contact pressures. The contact area tests were performed using the UoS Friction device, the Babolat Propulse UK 9 tennis shoe, and a frustrated totally internal reflected waveguide [75]. A schematic of this is set-up shown in Figure 6.4.

Normal loads used in these contact area tests were 1106 N and 595 N for the step and slide, respectively. Typically during hard court steps, only the forefoot makes contact with the

surface, therefore only the forefoot was loaded during step contact area tests. During sliding movements, the foot is flat on the surface, so during slide contact area tests the full shoe was loaded. Table 6.1 shows the resultant contact areas observed at the step and slide normal loads.

**Table 6.1** Details used to determine estimates of tread-surface contact pressures during steps and slides using contact area tests.

| <b>Movement type</b> | <b>Normal loads from biomechanics studies (N)</b> | <b>Contact area test normal load (N)</b> | <b>Part of shoe used</b> | <b>Contact area (mm<sup>2</sup>)</b> | <b>Average pressure (kPa)</b> |
|----------------------|---|--|--------------------------|--------------------------------------|-------------------------------|
| <b>Step</b>          | 650 - 1237  | 1106                                     | Forefoot                 | 1830                                 | 604                           |
| <b>Slide</b>         | 300 - 835   | 595                                      | Full                     | 1305                                 | 456                           |

It was observed that even though the full shoe was loaded and imaged for the slide test, a lower contact area (1305 mm<sup>2</sup>) was measured compared to the forefoot step contact area test (1830 mm<sup>2</sup>). This was due to the higher normal load used in the step test, deforming the shoe enough to create a large forefoot contact area.

The nominal contact area of the tread elements used in the friction experiments was 54.64 mm<sup>2</sup>, so normal loads of 33 N and 25 N were chosen for the step and slide friction tests, producing the same average contact pressures as those estimated from the contact area tests. Slide times were set at 10 s and 0.8 s for the step and sliding movements, respectively. This resulted in sliding lengths of 100 mm for the step tests, and 1600 mm for the slide tests. The slide distance used here was greater than that observed in elite tennis (0.41 – 0.72 m) but the test velocity (2 m/s) was less than those observed during visual analysis of elite level hard court slides (2.8 - 4.7 m/s).

**Table 6.2** Test parameters with mean (SD) of applied normal loads and slide speeds.

| <b>Experiment Type</b> | <b>Test Sample</b> | <b>Orientation</b> | <b>Normal Load (N)</b> | <b>Slide Speed (mm/s)</b> |
|------------------------|--------------------|--------------------|------------------------|---------------------------|
| Step                   | 1                  | Short              | 32.7 (0.46)            | 10 (0.9)                  |
|                        | 2                  | Long               | 32.7 (0.28)            | 10 (0.9)                  |
| Slide                  | 3                  | Short              | 22.3 (2.78)            | 1994 (10.5)               |
|                        | 4                  | Long               | 22.7 (3.05)            | 1993 (11.5)               |

Table 6.2 summarises the four test cases in this chapter. Two tread orientations were tested for both the step and slide movements, and for each test condition a new tread element was used, meaning four identical tread elements were used altogether.

In total, 30 repeats were conducted for each orientation and movement providing an understanding of how friction of tread elements changes over time. After the first 15 tests, the slide direction was reversed for an additional 15 tests. This was done to investigate whether the topographical changes, likely to occur via wearing mechanisms to the rubber elements, would result in directional friction asymmetry reported in other rubber friction studies. The surface and rubber were lightly brushed between tests to remove any wear debris and surface contaminants.

#### 6.2.4 Statistical Analysis

Three dependent and five independent t-tests with reported effect size (Hedges's  $g$  ( $g_s$ ) [97]) were used to investigate the effect of tread orientation, movement type (whether friction results observed for the step experiments are different from those observed for the slide experiments), and slide direction. Significance was assumed when  $p < 0.05$ , and when data has been used in multiple t-tests, a Holm correction was applied to the significance value [98]. To calculate  $g_s$ , a pooled SD was used. Equation 6.1 shows this calculation.

$$g_s = \frac{M_1 - M_2}{\sqrt{(SD_1^2 + SD_2^2)/2}} \times \left(1 - \frac{3}{4(n_1 + n_2) - 9}\right)$$

**Equation 6.1**

Where  $M$ ,  $SD$  and  $n$  represent the mean, standard deviations and sample size of compared groups. As a Cohen's  $d$ , corrected for small sample size,  $g_s$  values of 0.2, 0.5, 0.8 relate to small, medium and large effects, respectively [99]. All statistical analysis was conducted using the IBM SPSS 26 software.

### 6.3 Results

Table 6.3 shows the mean and corresponding standard deviation (SD) for all the  $\mu$  readings taken.

**Table 6.3** The mean and standard deviation, M (SD), of all  $\mu$  readings.

| Test  | Orientation | First 15 tests |             | Reverse 15 tests |             | All 30 tests |             |
|-------|-------------|----------------|-------------|------------------|-------------|--------------|-------------|
|       |             | $\mu_s$        | $\mu_k$     | $\mu_s$          | $\mu_k$     | $\mu_s$      | $\mu_k$     |
| Step  | Short       | 0.84 (0.06)    | 0.78 (0.01) | 0.70 (0.03)      | 0.67 (0.01) | 0.77 (0.09)  | 0.72 (0.05) |
|       | Long        | 0.85 (0.04)    | 0.77 (0.02) | 0.72 (0.03)      | 0.69 (0.01) | 0.78 (0.07)  | 0.73 (0.04) |
| Slide | Short       | -              | 1.03 (0.06) | -                | 0.99 (0.02) | -            | 1.01 (0.05) |
|       | Long        | -              | 0.94 (0.04) | -                | 0.91 (0.01) | -            | 0.93 (0.03) |

#### 6.3.1 Step Results

The mean (M)  $\mu_k$  for the long and short tread orientations during the first 15 step tests were 0.77 (SD = 0.02) and 0.78 (SD = 0.01), respectively, with no significant difference ( $t(28) = 1.61$ ,  $p = 0.118$ ,  $g_s = 0.6$ ). During the reverse 15 step tests however,  $\mu_k$  results for the long tread orientation (M = 0.69, SD = 0.01), compared to that for the short tread orientation (M = 0.67, SD = 0.01), were significantly higher,  $t(28) = 5.65$ ,  $p < 0.001$ ,  $g_s = 2$ .

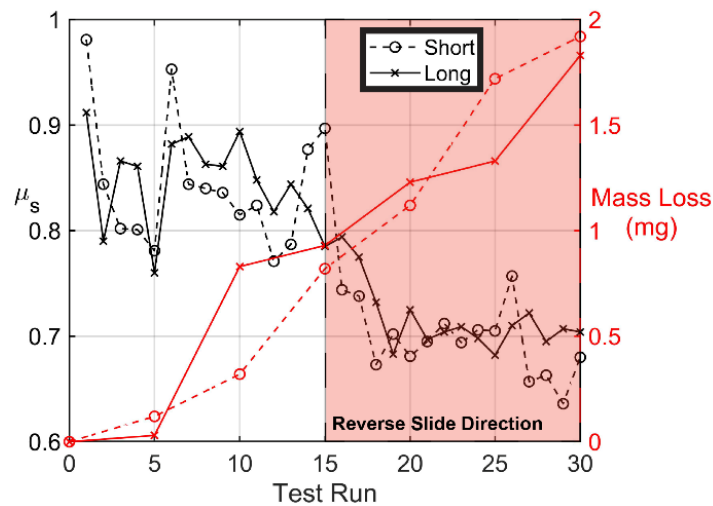


**Figure 6.5**  $\mu_s$  and wear graph for the step tests. The red shaded region indicates the change in slide direction after 15 runs.

Dependent t-tests showed that the  $\mu_s$  readings (for both orientations together) during the first 15 tests (M = 0.85, SD = 0.05) were significantly higher than those during the reverse 15 tests (M = 0.71, SD = 0.03),  $t(29) = 13.22$ ,  $p < 0.001$ ,  $g_s = 3.4$ . The  $\mu_k$  readings taken from the

first 15 tests ( $M = 0.77$ ,  $SD = 0.01$ ) were also shown to be significantly higher than those in the reverse 15 tests ( $M = 0.68$ ,  $SD = 0.01$ ),  $t(29) = 29.13$ ,  $p < 0.001$ ,  $g_s = 9$ .

Figure 6.5 shows all the individual  $\mu_s$  results recorded during the step tests, with the mass loss readings taken after every five tests. The same is shown for the  $\mu_k$  results in Figure 6.6. There was little observable difference between the short and long tread orientations in terms of wear. After all 30 step tests, the short and long tread elements produced similar mass loss readings of 1.9 mg and 1.8 mg, respectively.

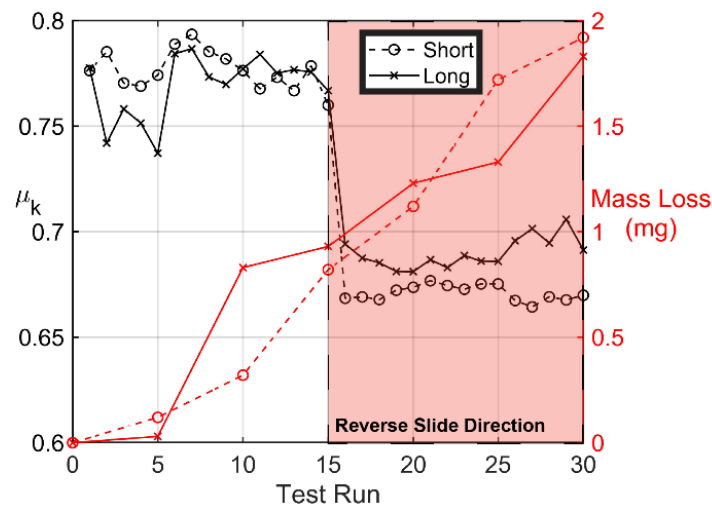


**Figure 6.6**  $\mu_k$  and wear graph for the step tests. The red shaded region indicates the change in slide direction after 15 runs.

### 6.3.2 Slide Results

The mean  $\mu_k$  for the long tread orientation during the first 15 slide tests was 0.94 ( $SD = 0.04$ ). This was significantly lower than the mean  $\mu_k$  of the short tread orientation during the first 15 slide tests (1.03 ( $SD = 0.06$ )): ( $t(28) = 4.72$ ,  $p < 0.001$ ,  $g_s = 1.8$ ). During the reverse 15 slide tests,  $\mu_k$  results for the long tread orientation ( $M = 0.91$ ,  $SD = 0.01$ ), compared to that for the short tread orientation ( $M = 0.99$ ,  $SD = 0.02$ ), were also significantly lower,  $t(28) = 15.15$ ,  $p < 0.001$ ,  $g_s = 5.1$ .

A dependent t-test determined that the  $\mu_k$  readings (for both orientations together) during the first 15 tests ( $M = 0.98$ ,  $SD = 0.07$ ) were significantly higher than those during the reverse 15 tests ( $M = 0.95$ ,  $SD = 0.04$ ),  $t(29) = 3.92$ ,  $p < 0.001$ ,  $g_s = 0.5$ .

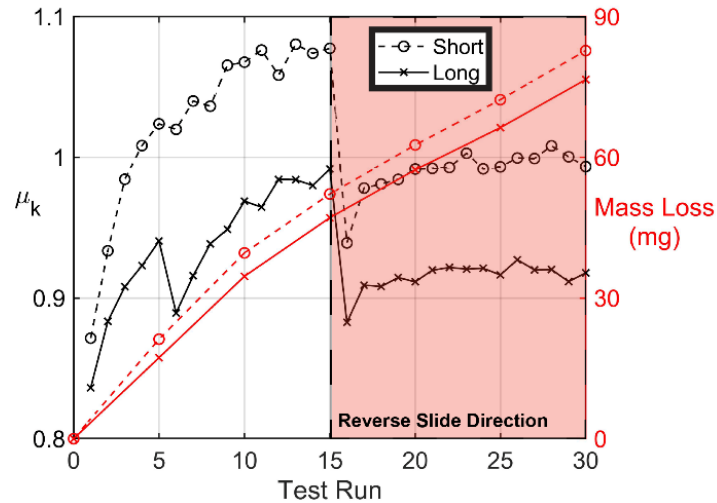


**Figure 6.7**  $\mu_k$  and wear graph for the slide tests. The red shaded region indicates the change in slide direction after 15 runs.

Figure 6.7 shows all  $\mu_k$  readings recorded for the slide tests, with mass loss values. The mass loss of the sliding elements increased at an almost linear rate, with a slight increased wear rate across the first 10 tests. The short tread element had a greater total mass loss of 83 mg, compared to the 77 mg mass loss by the long orientated tread element. It is worth noting the almost two order of magnitude increase in mass loss readings experienced during the slide experiments, compared to the step experiments. Calculating wear rate ( $\psi$ ) using Equation 6.2, the tread elements used during the step tests wore at a rate of  $0.61 \times 10^{-3}$  mg/mm and  $0.64 \times 10^{-3}$  mg/mm for the long and short orientations, respectively. During slide tests, the long orientated tread had a wear rate of  $1.60 \times 10^{-3}$  mg/mm and the short orientated tread wear rate was  $1.72 \times 10^{-3}$  mg/mm. In Equation 6.2, mass loss was measured in mg and distance travelled in mm.

$$\psi = \frac{\text{mass loss}}{\text{distance travelled}}$$

**Equation 6.2**

The observation that sliding tests resulted in a higher wear rate, even with a normal load 24% lower than the step tests, shows slide speed to be the influencing factor to the increased rubber wear.

Lastly, all the  $\mu_k$  readings from the slide experiment (M = 0.97, SD = 0.06), when compared to those of the step experiment (M = 0.73, SD = 0.05), were significantly higher:  $t(118) = 24.70$ ,  $p < 0.001$ ,  $g_s = 4.3$ .

### 6.3.3 Visual Wear Analysis

To investigate if changes to the rubber elements' surface topography could be influencing the friction in the step and slide experiments, surface scans and measures ( $S_a$  and  $S_q$ ) were taken after the first five tests for both movements. Before testing, tread surface roughness was  $S_a = 3.3 \mu\text{m}$ ,  $S_q = 4.1 \mu\text{m}$ . After five step tests these values increased to  $S_a = 8.4 \mu\text{m}$ ,  $S_q = 11.0 \mu\text{m}$ , which was less than half of that recorded after the five slide tests,  $S_a = 20.4 \mu\text{m}$ ,  $S_q = 26 \mu\text{m}$ . To further explore the topographical changes occurring during sliding, additional scans were taken after 15 tests, as well as after the 15 reverse direction slides which were performed afterwards.

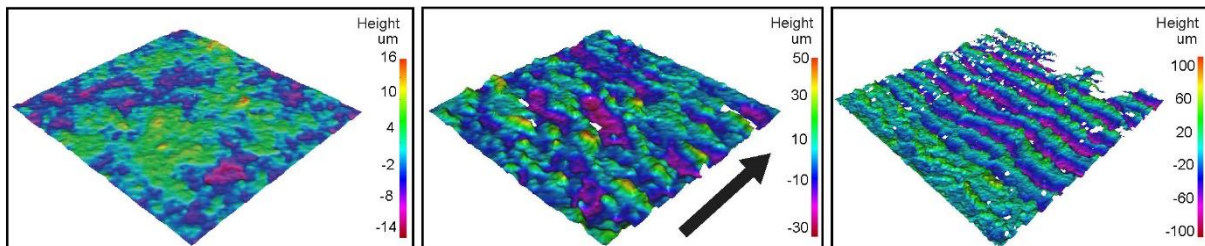


**Figure 6.8** Rubber surface scans taken of the short tread element used in the slide experiments. Before any slides (left). After five slides (middle). After 15 slides (right). The black arrow shows the relative sliding direction of the tread element along the hard court surface.

After 15 slides, the tread elements surface roughness again increased, to  $S_a = 24.7 \mu\text{m}$ ,  $S_q = 30.1 \mu\text{m}$ . Figure 6.8 shows the surface scans taken for the short orientated sliding tread element before testing, after five slides, and after 15 slides. Through observation of the colour bars in Figure 6.8, the increase in roughness magnitude is evident. It is also shown, that as slide number increased, a regular topography started to emerge in the form of ridges. After the 15 slides in the reverse direction, the surface roughness dropped again to values like that observed after the first five slides:  $S_a = 20.5 \mu\text{m}$ ,  $S_q = 25.4 \mu\text{m}$ . After the 15 slides in the reverse direction, the periodic nature of the roughness was still observable, with similar spacing between ridges ( $\approx 0.4 \text{ mm}$ ).

The movement of rubber in the opposite direction had little effect on ridge spacing, which is expected as the normal load was kept constant [100,101]. The direction reversal did however, alter the ridge profile. Before reverse direction tests, the ridges were formed as asymmetric structures with their sharpest edge towards the oncoming surface asperities. After the additional 15 runs in the reverse direction, these peaks lost their asymmetry and started to become symmetrical (Figure 6.9). Asymmetrical ridges on the surface of sliding rubber have been found to cause frictional differences, with the opposite sliding direction producing noticeably lower  $\mu_k$  ( $\leq 0.2$ ) [52], an observation also made in these experiments.

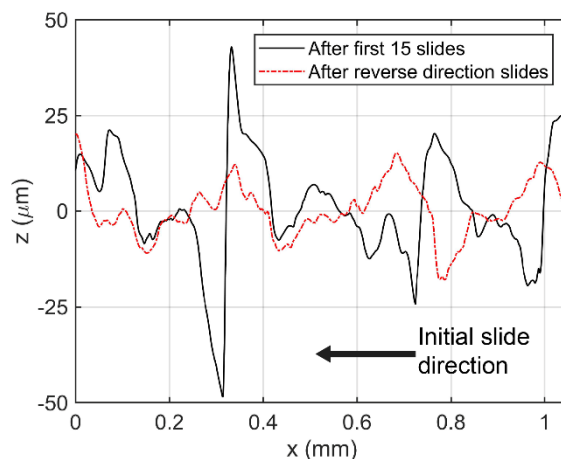


**Figure 6.9** 2D traces of the surface ridges on a short tread element used in slide experiments. The trace taken after the first 15 tests (black, solid) displays asymmetrical structures with the edge of highest gradient facing the direction of motion. After another 15 slides, in the reverse direction (red, dashed), this directional feature is removed. The arrow indicates the relative motion of the rubber element against the hard court surface in the first 15 slides.

## 6.4 Discussion

### 6.4.1 Effect of Movement Type

The  $\mu_k$  readings were found to be significantly higher for the slide experiments than the step, with a large effect size of 4.3. This finding can be understood as a combination of two primary mechanisms. The large increase in slide speed from the step to the slide, meant the frequencies of vibration transmitted to the rubber tread elements were much greater, incurring a greater hysteretic energy loss [21]. However, as is typically expected at speeds greater than 0.1 m/s, the frictional heat generated at the sliding interface would be great enough to reduce the hysteresis of the rubber through thermal softening [102]. In the present case it could be inferred that the effect of the increased perturbing frequencies of vibration on the rubber's hysteretic loss is the dominant mechanism, or that there is an additional mechanism that may also be increasing the  $\mu_k$  during slides. This additional mechanism may be the mass loss which was almost two orders of magnitude greater during the slide tests than the step tests, indicating wear to be a component factor to the increased friction.

Within this study, a cleaning protocol was incorporated to remove wear debris between tests. However, in hard court tennis, rubber wear from outsoles will be deposited on the court and may reduce the friction of slides over-time due to third-body rolling action.

Another difference between the results of the step and slide results, was how during the first 15 slides the  $\mu_k$  increased. Something not shown during the first 15 step tests. It is hypothesised that this  $\mu_k$  increase is due to the increasing size of the ridges (Figure 6.8) that form on the surface during the slide tests. This is a hypothesis supported by a study on rubber wear patterning which commented that friction force, though erratic, seemed to increase with an increase in ridge height [101].

#### **6.4.2 Effect of Tread Orientation**

In the latter 15 steps (in the reverse direction) the long tread orientation produced significantly higher  $\mu_k$  than the short ( $g_s = 5.1$ ). This is a similar finding to that observed in Chapter 5 for Rubber B. Similarly to Rubber B, the tread elements here experienced little wear (< 2 mg), supporting the notion that rubber's shape effect of friction is related to the wear resistance of the rubber grade itself in the tested scenario. As very little wear was observed for the step tests, differing friction-induced torque explains why the long orientation produced higher friction than the short for the last 15 tests when the surface patterning and change of direction reduced the overall SD in  $\mu_k$ .

The effect of tread orientation on the dynamic friction of sliding was juxtaposed to that of steps. The long tread orientation produced statistically lower  $\mu_k$  both before and after the change of direction. This result was expected as an effect of temperatures generated at the rubber-surface interface as consequence of the higher sliding velocity. As has been discussed previously in this thesis, the longer the shape is in the slide direction, the greater the heat experienced [59]. This heat induced frictional effect, though not directly measured within this present study, is thought to be the primary reason as to why during all the slide experiments the long tread element had a lower friction than the short tread element. Wear may also have been of influence as the short tread element also experienced the greater mass loss.

In one study, friction tests on a 3 cm × 9 cm outsole sample cut from another Babolat tennis shoe with similar tread elements to those in this chapter, observed that for normal loads between 100 – 400 N, the orientation at which the tread elements were shortest, produced lower mean  $\mu_s$  and  $\mu_k$  than when orientated with the tread elements close to their longest orientation (statistical analysis was not conducted) [61]. This matches the results observed for the step tests within this current study but is the opposite to that observed in the slide tests. As the tests performed in [61] were at slide speeds between 0.15 – 0.4 m/s, they fall between the speeds tested presently and suggest the friction mechanisms that cause long orientated tread to have a lower friction require a further increase in slide speed.

### **6.4.3 Effect of Slide Direction and Frictional Asymmetry**

Across all experimental conditions, the reversal of the slide direction resulted in a significant decrease in friction. This is believed to be the result of the topographical changes made to the surface of the tread elements during the first 15 steps or slides. These topographical changes, shown in Figures 6.8 and 6.9, are widely observed in rubber sliding scenarios [100,101,103,104].

A previous study investigating these patterns, observed that ridge height increased with repeat slides until the ridges reached a critical height ( $\approx 0.8$  mm) at which they broke off as wear debris [101]. This former study induced the formation of this wear pattern through contact between a rubber wheel which was loaded with a steel cylinder at 12 – 18 N. The cycle of ridge growth and detachment took around 30 repeat revolutions of the rubber wheel. In this chapter ridge heights reached a maximum of 0.9 mm after 15 slide tests (Figure 6.9). When the sliding direction was then reversed the height of these ridges decreased, and after 15 reverse slides, were a height of 0.3 mm. Maximum ridge heights with additional slides in the initial direction were not investigated, but it was noticed that the change in sliding direction effectively tears these asymmetric ridges reducing their height and asymmetric geometry. This geometric asymmetry means that the contact pressure will vary depending on the slide direction with the initial sliding direction having a more uniform pressure (typically causing higher friction) than the reverse direction [52].

Ridge patterning occurs after repetitive sliding in a single direction. As steps and slides performed in tennis often occur in various directions and at varying shoe orientations, the wear ridges will not develop to their maximum height and will not have such a prominent frictional effect as that observed here.

### **6.4.4 The Relevance of Findings to Footwear Design and Tennis**

Though the results presented in this chapter are obtained from a controlled environment, they are still relevant to the highly dynamic environment of hard court tennis. These results indicate that during step movements the orientation of the contacting tread elements will not cause frictional differences. This suggests that the orientation and shape of tread on shoes designed for slow movements with little or no sliding (such as walking), has little effect on their frictional performance. Contrarily, during sliding movements tread orientation is expected to have a frictional influence with long tread elements (in the direction of motion) producing lower dynamic friction. Therefore, shoes that will experience high-speed sliding movements should consider tread orientation, as longer tread elements in the slide direction will give the shoe a lower dynamic friction. The difference in mean  $\mu_k$  readings between the two orientations in the

first 15 slides is 0.09 ( $g_s = 1.8$ ). This means that a player performing a slide movement at a set leading leg angle to the horizontal will theoretically be able to perform the same slide by applying around 9% less force with the long tread elements compared to the short.

Due to the reciprocating lateral motion across the baseline typical in tennis, the frictional effects of changing tread topography will not be as pronounced as that shown here. This is because, by frequently changing direction, the ridges will not form asymmetrically. Instead, smaller symmetrical ridges like that shown after slides in both directions (red dashed line in Figure 6.9) will appear on tennis shoe treads, which would cause a drop in friction over time. It has been anecdotally reported that some tennis players deliberately choose pre-“worn-down” footwear during hard court tennis to improve their sliding performance. It could be that the cause of this drop in friction noticed by players is due to the symmetric topographical ridges observed after the tests in both directions in this study, and not due to the overall wearing down in tread height which would conversely result in higher contact areas, leading to lower contact pressures and higher  $\mu$ . Topographical analysis of game-worn footwear is needed to investigate this.

If there are areas of a tennis shoe outsole that only make contact during sliding in one direction, these contacting areas will form asymmetrical ridges on their surface, increasing friction in the slide direction over time and decreasing the friction at that point if any movements are performed that require shoe-surface sliding in the opposite direction.

Biomechanical analysis has shown that a 20% difference in mechanical shoe-surface dynamic friction can significantly affect the performance of basketball specific movements [3], while a 4% increase for futsal shoes significantly reduces the time it takes to perform a cutting movement [74]. A study with the design of these two previous research papers is required to determine whether a frictional difference of 9%, as produced in this current study by a change of tread orientation, will demonstrate an effect on playing performance in hard court tennis. It is acknowledged that any mechanical test does not accurately replicate the highly dynamic nature of human movement and the biomechanical adjustments that are innately made to changes in surface friction [9]. This study is also limited by its use of a single shoe tread design.

## 6.5 Conclusions

Using a mechanical test, the friction and wear of tennis shoe tread elements was investigated. Slide experiments were found to produce higher dynamic friction than step experiments, which were due to the increased frequencies transferred to the rubber causing increased hysteresis, and due to increased wear both of which are greatly influenced by slide speed. No significant

difference in static friction was observed for the change in tread orientation for step movements, though greater dynamic friction was observed for the short tread orientation during all slide tests. Both movements caused a roughening of the rubber surface which altered the friction and caused frictional asymmetry. The frictional effect of rubber's changing surface topography is something that is expected to affect the performance of step and slides over time in hard court tennis.

This chapter highlights another factor that can affect the friction of rubber on rough dry surfaces – topographical changes of the rubber. It also identifies the dependence of a rubber shape's frictional effect on the sliding conditions e.g. during slow step movements longer shapes had a higher dynamic friction. The opposite was observed during the faster sliding condition.

## 7 The Influence of Tennis Shoe Tread Contact Parameters on Friction

*The work in this chapter was presented at the joint conference of the 5<sup>th</sup> International Conference on BioTribology and the 23<sup>rd</sup> International Conference from Wear of Materials (27<sup>th</sup> April 2021).*

### 7.1 Introduction

Chapters 4 - 6 detail a series of exploratory experiments observing if, and why, different shapes of rubber produce different  $\mu$  when sliding over dry hard court tennis surfaces. It has thus been discovered that the friction between rubber and a rough surface is sensitive to changes in slide velocity, normal load, shape and wearability. However, it is still unknown as to how the identified frictional influencers affect the friction of real, full size, tennis shoe outsoles under loads characteristic of real tennis movements.

All previous experiments in this thesis have been conducted on well controlled shapes of rubber. For example, all the rubber shapes tested in Chapters 4 and 5 had a nominal contact area of 100 mm<sup>2</sup>. This was done so that nominal contact pressures (which influence friction) were consistent for all shapes tested, thus allowing an investigation of other shape parameters that influence friction. However, when comparing full shoe treads, contact areas will be different and need therefore to be quantified. Many papers omit this analysis, though there are numerous ways in which contact areas can be measured/estimated (see section 2.3.2). Currently there are no published methods that go beyond quantifying shoe tread contact areas to other parameters like leading edge lengths. The current inability of researchers to quantitatively characterise shoe tread patterns, despite scores of papers investigating the frictional effect of tread pattern on dry surfaces, means that little rationale for shoe tread designs is present. This hinders the development of effective shoe tread designs for sports like tennis.

Due to the viscoelastic properties of rubber, frictional heat can affect friction. In the previous chapters, frictional heat has not been directly measured. To conclusively determine whether it is affecting friction data from a given experiment, thermal analysis should be included. This can be performed using thermal cameras.

Within this chapter, a novel tread analysis method capable of quantitatively characterising complex shoe tread designs is proposed. An example of how this method can be used is presented with the frictional analysis of a tennis shoe on a hard court. As contact area is widely acknowledged as an influential factor to rubber friction, and previous chapters have shown correlations between leading edge length and friction, it is hypothesised that the sliding contact

area and overall leading edge length will be the most influential parameters when measuring the shoe-surface friction. Analysis of the frictional heat generated as a shoe slides is also included to determine how it influences friction.

## 7.2 Methodology

### 7.2.1 Shoe and Surface

Two identical tennis shoes (TS100 Multicourt, Artengo, Decathlon), size UK 9.5, were used for all analyses. The shoes were attached to a prosthetic foot (1D10 Dynamic Foot, Otto Bock, US), which could be rotated 360° in the foot's transverse plane, allowing the testing of multiple shoe orientations. The prosthetic foot was then fitted into the UoS Traction Device detailed in Chapter 2, Section 2.3.

The mean and standard deviation of the shoe outsole tread heights were 2.67 mm and 0.05 mm, respectively. These measures were taken using digital callipers at seven different regions of the outsole (Figure 7.1).



**Figure 7.1** UoS Traction Device shoe attachment (left) and a TS100 Multicourt shoe outsole with labelled areas where tread depths were taken (right).

The surface used for the friction experiments was a tennis hard court (Ace Surfaces North America), which consisted of a 13 mm thick layer of MDF, topped with a sand paint mixture, providing the rough surface topography ( $R_a = 27.5 \mu\text{m}$ ,  $R_q = 32.7 \mu\text{m}$ ). After every slide test, the surface and shoe were lightly brushed to remove any worn rubber debris.

### 7.2.2 Friction Experiments

The UoS Traction Device (Figure 7.2) was used for all friction experiments, a device that has been used previously to evaluate the friction of tennis shoes [64,72]. Changes were made from the device outlined previously in Chapter 2, Section 2.3, and were as follows:

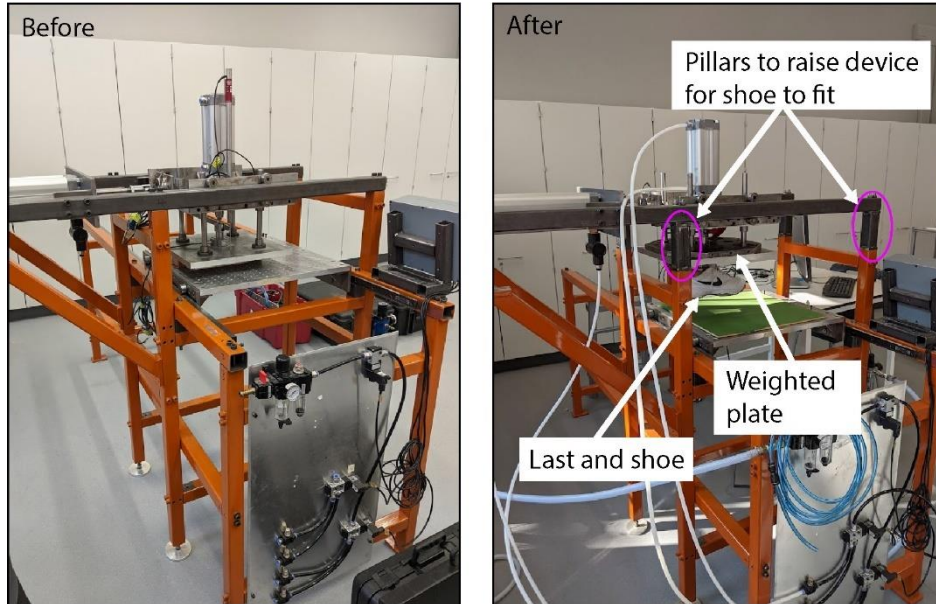


**Figure 7.2** UoS Traction Device before and after modifications.

- A prosthetic foot attachment was made to allow the testing of full shoe sample, not only the forefoot cuts which have been previously used.
- The top of the device was raised to allow the fitting of the new full shoe attachment.
- A weighted plate was manufactured and placed above the full shoe attachment, to apply a constant, known normal load.
- The vertical pneumatic cylinder was made detachable from the shoe attachment to allow for deadweight testing, instead of testing at normal loads provided by pneumatic cylinder.

Seven repeat friction tests were performed on the updated UoS Traction Device for nine different orientations of the TS100 shoes (Figure 7.3). The shoe was moved to the neighbouring orientation after every two tests. This prevented the development of asymmetrical wear patterns on the shoe tread, which could have led to frictional asymmetries.

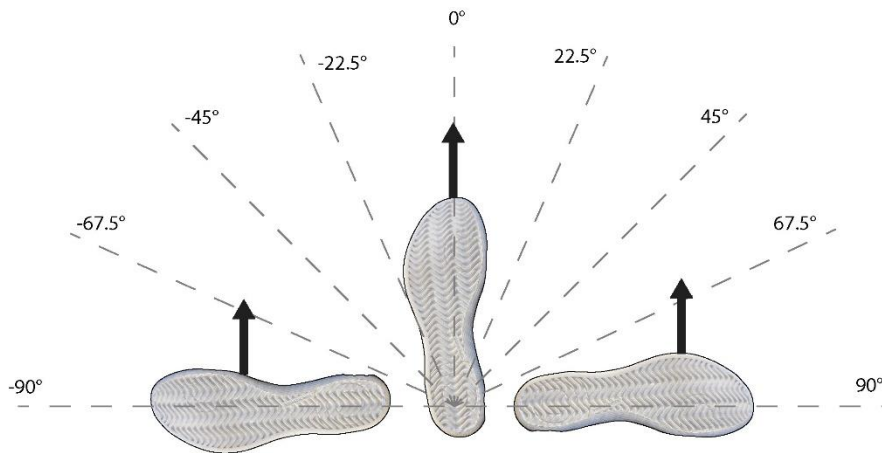


**Figure 7.3** The nine orientations at which the TS100 tennis shoes had their friction tested in the UoS Traction Device.

Before conducting these tests, an analysis of the UoS Traction Device was performed. Figure 7.4 shows four stages of a friction test on the UoS Traction Device. At the beginning of all tests, the shoe being tested was positioned above the hard court and was attached to the vertical pneumatic cylinder (A). The vertical cylinder was then initiated by the user, lowering the shoe until it contacts the hard court. The user then removed a pin that connected the vertical pneumatic cylinder to the shoe, before it is retracted, leaving the shoe in contact with the hard court (B). The user then initiated the horizontal pneumatic cylinder, which slid the shoe across the hard court, until full pneumatic cylinder extension is reached (25 cm) (C shows the end of slide). The user then re-initialised the vertical cylinder and returned the pin to connect vertical cylinder to shoe. The vertical cylinder was again retracted, lifting the shoe above the surface (D). The horizontal cylinder was then retracted, taking the shoe back to the initial position (A).

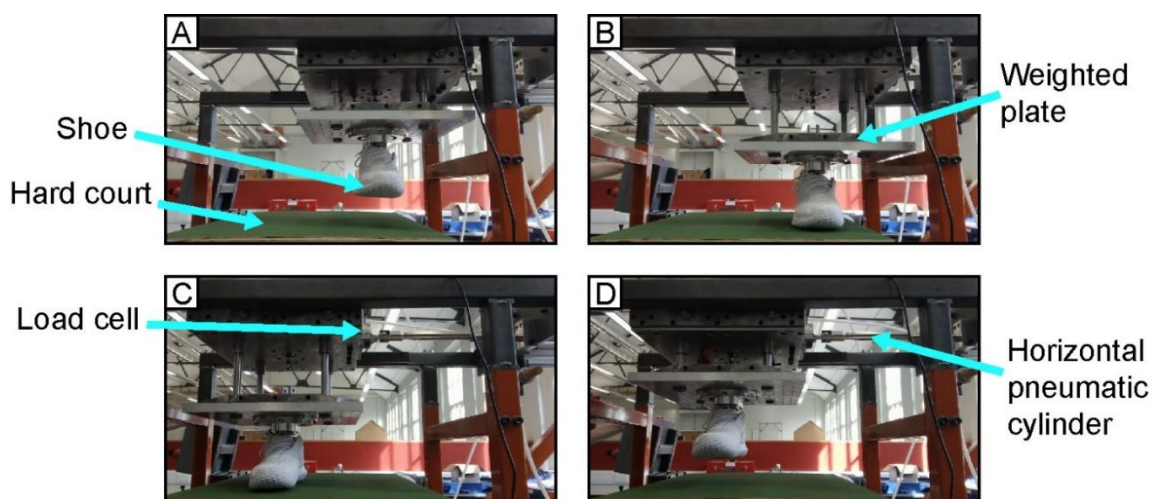


**Figure 7.4** UoS Traction Device at four stages: Before shoe is lowered (A), shoe-surface contact (B), end of slide (C), shoe retracted (D).

To understand the forces acting on the system, and how to calculate friction coefficients, a force diagram was drawn (Figure 7.5).

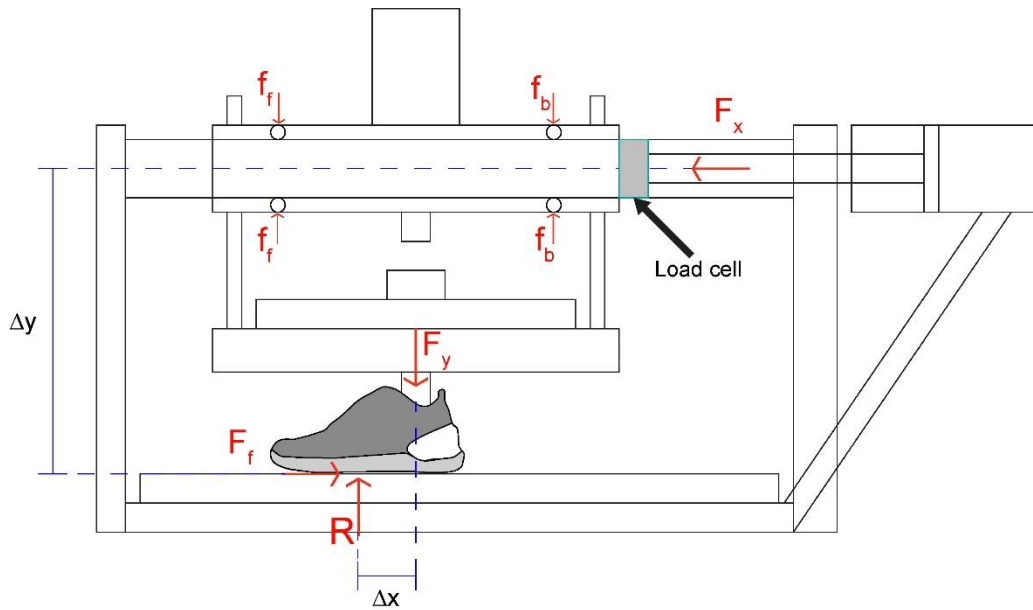


**Figure 7.5** Force diagram of the UoS Traction Device.

The placement of the load cell (shown in Figures 7.4 and 7.5) means it measured  $F_x$ . If the system was completely rigid, or if  $\Delta y = 0$ , then  $F_x = F_f$ . However, given that  $\Delta y \neq 0$ , a torque was experienced which distributed loads differently on the roller bearings at the front and rear of the upper section of the device ( $f_f$  and  $f_b$ ). Furthermore, if perfect rolling is not assumed, these bearings, even when loaded equally, will have their own friction which will be measured by the load cell. In short, the force measured by the load cell ( $F_x$ ) was a combination of the friction force at the shoe-surface interface, and internal friction forces within the device itself. To measure the internal friction of the device, to then subtract from  $F_x$  to give  $F_f$ , the shoe was replaced by a roller assumed to have minimal friction. The traces from the horizontal load cell for a test with the wheel and a shoe are shown in Figure 7.6.

Ten tests with the wheel were performed. An initial peak force of 452 N ( $\pm 15$  N) occurred as the wheel began to roll. As shown in Figure 7.6, the magnitude of this force was similar for the wheel and shoe tests. The similarity in the initial peak forces for the wheel and shoe tests, shows that the lateral force that must be overcome to initiate lateral motion was largely unaffected by the friction of the shoe fitted. Consequently, this device could not be used to extract a shoe  $\mu_s$ .

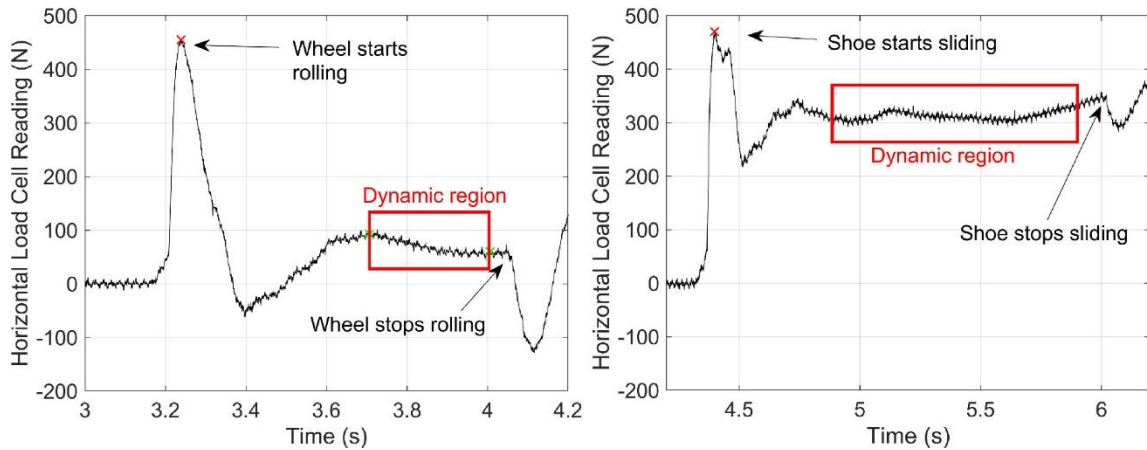


**Figure 7.6** Annotated force-time trace from an example wheel test on the UoS Traction Device (left) and an example trace from a shoe test (right).

After the initial peak, the lateral force dropped as the initial inertia of the device was overcome ( $0.36 \text{ s} (\pm 0.03 \text{ s})$  after the initial force peak) before rising again to  $71 \text{ N} (\pm 7 \text{ N})$  where it remained until the horizontal cylinder reached maximal extension. As such, during the subsequent shoe friction tests,  $71 \text{ N}$  was subtracted from the mean of the measured friction forces ( $F_x$ ) in the dynamic slide region, to give  $F_f$ .  $\mu_k$  was then calculated by dividing  $F_f$  by the normal force ( $F_y$  in Figure 7.5). To measure  $F_y$ , a loadcell was placed between the shoe and hard court. With the vertical pneumatic cylinder retracted,  $F_y$  (the weight of the system) was  $326 \text{ N}$ , a load similar to that recorded using a force platform during the sliding phase hard court slides ( $300 - 400 \text{ N}$ ) [71].

However, Figure 7.5 shows that, similarly to forces in the  $x$ -direction, forces in the  $y$ -direction were not collinear.  $\Delta x$  represents the distance in the  $x$ -direction between the applied normal force ( $F_y$ ) and the reaction force ( $R$ ) which acted at the centre of pressure on the shoe outsole. The presence of  $\Delta x$  produced another torque, which meant that  $R$  may not be the  $326 \text{ N}$  measured for  $F_y$ . Additionally, when testing at shoe orientations other than  $0^\circ$ , a  $\Delta z$  (going into the page in Figure 7.5) was also present, which varied with orientation.

To investigate how much shoe orientation influenced normal force (which would affect calculated  $\mu_k$ ), the hard court was replaced by a set of scales (ABCON, PROSHIP, UK) (resolution =  $0.05 \text{ kg}$ ) that measured the normal load (scale reading  $\times 9.81$ ) for all orientation tests. To take these readings, slides were filmed, with the digital scale display in shot. The static load was taken as the frame before sliding was initiated, and the dynamic load was taken from the frame when the shoe reached the slide mid-point. For all orientations, the static normal load was higher than the measured weight of the system ( $326 \text{ N}$ ). The load then

dropped towards 326 N during sliding. The static and dynamic normal loads, measured using the scales, are shown in Figure 7.7.

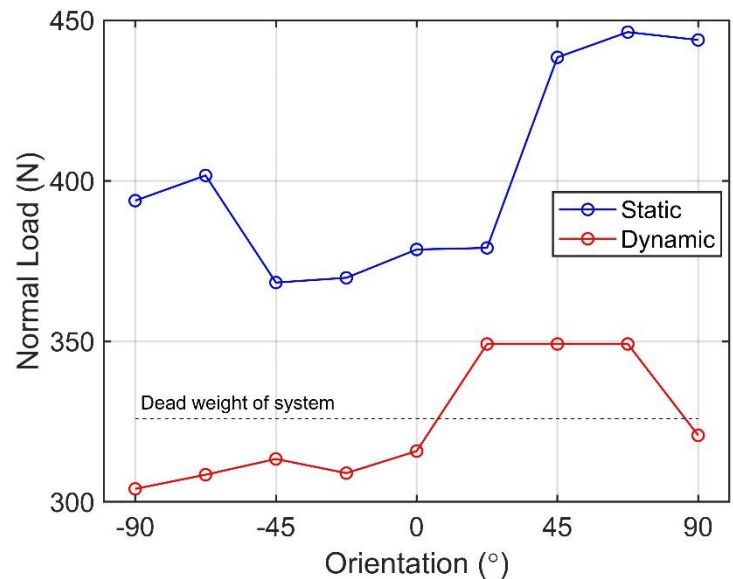


**Figure 7.7** Static and dynamic normal loads measured with scales at all nine orientations. Weight of the system (326 N) is marked by the dashed line.

The recorded static loads were higher than the weight of the system. This was because the shoe was lowered onto the surface by a vertical pneumatic cylinder, that applied additional normal load. Evidently, although the vertical cylinder was disengaged before sliding, residual force was present at the shoe-surface interface. This was because the bearings that allow the movement of the shoe vertically, misalign and “pinch” due to the torques caused by the force misalignments ( $\Delta x$ ,  $\Delta y$  and  $\Delta z$ ), preventing the retraction of the shoe when the vertical cylinder was disengaged.

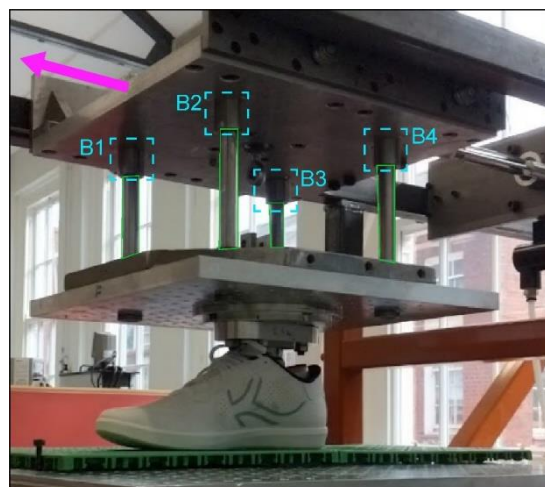


**Figure 7.8** The four rods that allow vertical displacements are shown in green. The dashed boxes with labels are the four bearings that affected normal loads.

Figure 7.8 shows the location of the vertical rods that allowed vertical motion, and the four bearings where misalignments, due to torques which varied with shoe orientation, resulted in non-uniform force distributions and pinching. Therefore, vertical loads were not the expected value of 326 N and varied with orientation. The measured normal dynamic forces in Figure 7.7 were used to calculate  $\mu_k$  values for each orientation.

### 7.2.3 Contact Area Imaging

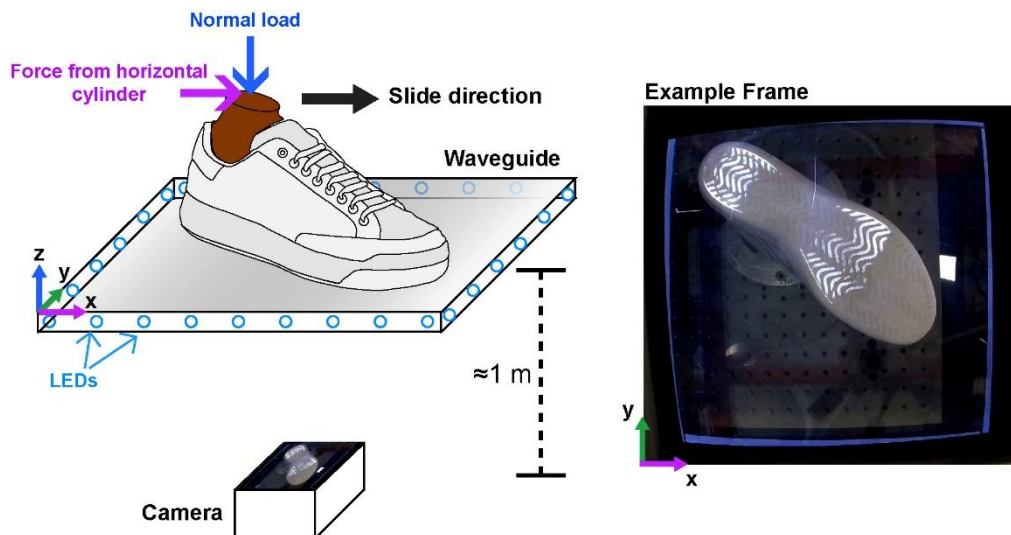


**Figure 7.9** How a waveguide and camera were used to extract contact area images.

To measure the nominal contact area between the outsole and surface, the hard court was replaced with a total internal reflection waveguide (Figure 7.9), as described in [95]. The waveguide (a polycarbonate sheet lined perimetrically with LEDs) refracts light at areas of contact between the Perspex sheet and the shoe. The resulting light pattern was imaged by a camera (HQ V1.0 2018 Raspberry Pi, UK) placed beneath the waveguide.

The same normal load of 326 N, as that used in the friction tests, pushed the shoe into contact with the waveguide, before the horizontal pneumatic cylinder was initiated, sliding the shoe over the waveguide. The contact area was filmed, and a frame was extracted when the shoe

was sliding. This was done for all orientations. Once a dynamic frame was extracted, it was processed to give an image that contained only the contacting tread regions (Figure 7.10).

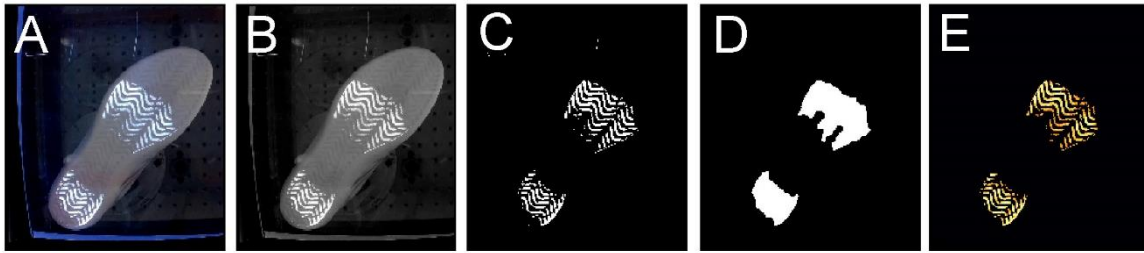


**Figure 7.10** Original image (A), image in grayscale (B), threshold applied to give binary image (C), image erosion and dilation applied to remove bright areas that are not part of the tread (D), final tread image (E).

Figure 7.10 shows how contact area images were processed. Firstly, images were converted from Red-Green-Blue (RGB) format, to grayscale. This meant that, whereas in RGB format, where each pixel had three different values for each of these three colours, in grayscale, those three values were averaged, leaving one value per pixel. The pixels had values between 0 – 256, which were then scaled to between 0 -1. A high-pass threshold of 0.65 was applied to the grayscale image, removing the background. Some scratches on the waveguide refracted light in areas that were not tread contact areas. To remove these, white areas were eroded and then dilated, producing the mask in Figure 7.10 (D). A final image was then produced by multiplying (C) and (D) to give (E) which was then coloured. This final image showed only the areas where the shoe outsole contacted the waveguide. This process was conducted on a frame during sliding from all nine orientations, producing nine images which were then quantified by extracting 18 variables. How all 18 variables were extracted is available in the Appendix, where the full Python code is written. Within this chapter, only the quantification of two variables (Contact Area (CA) and Leading Edge Length (LE)) is described. All image processing was performed using Python 3.

CA was calculated by counting the number of pixels with values  $> 0$  in the image and multiplying this number by the ratio of pixels to millimeters. For all the images taken, the size of its area was  $97650 \text{ mm}^2$ , and each image has a pixel area of  $353675 \text{ pix}^2$ , therefore the sum of all white pixels was multiplied by 0.276. To determine the standard deviation (SD) of the CA measure, the shoe was normally loaded nine times, in nine different locations on the waveguide. The mean (M) and SD of these contact area tests were  $2915.9 \text{ mm}^2$  and  $110.36 \text{ mm}^2$ , respectively, equating to a 3.8% SD in CA.

Leading edge length was defined as the sum of the rightmost pixels (sliding direction for all images was left to right) of all the white areas of an image. To isolate these pixels a horizontal Sobel edge filter was used, which multiplied all pixels by a kernel (shown in Figure 7.11) that passed across the image (convolution process). Consequently, the rightmost white pixels (the leading edges) got pixel values  $< 1$ , while the trailing edges (leftmost pixels) got values  $> 1$  and all other white pixels are reduced to zero. In the leading edge images, the only pixels with values  $< 1$  were those of leading edges, and were thus isolated, summed and converted to millimeters, giving an overall leading edge pixel number.

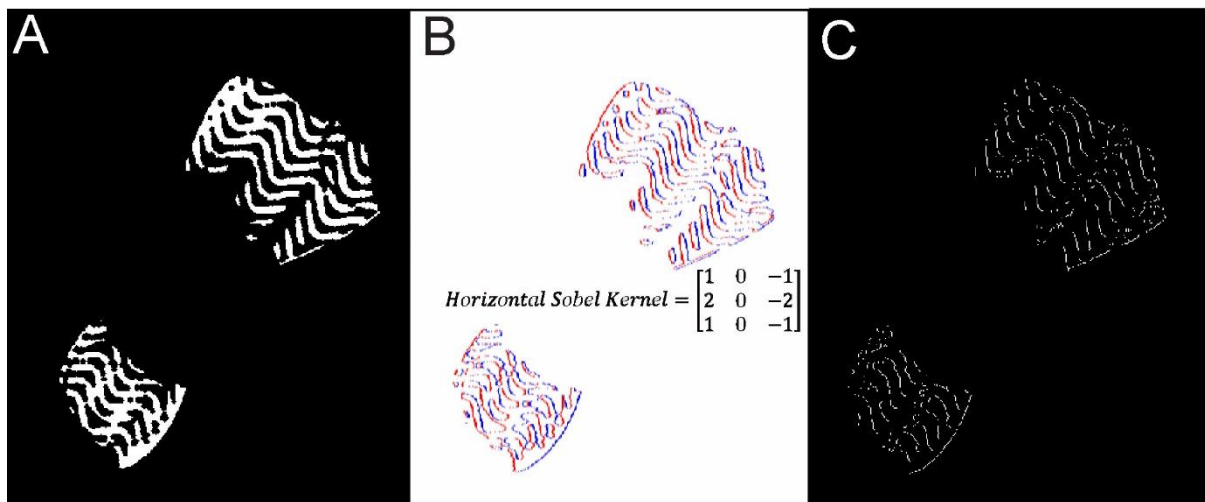


**Figure 7.11** For LE, a binary contact image (A) underwent convolution of a horizontal Sobel filter, which created an image showing only horizontal edges (B), where blue pixels had negative pixel values, and red had positive (white pixels = 0). The final image (C) shows only the pixels with a negative value in B (blue lines). These pixels were counted and converted to give overall LE in millimeters.

This process, and all variable extraction calculations, were performed for all orientation images, allowing quantitative comparisons of the contact images produced at different orientations.

#### 7.2.4 Thermal Analysis

The mechanical properties of rubber, and hence its friction, are temperature dependent. A thermal camera (thermoIMAGER TIM 190S, Micro-Epsilon, Germany) observed the heat trails left by the shoes as they slid over the hard court surface. This was done twice for orientations between  $0^\circ$  and  $90^\circ$  to investigate whether the change in orientation influenced the frictional heating, and therefore friction.

### 7.2.5 Statistical Analysis

An ANOVA with Bonferroni post-hoc test was selected to investigate whether shoe orientation had a significant effect on  $\mu_k$ . Pearson's-r correlations were used to investigate the correlation between the recorded friction coefficients and all parameters obtained from contact area image analysis. These correlations tested the null hypothesis that the correlation between  $\mu_k$  and each parameter was zero. A linear regression model was created to model  $\mu_k$  from image analysis parameters. Checks for normality and heterogeneity were conducted and passed for  $\mu_k$  data. IBM SPSS Statistics 26 was used for all statistical analysis.

### 7.3 Results

Shoe orientation had a significant effect ( $p < 0.05$ ) on  $\mu_k$  [ $F(8,54) = 4.86, p < 0.01$ ]. The  $22.5^\circ$  orientation produced the smallest mean  $\mu_k$  (0.78), and  $90^\circ$  produced the largest mean  $\mu_k$  (0.98) (Figure 7.12).

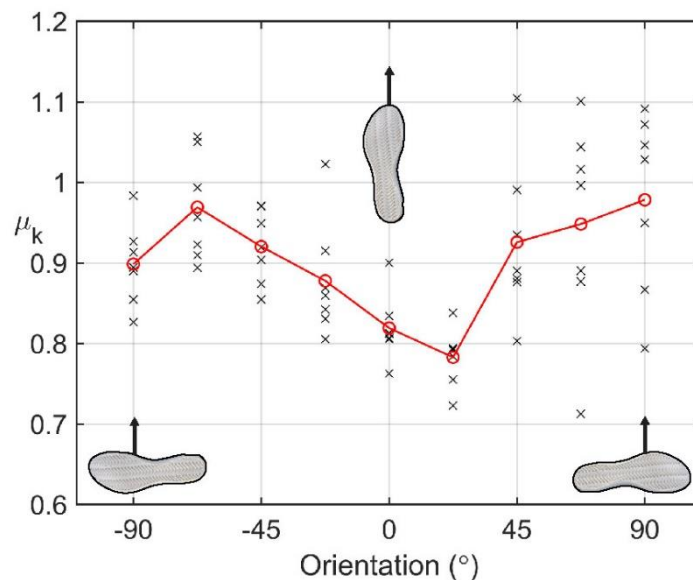


**Figure 7.12**  $\mu_k$  results for all shoe orientations. The red circles indicate the mean of the seven raw data points (black crosses) for all nine orientations.

Post-hoc tests revealed that significant differences were present between multiple orientations e.g. the  $22.5^\circ$  orientation produced significantly lower  $\mu_k$  ( $p = 0.001$ ) than the  $90^\circ$  shoe orientation. The full list of orientation comparisons is shown in Table 7.1. The correlations (Pearson's-r) between all image processing parameters are shown in Table A.1 in Appendix. Negative correlations with  $\mu_k$  were observed for contact area and leading edge length, and all correlations had a magnitude below 0.6. One of the strongest correlations was with leading edge length (mm),  $r(63) = -0.5, p < 0.001$ , and is shown in Figure 7.13.

**Table 7.1** Bonferroni orientation comparisons. Orientations that produced statistically different  $\mu_k$  results are marked in green.

|       | Shoe Orientation (°) |       |       |       |       |       |       |       |       |
|-------|----------------------|-------|-------|-------|-------|-------|-------|-------|-------|
|       | -90                  | -67.5 | -45   | -22.5 | 0     | 22.5  | 45    | 67.5  | 90    |
| -90   |                      | 1     | 1     | 1     | 1     | 0.311 | 1     | 1     | 1     |
| -67.5 | 1                    |       | 1     | 1     | 0.031 | 0.002 | 1     | 1     | 1     |
| -45   | 1                    | 1     |       | 1     | 0.756 | 0.074 | 1     | 1     | 1     |
| -22.5 | 1                    | 1     | 1     |       | 1     | 1     | 1     | 1     | 0.772 |
| 0     | 1                    | 0.031 | 0.746 | 1     |       | 1     | 0.541 | 0.130 | 0.015 |
| 22.5  | 0.311                | 0.002 | 0.074 | 1     | 1     |       | 0.050 | 0.010 | 0.001 |
| 45    | 1                    | 1     | 1     | 1     | 0.541 | 0.050 |       | 1     | 1     |
| 67.5  | 1                    | 1     | 1     | 1     | 0.130 | 0.010 | 1     |       | 1     |
| 90    | 1                    | 1     | 1     | 0.772 | 0.015 | 0.001 | 1     | 1     |       |

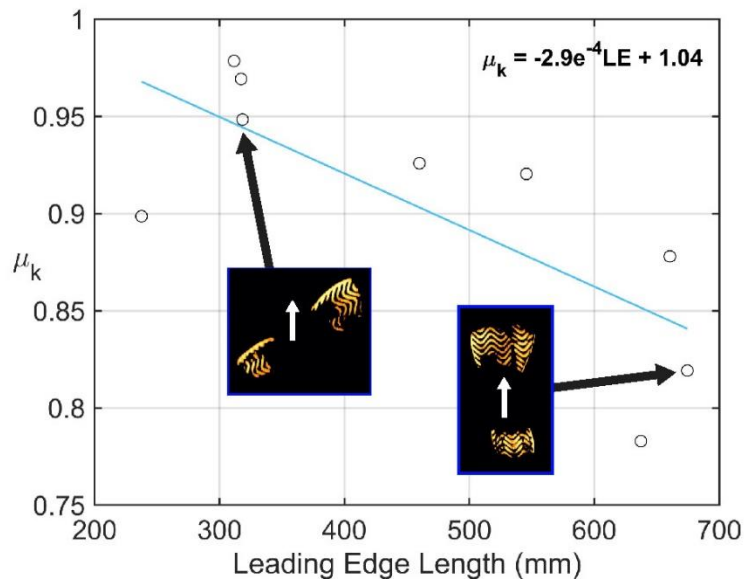


**Figure 7.13** Mean  $\mu_k$  results for all shoe orientations. Negative correlation observed between leading edge length and  $\mu_k$ .

A linear regression model was created with the following parameters: Leading Edge Length (LE) (mm), Contact Area (CA) (mm<sup>2</sup>) and Y-theta (YT) (°) (YT is the absolute orientation e.g. the YT of -90° and 90° both equal 90). How this model compared to mean friction data is shown in Figure 7.14. The correlations between all measured parameters are provided in Appendix, Table A.1.

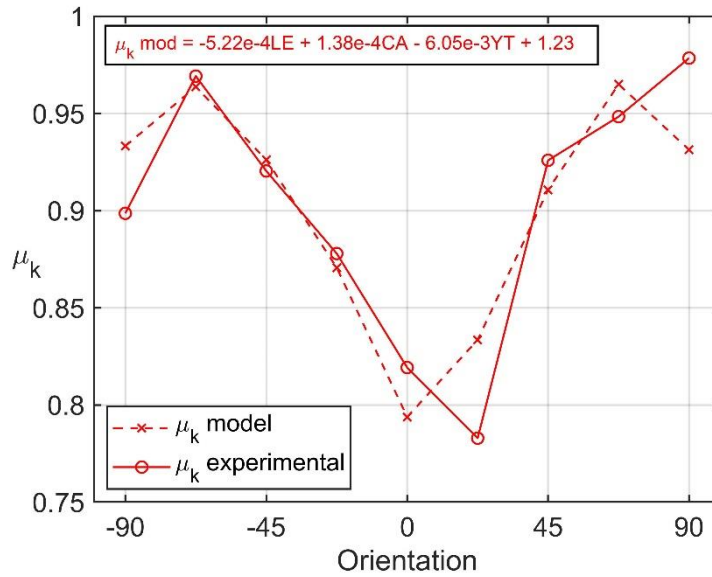


**Figure 7.14** Multivariate linear regression  $\mu_k$  model compared with experimental means.

The model shown in Figure 7.14 explained 80% of the variance in the mean  $\mu_k$  readings ( $n = 9$ ). However, when the model only explained 33% of the variance in the full data set ( $n = 63$ ). As shown previously in Figure 7.12, at each orientation, especially between orientations  $45^\circ - 90^\circ$ , there was a large SD of friction results. This intra-orientation variance explains why the model score is lower than would be expected from the fit in Figure 7.14.

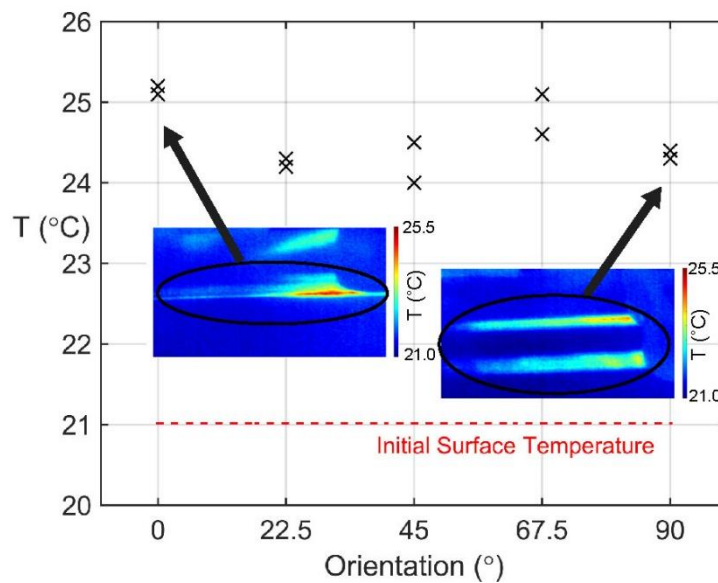


**Figure 7.15** Max temperature (T) readings from the hard court surface for two repeat tests at five orientations. Example infra-red images of  $0^\circ$  and  $90^\circ$  orientations shown.

The highest surface temperature was observed during 0° orientation tests (25.2 °C). The initial hard court temperature was 21 °C, meaning that the 0° orientation tests produced an increase of 4.2 °C. The lowest temperature increase was observed during 22.5° and 45° orientation tests (+3.25 °C). Figure 7.15 shows the temperatures recorded for five orientations.

The values shown are the max readings in the final frame of sliding. Examples of these frames for 0° and 90° orientation are also shown in Figure 7.15. During 0° tests, the heat trail of the forefoot and heel were in-line, leaving a single trail. At all other orientations, the forefoot and heel heat trails did not cross, leaving two distinct trails.

#### **7.4 Discussion**

Figure 7.14 shows that a multiple linear regression model with parameters LE, CA and YT, can explain the mean change in friction coefficients with orientation. The model coefficients in Figure 7.14 show that, in combination, both LE and YT have a negative correlation with friction, and CA has a positive correlation with friction. Why increased LE produced a decrease in friction can be understood in the same way as the block friction results in Chapters 5 - 6 where shorter shapes (with greater LE) produced lower friction than long shapes (small LE). This can reduce friction due to increased pressures on the leading edge. For the full shoe this could be occurring at all leading edges.

Alone, CA does not well describe the changes in friction observed with change in orientation (the correlation between CA and  $\mu_k$ ;  $r(63) = -0.5$ ,  $p < 0.001$ ). This correlation gives the misleading interpretation that increasing CA produces a decrease in friction, which is contrary to the generally accepted laws of rubber friction where the opposite is expected. However, when modelling friction along with LE and YT, the coefficient for CA is positive, showing that once the variances in friction that are due to LE and YT are accounted for, increases in CA produce an increase in friction. An example of this can be seen by comparing the results for the -90° and 90° test orientations (Figure 7.16).

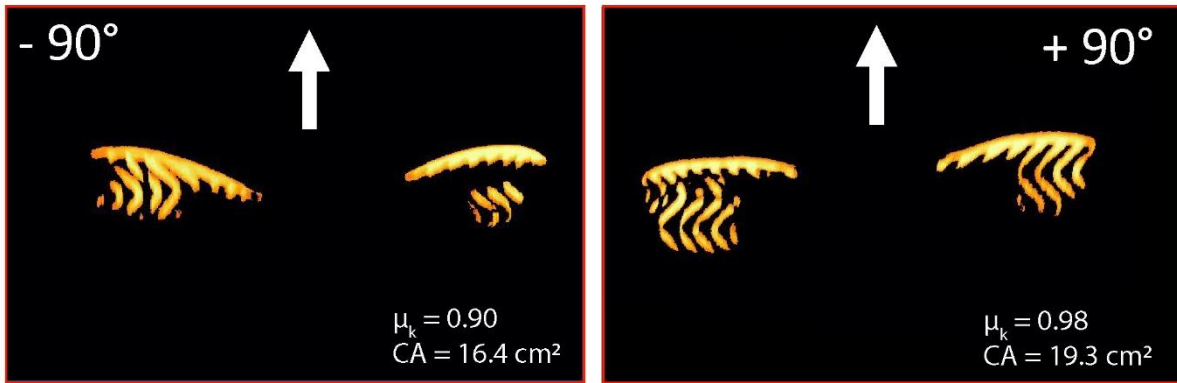


**Figure 7.16** Contact area images from  $-90^\circ$  (left) and  $90^\circ$  (right). The contact area images are very similar, though more tread makes contact ( $+2.9 \text{ cm}^2$ ) at the  $90^\circ$  orientation, which corresponds to an increase in  $\mu_k$  ( $+0.08$ ).

Infrared video of the hard court surface showed that the  $0^\circ$  orientation produced the highest surface temperatures (Figure 7.15). This is because the forefoot and heel contact areas were aligned, so that during sliding the surface in front of the heel contact region had already been heated by its interaction with the forefoot. Therefore, as the heel passes over this heated surface, the interaction further increases the temperature. This only occurred for the  $0^\circ$  orientation. At all other orientations, the heel and forefoot were not aligned in relation to the slide direction, so the heel and forefoot left two distinct heat trails that did not cross. The additional heat experienced by the heel of the shoe at  $0^\circ$  further reduced the overall friction, via thermal softening, which reduces the hysteresis of the rubber [59]. However, due to the low slide speeds capable by the test device, the temperatures generated during sliding were not different enough across orientations to explain the orientational variance in friction.

#### 7.4.4 Limitations of the contact area analysis method

The test method described in this chapter allows an observation of contact areas during sliding, that can be compared for different tread patterns and shoe orientations. However, the method is not without limitations, which are listed as follows:

- **Image resolution** – Each pixel in the contact images corresponds to an area of  $0.28 \text{ mm}^2$ . Any contact regions that are smaller than this area will not be shown in the image.
- **Waveguide pressure range** – There is a lower pressure threshold that must be exceeded before the light refracted at the contact area is significantly brighter than the background lighting and can be identified in the contact images. The exact pressure that must be exceeded has not been determined and will vary with outsole materials of different refractive indices, which are also affected by temperature and pressure itself, as well as the wavelength of light being used. Therefore, even if particular care

were taken to identify the pressure at which observable contact areas emerged, this would vary for other shoe outsoles (of different rubber compositions and colours), LEDs in the waveguide, and tread patterns (due to different internal pressures in the rubber tread shapes). The set-up also observed an upper threshold, which once exceeded gave light intensity values of 1. Though this upper limit did not affect CA, it did limit the detail that could be obtained regarding the pressure map. Large areas of the contact images had an upper value of 1, meaning that the light intensity had reached the camera brightness limit in these regions. Consequently, the exact regions that underwent the most pressure were unable to be determined. Camera brightness settings were altered to see whether all light intensity values could fall below the upper limit without sacrificing contact area by increasing the lower limit. Within the timeframe of this thesis an optimum set-up was not achieved to avert the problem of the waveguide-camera observable pressure range.

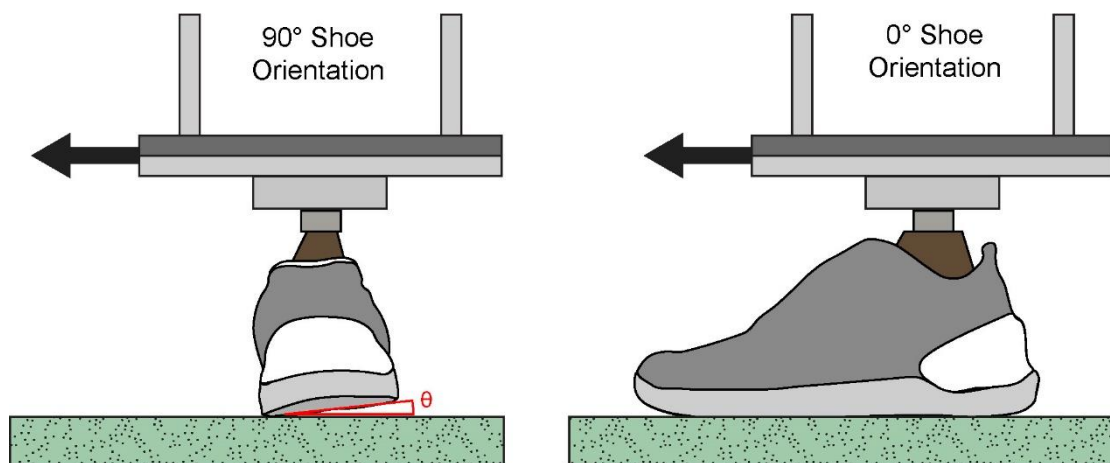


**Figure 7.17** Greater shoe tilt was observed for greater magnitude of shoe orientation.

This rotation and deformation of the shoe will incur energy losses that are not completely observable in the contact images.

- **Shoe slip** – By testing full shoes, fitted to a prosthetic foot by lacing alone, shoes could be efficiently attached and removed to reduce overall testing time. It also meant that the shoes were attached in a way replicable to how they are worn during tennis. This attachment method, however, was not rigid and resulted in the shoe slipping around the prosthetic foot during sliding. Qualitatively, this was observed to occur to a greater degree the greater the magnitude of orientation. How the shoe would noticeably tilt on the prosthetic foot during 90° tests, but not at 0°, is shown in Figure 7.17. The rotation and distortion of the shoe on the prosthetic foot will generate energy losses that are

not explained by the contact image. Thus, the contact images could not be used to quantify all energy losses in the system, and hence friction.

- **Waveguide vs hard court** – The method in this chapter compares the friction data from a shoe sliding on a hard court to the contact images of the same shoe on a clear Perspex sheet. The contact areas imaged will thus differ from that experienced on the hard court (a much rougher surface than the waveguide). Because the hard court is opaque, contact cannot be viewed in-situ and must be assumed from the images taken using the Perspex. Though CAs between Perspex and hard court surfaces will differ, it is assumed that the regions of the tread that contact the Perspex during a test are similar to those that contact the hard court.
- **Validity of pressure distribution** – During lateral steps and slides, the region of maximal contact pressure is on the medial side of the shoe [4]. This was not replicated by the UoS Traction Device. Instead, at 90° shoe orientation for example, max pressure was applied to the lateral side of the shoe (shown in Figure 7.16). To mechanically replicate the medial contact pressures observed in tennis, a complex lever system could be designed whereby the normal load is acting on the medial side of the shoe, producing a moment that applied pressure medially. Additionally, the last onto which the shoe is fitted, could be fixed with a small inversion angle. Though unable to apply these modifications to the UoS Traction Device, they should be addressed in the design of future test devices.
- **Influence of orientation on normal load** – As detailed previously in this chapter, the design of the device produced torques in three-dimensions which resulted in misalignments. These directly affected the friction and normal forces.
- **Slide speed** – Like the pressure distribution, the slide speeds capable with this device (0.1 – 0.8 m/s) were not replicable of those observed in tennis (2 – 5 m/s). To achieve higher slide speeds lateral motion must be applied to the shoe or surface using an alternative mechanism to a pneumatic cylinder.

These limitations question the suitability of this method in explaining shoe-surface friction. A device has been proposed in Chapter 9 which addresses some of these limitations.

## 7.5 Conclusion

A method aimed at modelling shoe-surface friction by analysing contact images has been proposed. It has been observed, that at comparable orientations (-90° and 90°, for example), an increase in CA causes an increase in friction. Shoe-surface friction has also been shown

to be orientation dependent, and a multivariate linear regression model of three parameters from the image analysis (CA, LE and YT) was shown to explain only 33% of the variance in  $\mu_k$ . This figure is low due to large intra-orientation variance. A more repeatable test is necessary to generate higher accuracy models. It was also shown that sliding temperatures are higher when the shoe is parallel to the sliding direction (0°) which will decrease friction by thermal softening of the rubber.

Though this method quantifies variables like LE, that have not previously been quantified during the study of shoe-surface friction, the method cannot comprehensively explain shoe-surface friction. The system's numerous limitations, in combination with the shoe's deformability, mean the method can realistically only in very specific cases compare the friction of shoes and orientations. These cases include testing the same shoe at comparable orientations, and testing shoes of identical manufacture varying only in tread pattern. An example of the latter case is shown in the following chapter.

## 8 A Frictional Comparison of Tennis Shoes

### 8.1 Introduction

There are currently no regulations that govern the design of tennis shoe outsoles used in hard court tennis. Consequently, patterns used on the rubber outsoles of hard court tennis shoes vary greatly from one shoe to another. In this chapter the friction of eight tennis shoes from four different brands were tested and compared. These friction tests were conducted on a hard court surface using the same methodology outlined in Chapter 7. In addition to friction, shoe measurements were taken that give insight into current tennis shoe construction and design. Comment is provided as to how certain shoe design parameters may influence friction during tennis.

### 8.2 Methodology

#### 8.2.1 Shoe Details

Figure 8.1 shows the outsoles of all eight tennis shoes (all size UK 9.5) used in the subsequent tests. Shoes were chosen based on their outsole colour (white gives the clearest image in contact area calculations) and to cover a range of brands. Six of the eight shoes were marketed as either hard court shoes or multicourt shoes, while Shoe G and Shoe H, were marketed as a clay and carpet shoe, respectively. These two shoes were included to determine whether shoes designed for other surfaces produce similar, or dissimilar, friction results to hard court shoes. Shoe A is the same shoe as was used in the experiments presented in Chapter 7.



**Figure 8.1** All eight shoes used in friction tests. Shoes A – F were marketed as hard court or multicourt shoes. Shoe G was a clay court shoe, and Shoe H was a carpet shoe.

For each pair of shoes purchased, the right shoe was used for friction measurements, and the left shoe was dissected and measured (see Figure 8.2). The measures taken from the left shoes were Outsole Shore A Hardness (O ShA), Tread Height (TH), Outsole Height (OH),

Midsole Height (MH), Insole Height (IH). O ShA was measured at five different areas of the outsole where there was a large enough area to use the durometer (SATRA STD 226 Digital Durometer). For measures OH, MH and IH, five repeat readings were taken at different locations across the width of the shoe (shown by dashed lines in Figure 8.2). TH was not taken at these five locations and was instead taken as the mean of eight readings from designated areas of the shoe outsoles, (shown in the previous chapter in Figure 7.1). FFW was taken as the width of the widest part of the forefoot. As all the shoes curved at the edges with different radii, FFW was measured as the width of the shoe that sat flat on the surface when unloaded. The contact area images in Chapter 7 showed that contact was always made at some point along the widest part of the shoe. Furthermore, biomechanics studies of tennis sliding movements have shown max pressures to occur at the medial forefoot, which is intersected by the line between the forefoot's widest points. As such, this area was deemed an area of interest, and was selected as the location by which shoes were compared by their OH, MH, IH and FFW. All length and height measurements were taken using digital callipers (6" Electronic SPI Calliper).

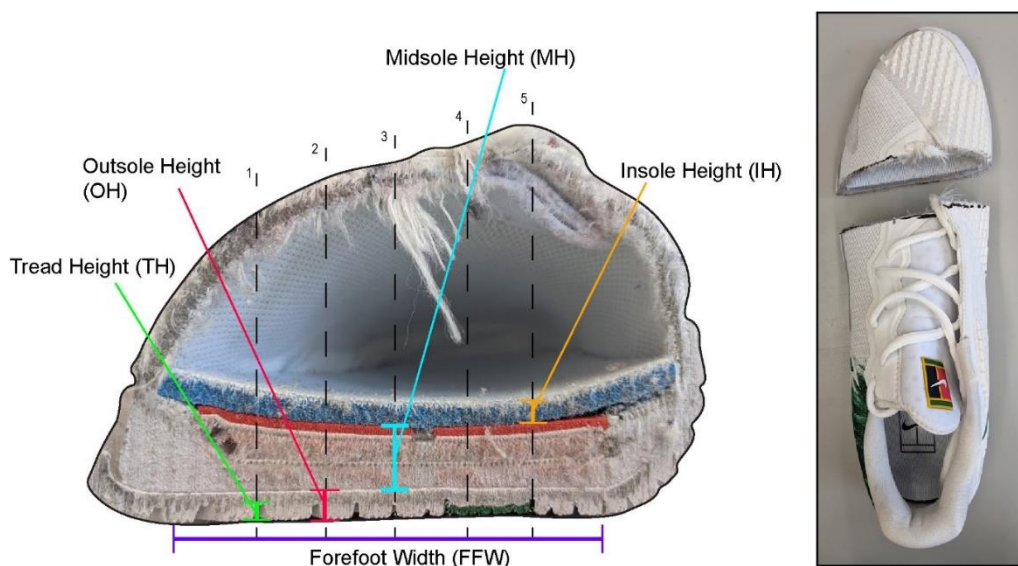


**Figure 8.2** How shoes were cut and measured. Measurements provided in Table 8.1.

The means of the measures taken are summarised in Table 8.1, with the makes and models of all eight shoes. In Table 8.1, MH is omitted for Shoe A as it had no separate midsole, and instead had a thicker outsole and insole. TH is omitted for Shoe H, as it was primarily flat, and had no tread to take heights from.

**Table 8.1** Measurements from eight tennis shoes. ShA = Shore A hardness, O = Outsole, M = Midsole, I = Insole, T = Tread, H = Height, FFW = Forefoot Width. All measures are a mean of five repeats, except for TH which is the mean of eight readings. Standard deviations shown in brackets.

| Label       | Make      | Model                     | Surface | O<br>ShA      | OH<br>(mm)   | MH<br>(mm)    | IH<br>(mm)   | FFW<br>(mm)  | TH<br>(mm)   |
|-------------|-----------|---------------------------|---------|---------------|--------------|---------------|--------------|--------------|--------------|
| A           | Decathlon | TS100                     | Multi   | 68.9<br>(1.3) | 7.3<br>(1.3) | -             | 6.4<br>(0.0) | 97           | 2.7<br>(0.0) |
| B           | adidas    | SoleCourt                 | Hard    | 77.8<br>(0.8) | 4.7<br>(0.6) | 11.1<br>(1.6) | 4.9<br>(0.2) | 114          | 2.3<br>(0.5) |
| C           | adidas    | Adizero<br>Ubersonic 2    | Hard    | 79.4<br>(1.0) | 3.8<br>(0.1) | 9.2<br>(1.4)  | 4.5<br>(0.3) | 101          | 2.2<br>(0.5) |
| D           | Nike      | Air Zoom Turbo<br>Sn12    | Hard    | 74.3<br>(2.1) | 5.5<br>(0.6) | 10.3<br>(0.6) | 5.5<br>(0.1) | 103          | 2.1<br>(0.7) |
| E           | Nike      | Air Zoom<br>Vapour Cage 4 | Hard    | 76.1<br>(1.0) | 5.1<br>(0.2) | 12.7<br>(1.1) | 4.6<br>(0.1) | 100          | 2.5<br>(0.5) |
| F           | Asics     | Gel Court<br>Speed        | Hard    | 76.3<br>(0.9) | 3.9<br>(0.7) | 9.2<br>(0.4)  | 4.9<br>(0.1) | 104          | 2.1<br>(0.3) |
| G           | Nike      | Prestige                  | Clay    | 75.3<br>(1.2) | 3.8<br>(0.0) | 9.5<br>(1.6)  | 4.9<br>(0.1) | 107          | 2.0<br>(0.1) |
| H           | Nike      | Prestige                  | Carpet  | 75.1<br>(1.5) | 4.6<br>(0.3) | 9.5<br>(1.3)  | 5.0<br>(0.1) | 105          | -            |
| <b>Mean</b> |           |                           |         | 75.4<br>(2.9) | 4.8<br>(1.1) | 10.2<br>(1.2) | 5.1<br>(0.6) | 104<br>(4.8) | 2.3<br>(0.2) |

These measures (Table 8.1) can assist in the interpretation of frictional differences between shoes. For example, if two shoes had similar tread patterns but produced dissimilar friction results, a measured difference in TH or another parameter may explain the difference in friction. Additionally, these measures provide tennis shoe designers with dimensions they can compare against.

### 8.2.2 Friction Experiments and Contact Imaging

The methodology was the same as that presented in Chapter 7 (with the same surface). The only difference was that for each shoe, only five orientations were tested (0°, 22.5°, 45°, 67.5°, 90°), with five repeats at each. This is compared to the nine orientations in the previous chapter, with seven repeats. The reduction in orientations, reduced overall testing time, while focusing on realistic slide orientations (sliding doesn't occur with the medial side of the shoe facing forward).

Contact images were obtained in the same way as previously described (Section 7.2.3). However, given the method limitations (Section 7.4.4) these images were only used to understand frictional differences in select scenarios, i.e. when comparing shoes of similar constructions, at the same orientation.

### 8.2.3 Statistical Analysis

A one-way ANOVA with Bonferroni post hoc test was used to determine whether there was a significant difference in the friction results of the eight tested shoes. This test was performed using IBM SPSS Statistics 26.

### 8.3 Results

All mean friction results for all orientations are shown in Figure 8.3. The shoe used in the friction tests had a significant effect ( $p < 0.05$ ) on  $\mu_k$  [ $F(7,192) = 15.10, p < 0.01$ ]. The highest overall  $\mu_k$  was recorded by Shoe D, a hard court design (1.25). The lowest mean  $\mu_k$  was recorded by Shoe A, a multi-surface shoe (0.92). As shown in Figure 8.3 it was not simply the case that one shoe produced the highest, or lowest friction at all orientations. At  $0^\circ$  Shoe E had the highest friction and Shoe A had the lowest friction. Whereas at  $45^\circ$  Shoe D had the highest friction and Shoe B had the lowest friction. If a tennis player likes to slide at a particular shoe orientation, a shoe with a low friction at that same orientation should be selected.

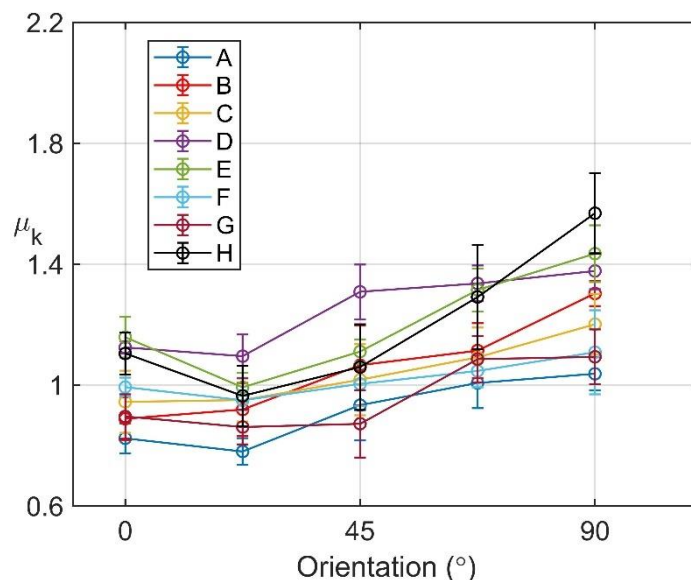


**Figure 8.3** Mean  $\mu_k$  results for all eight shoes. Error bars represent the standard deviation of the five repeats at each orientation.

The results of the Bonferroni tests are shown in Table 8.2 on the following page. Table values  $< 0.05$  indicate that the two shoes being compared produced significantly different  $\mu_k$  results.

**Table 8.2** Bonferroni post hoc results comparing the mean  $\mu_k$  of each shoe. Significance values below 0.05 are shown in green.

|   | Shoe    |       |         |         |         |         |         |         |
|---|---------|-------|---------|---------|---------|---------|---------|---------|
|   | A       | B     | C       | D       | E       | F       | G       | H       |
| A |         | 0.044 | 0.148   | < 0.001 | <0.001  | 0.553   | 1.000   | < 0.001 |
| B | 0.044   |       | 1.000   | 0.001   | 0.037   | 1.000   | 0.855   | 0.053   |
| C | 0.148   | 1.000 |         | < 0.001 | 0.010   | 1.000   | 1.000   | 0.014   |
| D | < 0.001 | 0.001 | < 0.001 |         | 1.000   | < 0.001 | < 0.001 | 1.000   |
| E | < 0.001 | 0.037 | 0.010   | 1.000   |         | 0.002   | < 0.001 | 1.000   |
| F | 0.553   | 1.000 | 1.000   | < 0.001 | 0.002   |         | 1.000   | 0.002   |
| G | 1.000   | 0.855 | 1.000   | < 0.001 | < 0.001 | 1.000   |         | < 0.001 |
| H | < 0.001 | 0.053 | 0.014   | 1.000   | 1.000   | 0.002   | < 0.001 |         |

Comparing means of all  $\mu_k$  readings for all shoes (Figure 8.4), Shoe A provided the lowest friction, shoes A, B, F and G generally produced medium friction, and shoes D, E and H generally provided a higher friction. Shoes G and H were the same model (Nike Prestige) and differed only in tread pattern. Shoe H produced a significantly ( $< 0.001$ ) higher  $\mu_k$  than Shoe G (+ 24.5%). Contact image analysis observed that this frictional difference occurs with a larger CA caused by the flat tread pattern of Shoe H. Figure 8.5 shows the dynamic contact images of Shoe G and Shoe H at 45° orientation. The shape of the contact patch is almost identical for both shoes, but the herringbone tread pattern on Shoe G provides the shoe with a smaller CA. Error bars are large as they consider all friction results from all orientations.

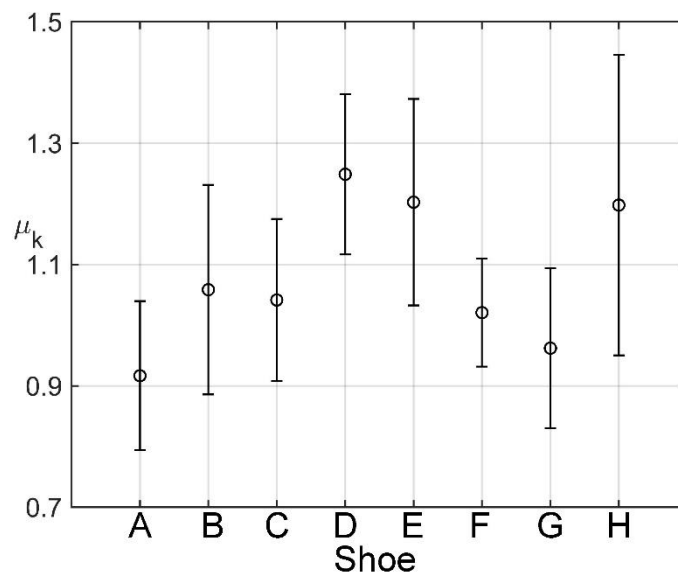


**Figure 8.4** Mean and standard deviation of all  $\mu_k$  readings for all shoes and orientations.

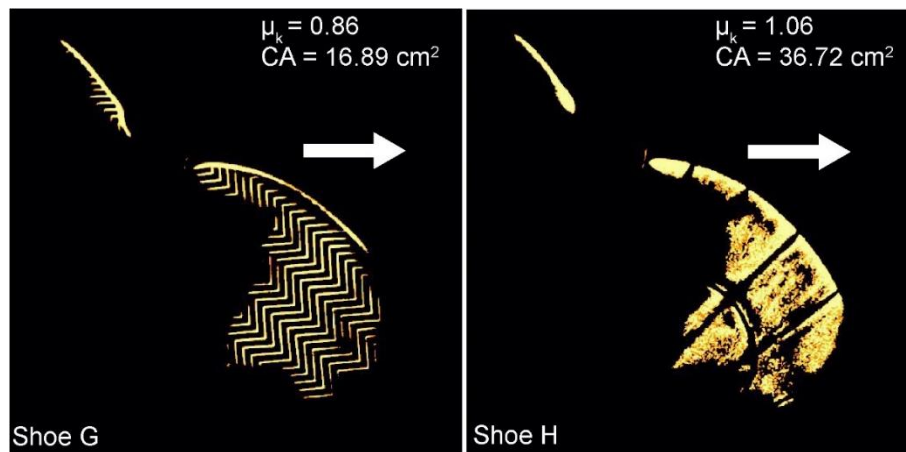


**Figure 8.5** Contact images of Shoe G and Shoe H at 45° slide orientation. These shoes were identical in their construction, except for their tread patterns.

In the previous chapter, an empirical friction model was suggested, which modelled the friction of a single tennis shoe tested at multiple orientations using three parameters: LE, CA and YT. These parameters were submitted to a linear regression model, to observe whether they can be used to model the friction of other tennis shoes on hard courts. As can be seen in Table 8.3, not only did the success of the resultant models vary greatly between shoes (R-Squared score ranged from 0.33 – 0.83), but the relationships between the model parameters and friction, also changed. For example, for shoes A and G the three parameters accounted for more variance in  $\mu_k$  when CA had a positive coefficient, and LE had a negative coefficient. Conversely, models for shoes B, E and H used negative coefficients for both CA and LE to explain variance in  $\mu_k$ . The content of Table 8.3 is based on how models describe  $\mu_k$ .

**Table 8.3** Coefficients and results of linear regression models used to model the  $\mu_k$  data for each of the eight shoes individually.

| Shoe | Coefficients |                       |          | Result      |           |
|------|--------------|-----------------------|----------|-------------|-----------|
|      | LE (mm)      | CA (mm <sup>2</sup> ) | YT (°)   | y-intercept | R-Squared |
| A    | -5.22e-4     | 1.38e-4               | -6.05e-3 | 1.23        | 0.33      |
| B    | -2.85e-4     | -1.01e-3              | 4.35e-3  | 2.67        | 0.77      |
| C    | 8.68e-4      | -1.28e-3              | 7.86e-3  | 1.60        | 0.53      |
| D    | 3.23e-4      | -3.12e-4              | 1.41e-3  | 1.51        | 0.73      |
| E    | -1.13e-3     | -2.94e-4              | 3.96e-3  | 2.07        | 0.83      |
| F    | 2.28e-3      | -9.94e-5              | 4.21e-3  | 0.24        | 0.37      |
| G    | -8.94e-4     | 8.50e-4               | 5.01e-3  | -0.03       | 0.59      |
| H    | -2.56e-3     | -4.49e-5              | -3.77e-3 | 2.54        | 0.76      |

## 8.4 Discussion

There were noticeable similarities and differences in the constructions of the eight tennis shoes. The similarities were:

- **Outsole Shore A Hardness** – The SD of the Shore A hardness means for all the shoes was 2.9. By omitting Shoe A (the only shoe that used a single rubber with no separate midsole material) the SD was reduced to 1.6. This similarity in outsole rubber hardness indicates similar grades of rubber being used. To confirm this, DMA could be conducted on samples of each outsole rubber, identifying which outsoles will generate greater hysteresis. However, prismatic samples of the required dimensions (30 mm × 10 mm × 10 mm) could not be cut from the outsoles, and manufacturers would not provide them.
- **Component Heights** – Omitting Shoe A, the OH, MH, IH, and TH SDs for all shoes were 0.6 mm, 1.2 mm, 0.3 mm and 0.2 mm, respectively. Why similar dimensions were adopted by all the represented manufacturers is unclear. It is especially unusual for all the shoes to have similar heights when their midsole constructions were so varied.

Noticeable differences in tennis shoe design were:

- **Midsole Construction** – Except for maybe tread pattern, the greatest observable difference between the eight tennis shoes tested, were their midsole constructions. To visualise this, the cross-section of Shoe B and D are provided in Figure 8.6. Shoe B had a dual midsole component - consisting of “Boost” (low hardness (ShA = 17.9) polyurethane) and a harder material (ShA = 31.2) likely to be Ethylene-Vinyl Acetate (EVA). The midsole of Shoe D consisted of a thin layer of an EVA-like material (ShA = 40.1), a stiff plastic plate, and a compressed airbag filled with fibres. These contrasting midsoles will result in contrasting energy losses when loaded and unloaded.

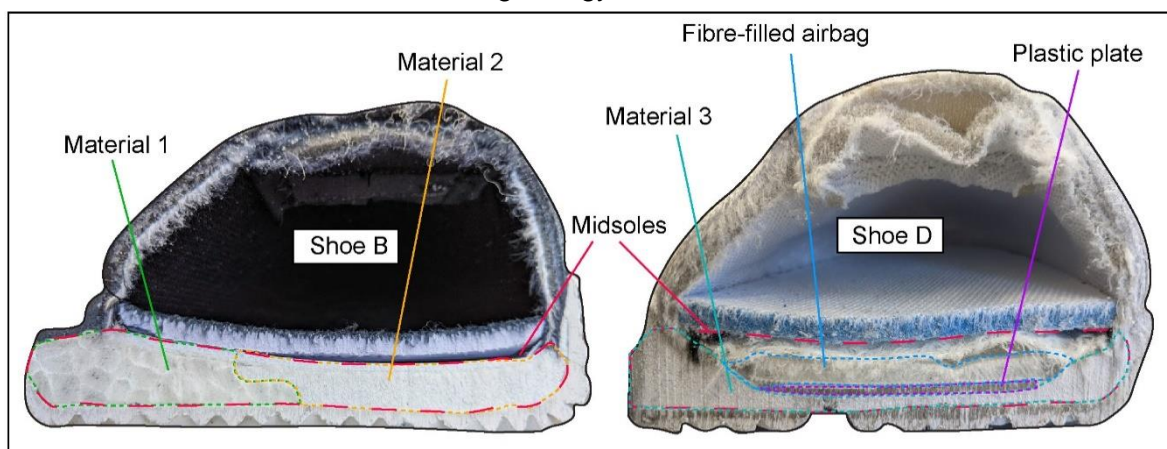


**Figure 8.6** Cross-sections of two hard court tennis shoes.

- Tread Pattern** – Six out of the eight tennis shoes tested, had aspects of the herringbone tread pattern. The only shoe treads not to visually resemble the herringbone pattern were Shoe E and Shoe H (the shoe designed for use on a carpet court). Why the herringbone pattern is so popular on tennis shoes, and other sports shoes, is still yet to be explained. The only published study that compares the herringbone tread pattern against other designs (flat and concentric circles) is that by Valiant, who observed that on an indoor basketball court, the herringbone design had a lower friction than the other two designs [60]. Therefore, herringbone may be used to reduce shoe-surface friction, which would make sliding easier, and reduce the chance of overuse injuries.

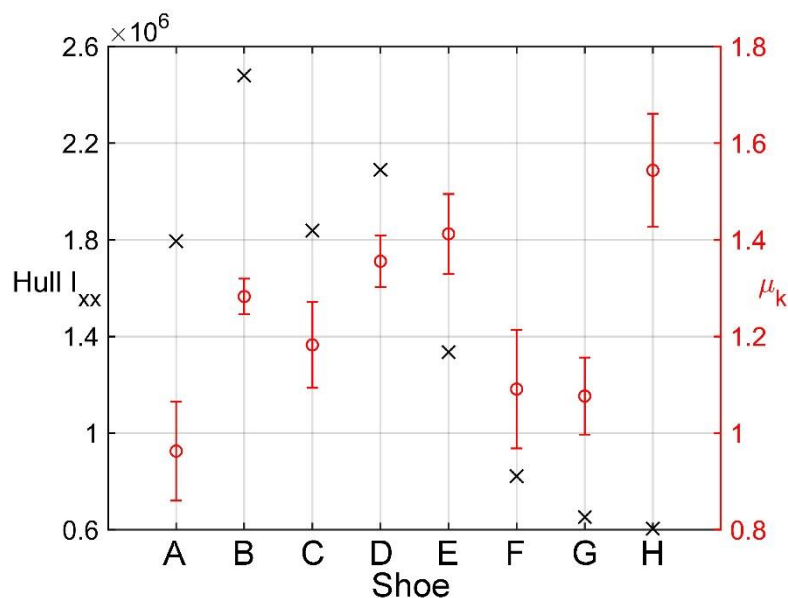


**Figure 8.7** The Hull  $I_{xx}$  and mean  $\mu_k$  of all shoes at the 90° test orientation. The error bars on  $\mu_k$  data are the SDs of five tests.

- Forefoot Width (FFW)** –The standard deviation in FFW was 4.8 mm. The shoe with the widest FFW was Shoe B, pictured in Figure 8.6. Shoe B’s width was increased by a lip to the lateral side of the shoe, which increased FFW. This feature was only present on Shoe B. The lip widened the contact patch during sliding at 90°. Hull  $I_{xx}$  is a parameter calculated during contact analysis, which determined the second moment of area in the sliding direction ( $I_{xx}$ ) for the smallest convex polygon that surrounded tread contact pixels in the input (hull). Figure 8.7 shows that Shoe B had the largest Hull  $I_{xx}$  due to the additional lateral lip. Figure 8.7 also shows that the current study is unable to determine how an increase in Hull  $I_{xx}$  influences friction. Shoes of identical manufacture would be needed, with varying widths of additional lips, to determine the influence of increasing Hull  $I_{xx}$ . The increased Hull  $I_{xx}$  are likely to increase friction by

increasing CA, reducing contact pressures. Shoe H is shown to have the lowest Hull  $I_{xx}$ , but the highest  $\mu_k$ . This is because Shoe H had no tread, producing the highest CA and therefore friction.

The use of a different tennis shoe can have a significant effect on the friction measured by the test device. It is therefore likely that they will provide a tennis player with different levels of friction during play. Even with contact area analysis and shoe dimensions, it is unclear why some shoes produce higher friction than others. To achieve this understanding, a series of experiments are needed where a matrix of testing is conducted on shoes that vary by only one feature at a time. This would allow the isolation of features to determine their frictional influence. This project was unable to find a shoe manufacturer to provide these prototypes. Hence, the influence of tread features could not be conclusively determined. Nevertheless, Shoes G and H were the same model and differed only by their tread pattern. Shoe G had a herringbone design and Shoe H had a flat outsole. The flat outsole produced the higher friction due to the higher contact area.

Shoe G was a clay court shoe; Shoe H was a carpet shoe. Across all orientations, Shoe G produced the second lowest friction of all the tested shoes, and Shoe H produced the second highest friction. Shoe G produced friction results not significantly different to four hard court shoes (A, B, C, F), and Shoe H produced friction results not significantly different to three hard court shoes (B, D, E).

## 8.5 Conclusion

Different tennis shoes can produce significantly different friction results on hard courts. Without experiments using controlled shoe designs, the influence of specific design features can't be quantified. In a single case however, shoes varying by tread pattern alone (G and H) showed that an increase in CA produced an increase in friction (Figure 8.5). Other than this case, the method detailed in this chapter cannot identify the tread parameters that influence friction. Studies need to be conducted on bespoke footwear designs, which vary only in tread design, to further identify and quantify the influence of the tread design parameters measured in this thesis (LE, CA, Hull  $I_{xx}$  etc.).

This study observed that the friction of a clay (G) and a carpet shoe (H) on a hard court, was not significantly different to that of hard court shoes (A – F). Though the carpet shoe produced a significantly higher friction than the clay court shoe of the same model, showing that tread pattern does influence friction.

Across the eight tennis shoes tested, many differences in midsole constructions were seen, though features such as midsole height and tread heights were consistent across all designs.

There is no published evidence that suggests a tread height of 2.3 mm improves performance, or that a midsole height of 10.2 mm is desirable. It is assumed that these parameters are simply imitated from rival products with little rationale, or it indicates protected information on the subject which is known by manufacturers. Future research could investigate how controlled changes in these parameters influence friction, as well as player comfort.

This chapter provided a frictional comparison of eight tennis shoes on a dry hard court. Significant difference was observed between the shoes, and although no shoe characteristic can be conclusively linked to friction, initial evidence suggests an increase in CA results in an increase in friction. As such, if a designer intends to increase the friction of a shoe, altering the tread pattern to produce a higher CA is suggested. This could be achieved by widening the contacting areas of tread patterns.

This chapter concludes the experiments presented in this thesis. The following chapter details the design of a test device, the manufacture of which is considered future work. Following Chapter 9, a final thesis discussion is provided in Chapter 10.

## 9 Novel Tennis Shoe Friction Device – Design and Development

Chapters 4 – 7 detail a series of tribological experiments that investigate shoe-surface friction on dry hard courts. It is however realised, that although representative normal loads and contact pressures have in some cases been achieved, observed hard court slide linear speeds have not yet been tested. This was due to the mechanical limitation of current test devices.

This current chapter describes the product design process utilised to ensure the design of a test device which closer replicates such speeds and thus hard court slides generally. In future work, this device should be manufactured and used to better understand shoe-surface tribology during hard court slides.

### 9.1 Product Design Process

The Product Design Process (PDP) is a complex and iterative process which becomes bespoke to each design project. Selecting a generic geometric model, such as that shown in Figure 9.1, provides guidance to the design process, but will ultimately be modified based on the constraints specific to the project at hand.

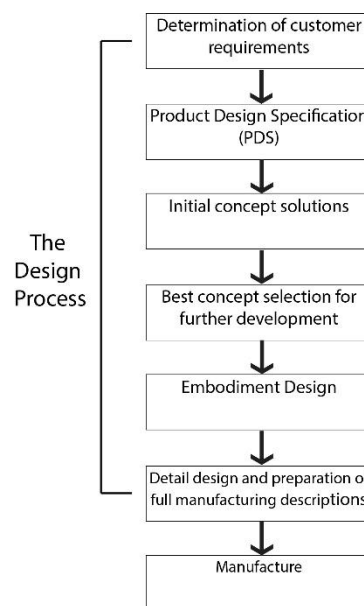


**Figure 9.1** The French product design process.

Almost all PDP models are loosely based on the basic linear model attributed to French shown in Figure 9.1 [105]. This model details a series of six steps that make up the PDP from determining customer requirements to explicitly detailing a design of a chosen concept. In real terms this process is never completely linear [106]. More detailed PDP models such as the

VDI 2206 guideline and Pugh's model [107] involve numerous feedback loops and verifications as the design manifests itself. Both of these models are shown in Figure 9.2.

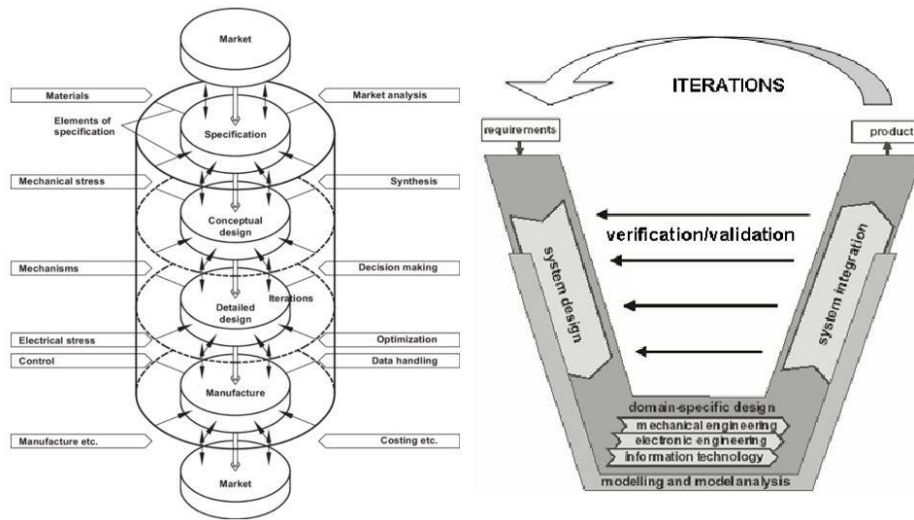


**Figure 9.2** The Pugh total design process (left) [111] and the VDI 2206 model (right) [112].

To design a shoe-surface friction test device, a bespoke PDP was created. This PDP was an adaption of the Pugh total design process and accounted for all the facets of the project (Figure 9.3).

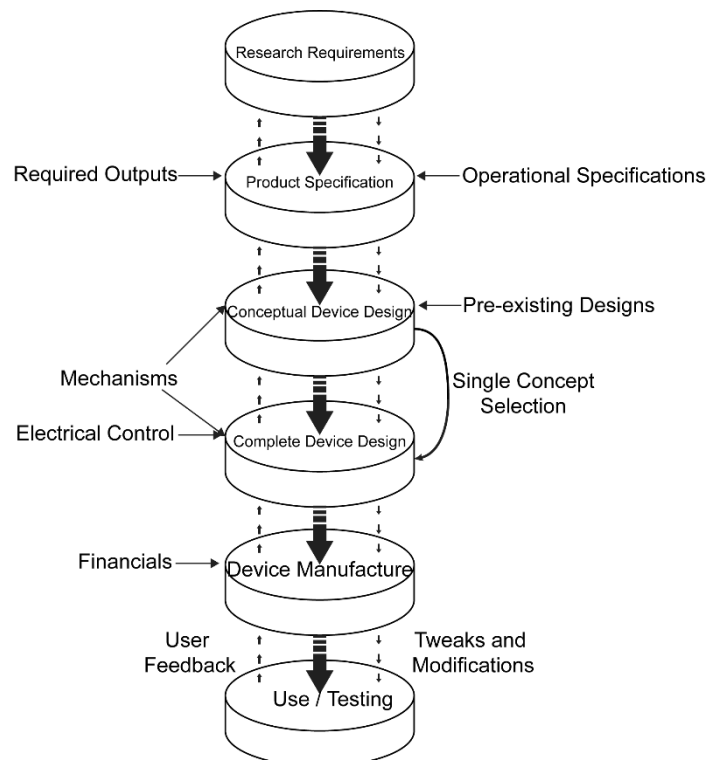


**Figure 9.3** Adapted Pugh PDP model used to design a tennis shoe-surface friction test device.

The PDP shown in Figure 9.3 was progressively worked through for the duration of this chapter.

## 9.2 Research Requirements

This section in the PDP model (Figure 9.3) relates to the questions that needed to be answered by the device, and what parameters must be controlled to achieve this. Determining the specific research requirements for a test device can be difficult and time consuming, as an in-depth understanding of the research field is required to ensure the developed device is not misinformed in its nature. The primary requirement of the device was to provide a means of differentiating tennis shoes based on their frictional performance during a slide. This could be achieved by outputting  $\mu_s$ ,  $\mu_k$  or both.

The previous chapters of this thesis highlight the multitude of parameters by which the friction between tennis shoes and hard court surfaces could be affected. Some of these are collated in Table 9.1.

**Table 9.1** Parameters that affect friction and how, including estimated values for hard court slides.

| Parameter         | How they affect friction  | Value for hard court tennis slides                                       |
|-------------------|---|--|
| Slide Speed       | Vary amount of frictional heat and hysteresis   | 2.8 – 4.7 m/s [71]   |
| Normal Load       | Influences amount of wear. $\mu$ often decreases with increased normal load                                 | 300 - 500 N<br>Estimated Calc. from [9]                                  |
| Surface Roughness | Influence the hysteresis, wear, frictional heating, and real area of contact                                | $R_a = 72 \mu\text{m}$ , $R_q = 91 \mu\text{m}$<br>See PSD in Figure 3.8 |
| Contact Motion    | If normal load is applied before horizontal, an increase in static contact time will result in higher $\mu$ | Application of horizontal and normal loads are simultaneous              |

Table 9.1 does not include parameters such as rubber material characteristics or rubber shape, as these are attributes of the tennis shoes themselves, and will not be determined by the test device used to test them.

To test the friction of tennis shoes in a repeatable and valid way, the parameters outlined in Table must not only be controlled, but also be similar to the values observed for real tennis slides in hard court tennis.

### 9.3 Product Specification

Table 9.2 outlines the overall product specification of the proposed device. “Demand/Wish” and “Limit” columns were included to provide understanding as to how much flexibility there was in each specification.

**Table 9.2** Overall product specification of the proposed device. Demand/Wish and Limit columns are included to provide understanding as to how much flexibility there is in each specification.

| Overall product specification   | Demand / Wish | Limit  |
|---|---------------|--|
| Easy operation  | W             | Can be operated by a single person with an hour of training.   |
| Measure shoe-surface friction   | D             | Can determine which shoes allow easier hard court sliding.   |
| Replicate hard court tennis slide normal loads and contact pressure distributions | D             | Apply a normal force large enough to produce realistic contact pressures (21 – 43 kPa) with the max pressure on the medial forefoot. |
| Replicate hard court tennis slide speed at impact                                 | D             | The relative speed between shoe and surface to be between 2 – 3 m/s at point of impact   |
| Replicate sliding speed   | D             | Average sliding speed $\approx$ 2-3 m/s  |
| Replicate slide distance  | D             | Slide lasts for a distance between 0.3 -0.7 m.   |
| Test full shoes without need for modifications                                    | D             | A full shoe can fit in the device and be tested.   |
| Shoes easily attached and removed   | D             | Shoes can be attached and detached by lacing and unlacing.   |
| Used in a laboratory  | D             | Electrical components are PAT tested and a Risk Assessment complete.   |
| Low wearing surface   | W             | Reusable surface after cleaning process following each test.   |
| Repeatable outputs  | D             | Low unsystematic measurement error.  |
| Reliable outputs  | D             | Repeating the same test gives the same result.   |

The most difficult part of the device design is ensuring the tennis slide conditions can all be achieved. To determine how these loads, distances and speeds can be generated mechanically, Table 9.3 has been formulated. This table includes a cost column to further differentiate the suitability of certain methods. In summary of Table 9.3, it could be perceived that the weights (in combination with pulleys) are the best way to generate the desired characteristics in the device. However, as is mentioned within the table, this method of applying forces and incurring speeds, would require a significant amount of weight (120 kg). This amount of weight seems unnecessary when other lightweight systems were available (e.g. linear actuators).

**Table 9.3** How four different mechanisms address the requirements of tennis slide test device.

| <b>Mechanism</b>           | <b>Normal Force</b>                         | <b>Shear Load</b>                                  | <b>Slide Speed</b>                                    | <b>Slide Distance</b>                                   | <b>Cost/Availability</b> | <b>Notes</b>  |
|----------------------------|---|--|---|---|--------------------------|---|
| Weight                     | Controlled normal load.<br>(36 kg / 350 N)  | Requires horizontal pulley.<br>(61 kg / 600 N)     | Estimated using SUVAT equations.<br>( $\leq 3.5$ m/s) | Determined by height of weight from floor ( $\leq 1$ m) | £50 - £200               | Known force and speed.<br>Very heavy (> 100 kg).    |
| Pneumatic Cylinder         | Can achieve normal load<br>( $\leq 2000$ N) | Horizontal or angled cylinder.<br>( $\leq 2000$ N) | $\leq 0.8$ m/s with exhaust valves.                   | Depends on stroke length<br>( $\leq 0.5$ m).            | £70 - £300               | Versatile but not capable of required slide speeds. |
| Electronic Linear Actuator | Cannot provide normal force.                | $\leq 5000$ N                                      | $\leq 5$ m/s  | $\leq 2$ m  | £3k - £6k                | Can achieve slide speed but not normal load.        |
| Instron Machine            | $\geq 591$ N                                | Pulley needed for shear<br>( $\geq 591$ N).        | Not speed controlled<br>( $\leq 0.01$ m/s).           | $\leq 1$ m  | £10k - £20k +            | No speed control, and expensive.                    |

## 9.4 Conceptual Device Design

Following the identification of the required test device specifications, and the potential equipment that could be used to meet these specifications, concept drawings were produced (Figure 9.4). These concepts took inspiration from the pre-existing designs described in Section 2.3.1. Through the sketching process, an understanding was developed of how the mechanisms in Table 9.3 could be utilised in combination with one another to produce the desired tennis slide conditions.

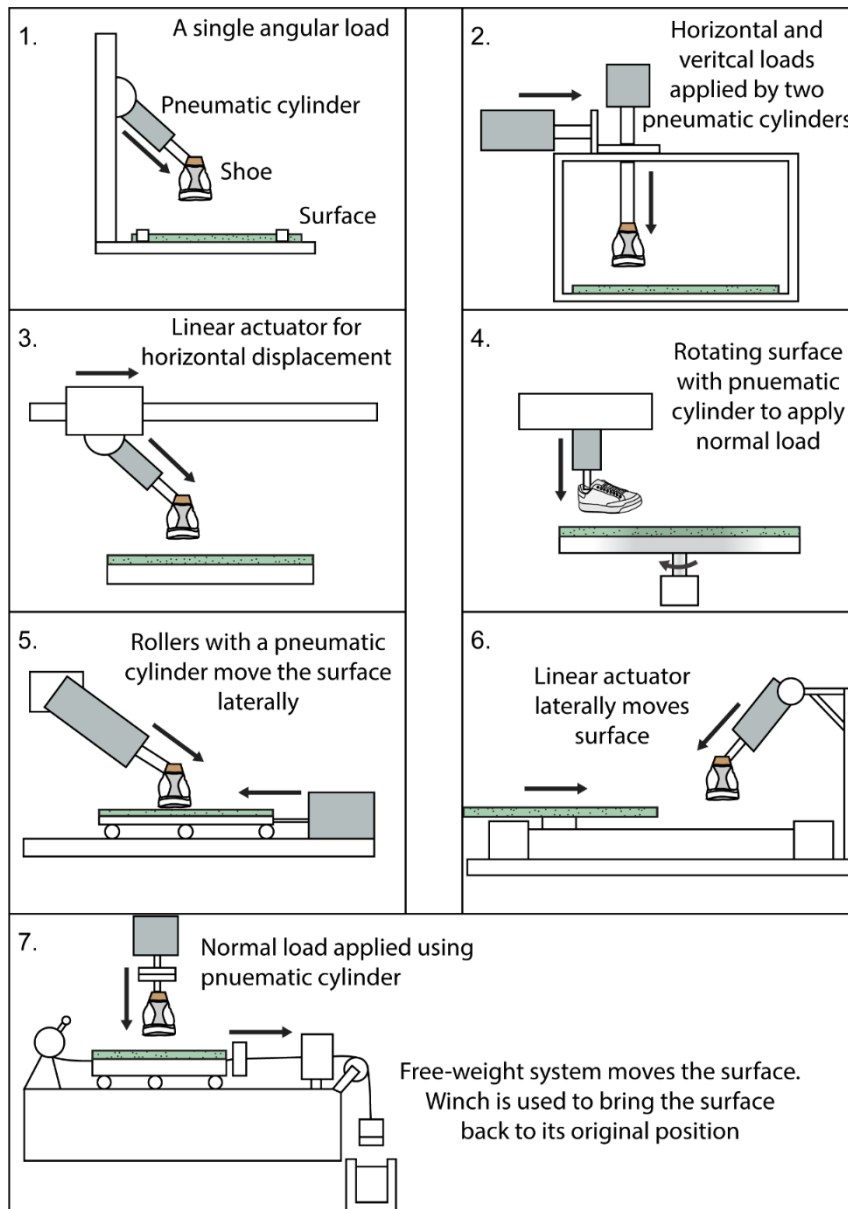


**Figure 9.4** Seven initial concept sketches of the proposed test device.

On the following pages, brief descriptions are provided to accompany the concepts depicted in Figure 9.4.

**Concept 1** – This concept uses an L-shaped structure, holding a stationary surface on the horizontal, and attaching a pneumatic cylinder to the vertical. When initiated, the pneumatic cylinder applies a force to a last which has a shoe attached to it. The shoe will then impact the surface and if a slide does not occur, the angle can be adjusted until the shoe slides. When a slide occurs,  $\mu_s$  can be determined. This design is inspired by the TSST (Ura, 2016). It only differs by orientation of the shoe, and the increase in size needed to accommodate a full shoe.

**Concept 2** – Here the surface is again kept stationary, while separate vertical and horizontal forces are applied to the shoe allowing it to slide. Knowing both force components from stationary to the end of a slide, both  $\mu_s$  and  $\mu_k$  can be extracted. This design takes inspiration from the UoS Traction Device.

**Concept 3** – Two rails are attached to the top of a pneumatic cylinder with a shoe attached to the end of a pneumatic cylinder. The shoe-cylinder unit is moved parallel to the test surface using a linear actuator which attaches to the slider on rails. This supplies horizontal sliding speed. The pneumatic cylinder actuates to apply normal load.

**Concept 4** – An electrical motor rotates a circular surface. When the speed of the surface is equal to what is desired, the pneumatic cylinder applies a normal load to the shoe to contact the rotating surface.

**Concept 5** – Both shoe and surface move in this configuration. A pneumatic cylinder moves the surface in one direction while another pushes the shoe in the opposite direction at an angle to ensure the shoe contacts the moving surface. Load cells attached to both cylinders would ensure all forces can be accurately measured and therefore coefficients of friction can be determined.

**Concept 6** – Similar to Concept 3 but replaces the horizontal pneumatic cylinder with a belt driven electronic linear actuator to move the surface at higher speeds.

**Concept 7** – A mass is attached to the end of a cable which connects to the surface which is on wheels or a low friction surface. A fixed pneumatic cylinder applies normal load to the shoe which impacts the surface when the speed of the surface is in the desirable range.

## 9.5 Concept Evaluation and Selection

To select the concept that was put forward to the Complete Device Design part of the PDP, all concepts were critically assessed. Following this evaluation process, Concept 6 was taken forward with some modifications. Table 9.4 provides some reasoning as to Concept 6's selection by outlining the positives and negatives of each concept.

**Table 9.4** Positives and reasons for deselection of initial concepts.

| Concept | Positives   | Reasons for Deselection   |
|---------|---|---|
| 1       | <ul style="list-style-type: none"> <li>- Simple construction</li> <li>- Financially inexpensive</li> <li>- Easy to determine <math>\mu_s</math></li> <li>- Applies force at an angle comparable to real tennis situations</li> </ul>                  | <ul style="list-style-type: none"> <li>- Cannot achieve desired impact speeds</li> <li>- Cannot determine <math>\mu_k</math></li> </ul>                     |
| 2       | <ul style="list-style-type: none"> <li>- Complete control of horizontal and normal force</li> <li>- Can easily determine both <math>\mu_s</math> and <math>\mu_k</math></li> </ul>  | <ul style="list-style-type: none"> <li>- Cannot achieve desired speeds</li> </ul>   |
| 3       | <ul style="list-style-type: none"> <li>- If timed correctly, correct speeds and forces could be produced at a correct angle</li> </ul>  | <ul style="list-style-type: none"> <li>- May have issues with rigidity and integrity of the suspended rails when shoe contacts surface</li> </ul>           |
| 4       | <ul style="list-style-type: none"> <li>- Can easily achieve and control desired sliding speeds</li> <li>- Normal force can be easily controlled and depending on set-up both <math>\mu_s</math> and <math>\mu_k</math> could be outputted</li> </ul>  | <ul style="list-style-type: none"> <li>- Would require production of circular tennis court surfaces</li> <li>- Does not replicate a linear slide</li> </ul> |
| 5       | <ul style="list-style-type: none"> <li>- Easy to extract horizontal and normal load</li> </ul>  | <ul style="list-style-type: none"> <li>- Speed of the pneumatic cylinders is too small</li> </ul>   |
| 6       | <ul style="list-style-type: none"> <li>- Can achieve slide speeds</li> <li>- Can achieve desired normal loads</li> <li>- Can achieve slide distances</li> <li>- Linear actuator bending stresses will be reduced by support from the floor</li> </ul> |   |
| 7       | <ul style="list-style-type: none"> <li>- Can achieve slide speeds</li> <li>- Can achieve desired normal loads</li> <li>- Can achieve slide distances</li> </ul>   | <ul style="list-style-type: none"> <li>- Difficult to return the surface to its initial position</li> <li>- Heavy</li> </ul>                                |

## 9.6 Complete Device Design

Selecting Concept 6, the concept design was further developed. A more detailed illustration of the concept was produced and is shown in Figure 9.5.

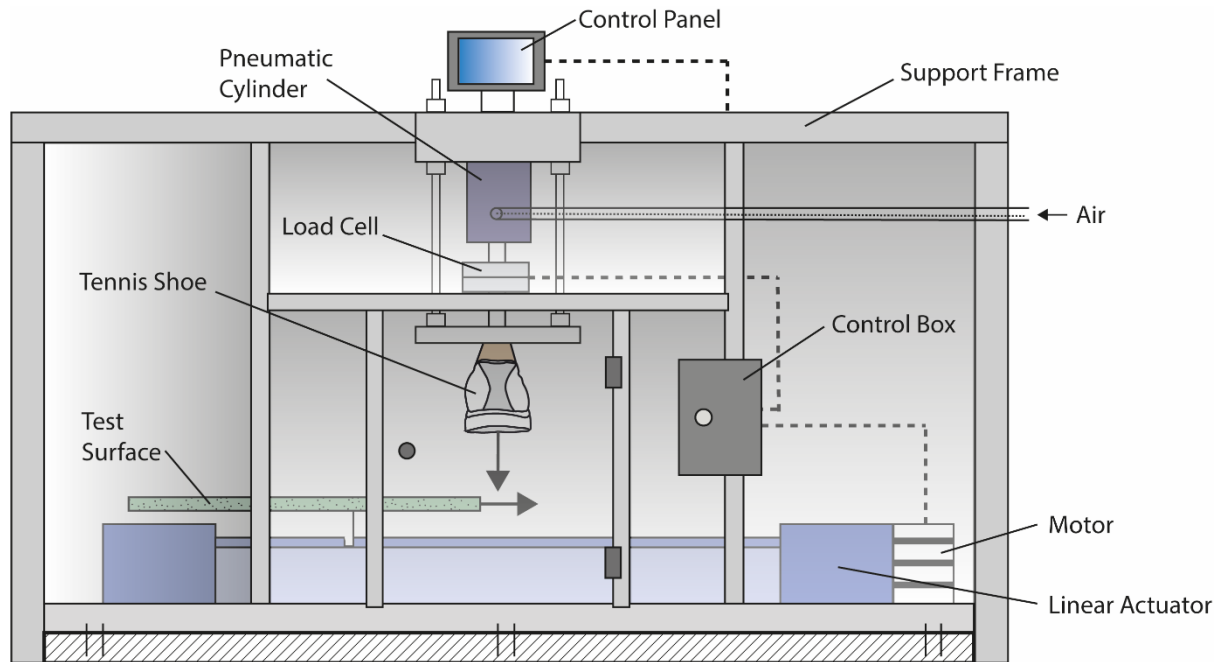


**Figure 9.5** Detailed illustration of the chosen test device concept.

The most noticeable modification, from the concept stage, is a support frame with plastic panels that encapsulate the design. This was added to adhere to the health and safety regulations in the laboratory where it would be placed. Additionally, the angle of the pneumatic cylinder to which the tennis shoe is fitted, is now vertical, as opposed to being angled. This modification to the initial sketch was made to simplify the outputs of the device. In the new vertical set-up, the slide speed is controlled solely by the linear actuator to which the surface is attached. This means that it can be easily set and outputted with little additional calculation. In comparison, the previous angled set-up would have required a measurement of the pneumatic cylinder speed as this would influence the overall relative speed between both shoe and surface.

Another component shown in Figure 9.5, that is not shown in the initial sketch of Concept 6 is the load cell positioned between the shoe last and the pneumatic cylinder. This bi-axial load cell will, determine the frictional and normal forces in the contact, yielding both  $\mu_s$  and  $\mu_k$ . This addresses some of the problems observed in Chapter 8, as any variance in normal load would be measured.

## 9.7 Device Manufacture

The finalised concept design was discussed with technical staff at the university, and a SolidWorks computer model was created, and parts were sourced. It was determined that to complete the build of the device, additional funding was required. This funding was initially granted before being retracted given the uncertainty caused as a result of COVID-19 and the subsequent lockdown in the UK and abroad. As such, it was decided the device could not be manufactured within the timeline of this PhD. Instead, the design process was completed, and the manufacture of the device would begin once funds were available, potentially in future projects, separate from this PhD study.

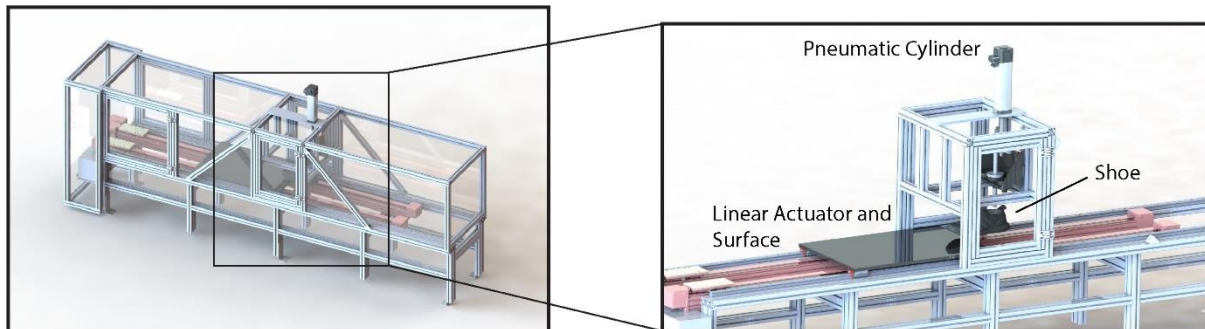


**Figure 9.6** CAD of the full test device with a focus on the device's main components.

The SolidWorks model shown in Figure 9.6 depicts the finalised design. Although the device cannot be built and used within this project, the outputs can be partially simulated.

## 9.8 Device Output Simulation and Interpretation

As the design of the device was completed, outputs could be predicted. This was of benefit, as it allowed the development of data analysis programs that can be used to interpret the data output by the device once built, without waiting for the build itself.

The first step in achieving this was by the identification of the inputs that will control the device, and the available outputs. Figure 9.7 shows a flow chart of the inputs and outputs from the finalised device design.



**Figure 9.7** Horizontal flow-chart of inputs and outputs from proposed test device.

The two inputs shown in the Figure 9.7, are the user-selected slide speed and the user selected normal force. These would be defined by the user prior to initiating the test device.

Inputs:

- (1) Slide Speed – This parameter is specified by the user to the control of the linear actuator. This value has a range of 0 – 2.3 m/s and has an acceleration/deceleration rate of 3.5 m/s<sup>2</sup> (controlled by the actuator specification). Once the target speed is achieved, a feedback loop ensures this speed is maintained.
- (2) Normal Force – Unlike slide speed, normal force is not applied directly. Instead, a pneumatic cylinder pressure would be selected by the user, which corresponds to a normal force. The relationship between normal force ( $N$ ) and pneumatic cylinder pressure ( $p$ ) is shown in Equation 9.1. As shown, the resultant normal force from the cylinder air pressure depends on the piston diameter ( $d$ ) which is 50 mm in the present case.

$$N = p\pi\left(\frac{d^2}{4}\right)$$

**Equation 9.1**

Knowing the piston diameter and the working range of air pressures, the normal force vs air pressure line can be plotted (Figure 9.8). When the user wants to set a normal load to test at, they must consult this plot and manually set the corresponding air pressure.

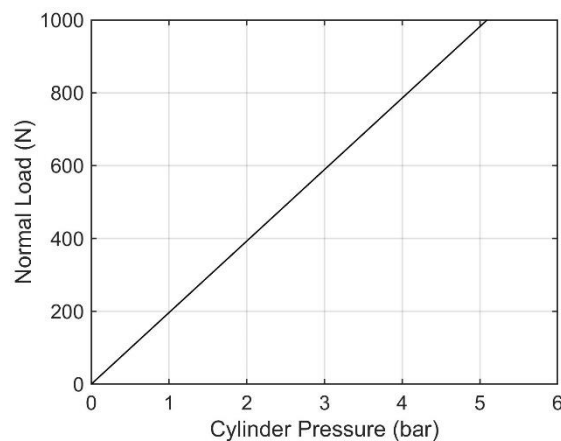


**Figure 9.8** When the user chooses a normal load to apply to the shoe, the corresponding air pressure must be selected.

When the user has set their inputs, the device control system must ensure that the pneumatic cylinder is initiated at the time which will ensure maximal slide distance between shoe and surface. This involves predicting the time at which the fast moving surface will be beneath the shoe. If the vertical cylinder is initiated too early, the moving surface will collide with the shoe,

causing damage to the device. Contrarily, if the cylinder is initiated too late, it will miss the surface and no friction readings will be output. These timings will inevitably change as the linear slide speed is changed and the device must automatically adjust the cylinder initiation times in accordance with these. Figure 9.9 shows three sets of example linear actuator speed and displacement traces, with input speeds of 0.5, 1 and 2.3 m/s.

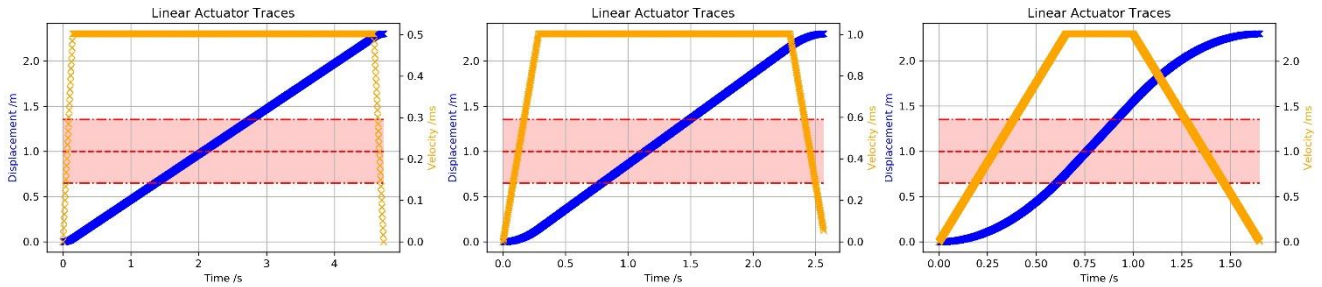


**Figure 9.9** Surface speed and displacement plots for selected surface speeds of 0.5 (left), 1 (middle) and 2.3 m/s (right).

The time at which the displacement curve (blue) enters the shaded red region, is the time at which the surface is beneath the shoe and initiation is safe to occur. When this blue trace leaves the red shaded area is when the surface is no longer underneath the shoe, and the shoe must be retracted. To run these simulations, a surface length of 0.7 m was assumed. For the max speed of 2.3 m/s, contact will be made for less than 0.5 s. As such, it is critical this timing is exact.

When contact is made between shoe and surface, there will be an initial spike in the frictional force trace which will quickly drop and level to a relatively constant value for the rest of the slide. This point will be located in post-hoc analysis using peak finding techniques and will be used with the normal load at that same timeframe to determine the  $\mu_s$ . The friction force values following this peak, and before the end of contact, will be divided by the normal load and summed to give the  $\mu_k$ . Equation 9.2 and 9.3 will be used to conduct these calculations.

$$\mu_s = \frac{F_{peak}}{N_{peak}}$$

**Equation 9.2**

$$\mu_k = \sum_{i=peak+1}^n \frac{F_i}{N_i}$$

**Equation 9.3**

Where  $n$  is equal to the number of data points between the friction force peak and when contact finishes. Assuming a load cell of 1 kHz capture rate, this would mean around 500 data points would be used in the  $\mu_k$  calculations at the max slide speed of 2.3 m/s.

In isolation it is easy to simulate the speed vs time and normal load vs time traces. However, as you consider the interaction between the linear actuator and the pneumatic cylinder, simulation becomes more difficult. The applied normal load and the  $\mu$  between the shoe and surface will on impact, affect the surface speed applied by the linear actuator before the control system can achieve the desired speed. A similar process will also occur as the shoe is retracted from the surface. However, initiating and retracting the test shoe based on the method described above, will ensure in all cases that the shoe contacts the surface and is retracted in time.

Figure 9.10 breaks the running of the test device into four key stages.

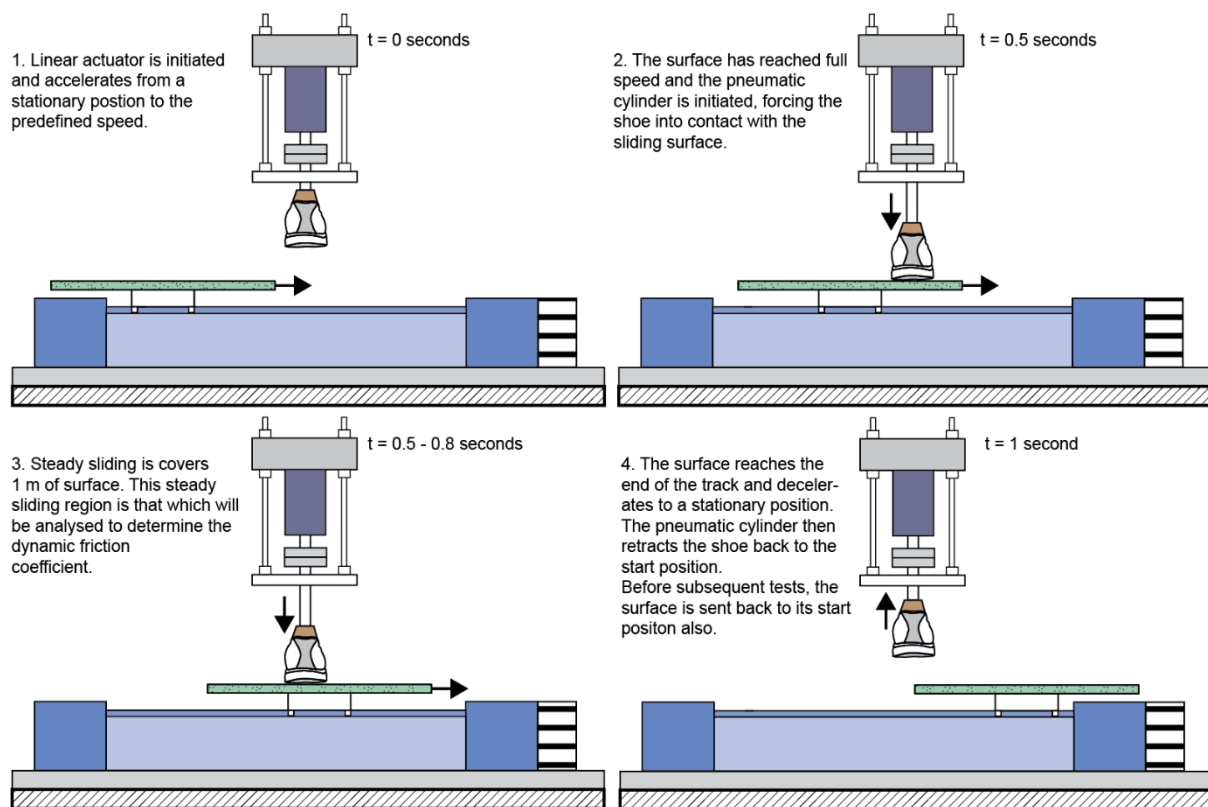


Figure 9.10 Schematics of the key stages in the running of the test rig.

### 9.9 Device Limitations and Conclusion

The proposed device outlined in this chapter can test the friction of full tennis shoes under normal loads replicative of those expected during hard court slide movements. Slide distances and contact times are comparable to those seen in professional tennis, though the speed is still below the target speed range.

The high speeds of hard court slides are very difficult to replicate mechanically - the principal challenge when designing such a device. It is deemed that a speed of 2.3 m/s (0.5 m/s slower than that measured from professional slides) is as fast as is currently feasible for a mechanical test device. Going above this speed towards the range of 2.8 – 4.7 m/s would require actuators of much greater expense, with longer rails and surface samples. Without these, a combination of two actuators (moving the shoe and the surface in opposing directions) would be necessary to create a great enough relative slide speed. This second approach would impose more complex control systems to ensure the shoe and surface impact each other at the correct points at different selected speeds.

The device proposed here better replicates the shoe-surface tribological conditions of hard court slides than any known test device. It is expected that in future projects this device will be manufactured and used to test and compare the frictional performance of tennis shoes.

## 10 Discussion

The main aim of this thesis (described in full in Section 1.1) was as follows:

*“To improve the overall understanding of rubber tribology during sliding on dry surfaces, and then apply this knowledge to the case of tennis shoe friction on hard court surfaces.”*

To show how this aim was achieved, the key outcomes of each chapter are provided below.

### 10.1 Key Outcomes

Previous research into shoe-surface friction largely ignored the findings of fundamental rubber tribology studies. Though it is typical for a statement like “rubber has a hysteretic contribution to friction” to be followed by a citation to Persson’s theory of viscoelastic friction, little more tribological theory is usually applied to shoe friction studies. The Persson and HK rubber friction models characterise rubber with viscoelastic master curves, and surfaces with PSDs. Most shoe friction studies however, use Shore A hardness and single value roughness measures ( $R_a, R_q$  etc.) [73,77,108,109]. These choices hinder the understanding of shoe-surface friction mechanisms. Chapter 3 details how these measures can be obtained, as well as their use in analysing shoe-surface friction. This will help improve the tribological understanding of future shoe friction studies.

During the literature review, gaps were found in both fundamental and shoe friction research. Previous experiments found that different orientations of a rectangular rubber block result in different dynamic frictions due to varied amounts of frictional heat [59], and that increasing the number of grooves on a rubber block reduces dynamic friction due to a reduced contact area that occurs during sliding [67]. However, little was reported on the frictional effect of rubber shape and how it may vary for different rubbers. This is important as it could inform the shapes used on tread patterns for shoes and tyres. Chapters 4 and 5 investigated the frictional effect of shape. Rubber shape was identified as a factor that influences the friction between rubber and dry hard courts, contradicting the classical laws of friction. It was identified that because of the deformability of rubber, different shapes (even with the same nominal contact area) produced different contact areas and pressures. In some cases, this caused dissimilar wearing which influences friction. In other cases, the change in contact pressure changed friction by a change in lateral coupling of asperity contacts and frictional heat. To further understand these effects of rubber shape on friction, in Chapter 5 the friction of two rubbers of different wearability were tested and modelled with an analytical model. Analytical rubber friction models cannot yet accurately predict the friction of a rubber block on a dry surface. It was found however, that a simple model could determine which rubber will have the higher friction but was unable to account for the contributions to friction that stem from shape and wear.

Chapter 5 also showed that the effect of shape on rubber friction was less prominent for rubbers with a greater tensile strength, and therefore improved wear resistance. This finding strengthens the likelihood that the effect of shape on rubber friction is linked to the rubber's wearability. Previous literature had linked the tensile strength of rubber to wear [48,110] and observed correlations between friction and wear [36], but this was the first time these connections had been used to explain the frictional differences of rubber shape.

The tests of Chapters 4 and 5 were at low load (10 N), low speed (< 10 mm/s) and on simple cuts of rubber. To determine whether the findings of these previous chapters apply to conditions like those experienced during hard court slides, the friction of tennis shoe tread elements was measured at loads and speeds close to that of hard court slides. This was important to test as rubber's viscoelastic properties means that friction is speed dependent [21]. Shape was found to have no effect on static friction, but longer shapes produced lower dynamic friction during high speed slides. A patterning was also observed on the contacting face of the rubber, in the form of ridges, perpendicular to the direction of travel. These were shown to produce a higher friction in one sliding direction compared to another. A survey of worn tennis shoes is needed to confirm that the asymmetric wear observed experimentally occurs during hard court tennis as it could have an influence of the frictional performance of shoes over time.

In addition to the lack of literature on the effect of shape on the friction of rubber, there was also no available methods to quantify shoe tread parameters beyond their contact area. Previous shoe friction studies had made it clear that different tread patterns produce different friction coefficients, which can influence the athletic performance [60,74]. But because of the lack of quantitative tread characterisation, very little is still known about which tread parameters influence friction and why. Therefore, in Chapter 7 a contact area image analysis method for quantifying tread geometries was created. This method took images of shoe-surface contacts and quantified numerous tread parameters (contact area, leading edge lengths, Hull  $I_{xx}$  etc.) using computer vision techniques. This new method still has limitations which prevent it from comprehensively explaining shoe-surface friction. Nevertheless, it gives more detail of tread patterns than anything previously published.

To determine whether the frictional effects observed during small scale friction experiments apply to full shoes, the friction of eight tennis shoes was taken and interpreted using the tread quantification method from Chapter 7 and measures taken by hand. Shoes produced dissimilar friction and had varied midsole constructions. By comparing two shoes differing only in tread pattern, higher contact area was observed to result in higher friction, supporting a finding made in a similar study [76]. This suggests that on dry surfaces, tread patterns that

produce higher contact areas produce higher friction. This finding could be used by shoe designers to improve the friction of footwear.

A limitation of the friction experiments in Chapter 7 and 8, was the test device used not being able to test at high slide speeds (as would be expected during hard court slides and other sporting movements). The need of more valid friction test devices, imitating real shoe-surface interactions, is a limitation of many sports shoe friction experiments [69]. To address this, a novel test device, valid to hard court slides, was proposed in Chapter 9. Though unable to be manufactured during this PhD (due to loss of additional funding related to COVID-19), the presented test device offers a method for the frictional analysis of tennis shoes in the future, allowing the opportunity for tennis shoes to be tested in conditions closer to real tennis movements. By conducting valid friction tests, shoes can then be better compared and assessed.

The friction of rubber on dry surfaces is a widely studied problem. This thesis builds on the previous knowledge in this area, focusing on the effect rubber shape can have on friction as this was not previously understood. The thesis then applies this knowledge and findings to the friction of tennis shoes on hard courts - a real situation that has implications to sporting performance and injury-rates. The findings of this thesis inform the ITF and shoe manufacturers of how tread can influence friction on dry surfaces, and a direction of future work that will further improve our understanding of this complex problem.

## 10.2 Thesis Limitations

Limitations are specified in the chapters throughout this thesis. This section mentions the main limitations of the overall work and approach of this thesis.

**Test device performance** – Friction experiments were performed on a UMT and the UoS Traction Device. Neither device was able to replicate the linear slide speeds and normal loads needed to produce comparable tribological conditions to those of hard court slides. A device capable of these parameters was designed (Chapter 9).

**Limited surfaces** – All the experiments in this thesis were performed on one surface type (hard court) from a single court manufacturer (Ace Surfaces North America). As such, whether the findings observed occur on other hard courts, from other manufacturers, is unknown. A thesis published in 2017 provides more detail on how surface parameters like roughness can influence friction [12].

**No athlete testing** – The experiments in this thesis were conducted using mechanical test devices instead of athlete testing. It is therefore not known whether the changes in friction

measured using the test devices are perceived by athletes, and whether they affect performance of real tennis movements.

Limitations such as using a single surface and only conducting mechanical tests allowed a greater focus on the tribological performance of the tested shoes and rubbers. However, they reduced the validity of experiments to the playing of tennis. It is intended that this thesis informs future research in the field of tennis shoe tribology. How this can be achieved is detailed in the following section of this chapter.

### 10.3 Overall Impact and Potential Future Use

The outcomes of this thesis improve the understanding of shoe-surface friction in hard court tennis, but more work is required before tribologically informed tennis shoes can be produced. Shoes designed for optimal friction could improve sporting performance and reduce injury rates. How this thesis informs future work in this field is shown on the following page in Figure 10.1.

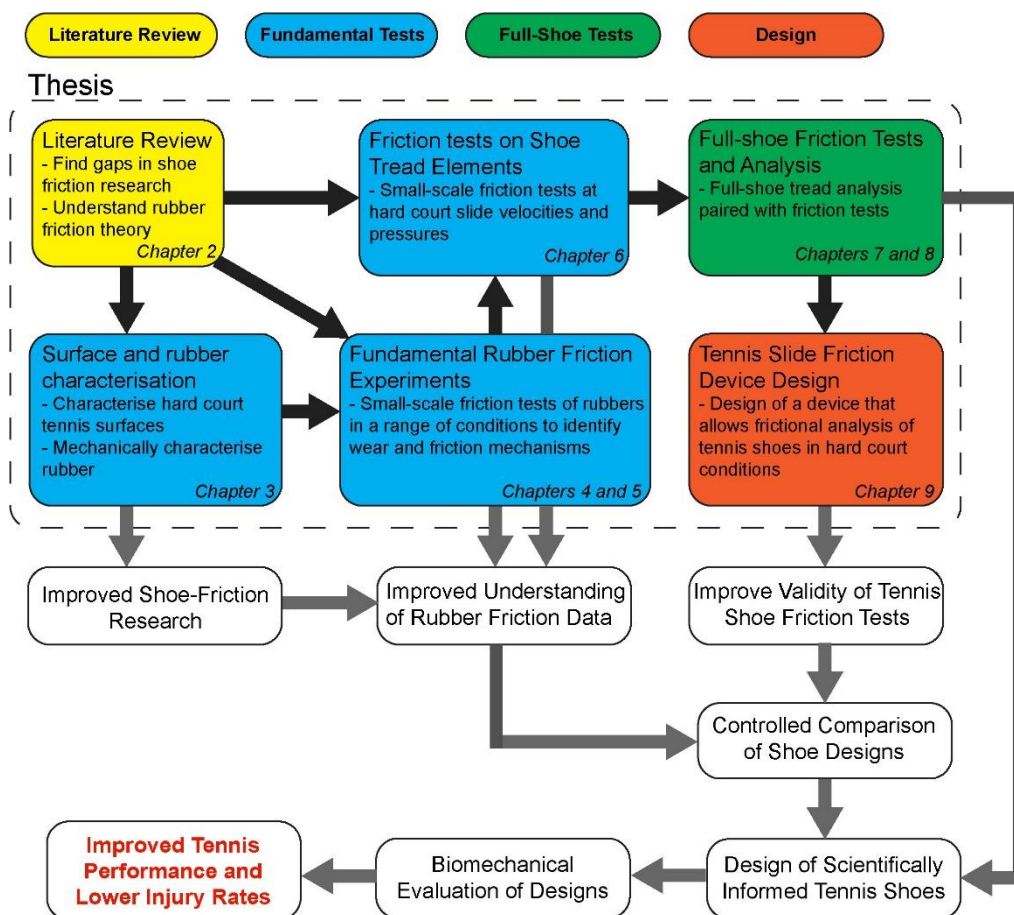


**Figure 10.1** How the thesis feeds into further research in the field, resulting in improved performance and reduced injury rates due to well-designed shoes.

The white sections of Figure 10.1 are the future work which links the content of this thesis to the final aim of improving tennis performance and lowering injury rates through the design and manufacture of shoes with optimal friction. In more detail, these recommended future steps are as follows:

- **Improved Shoe-Friction Research** – Findings from fundamental rubber tribology studies can be used to interpret the results of shoe friction studies. This can begin by using the characterisation techniques in Chapter 3 to provide a more relevant description of the rubber and surfaces being used in experiments. It is however acknowledged that this can be difficult if unable to obtain prismatic shaped cuts of the rubber for DMA or when there is no access to DMA machines.
- **Improved Understanding of Rubber Friction Data** – By better understanding the tribological mechanisms that affect rubber and how these change with sliding conditions and geometries, friction data from shoes can be better understood. Future work investigated shoe-surface friction should utilise the findings of fundamental rubber friction studies, even though they are typically aimed at automotive tyres.
- **Improved Validity of Tennis Shoe Friction Tests** – In Chapter 9 a test device is proposed that would allow the frictional analysis of full tennis shoes at speeds and loads closer to that of hard court slides, than is currently achievable. Though the financial uncertainty of the COVID-19 pandemic meant this could not be produced during this thesis, a device that utilises the mechanisms described in Chapter 9 would provide a more valid analysis of tennis shoe friction. Such tests would inform as to which shoes will produce dissimilar friction during hard court slides.
- **Controlled Comparisons of Shoe Designs** – To quantify how much different tread parameters influence friction, they must be well controlled. It is recommended to manufacture a series of tennis shoes that vary only in tread design, and then test their friction. Similar tread designs with small changes in contact area, beam stiffness or leading edges, would give a better understanding of how influential these parameters are, and what is worth changing in the design process of shoes.
- **Design of Scientifically Informed Tennis Shoes** – If the above steps are completed, tennis (and other similar sports) shoes could be manufactured with rubber grades, and tread patterns informed by tribological theory and empirical data. Once manufactured, these shoes would need to be tested by athletes in game situations, to determine whether the scientifically informed treads produce a noticeable effect on performance or the athlete's playing experience.

- **Biomechanical Evaluation of Designs** – Controlled biomechanics studies are needed to evaluate the tribologically informed tennis shoe designs before they are made commercially available. Such studies can focus on the performance of change of direction movements (timing how long it takes for athletes to perform the movements in different shoes), the perception of the shoe's performance by the athlete (using questionnaires), and over a longer time-frame, the injury-rate with different shoe designs (measuring impact forces and tracking athlete injuries over time).

#### 10.4 Tread Design Recommendations

The friction between a tennis shoe and a hard court surface is influenced by changes in rubber grade, slide speed, normal load and rubber shape, amongst others. Often, like in the case of hysteresis and slide velocity, the frictional influences simultaneously compete with one another and, like the frictional effect of wear, vary depending on the tread's sliding history. As such, detailed and complete predictive modelling of the frictional performance of tennis shoes is still a distant goal. Considering the intricacies of rubber's composition and surface roughness alone, it is understandable that even complex analytical rubber friction models require the use of open parameters based on experimental data. Thus, to formulate a shoe-friction model that gives accurate friction coefficients, it is recommended a group of researchers with varied expertise ranging from rubber rheology, rubber chemistry, mathematics and engineering be formed to do so. However, from the findings of this thesis and an extensive knowledge of rubber and shoe-surface friction research, some basic suggestions can be proposed which can assist tennis shoe outsole design. These are for shoes with rubber outsoles on a dry, rough surface:

- **Outsole Material** - To increase friction, determine the surface PSD and relevant slide speed to identify the operational frequency range. Then select a rubber with a higher loss  $\delta$  in this frequency range. To reduce wear, select a rubber with a high tensile strength.
- **Tread Pattern** - To increase friction, change the tread pattern to produce higher contact areas. This can be done in specific regions of the outsole that make contact during particular movements, or on the entire outsole. This thesis has been unable to categorically identify the specifics of tread shapes that influence friction on full tennis shoes, but the fundamental tests in this thesis (Chapters 4 – 6) suggest that longer shapes in the sliding direction will increase friction, providing the outsole material has a low wear-rate and the slide speed is low ( $< 1$  m/s). The opposite is true for high-speed scenarios ( $> 1$  m/s).

These simple suggestions do not lead to an optimum tread design. However, they provide insights into footwear outsole design which have not been collated before. As such, these suggestions, and the thesis in full provides a resource for future rubber/footwear friction researchers to quickly improve their understanding of rubber friction research and how it relates to aspects of footwear outsole design.

## 11 Conclusions

A review of literature found that many studies observe frictional differences between different shoes on dry surfaces. Due to the complexity of rubber tribology, scientific explanation for the findings of shoe-friction studies is often missing. Biomechanical analysis must control inter- and intra- participant variability to isolate frictional changes at the shoe-surface interface, and full-shoe mechanical analysis must use shoe constructions that are well controlled to negate energy losses in varying midsoles and uppers. This thesis adopted an engineering science approach to understanding shoe-surface tribology during hard court tennis, using mechanical test devices and experiments.

Chapter 3 detailed how key measures for rubber tribology (PSD and viscoelastic master curves) can be obtained and used. These measures can be utilised to compare the friction of rubber compounds. However, these measures are more complicated to obtain and interpret than the single value measures often used in shoe-friction research, notably  $Sh_A$  and  $R_a$ . However, by using these simple measures, the rubber and surfaces are under-characterised. In neither of the two most used analytical rubber friction models (Persson and HK), is  $Sh_A$  or  $R_a$  used.

In Chapter 4, obtained viscoelastic mater curves and PSD were used to interpret the results of small-scale friction experiments. These friction experiments focused on understanding how differences in rubber shape influence friction. This is a topic that is largely under-researched but has application to shoe-surface friction. It was observed that change in shape produced a change in friction when sliding over a hard court surface. The longer the shape in the sliding direction (with the same nominal contact area), the lower the friction. This was due to lower wear at the shorter leading edge, and increased temperature experienced by longer sliding shapes. An increase in slide speed produced an increase in friction- a result explained by the rubber's viscoelastic master curve. This study used a single commercially available rubber compound.

In Chapter 5 the friction of two rubber compounds with different mechanical characteristics was tested. The effect of shape on friction was different for the two rubbers. A wear test observed differences in the magnitude of wear experienced, and the wear scars implied contrasting wear mechanisms which may explain the frictional differences. A simplified version of the Persson friction model was able to predict which rubber compound produced the highest overall friction but was unable to predict the magnitude of the friction coefficients observed experimentally. The implication of this for tennis shoe designers, is that friction models can be used to compare the friction of different rubber compounds, but they are unable to accurately

determine friction coefficients or the effect shape will have on that rubber's friction. To understand how shape will influence the rubber's friction, tensile tests, and ideally wear tests must be conducted.

In Chapter 6, individual tread elements were cut from a tennis shoe, and had their friction tested. Unlike the testing in Chapters 4 and 5, loads and speeds close to those of real hard court steps and slides were used. No difference in static friction was observed for the change in tread orientation for step movements, though greater dynamic friction was observed for the short tread orientation during all slide tests. During testing, asymmetric ridges formed on the tread elements, which resulted in a frictional asymmetry. These would affect how a tennis shoe performs over time.

Chapter 7 outlined a series of full shoe friction tests using a modified version of the UoS Traction device. A single shoe was slid on a hard court surface at nine orientations. A bespoke contact imaging technique was created which allowed the quantification of contact areas-extracting parameters that described the contact patch. Due to test device limitations, links between contact patch parameters and shoe friction could not be conclusively made. However, in cases where comparable orientations were tested, the method gave insight into why friction was different.

Chapter 8 described the final set of experiments in this thesis. The friction of eight tennis shoes, from four different companies, were measured and compared. Shoes produced a significant difference in friction coefficient, and in a comparison of two shoes of the same model, with different tread patterns, the tread with the higher contact area, produced the higher friction. Though shoes varied a lot in the materials and mechanisms used in the midsoles, similarities across the shoes were also observed e.g. similar tread heights and midsole thicknesses. The results of this chapter suggest that an increase in tread contact area produces an increase in friction, when all other shoe features are equal. This finding, and the midsole and outsole measurements reported, could be of use to footwear engineers and designers.

Chapter 9 detailed the design and development of a novel test device. This device offered a solution to the current inability to mechanically test the friction of shoes at slide speeds close to that of hard court slides. Although useful information can be obtained at non-representative loads and speeds, the friction of viscoelastic materials is speed dependent, so valid friction coefficients can't be determined until representative test speeds are achieved.

In this thesis, the frictional influence of rubber shape was identified and investigated, a novel tread quantification method was created, and the frictional performance of current tennis

shoes was compared. To investigate tribological mechanisms, mechanical tests were used instead of biomechanical analyses. Though many uncertainties are still present regarding how tread design influences shoe-surface friction during hard court tennis movements, this thesis improves understanding of the interaction. Continued research in this field will result in the development of shoes designed using tribological principals. Such footwear will improve performance and reduce injury rates in tennis and other sports.

## 12 References

- [1] Nigg, B. M., Stefanyshyn, D. J., Rozitis, A. I., & Mündermann, A. (2009). Resultant knee joint moments for lateral movement tasks on sliding and non-sliding sport surfaces. *Journal of sports sciences*, 27(5), 427-435. doi:10.1080/02640410802669161.
- [2] Luo, G., & Stefanyshyn, D. (2011). Identification of critical traction values for maximum athletic performance. *Footwear Science*, 3(3), 127-138. doi:10.1080/19424280.2011.639807.
- [3] Worobets, J., & Wannop, J. W. (2015). Influence of basketball shoe mass, outsole traction, and forefoot bending stiffness on three athletic movements. *Sports Biomechanics*, 14(3), 351-360. doi:10.1080/14763141.2015.1084031.
- [4] Starbuck, C., Damm, L., Clarke, J., Carré, M., Capel-Davis, J., Miller, S., Stiles, V., Dixon, S. (2016). The influence of tennis court surfaces on player perceptions and biomechanical response. *Journal of sports sciences*, 34(17), 1627-1636. doi:10.1080/02640414.2015.1127988.
- [5] Villwock, M. R., Meyer, E. G., Powell, J. W., Fouty, A. J., & Haut, R. C. (2009). Football playing surface and shoe design affect rotational traction. *The American journal of sports medicine*, 37(3), 518-525. doi:10.1177/0363546508328108.
- [6] Carré, M. J., Clarke, J. D., Damm, L., & Dixon, S. J. (2014). Friction at the tennis shoe-court interface: how biomechanically informed lab-based testing can enhance understanding. *Procedia Engineering*, 72, 883-888. doi:10.1016/j.proeng.2014.06.151.
- [7] Barry, B., & Milburn, P. (2013). Tribology, friction and traction: understanding shoe-surface interaction. *Footwear Science*, 5(3), 137-145. doi:10.1080/19424280.2013.797030.
- [8] Ura, D., Carré, M. J., Charlton, H., Capel-Davies, J., Miller, S., Almenara, M. S., Astiz, J., de Alfonso Mustienes, A. (2014). Influence of clay properties on shoe-kinematics and friction during tennis movements. *Procedia Engineering*, 72, 889-894. doi:10.1016/j.proeng.2014.06.152.
- [9] Starbuck, C., Stiles, V., Urà, D., Carré, M., & Dixon, S. (2017). Biomechanical responses to changes in friction on a clay court surface. *Journal of science and medicine in sport*, 20(5), 459-463. doi:10.1016/j.jsams.2016.08.019.
- [10] Ura, D., Carré, M., & Dominguez-Caballero, J. A. (2015). Tennis shoe-court interactions: examining relationships between contact area, pressure and available friction. *Footwear Science*, 7(sup1), S87-S89. doi:10.1080/19424280.2015.1038624.
- [11] Damm, L., Starbuck, C., Stocker, N., Clarke, J., Carré, M., & Dixon, S. (2014). Shoe-

- surface friction in tennis: influence on plantar pressure and implications for injury. *Footwear Science*, 6(3), 155-164. doi:10.1080/19424280.2014.891659.
- [12] Ura, D. (2017). Development of a test device to measure the tribological behaviour of shoe-surface interactions in tennis (Doctoral dissertation, PhD Thesis, University of Sheffield, Sheffield, UK). Access online at: [https://etheses.whiterose.ac.uk/16882/1/Daniel%20Ura%20Thesis\\_R1.pdf](https://etheses.whiterose.ac.uk/16882/1/Daniel%20Ura%20Thesis_R1.pdf)
- [13] Pavaille, S., & Horvais, N. (2014). Sliding allows faster repositioning during tennis specific movements on hard court. *Procedia Engineering*, 72, 859-864. doi:10.1016/j.proeng.2014.06.157.
- [14] Roth, F. L., Driscoll, R. L., & Holt, W. L. (1943). Frictional properties of rubber. *Rubber Chemistry and Technology*, 16(1), 155-177. doi:10.6028/jres.028.016.
- [15] Schallamach, A. (1952). The load dependence of rubber friction. *Proceedings of the Physical Society. Section B*, 65(9), 657. doi:10.1088/0370-1301/65/9/301.
- [16] Greenwood, J. A., & Tabor, D. (1958). The friction of hard sliders on lubricated rubber: the importance of deformation losses. *Proceedings of the Physical Society (1958-1967)*, 71(6), 989. doi:10.1088/0370-1328/71/6/312.
- [17] Persson B.N.J. Persson, B. N. (1998). On the theory of rubber friction. *Surface science*, 401(3), 445-454. doi:10.1016/S0039-6028(98)00051-X.
- [18] Persson, B. N. (2000). *Sliding friction: physical principles and applications*. Springer Science & Business Media. doi:10.1007/978-3-662-04283-0.
- [19] Archard, J. (1953). Contact and rubbing of flat surfaces. *Journal of applied physics*, 24(8), 981-988. doi:10.1063/1.1721448.
- [20] Greenwood, J. A., & Williamson, J. P. (1966). Contact of nominally flat surfaces. *Proceedings of the royal society of London. Series A. Mathematical and physical sciences*, 295(1442), 300-319. doi:10.1098/rspa.1966.0242
- [21] Persson, B. N. (2001). Theory of rubber friction and contact mechanics. *The Journal of Chemical Physics*, 115(8), 3840-3861. doi:10.1063/1.1388626.
- [22] Carbone, G., Lorenz, B., Persson, B. N., & Wohlers, A. (2009). Contact mechanics and rubber friction for randomly rough surfaces with anisotropic statistical properties. *The European Physical Journal E*, 29(3), 275-284. doi:10.1140/epje/i2009-10484-8.
- [23] Persson, B. N., Albohr, O., Tartaglino, U., Volokitin, A. I., & Tosatti, E. (2004). On the nature of surface roughness with application to contact mechanics, sealing, rubber friction and adhesion. *Journal of physics: Condensed matter*, 17(1), R1. doi:10.1088/0953-8984/17/1/R01.
- [24] Wagner, P., Wriggers, P., Klapproth, C., Prange, C., & Wies, B. (2015). Multiscale FEM approach for hysteresis friction of rubber on rough surfaces. *Computer Methods in Applied Mechanics and Engineering*, 296, 150-168. doi:10.1016/j.cma.2015.08.003.
- [25] Tiwari, A., Miyashita, N., Espallargas, N., & Persson, B. N. (2018). Rubber friction: the contribution from the area of real contact. *The Journal of chemical physics*, 148(22), 224701. doi:10.1063/1.5037136.
- [26] Le Gal, A., & Klüppel, M. (2007). Investigation and modelling of rubber stationary friction on rough surfaces. *Journal of Physics: Condensed Matter*, 20(1), 015007. doi:10.1088/0953-8984/20/01/015007.

- [27] Persson, B. N. J. (2010). Rubber friction and tire dynamics. *Journal of Physics: Condensed Matter*, 23(1), 015003. doi:10.1088/0953-8984/23/1/015003.
- [28] Lang, A., & Klüppel, M. (2017). Influences of temperature and load on the dry friction behaviour of tire tread compounds in contact with rough granite. *Wear*, 380, 15-25. doi:10.1016/j.wear.2017.02.047.
- [29] Tiwari, A., Dorogin, L., Bennett, A. I., Schulze, K. D., Sawyer, W. G., Tahir, M., Heinrich, G., Persson, B. N. J. (2017). The effect of surface roughness and viscoelasticity on rubber adhesion. *Soft matter*, 13(19), 3602-3621. doi:10.1039/c7sm00177k.
- [30] Savkoor, A. R., & Briggs, G. A. D. (1977). The effect of tangential force on the contact of elastic solids in adhesion. *Proceedings of the Royal Society of London. A. Mathematical and Physical Sciences*, 356(1684), 103-114. doi:10.1098/rspa.1977.0123.
- [31] Fuller, K. N. G., & Tabor, D. (1975). The effect of surface roughness on the adhesion of elastic solids. *Proceedings of the Royal Society of London. A. Mathematical and Physical Sciences*, 345(1642), 327-342. doi: 10.1098/rspa.1975.0138
- [32] Briggs, G. A. D., & Briscoe, B. J. (1977). The effect of surface topography on the adhesion of elastic solids. *Journal of Physics D: Applied Physics*, 10(18), 2453. doi:10.1088/0022-3727/10/18/010.
- [33] Persson, B. N. J., & Tosatti, E. (2001). The effect of surface roughness on the adhesion of elastic solids. *The Journal of Chemical Physics*, 115(12), 5597-5610. doi:10.1063/1.1398300.
- [34] Tolpekina, T. V., & Persson, B. N. J. (2019). Adhesion and friction for three tire tread compounds. *Lubricants*, 7(3), 20. doi:10.3390/lubricants7030020.
- [35] Genovese, A., Farroni, F., Papangelo, A., & Ciavarella, M. (2019). A discussion on present theories of rubber friction, with particular reference to different possible choices of arbitrary roughness cutoff parameters. *Lubricants*, 7(10), 85. doi:10.3390/lubricants7100085.
- [36] Emami, A., & Khaleghian, S. (2019). Investigation of tribological behavior of Styrene-Butadiene Rubber compound on asphalt-like surfaces. *Tribology International*, 136, 487-495. doi:10.1016/j.triboint.2019.04.002.
- [37] Ferry, J. D. (1980). *Viscoelastic properties of polymers*. John Wiley & Sons. 3rd Edition.
- [38] Le Gal, A., Yang, X., & Klüppel, M. (2005). Evaluation of sliding friction and contact mechanics of elastomers based on dynamic-mechanical analysis. *The Journal of chemical physics*, 123(1), 014704. doi:10.1063/1.1943410.
- [39] Ciavarella, M. (2018). A simplified version of Persson's multiscale theory for rubber friction due to viscoelastic losses. *Journal of Tribology*, 140(1). doi:10.1115/1.4036917.
- [40] Carbone, G., & Putignano, C. (2013). A novel methodology to predict sliding and rolling friction of viscoelastic materials: Theory and experiments. *Journal of the Mechanics and Physics of Solids*, 61(8), 1822-1834. doi:10.1016/j.jmps.2013.03.005.
- [41] Wu, J., Wang, Y. S., Su, B. L., & Liu, Q. (2014). Experimental and numerical studies on tire tread block friction characteristics based on a new test device. *Advances in*

- Materials Science and Engineering, 2014. doi:10.1155/2014/816204.
- [42] Burwell Jr, J. T. (1957). Survey of possible wear mechanisms. *Wear*, 1(2), 119-141. doi:10.1016/0043-1648(57)90005-4.
- [43] Stachowiak GW. (2006) *Wear: materials, mechanisms and practice*. John Wiley & Sons.
- [44] Nguyen, V. H., Zheng, D., Schmerwitz, F., & Wriggers, P. (2018). An advanced abrasion model for tire wear. *Wear*, 396, 75-85. doi:10.1016/j.wear.2017.11.009.
- [45] Clarke, J., Carré, M., Damm, L., & Dixon, S. (2012). Understanding the influence of surface roughness on the tribological interactions at the shoe–surface interface in tennis. *Proceedings of the Institution of Mechanical Engineers, Part J: Journal of Engineering Tribology*, 226(7), 636-647. doi:10.1177/1350650112444694.
- [46] Williams, J. (2005). *Engineering tribology*. Cambridge University Press. doi:10.1017/CBO9780511805905.
- [47] Cole, K. (2017) *Evaluation of a portable device to assess shoe- court interactions in tennis*. University of Sheffield dissertation.
- [48] Muhr, A. H., & Roberts, A. D. (1992). Rubber abrasion and wear. *Wear*, 158(1-2), 213-228. doi:10.1016/0043-1648(92)90040-F.
- [49] Bui, Q. V., & Ponthot, J. P. (2002). Estimation of rubber sliding friction from asperity interaction modeling. *Wear*, 252(1-2), 150-160. doi:10.1016/S0043-1648(01)00864-X.
- [50] Emami, A., Khaleghian, S., Bezek, T., & Taheri, S. (2020). Design and development of a new portable test setup to study friction and wear. *Proceedings of the Institution of Mechanical Engineers, Part J: Journal of Engineering Tribology*, 234(5), 730-742. doi:10.1177/1350650119867795.
- [51] Baek, D. K., & Khonsari, M. M. (2008). Fretting behavior of a rubber coating: Effect of temperature and surface roughness variations. *Wear*, 265(5-6), 620-625. doi:10.1016/j.wear.2007.12.002.
- [52] Tiwari, A., Dorogin, L., Steenwyk, B., Warhadpande, A., Motamedi, M., Fortunato, G., Ciaravola, V., Persson, B. N. J. (2017). Rubber friction directional asymmetry. *EPL (Europhysics Letters)*, 116(6), 66002. doi:10.1209/0295-5075/116/66002.
- [53] Clarke, J., Carré, M., Damm, L., & Dixon, S. (2012). The influence of surface characteristics on the tribological interactions at the shoe-surface interface in tennis. *Procedia Engineering*, 34, 866-871. doi:10.1016/j.proeng.2012.04.148.
- [54] Pal, K., Pal, S. K., Das, C. K., & Kim, J. K. (2010). Relationship between normal load and dynamic co-efficient of friction on rock-rubber wear mechanism. *Materials & Design*, 31(10), 4792-4799. doi:10.1016/j.matdes.2010.05.006.
- [55] Dannenberg, E. M. (1982). Filler choices in the rubber industry. *Rubber Chemistry and Technology*, 55(3), 860-880. doi:10.5254/1.3535905.
- [56] Norman, D. T. (1990). *Rubber Grade Carbon Blacks*. The Vanderbilt Rubber Handbook, Ohm, RF Eds., RT Vanderbilt Company. Inc.: Connecticut. Accessed online at: [http://www.continentalcarbon.com/pdfs/What\\_Is\\_Carbon\\_Black.pdf](http://www.continentalcarbon.com/pdfs/What_Is_Carbon_Black.pdf)
- [57] Persson, B. N., & Tosatti, E. (2000). Qualitative theory of rubber friction and wear. *The Journal of Chemical Physics*, 112(4), 2021-2029. doi:10.1063/1.480762.

- [58] Bhattacharya, M., & Bhowmick, A. K. (2010). Analysis of wear characteristics of natural rubber nanocomposites. *Wear*, 269(1-2), 152-166. doi:10.1016/j.wear.2010.03.022.
- [59] Fortunato, G., Ciaravola, V., Furno, A., Lorenz, B., & Persson, B. N. J. (2015). General theory of frictional heating with application to rubber friction. *Journal of Physics: Condensed Matter*, 27(17), 175008. doi:10.1088/0953-8984/27/17/175008.
- [60] Valiant, G. A. (1986). The effect of outsole pattern on basketball shoe traction. In *ISBS-Conference Proceedings Archive*. Accessed online at: <https://ojs.ub.uni-konstanz.de/cpa/article/view/1497>
- [61] Goff, J. E., Ura, D., Boswell, L., & Carré, M. J. (2016). Parametric study of simulated tennis shoe treads. *Procedia engineering*, 147, 443-448. doi:10.1016/j.proeng.2016.06.338.
- [62] Goff, J. E., Boswell, L., Ura, D., Kozy, M., & Carré, M. J. (2018). Critical shoe contact area ratio for sliding on a tennis hard court. *Proceedings of the Institution of Mechanical Engineers, Part P: Journal of Sports Engineering and Technology*, 232(2), 112-121. doi:10.1177/1754337117715341.
- [63] Braun, O. M., Steenwyk, B., Warhadpande, A., & Persson, B. N. J. (2016). On the dependency of friction on load: Theory and experiment. *EPL (Europhysics Letters)*, 113(5), 56002. doi:10.1209/0295-5075/113/56002.
- [64] Ura, D., Clarke, J., & Carré, M. (2013). Effect of shoe orientation on shoe-surface traction in tennis. *Footwear Science*, 5(sup1), S86-S87. doi:10.1080/19424280.2013.799573.
- [65] Scaraggi, M., & Persson, B. N. (2015). General contact mechanics theory for randomly rough surfaces with application to rubber friction. *The Journal of chemical physics*, 143(22), 224111. doi:10.1063/1.4936558.
- [66] Heinrich, G., & Klüppel, M. (2008). Rubber friction, tread deformation and tire traction. *Wear*, 265(7-8), 1052-1060. doi:10.1016/j.wear.2008.02.016.
- [67] Maegawa, S., Itoigawa, F., & Nakamura, T. (2016). Effect of surface grooves on kinetic friction of a rubber slider. *Tribology International*, 102, 326-332. doi:10.1016/j.triboint.2016.05.019.
- [68] Hofstetter, K., Grohs, C., Eberhardsteiner, J., & Mang, H. A. (2006). Sliding behaviour of simplified tire tread patterns investigated by means of FEM. *Computers & structures*, 84(17-18), 1151-1163. doi:10.1016/j.compstruc.2006.01.010.
- [69] Chang, W. R., Grönqvist, R., Leclercq, S., Brungraber, R. J., Mattke, U., Strandberg, L., Thorpe, S. C., Myung, R., Makkonen, L., Courtney, T. K. (2001). The role of friction in the measurement of slipperiness, Part 2: Survey of friction measurement devices. *Ergonomics*, 44(13), 1233-1261. doi:10.1080/00140130110085583.
- [70] Clarke, J., Carre, M. J., Damm, L., & Dixon, S. (2013). The development of an apparatus to understand the traction developed at the shoe-surface interface in tennis. *Proceedings of the Institution of Mechanical Engineers, Part P: Journal of Sports Engineering and Technology*, 227(3), 149-160. doi:10.1177/1754337112469500.
- [71] Ura, D., & Carré, M. (2016). Development of a novel portable test device to measure the tribological behaviour of shoe interactions with tennis courts. *Procedia engineering*, 147, 550-555. doi:10.1016/j.proeng.2016.06.237.

- [72] Clarke, J., Dixon, S. J., Damm, L., & Carré, M. J. (2013). The effect of normal load force and roughness on the dynamic traction developed at the shoe–surface interface in tennis. *Sports Engineering*, 16(3), 165-171. doi:10.1007/s12283-013-0121-3.
- [73] Damm, L. C., Low, D., Richardson, A., Clarke, J., Carre, M., & Dixon, S. (2013). The effects of surface traction characteristics on frictional demand and kinematics in tennis. *Sports Biomechanics*, 12(4), 389-402. doi:10.1080/14763141.2013.784799.
- [74] Ismail SI, Nunome H, Tamura Y. (2020). Does visual representation of futsal shoes outsole tread groove design resemblance its mechanical traction, dynamic human traction performance, and perceived traction during change of direction and straight sprint tasks? *Footwear Science*, 13(1), 79-89. doi:10.1080/19424280.2020.1825534.
- [75] Needham, J. A., & Sharp, J. S. (2016). Watch your step! A frustrated total internal reflection approach to forensic footwear imaging. *Scientific reports*, 6(1), 1-7. doi:10.1038/srep21290.
- [76] Moriyasu, K., & Nishiwaki, T. (2015). Basic study on grip generation mechanism based on quantitative contact area measurement. *Footwear Science*, 7(sup1), 89-91. doi:10.1080/19424280.2015.1038625.
- [77] Li, K. W., Hsu, Y. W., Chang, W. R., & Lin, C. H. (2007). Friction measurements on three commonly used floors on a college campus under dry, wet, and sand-covered conditions. *Safety Science*, 45(9), 980-992. doi:10.1016/j.ssci.2006.08.030.
- [78] Kunz, J., & Studer, M. (2006). Determining the modulus of elasticity in compression via Shore-A hardness. *Kunststoffe international*, 96(6), 92-94. Accessed online at: <https://www.semanticscholar.org/paper/Determining-the-Modulus-of-Elasticity-in-via-the-A-Kunz-Studer/bff0d22268480a46f513047d518c444e15715a46>
- [79] Chang, W. R. (2001). The effect of surface roughness and contaminant on the dynamic friction of porcelain tile. *Applied ergonomics*, 32(2), 173-184. doi:10.1016/S0003-6870(00)00054-5.
- [80] Jacobs, T. D., Junge, T., & Pastewka, L. (2017). Quantitative characterization of surface topography using spectral analysis. *Surface Topography: Metrology and Properties*, 5(1), 013001. doi:10.1088/2051-672X/aa51f8.
- [81] Scaraggi, M., & Persson, B. N. J. (2015). Friction and universal contact area law for randomly rough viscoelastic contacts. *Journal of Physics: Condensed Matter*, 27(10), 105102. doi:10.1088/0953-8984/27/10/105102.
- [82] Fortunato, G., Ciaravola, V., Furno, A., Scaraggi, M., Lorenz, B., & Persson, B. N. (2017). Dependency of rubber friction on normal force or load: theory and experiment. *Tire science and technology*, 45(1), 25-54. doi:10.2346/tire.17.450103.
- [83] Kanafi, M. M., & Tuononen, A. J. (2017). Application of three-dimensional printing to pavement texture effects on rubber friction. *Road Materials and Pavement Design*, 18(4), 865-881. doi:10.1080/14680629.2016.1194883.
- [84] Shepard, M. K., Campbell, B. A., Bulmer, M. H., Farr, T. G., Gaddis, L. R., & Plaut, J. J. (2001). The roughness of natural terrain: A planetary and remote sensing perspective. *Journal of Geophysical Research: Planets*, 106(E12), 32777-32795. doi:10.1029/2000JE001429.
- [85] Lorenz, B., Oh, Y. R., Nam, S. K., Jeon, S. H., & Persson, B. N. J. (2015). Rubber friction on road surfaces: Experiment and theory for low sliding speeds. *The Journal of chemical physics*, 142(19), 194701. doi:10.1063/1.4919221.

- [86] Kummer, H. W. (1996) Unified theory of rubber and tire friction. University Park : Pennsylvania State University, College of Engineering.
- [87] Maegawa, S., Itoigawa, F., & Nakamura, T. (2016). A role of friction-induced torque in sliding friction of rubber materials. *Tribology International*, 93, 182-189. doi:10.1016/j.triboint.2015.08.030.
- [88] Ido, T., Yamaguchi, T., Shibata, K., Matsuki, K., Yumii, K., & Hokkirigawa, K. (2019). Sliding friction characteristics of styrene butadiene rubbers with varied surface roughness under water lubrication. *Tribology International*, 133, 230-235. doi:10.1016/j.triboint.2019.01.015.
- [89] Scaraggi, M., & Persson, B. N. J. (2016). The effect of finite roughness size and bulk thickness on the prediction of rubber friction and contact mechanics. *Proceedings of the Institution of Mechanical Engineers, Part C: Journal of Mechanical Engineering Science*, 230(9), 1398-1409. doi:10.1177/0954406216642261.
- [90] Kanafi, M. M., Tuononen, A. J., Dorogin, L., & Persson, B. N. (2017). Rubber friction on 3D-printed randomly rough surfaces at low and high sliding speeds. *Wear*, 376, 1200-1206. doi:10.1016/j.wear.2017.01.092.
- [91] Gordon, A., Glazko, G., Qiu, X., & Yakovlev, A. (2007). Control of the mean number of false discoveries, Bonferroni and stability of multiple testing. *The Annals of Applied Statistics*, 1(1), 179-190. doi:10.1214/07-aos102.
- [92] Makhovskaya, Y. (2019). Modeling sliding friction of a multiscale wavy surface over a viscoelastic foundation taking into account adhesion. *Lubricants*, 7(2), 13. doi:10.3390/lubricants7020013.
- [93] Hale, J., O'Connell, A., Lewis, R., Carré, M. J., & Rongong, J. A. (2021). An Evaluation of Shoe Tread Parameters using FEM. *Tribology International*, 153, 106570. doi:10.1016/j.triboint.2020.106570.
- [94] Ciavarella, M., & Papangelo, A. (2019). Some simple results on the multiscale viscoelastic friction. *Facta Universitatis, Series: Mechanical Engineering*, 17(2), 191-205. *Facta Univ Ser Mech Eng* 2019;17. doi:10.22190/FUME190215025C.
- [95] Tolpekina, T. V., Pyckhout-Hintzen, W., & Persson, B. N. J. (2019). Linear and nonlinear viscoelastic modulus of rubber. *Lubricants*, 7(3), 22. doi:10.3390/lubricants7030022.
- [96] Damm, L., Low, D., Richardson, A., Clarke, J., Carre, M., & Dixon, S. (2011). Modulation of tennis players' frictional demand according to surface traction characteristics. In *ISB 2011: Proceedings of the International Society of Biomechanics Congress XXIII*. Accessed online at: <https://www.semanticscholar.org/paper/Modulation-of-tennis-players%E2%80%99-frictional-demand-to-Damm-Low/eed84ca775f3a0b63c3b6a37be6be83a8748ee90>
- [97] Lakens, D. (2013). Calculating and reporting effect sizes to facilitate cumulative science: a practical primer for t-tests and ANOVAs. *Frontiers in psychology*, 4, 863. doi:10.3389/fpsyg.2013.00863.
- [98] Holm, S. (1979). A simple sequentially rejective multiple test procedure. *Scandinavian journal of statistics*, 65-70. Accessed online at: <https://www.jstor.org/stable/4615733>
- [99] Rice, M. E., & Harris, G. T. (2005). Comparing effect sizes in follow-up studies: ROC Area, Cohen's d, and r. *Law and human behavior*, 29(5), 615. doi:10.1007/s10979-005-6832-7.

- [100] Iwai, T., Uchiyama, Y., Shimosaka, K., & Takase, K. (2005). Study on the formation of periodic ridges on the rubber surface by friction and wear monitoring. *Wear*, 259(1-6), 669-675. doi:10.1016/j.wear.2005.01.012.
- [101] Uchiyama, Y., & Ishino, Y. (1992). Pattern abrasion mechanism of rubber. *Wear*, 158(1-2), 141-155. doi:10.1016/0043-1648(92)90035-7.
- [102] Persson, B. N. J. (2014). Role of frictional heating in rubber friction. *Tribology letters*, 56(1), 77-92. doi:10.1007/s11249-014-0386-0.
- [103] Wang, Z., Hu, S., Miao, Z., & Ma, L. (2018). Application of Multifractal Spectrum Calculation Program in Rubber Wear Under High Temperature. *Wireless Personal Communications*, 103(1), 1-9. doi:10.1007/s11277-018-5419-9.
- [104] Hakami, F., Pramanik, A., Ridgway, N., & Basak, A. K. (2017). Developments of rubber material wear in conveyer belt system. *Tribology International*, 111, 148-158. doi:10.1016/j.triboint.2017.03.010.
- [105] French, M. J. (1971) *Engineering Design: The Conceptual Stage*. 1st ed. London: Heinemann.
- [106] Wright, I. C. (1998) *Design Methods in Engineering and Product Design*. 1st ed. United Kingdom: McGraw-Hill.
- [107] Pugh, S. (1990) *Total design integrated methods for successful product engineering*. 1st ed. Wokingham: Addison-Wesley.
- [108] Clarke J, Carré M, Richardson A, Yang Z, Damm L, Dixon S. (2011). Understanding the traction of tennis surfaces. *Procedia Engineering*, 13, 402-408. doi:10.1016/j.proeng.2011.05.105.
- [109] Tsai HK, Li KW, Chen CC.(2016). Effects of footwear sample area on the friction coefficient on the floor. *IEEE International Conference on Industrial Engineering and Engineering Management (IEEM)*, 1, 338-341. doi:10.1109/IEEM.2015.7385664.
- [110] Grosch KA, Schallamach A. (1966). Relation between Abrasion and Strength of Rubber. *Rubber Chemistry and Technology*, 39(2), 287-305. doi:10.5254/1.3544841.
- [111] Childs, P. R. N. (2004) *Mechanical Design*. 2nd ed. London: Elsevier.
- [112] Sell, R., & Tamre, M. (2005). Integration of V-model and SysML for advanced mechatronics system design. In *The 6th International Workshop on Research and Education in Mechatronics REM* (pp. 276-280). Accessed online at: <https://www.semanticscholar.org/paper/Integration-of-V-model-and-SysML-for-advanced-Sell-Tamre/3f111827925c6c7f5138695b4d85fbaea233fcb3>

# Appendix

Full code for image processing in Chapter 7 (written using Jupyter Notebooks in Python 3):

## Shoe Parameters

This script runs a function on all images in a folder, outputting three text files (start, dyn, end). - John Hale (04/2021)

- Define the function, this is shown for clarity.

```
def TreadAnalyser(Shoename = 'ADIsol', Threshold=0.65, Angs = ['0','225','45','675','90'], save = 'N'):  
  
    if Shoename == 'DEC_01' or "2DEC":  
        Angs = ['-90','-675','-45','-225','0','225','45','675','90'] #Dec was tested at a large range of orientations  
  
    from PIL import Image  
    import matplotlib.pyplot as plt  
    from matplotlib import image as mp_image  
    import numpy as np  
  
    #Create filenames  
    path = 'C:\\Users\\John Hale\\Desktop\\PhD\\Papers\\Image Processing Method Paper\\Method\\'+Shoename+'\\Importantframes'  
    Movs = ['static','dynamic','end']  
    FileNames = []  
    for i in Angs:  
        for j in Movs:  
            FileNames.append(i+'deg_'+j+'.jpg')  
  
    FullFileNames = []  
    for i in FileNames:  
        FullFileNames.append(path+i)  
  
    #Crop and grayscale all images  
    import skimage as sk  
    from skimage import io as sk_io  
    from skimage.io._plugins.pil_plugin import pil_to_ndarray  
  
    CropRect = [100,100,850,950]  
    G_CropImages = []  
    for i in FullFileNames:  
        IM = Image.open(i)  
        IMCrop = IM.crop(CropRect)  
        sk_image = pil_to_ndarray(IMCrop)  
        gray_image = sk.color.rgb2gray(sk_image)  
        G_CropImages.append(gray_image)  
  
    #Threshold images (at 0.65)  
    from skimage.morphology import erosion, dilation, opening, closing  
  
    from skimage.morphology import disk  
    from skimage import morphology as sk_mm  
    from skimage.measure import label, regionprops, regionprops_table  
    from skimage import morphology  
    import pandas as pd  
  
    Fin_Images = []  
    kernel_t = disk(2) #may be too high 10- used on decathlon  
    kernel_t2 = disk(10) #5 for decathlon / 8  
    kernel_t3 = disk(10)  
    thresh = Threshold  
  
    #The for loop below generates the grayscale images of just the tread contact.  
    #From these images, we want to take some details of light intensities, before binarising for further tread analysis  
  
    MaxInt = [] #max light intensity in final image (by final image the infernos are a depiction of this) #Variable 1  
    MeanInt = [] #mean light intensity in final image, ignoring the zero regions #Variable 2  
    SumInt = [] #sum of all intensity values  
  
    for i in G_CropImages:  
        T_im = i>thresh  
        T_im[T_im>thresh]=1  
        T_im2 = T_im*i  
        if Shoename == 'DEC_01':  
            kernel_t = disk(10)  
            kernel_t2 = disk(5)  
            closed = closing(T_im, kernel_t) #used for decathlon  
            opened = opening(closed, kernel_t2) #used for decathlon  
            ObRem = 1700 #This removes a big light area on these images, which was consequence of not properly blocking out  
        else:  
            if Shoename == 'ADIsup':  
                kernel_t = disk(1)  
                kernel_t2 = disk(5)  
                ObRem = 100  
            if Shoename == 'ADIsol':  
                kernel_t = disk(2)  
                kernel_t2 = disk(10)  
                ObRem = 200  
            else:  
                ObRem = 200  
            eros = erosion(T_im, kernel_t)  
            opened = dilation(eros, kernel_t2) #t2  
  
        fin_im = opened  
        label_img = label(fin_im)  
        Mask = morphology.remove_small_objects(label_img, ObRem) #1700 used for decathlon  
        if Shoename is not 'DEC_01':
```

```

        if Shoename == 'ADIsup':
            kernel_t3 = disk(5)
        if Shoename == 'ADIsol':
            kernel_t3 = disk(2)
        else:
            kernel_t3 = disk(10)
        Mask = dilation(Mask, kernel_t3) #t3

Mask[Mask>1] = 1
Gfinal = T_im2*Mask
Fin_Images.append(Gfinal) # saves grayscale images of just tread contact

locs = np.where(Gfinal > 0.64)
pixels = Gfinal[locs]
MeanInt.append(np.mean(pixels))
MaxInt.append(np.amax(Gfinal))
SumInt.append(np.sum(pixels))

#make sure white areas are set at a value of 1 for all images (setting to binary for the tread analysis)
BWs = []
for i in Fin_Images:
    BW = 1
    BW[BW>0] = 1
    BWs.append(BW)

if save == 'Y':
    from PIL import Image
    from matplotlib import cm

    svfilepath = path+'Pr_images'
    n = 0
    for i in Fin_Images:
        ims = Image.fromarray(np.uint8((cm.inferno(i))*255))
        rgb_im = ims.convert('RGB')
        ims = rgb_im.save(svfilepath+'\\Pr'+FileNames[n]) #Use to save image
        n += 1

#Find pixel and mm contact areas
CA_px2 = [] # raw pixel areas #Not really necessary to save pixels
CA_mm2 = [] # mm2 areas #Variable 3 -
CoM_X = [] #x-coordinate of tread CoM
CoM_Y = [] #y-coordinate of tread CoM
from scipy import ndimage

for i in Fin_Images: #Fin_Images not BWs?
    n_white_pix = np.sum(i==1)
    CA_px2.append(n_white_pix)
    CA_mm2.append(round(n_white_pix*0.165762,2)) #correct conversion to area in mm2
    CoM = ndimage.measurements.center_of_mass(i*255)
    X = CoM[1]
    Y = CoM[0]
    CoM_X.append(X)
    CoM_Y.append(Y)

#Before running further tread analysis, fill small holes to make analysis clearer
kernel = disk(3) # fill holes
fil_BWs = []
for i in BWs:
    closed_im = sk_mm.closing(i, kernel)
    fil_BWs.append(closed_im)

#Use this filled image to quantify tread parameters
from skimage.morphology import convex_hull_image
from skimage.morphology import skeletonize
from scipy import ndimage

HullIyys = [] #Variable 4 -
HullIxxs = [] #Variable 5 -
HullArea = [] #Variable 6 -
LE_ims = [] #Just images of leading edges -
Edge_mm = [] #Variable 7 -
NoAreas = [] #Variable 8 -
LargestArea = [] #Variable 9 -
MeanPartArea = [] #Variable 10 -
MeanIyy = [] #Variable 11 -
MeanIxx = [] #Variable 12 -
MaxIyy = [] #Variable 13 -
MaxIxx = [] #Variable 14 -
Width = []
Height = []

n = 1
for i in fil_BWs:
    #first convex hull and find details
    Chull = convex_hull_image(i) #convex hull of binary
    label_Chull = label(Chull)
    props = regionprops_table(label_Chull, properties=('moments_central', 'area'))
    DF_props = pd.DataFrame(props)

    Hull_Iyy = DF_props["moments_central-2-0"][0]*0.0256 #convert to mm4 (same as 0.4^4)
    Hull_Ixx = DF_props["moments_central-0-2"][0]*0.0256 # convert to mm4 (same as 0.4^4)
    Hull_Area = DF_props["area"][0]*0.165762 # convert to mm2

    HullIyys.append(round(Hull_Iyy,2))
    HullIxxs.append(round(Hull_Ixx,2))
    HullArea.append(round(Hull_Area,2))

```

```

#width and height of hull
import cv2

Chullcont = np.array(Chull, dtype=np.uint8)

cnts = cv2.findContours(Chullcont,cv2.RETR_EXTERNAL, cv2.CHAIN_APPROX_SIMPLE)
cnts = cnts[0] if len(cnts) == 2 else cnts[1]
c = max(cnts, key=cv2.contourArea)

left = tuple(c[c[:, :, 0].argmin()][0])
right = tuple(c[c[:, :, 0].argmax()][0])
top = tuple(c[c[:, :, 1].argmin()][0])
bottom = tuple(c[c[:, :, 1].argmax()][0])

width = (right[0] - left[0])*0.4 #convert to mm
height = (bottom[1] - top[1])*0.4 #due to axis method on images

Width.append(width)
Height.append(height)

#second details of non-conv hull
label_im = label(i)
improps = regionprops_table(label_im, properties=('moments_central','area'))
DF_improps = pd.DataFrame(improps)

nonZindAreas = [] #all areas over 1 pix
nonZindIyy = []
nonZindIxx = []

DFlen = DF_improps.shape
DFlen = DFlen[0]
for j in range(0,DFlen):
    if float(DF_improps["area"][j]) > 1:
        nonZindAreas.append(DF_improps["area"][j])
        nonZindIyy.append(DF_improps["moments_central-2-0"][j]*0.0256)
        nonZindIxx.append(DF_improps["moments_central-0-2"][j]*0.0256)

NoAreas.append(len(nonZindAreas))
LargestArea.append(np.max(nonZindAreas))
MeanPartArea.append(np.mean(nonZindAreas))
MeanIyy.append(np.mean(nonZindIyy))
MeanIxx.append(np.mean(nonZindIxx))
MaxIyy.append(np.max(nonZindIyy))
MaxIxx.append(np.max(nonZindIxx))

#thirdly leading edge in slide direction
h_e = ndimage.sobel(i, 1) # horizontal derivative
rightside = h_e<0
skeleton = skeletonize(rightside)
n_white_pix = np.sum(skeleton==1)

LE_Imms.append(skeleton)
Edge_mm.append(round(n_white_pix*0.4,2)) # 1 vert pix = 0.4 mm.

#Outputting function
def dataout(statdynend,Shoename,thresh):
    #should output in order of -90 to 90
    S_fn = []
    for i in Angs:
        S_fn.append(i+'deg_'+statdynend+'.jpg')

    st_loc = []
    for i in S_fn:
        st_loc.append(FileNames.index(i))

    F_MaxInt = [] #Variable 1 - The max light intensity in contact image
    F_MeanInt = [] #Variable 2 - The mean light intensity in contact image
    F_CA_mm2 = [] #Variable 3 - The overall contact area
    F_HullIyys = [] #Variable 4 - The hull Iyy
    F_HullIxxs = [] #Variable 5 - The hull Ixx
    F_HullArea = [] #Variable 6 - The hull area
    F_Edge_mm = [] #Variable 7 - The leading edge Length
    F_NoAreas = [] #Variable 8 - The number of tread contact areas
    F_LargestArea = [] #Variable 9 - The largest area of all the tread contact areas
    F_MeanPartArea = [] #Variable 10 - The mean area of all the tread contact areas
    F_MeanIxx = [] #Variable 11 - The mean Ixx of all the tread contact areas
    F_MeanIyy = [] #Variable 12 - The mean Iyy of all the tread contact areas
    F_MaxIyy = [] #Variable 13 - The max Iyy of the tread contact areas
    F_MaxIxx = [] #Variable 14 - The max Ixx of the tread contact areas
    F_SumInt = []
    F_Width = []
    F_Height = []
    F_CoMX = []
    F_CoMY = []

    for i in st_loc:
        F_MaxInt.append(MaxInt[i])
        F_MeanInt.append(MeanInt[i])
        F_CA_mm2.append(CA_mm2[i])
        F_HullIyys.append(HullIyys[i])
        F_HullIxxs.append(HullIxxs[i])
        F_HullArea.append(HullArea[i])
        F_Edge_mm.append(Edge_mm[i])
        F_NoAreas.append(NoAreas[i])
        F_LargestArea.append(LargestArea[i])
        F_MeanPartArea.append(MeanPartArea[i])
        F_MeanIxx.append(MeanIxx[i])

```

```

F_MeanIxx.append(MeanIxx[i])
F_MeanIyy.append(MeanIyy[i])
F_MaxIyy.append(MaxIyy[i])
F_MaxIxx.append(MaxIxx[i])
F_SumInt.append(SumInt[i])
F_Width.append(round(Width[i],1))
F_Height.append(round(Height[i],1))
F_CoMX.append(round(CoM_X[i],2))
F_CoMY.append(round(CoM_Y[i],2))

data = [F_MaxInt,F_MeanInt,F_CA_mm2,F_HullIyys,F_HullIxxs,F_HullArea,F_Edge_mm,F_NoAreas,F_LargestArea,F_MeanPartArea,F_
with open(path+str(thresh)+statdynend+"output2.txt", "w") as txt_file:
    for line in data:
        txt_file.write("".join(str(line))+'\n')

statdynend = ['static','dynamic','end']#dynamic or end
for i in statdynend:
    dataout(i,Shoename,thresh) # run output function

```

- Run for all shoes. dilation and erosion (to remove scratches) of the decathlon, and two adidas shoes was different to the others, this is done automatically within the function based on the Shoename.

```

Shoename = ['2DEC'] #, 'ADIsol', 'ADIsup', 'ASIspeed', 'NIKcagehc', 'NIKpresclay', 'NIKpresflat', 'NIKturbo'

Threshold=[0.15]
for i in Shoename:
    for j in Threshold:
        TreadAnalyser(i,j,save = 'V')

```

End of Python code.

**Table A.1** All correlations for all parameters during friction tests of TS100 tennis shoe through nine orientations.

|                        |                     | Correlations |                        |                    |               |               |                 |                   |              |                    |                      |                    |                    |                   |                   |                |         |
|------------------------|---------------------|--------------|------------------------|--------------------|---------------|---------------|-----------------|-------------------|--------------|--------------------|----------------------|--------------------|--------------------|-------------------|-------------------|----------------|---------|
|                        |                     | Orien        | Mean Light Int (0 - 1) | Contact Area (mm2) | Hull Iy (mm4) | Hull Ix (mm4) | Hull Area (mm2) | Leading Edge (mm) | No. of Areas | Largest Area (mm2) | Mean Part Area (mm2) | Mean Part Ix (mm4) | Mean Part Iy (mm4) | Max Part Ix (mm4) | Max Part Iy (mm4) | absYplaneangle | adjDCoF |
| Orien                  | Pearson Correlation | 1            |                        |                    |               |               |                 |                   |              |                    |                      |                    |                    |                   |                   |                |         |
|                        | Sig. (2-tailed)     |              | 0.98                   | 0.78               | 0.78          | 0.78          | 0.78            | 0.78              | 0.78         | 0.78               | 0.78                 | 0.78               | 0.78               | 0.78              | 0.78              | 0.78           | 0.78    |
|                        | N                   | 63           | 63                     | 63                 | 63            | 63            | 63              | 63                | 63           | 63                 | 63                   | 63                 | 63                 | 63                | 63                | 63             | 63      |
| Mean Light Int (0 - 1) | Pearson Correlation |              | 1                      |                    |               |               |                 |                   |              |                    |                      |                    |                    |                   |                   |                |         |
|                        | Sig. (2-tailed)     |              |                        | 0.98               | 0.78          | 0.78          | 0.78            | 0.78              | 0.78         | 0.78               | 0.78                 | 0.78               | 0.78               | 0.78              | 0.78              | 0.78           | 0.78    |
|                        | N                   |              | 63                     | 63                 | 63            | 63            | 63              | 63                | 63           | 63                 | 63                   | 63                 | 63                 | 63                | 63                | 63             | 63      |
| Contact Area (mm2)     | Pearson Correlation |              |                        | 1                  |               |               |                 |                   |              |                    |                      |                    |                    |                   |                   |                |         |
|                        | Sig. (2-tailed)     |              |                        |                    | 0.98          | 0.78          | 0.78            | 0.78              | 0.78         | 0.78               | 0.78                 | 0.78               | 0.78               | 0.78              | 0.78              | 0.78           | 0.78    |
|                        | N                   |              |                        | 63                 | 63            | 63            | 63              | 63                | 63           | 63                 | 63                   | 63                 | 63                 | 63                | 63                | 63             | 63      |
| Hull Iy (mm4)          | Pearson Correlation |              |                        |                    | 1             |               |                 |                   |              |                    |                      |                    |                    |                   |                   |                |         |
|                        | Sig. (2-tailed)     |              |                        |                    |               | 0.98          | 0.78            | 0.78              | 0.78         | 0.78               | 0.78                 | 0.78               | 0.78               | 0.78              | 0.78              | 0.78           | 0.78    |
|                        | N                   |              |                        |                    | 63            | 63            | 63              | 63                | 63           | 63                 | 63                   | 63                 | 63                 | 63                | 63                | 63             | 63      |
| Hull Ix (mm4)          | Pearson Correlation |              |                        |                    |               | 1             |                 |                   |              |                    |                      |                    |                    |                   |                   |                |         |
|                        | Sig. (2-tailed)     |              |                        |                    |               |               | 0.98            | 0.78              | 0.78         | 0.78               | 0.78                 | 0.78               | 0.78               | 0.78              | 0.78              | 0.78           | 0.78    |
|                        | N                   |              |                        |                    |               | 63            | 63              | 63                | 63           | 63                 | 63                   | 63                 | 63                 | 63                | 63                | 63             | 63      |
| Hull Area (mm2)        | Pearson Correlation |              |                        |                    |               |               | 1               |                   |              |                    |                      |                    |                    |                   |                   |                |         |
|                        | Sig. (2-tailed)     |              |                        |                    |               |               |                 | 0.98              | 0.78         | 0.78               | 0.78                 | 0.78               | 0.78               | 0.78              | 0.78              | 0.78           | 0.78    |
|                        | N                   |              |                        |                    |               |               | 63              | 63                | 63           | 63                 | 63                   | 63                 | 63                 | 63                | 63                | 63             | 63      |
| Leading Edge (mm)      | Pearson Correlation |              |                        |                    |               |               |                 | 1                 |              |                    |                      |                    |                    |                   |                   |                |         |
|                        | Sig. (2-tailed)     |              |                        |                    |               |               |                 |                   | 0.98         | 0.78               | 0.78                 | 0.78               | 0.78               | 0.78              | 0.78              | 0.78           | 0.78    |
|                        | N                   |              |                        |                    |               |               |                 | 63                | 63           | 63                 | 63                   | 63                 | 63                 | 63                | 63                | 63             | 63      |
| No. of Areas           | Pearson Correlation |              |                        |                    |               |               |                 |                   | 1            |                    |                      |                    |                    |                   |                   |                |         |
|                        | Sig. (2-tailed)     |              |                        |                    |               |               |                 |                   |              | 0.98               | 0.78                 | 0.78               | 0.78               | 0.78              | 0.78              | 0.78           | 0.78    |
|                        | N                   |              |                        |                    |               |               |                 |                   | 63           | 63                 | 63                   | 63                 | 63                 | 63                | 63                | 63             | 63      |
| Largest Area (mm2)     | Pearson Correlation |              |                        |                    |               |               |                 |                   |              | 1                  |                      |                    |                    |                   |                   |                |         |
|                        | Sig. (2-tailed)     |              |                        |                    |               |               |                 |                   |              |                    | 0.98                 | 0.78               | 0.78               | 0.78              | 0.78              | 0.78           | 0.78    |
|                        | N                   |              |                        |                    |               |               |                 |                   |              | 63                 | 63                   | 63                 | 63                 | 63                | 63                | 63             | 63      |
| Mean Part Area (mm2)   | Pearson Correlation |              |                        |                    |               |               |                 |                   |              |                    | 1                    |                    |                    |                   |                   |                |         |
|                        | Sig. (2-tailed)     |              |                        |                    |               |               |                 |                   |              |                    |                      | 0.98               | 0.78               | 0.78              | 0.78              | 0.78           | 0.78    |
|                        | N                   |              |                        |                    |               |               |                 |                   |              |                    | 63                   | 63                 | 63                 | 63                | 63                | 63             | 63      |
| Mean Part Ix (mm4)     | Pearson Correlation |              |                        |                    |               |               |                 |                   |              |                    |                      | 1                  |                    |                   |                   |                |         |
|                        | Sig. (2-tailed)     |              |                        |                    |               |               |                 |                   |              |                    |                      |                    | 0.98               | 0.78              | 0.78              | 0.78           | 0.78    |
|                        | N                   |              |                        |                    |               |               |                 |                   |              |                    |                      | 63                 | 63                 | 63                | 63                | 63             | 63      |
| Mean Part Iy (mm4)     | Pearson Correlation |              |                        |                    |               |               |                 |                   |              |                    |                      |                    | 1                  |                   |                   |                |         |
|                        | Sig. (2-tailed)     |              |                        |                    |               |               |                 |                   |              |                    |                      |                    |                    | 0.98              | 0.78              | 0.78           | 0.78    |
|                        | N                   |              |                        |                    |               |               |                 |                   |              |                    |                      |                    | 63                 | 63                | 63                | 63             | 63      |
| Max Part Ix (mm4)      | Pearson Correlation |              |                        |                    |               |               |                 |                   |              |                    |                      |                    |                    | 1                 |                   |                |         |
|                        | Sig. (2-tailed)     |              |                        |                    |               |               |                 |                   |              |                    |                      |                    |                    |                   | 0.98              | 0.78           | 0.78    |
|                        | N                   |              |                        |                    |               |               |                 |                   |              |                    |                      |                    |                    | 63                | 63                | 63             | 63      |
| Max Part Iy (mm4)      | Pearson Correlation |              |                        |                    |               |               |                 |                   |              |                    |                      |                    |                    |                   | 1                 |                |         |
|                        | Sig. (2-tailed)     |              |                        |                    |               |               |                 |                   |              |                    |                      |                    |                    |                   |                   | 0.98           | 0.78    |
|                        | N                   |              |                        |                    |               |               |                 |                   |              |                    |                      |                    |                    |                   | 63                | 63             | 63      |
| absYplaneangle         | Pearson Correlation |              |                        |                    |               |               |                 |                   |              |                    |                      |                    |                    |                   |                   | 1              |         |
|                        | Sig. (2-tailed)     |              |                        |                    |               |               |                 |                   |              |                    |                      |                    |                    |                   |                   |                | 0.98    |
|                        | N                   |              |                        |                    |               |               |                 |                   |              |                    |                      |                    |                    |                   |                   | 63             | 63      |
| adjDCoF                | Pearson Correlation |              |                        |                    |               |               |                 |                   |              |                    |                      |                    |                    |                   |                   |                | 1       |
|                        | Sig. (2-tailed)     |              |                        |                    |               |               |                 |                   |              |                    |                      |                    |                    |                   |                   |                |         |
|                        | N                   |              |                        |                    |               |               |                 |                   |              |                    |                      |                    |                    |                   |                   |                | 63      |

\*. Correlation is significant at the 0.05 level (2-tailed).

\*\* Correlation is significant at the 0.01 level (2-tailed).